Safe Navigation of Autonomous Vessels in Inland Waterways under Uncertain and Abnormal Operational Conditions

Abhishek Dhyani

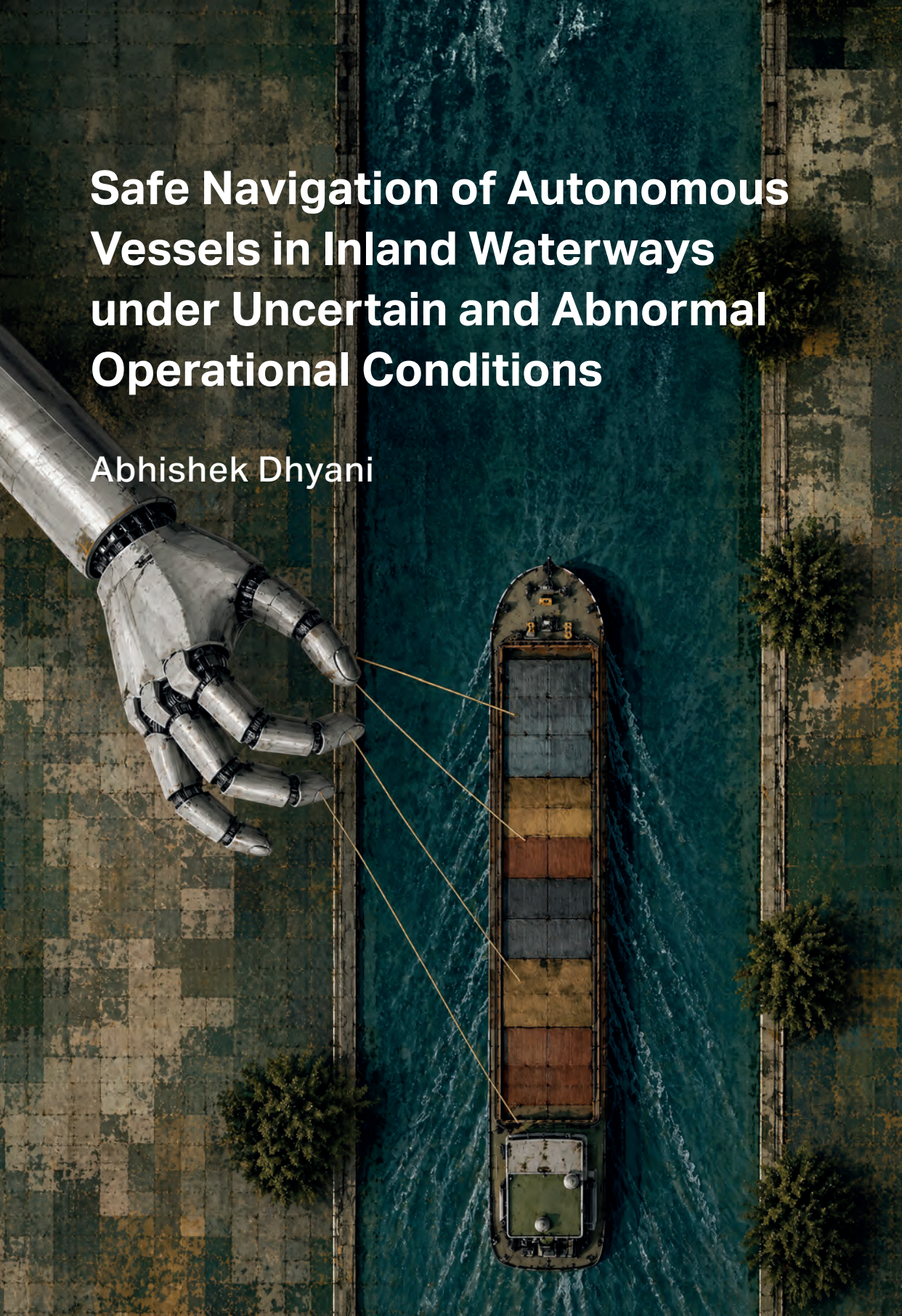

Safe Navigation of Autonomous Vessels in Inland Waterways under Uncertain and Abnormal Operational Conditions

Abhishek DHYANI

Safe Navigation of Autonomous Vessels in Inland Waterways under Uncertain and Abnormal Operational Conditions

Dissertation

for the purpose of obtaining the degree of doctor
at Delft University of Technology
by the authority of the Rector Magnificus, Prof. dr. ir. H. Bijl,
chair of the Board for Doctorates
to be defended publicly on
Tuesday, 23 June 2026 at 10:00

by

Abhishek DHYANI

This dissertation has been approved by the promotors.

Composition of the doctoral committee:

Rector Magnificus	Chairperson
Prof. dr. R.R. Negenborn	Delft University of Technology, promotor
Dr. V. Reppa	Delft University of Technology, promotor

Independent members:

Prof. dr. ir. P.H.A.J.M. van Gelder	Delft University of Technology
Dr. L. Ferranti	Delft University of Technology
Dr. S. Sharif Azadeh	Delft University of Technology
Prof. dr. C. Stoica	CentraleSupélec
Prof. dr. ir. D. Pissoort	Katholieke Universiteit Leuven
Prof. dr. ir. M. van Koningsveld	Delft University of Technology, reserve member

The research leading to this thesis has received funding from the European Union's Horizon 2020 research and innovation programme under the Marie Skłodowska-Curie grant agreement No. 955768 (MSCA-ETN AUTOBarge).

TRAIL Thesis Series no. T2026/11, The Netherlands Research School TRAIL
TRAIL, P.O. BOX 5017, 2600 GA Delft, The Netherlands, E-mail: info@rsTRAIL.nl

ISBN: 978-90-5584-386-2
Published and distributed by: A. Dhyani

Keywords: Autonomous Surface Vessels (ASVs), Maritime Safety, Inland Waterways, Maneuvering Model Identification, Sensor Fault Diagnosis, Model Predictive Control (MPC).

Printed in the Netherlands

To my parents,
Binda Dhyani and Late Sushil Chandra Dhyani

Preface

This thesis consolidates the research I conducted as a PhD candidate at TU Delft over the past four years. Reflecting on this journey, I feel very grateful for this opportunity and humbled by the outcome. Certainly, it wouldn't have been the same without all the people that I met, collaborated with, and learned from. I would like to take this opportunity to thank these people for crossing their paths with me.

Firstly, I want to thank my supervisors, Rudy Negenborn and Vasso Reppa, as this thesis would not have been possible without standing on their shoulders. They had to spend a significant amount of time with me, which must have required considerable restraint and patience. Dear Rudy and Vasso, I thank you wholeheartedly for that. Rudy, thank you for trusting me with developing my own ideas and for always making me look at the bigger picture. I will greatly cherish our conversations over a lunch walk or on the way to an event in your car. Vasso, you have been an inspirational and supportive teacher to me. Over the years, I have imbibed many things from you, especially your analytical mindset and professionalism. At the same time, you have been a friendly and approachable person, making working together much more enjoyable.

I would also like to express my sincere gratitude to Laura Ferranti, Pieter van Gelder, Davy Pissoort, Shadi Sharif Azadeh, and Cristina Stoica for agreeing to serve on my PhD assessment committee. I am thankful to you for taking the time to read this thesis and for providing your valuable feedback.

My PhD project was supported by the Marie Skłodowska-Curie Actions grant for the AUTOBarge project, which enabled me to meet and collaborate with a consortium of experts from across Europe. I also had the opportunity to make two research visits. The first one was at KU Leuven, where I had the opportunity to work with Davy Pissoort and Mathias Verbeke, as well as researchers from the M-group, and where I made some lifelong friends. Secondly, I visited Damen Research, Development and Innovation in Gorinchem. I am thankful to Kasper van der El and Dimitrios Kotiadis for having me there and for sharing their experience from the maritime industry.

I am also grateful for the friendship and company of my colleagues from the MTT department. I am very glad to have met Adrian, Alejandro, Annabel, Ege, Esma, Evelien, Jayvee, Kostas[2], Kris, Miguel, Nikos[2], Rafael, and Shaheen. Whether it was at the 3rd-floor coffee corner or after work at the city center, I am grateful for the light-hearted moments I shared with you all. My heartfelt thanks also go out to my friends and colleagues from the Safe-NET group, Andrea, Estelle, Nikos, and Tasos. I was also lucky to have Niek, Richmond, and Xinyu as my officemates. You can say that we were all in the same boat (pun intended), but some would argue that we were in the same aquarium (no pun intended). I owe special thanks to Bojan and Niek for all the memorable moments, and especially for being my PhD paranymphs. Thank you to my childhood friend, Yagnesh, for helping me create the cover art for this book. To my

colleagues from the AUTOBarge project, Yan-Yun, Martin, Zhongbi, Hoang, Amir, Dhanika, Yuhan, Chengqian, Yunjia, Rana, Lingyu, Dhanes, Sophie, and Camilla, I thoroughly enjoyed our collaborations, and I wish you all great success in life. I wrote the acknowledgments during the two-week period in which the coffee machine was broken. If I forgot to mention you, my humble apologies, but I hope you now understand why.

Finally, I am thankful for my family, who stood by me and were my pillars of support throughout these years. I wish peace to my father, who was always very proud of me. I am grateful for my mother, who stood strong in the face of hardships. I am thankful for my brother, my sister-in-law, and my niece for their love. Finally, I am so very lucky to have you, Miri. You have been my source of joy and peace each day.

Abhishek Dhyani
Delft, May 2026

Contents

Chapter 1

Introduction

1.1 Background

The transportation sector faces unique challenges today due to increasing demand for cargo and passenger transport, decarbonisation goals set by governments and industries, as well as congestion and disruptions in global trade routes. Among the various modes of transport, waterborne transport remains the backbone of global trade, accounting for 80% of international trade in goods by volume [1]. For regional freight systems, inland waterways play a strategically important role, especially in Europe, supporting high-volume transport along major corridors. Consequently, improvements in maritime safety, efficiency and sustainability can have significant societal and economic impacts, leading to extensive research and development underway in the maritime domain. This includes studies on the means (vessels) and infrastructure (bridges, terminals, buoys, etc.) involved. In recent years, numerous research projects have been established, focusing on alternative fuels [2, 3], improved ship designs [4], and enhanced autonomy [5, 6], among others.

Despite the strict regulations and conventions in place for maritime navigation and collision prevention, such as the COLREGs [7] and SOLAS [8], ensuring safety remains a critical issue for the maritime transport sector to date. The socio-economic and environmental impacts of maritime accidents can be severe and long-term. For instance, on March 26, 2024, due to the loss of its steering power, the container ship MV *Dali* collided with the Francis Scott Key Bridge in Baltimore, US, resulting in casualties of unaware construction workers on the bridge and severe infrastructure damage (Figure 1.1a) [9]. Obviously, accidents on inland waterways also have severe consequences. For instance, in March 2021, the 20,000 TEU container ship *Ever Given* was grounded in the Suez Canal, leading to six days of blocking of the canal, and a prevention of trade worth an estimated US $9.6 billion each day (Figure 1.1b) [10]. This incident exposed how little room for error there is in the confined waterways that carry the world's largest ships, and how difficult it is for a human crew to respond in a timely manner.

As per the Allianz Commercial's Safety and Shipping Review report 2025 [12], out of the 28,331 shipping casualties/incidents reported globally in the last decade, machinery damage/ failure was the top cause, accounting for about 44% of the total reported casualties/incidents (see Figure 1.2). Another report by the European Maritime Safety Agency (EMSA) [13] presents a classification of maritime casualties and incidents reported in the European Union

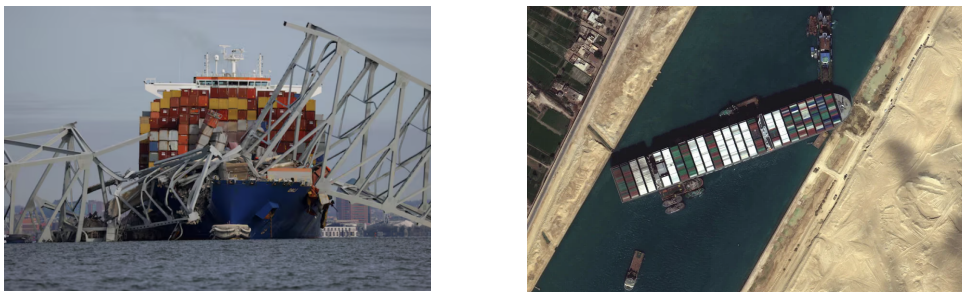

(a) (b)

Figure 1.1: (a) The 300-metre-long container ship MV *Dali* after collision with the historic Francis Scott Key Bridge in Baltimore, United States [JULIA NIKHINSON / REUTERS]. (b) The 400-metre-long and 20,000 TEU capacity container ship *Ever Given* obstructing the Suez Canal traffic in March 2021 [SATELLITE IMAGE, [11]].

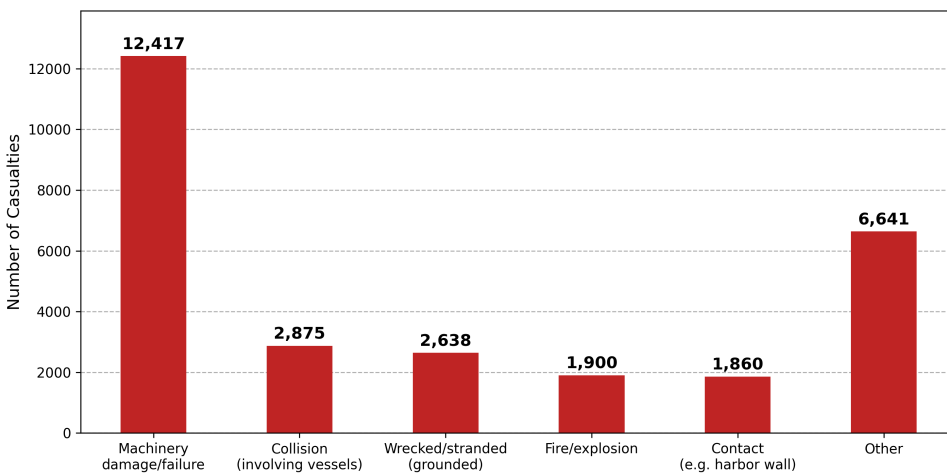

Figure 1.2: The global top causes of shipping casualties/incidents from January 1, 2015, to December 31, 2024, according to Allianz Commercial's annual Safety and Shipping Review report 2025 [12].

between 2015 and 2024, as shown in Figure 1.3. According to this report, navigational casualties (collisions, contacts, and groundings/strandings) account for approximately 46% of all reported casualty events. It also attributes human action and behaviour to 78.8% of marine casualties and incidents. The key factors identified for human error leading to maritime accidents include fatigue, inadequate crew-to-crew, vessel-to-vessel, and pilot-to-bridge communications, decisions based on insufficient information, poor maintenance, etc. [14].

The statistics from 2024 indicate a reduction in total vessel losses; however, shipping incidents and casualties have increased by 10%. These incidents are rarely the result of a single failure, but rather the compounding of human and organisational factors, as well as technical issues. This motivates maritime stakeholders to accelerate the adoption of digitalisation and

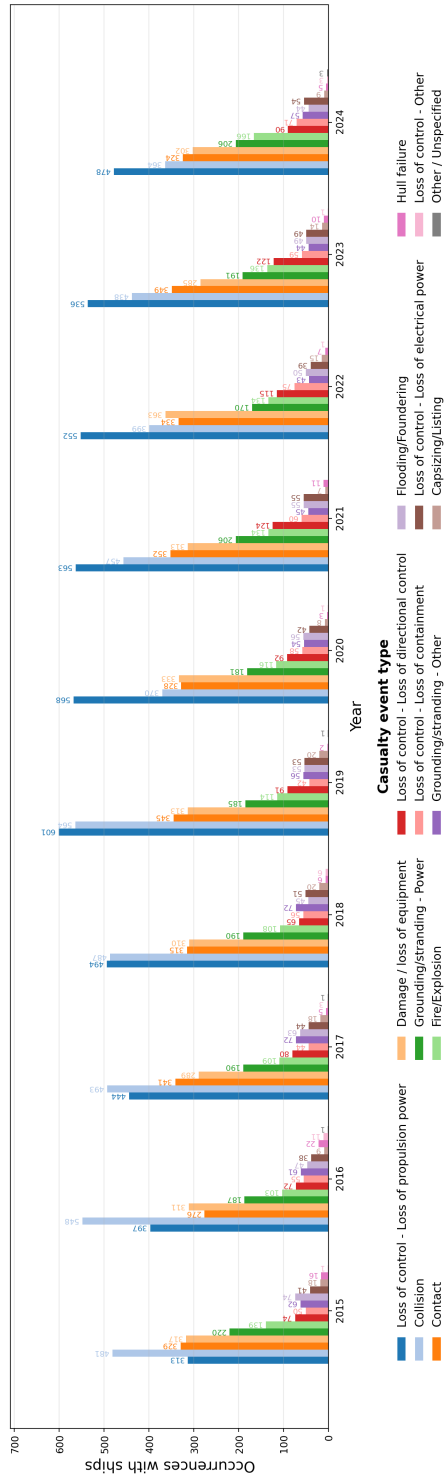

Figure 1.3: Classification of the reported casualty events with a ship according to the EMSA annual overview of marine casualties and incidents report, 2025 [13].

automation across maritime operations.

1.2 Autonomy for Smart Inland Shipping

Integrating autonomy across different modes of transportation is expected to mitigate congestion and capacity constraints while enabling safer, more efficient and resilient transportation networks. For maritime operations, increasing autonomy could significantly enhance economic viability by reducing operational costs and improving safety. Reduced onboard crew requirements for autonomous surface vessels (ASVs) not only facilitate the deployment of smaller, energy-efficient vessels but also reduce the risk of human injury in the event of an accident. Autonomy can also enhance operational safety by monitoring onboard components and enhancing a vessel's decision-making capabilities, thereby contributing to the overall safety of the maritime ecosystem. For these reasons, autonomous vessels are predicted to be among the key technological trends in the maritime sector [15].

For inland freight transportation, waterways are vastly underutilised. Europe alone features a vast network of navigable inland water bodies, covering approximately 37,000 kilometres. Inland waterways offer an attractive possibility for the mass deployment of autonomous vessels, as they provide less unpredictable environmental conditions than the open sea and can potentially reduce traffic congestion on roads. Inland waterway vessels (IWVs) are also more cost-effective and fuel-efficient compared to railways and trucks [16]. However, many navigational challenges must be addressed to make mass autonomous inland shipping a reality, such as handling the complex interactions of ASVs with infrastructural components like bridges and locks, complying with the strict navigational constraints due to narrow canals and passing vessels, as well as constraints on the water depth, and congestion at port terminals [17].

The autonomy stack comprises various systems that connect the acquisition of information through sensing to the execution of the vessel's motion. It can be designed as a monolithic system that directly transforms raw sensing inputs into control signals, or as a modular system comprising multiple subsystems. Typically, a modular software stack is preferred over an end-to-end approach for its simplicity, transparency, and ease of debugging. The overall autonomy stack can be visualised using a block diagram as shown in Figure 1.4. The comprising systems can be broadly classified as follows:

1. **Sensing and Perception system**: A key physical difference between a conventional vessel and an ASV is the additional sensors available onboard to assist the remote operator or the onboard supervisor/computer in decision-making by providing enriched information regarding the vessel's states (position, orientation, velocity, etc.), the external environment (wind, waves, and current) and obstacles (other vessels, bridges, etc.). In addition to conventional sensors such as the global navigation satellite system (GNSS), gyroscope, compass, and inertial measurement unit (IMU), modern ships are also equipped with LIDARs, cameras, radar, sonar, etc. The measurements are fused using sensor fusion algorithms to obtain accurate vessel states and a "World Model", which represents the vessel's environment [18]. This information is used for vessel localisation and situational awareness, enabling the other systems in the autonomy stack to perform tasks such as motion planning, control, collision avoidance and fault diagnosis.

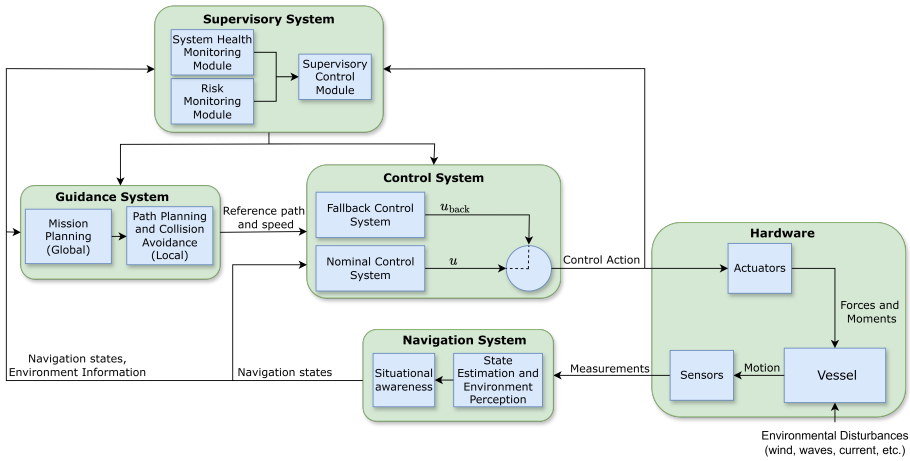

Figure 1.4: Block diagram representation of the autonomy stack for an ASV.

2. **Planning system**: The planning system is responsible for determining the vessel's reference trajectory for safe navigation. It comprises two main subsystems, namely a global path planner and a local path planner. The global planner is responsible for calculating an optimal path from the origin to the destination, taking into account various physical and environmental constraints. The local planner continuously modifies the global plan to achieve two primary objectives: collision avoidance with both static and dynamic obstacles, and adherence to navigational rules, such as the COLREGs.

3. **Control system**: The control system converts the reference trajectory calculated by the planning system into physical commands provided to the actuators (rudders, propellers, thrusters) under modelling uncertainty and disturbances. A (model-based) control algorithm relies on a detailed mathematical model representing the vessel's maneuvering dynamics. It is often decomposed into a higher-level controller for generalized force calculation and a lower-level controller for thrust allocation, respectively.

4. **Supervisory system**: A supervisory system can operate across the complete autonomy stack and is responsible for various functions, including health monitoring, fault management and risk mitigation through fail-safe and fail-operational actions. It thereby manages the safety, integrity and operational risk of the autonomous system at a higher level.

Typically, the modular stack results in the decomposition of the autonomous system into a Guidance, Navigation, and Control (GNC) system [19]. However, it is worth noting that the aforementioned stack additionally includes the supervisory and fallback control systems. The supervisory system oversees the overarching functions and plays a critical role in ensuring the safety and reliability of the underlying hardware and software. In conjunction, the fallback control system executes a higher-level control strategy provided by the supervisory system by overriding the nominal control action.

At a larger operational scale, autonomy extends to cooperation between multiple ASVs to perform the required tasks while achieving high efficiency, robustness and reliability. Multiple-vessel cooperation enables the execution of a wide range of operations that a single vessel is

incapable of or inefficient at performing, such as bulk cargo transportation, the manipulation of large structures, and assisted ship berthing [20]. Establishing communication with other vessels will also reduce the possibility of accidents, thereby enhancing the safety of inland transportation. Similarly, for a seamless movement through infrastructural landmarks such as bridges and locks, the ASVs must also be capable of communicating with these structures [21]. The communication requirements for the cooperative control of ASVs can therefore be broadly classified into V2V and V2I communication, respectively [22].

To incorporate these additional functionalities into the inland waterway transportation (IWT) system, the physical systems must be integrated with improved computational, communication and control capabilities. In this integrated system, a Vessel Controller (VC) will be responsible for controlling the vessel, whereas an Infrastructure Controller (IC) will be responsible for resolving conflicts between vessels at the infrastructure. The result is a highly complex and coupled system composed of physical and software components. Such systems can be defined as Cyber Physical Systems (CPS), due to the strong interdependence between the cyber domain, namely the embedded computers and communication network and the physical domain, which comprises the physical part of the vessels and infrastructures, including the actuators and sensors.

1.3 Challenges

To realise autonomous and smart shipping at a large scale, six key areas requiring further research were identified in [23], described as follows:

1. **Challenges at different levels of autonomy**: Various challenges across IMO autonomy levels must be addressed, including developing operational guidelines and mature sensing, perception and cooperative navigation capabilities. These advances must explicitly account for mixed traffic environments involving both human-operated and unmanned vessels.

2. **(Re-)defining human roles**: The responsibilities of humans must be defined while considering human-machine interaction, both onboard and onshore. It is also required to design and validate interfaces and procedures for remote supervision and decision support.

3. **Assuring safety and security**: Safe and secure autonomy necessitates translating high-level guidelines into requirements specific to the operational context. This can be achieved by developing technologies for fault management, smart maintenance, reliable communication, and cyber risk mitigation, among other things.

4. **Port and hinterland integration**: Port infrastructure and operations must be adapted to support the arrival and departure of autonomous vessels through automated pilotage and tug assistance, digital mooring and berth allocation services. Furthermore, interoperability across port systems and connected logistics chains must be ensured.

5. **Legal and regulatory framework**: Given the limited accommodation of autonomous operations in the current legal and regulatory framework, it is essential to update mar-

itime law for autonomous shipping, harmonising IMO codes with other regulations and addressing challenges related to code verification, operator training, and civil liability.

6. **Socio-economic case and public acceptance**: Building a socio-economic case for autonomous and smart shipping requires quantification of the economic, environmental, and safety costs and benefits, including impacts on employment, re-skilling needs, and market power. Public risk perception must also be understood, taking into account conflicting worldviews and ensuring equitable stakeholder involvement in decision-making.

Despite numerous advances in autonomous and smart inland shipping research over the past decade, many of the aforementioned challenges remain unresolved. To address them, the AUTOBarge project was initiated, with the goal of realising a safe, efficient, and reliable inland waterway ecosystem enabled by autonomous ships and smart infrastructure [6, 16].

The IWV autonomy stack design requires numerous considerations to address the aforementioned research gaps. This is because rivers and canals introduce hydrodynamic and operational complexities not found in open seas. Hydrodynamic phenomena such as bank and shallow-water effects and ship-to-ship interactions, impact vessel maneuverability, leading to an increased risk of collision and grounding [24]. In model-based design, these environment-specific factors lead to modelling uncertainties that must be accounted for to ensure safe operation. This requires, among other considerations, a) explicit modelling of the impact of these phenomena on vessel dynamics, b) robust identification of vessel dynamics considering uncertainties and real-world conditions, and c) designing control solutions catered to inland waterway vessels.

Navigation integrity also relies on multiple heterogeneous, redundant sensors that provide the vessel's situational awareness, notwithstanding noise, faults, and external interference. A fault in one or more sensors during an ongoing operation may degrade performance or cause system instability, leading to unwanted delays, disruptions, infrastructure damage, or even loss of life. While transients having a small effect on the system can be easily compensated for by a robust controller, a fault with a more significant impact cannot be neglected. It is therefore critical that a fault is diagnosed as soon as possible and that action is taken to accommodate it (switching to manual control, reconfiguring the controller, or employing virtual or physical sensor redundancy). Before accommodating one or more sensor faults, it is necessary not only to detect the fault but also to isolate the affected sensor. The common term for this fault diagnosis process is Fault Detection and Isolation (FDI).

Sensor faults are among the numerous internal and external factors that can lead to hazardous situations. Inland waterways present many pitfalls for system-level failures, such as collisions and grounding, due to the complexity of the IWV and the IWT domain. To ensure safety, continuous risk monitoring is required during navigation. Minimum-risk conditions must be maintained, especially in the event of failures compounded by other factors such as dense traffic or adverse weather. These objectives align with the supervisory system's role, which couples situational awareness with planning and control decisions and facilitates fallback operations.

To summarise, some of the technical challenges concerning the autonomy stack of IWVs can be addressed through four main topics, namely: 1) maneuvering modelling and robust identification, 2) path-planning and control, 3) sensor fault diagnosis, and 4) risk-aware decision-

making. The research gaps will be further established through a literature review on these topics presented in Chapter 2.

1.4 Research Questions

The main research question that this thesis will address is as follows:
How to design model-based control and fault diagnosis methods that ensure the safe navigation of autonomous vessels under uncertain and abnormal operational conditions?

This question is addressed through several sub-questions as follows:

RQ1: *What are the state-of-the-art and research gaps regarding the safe navigation of autonomous vessels in inland waterways?*

A systematic review of the current state-of-the-art is required to identify research gaps in the literature on autonomous navigation of IWVs. For this, the research topics identified in the previous section will be used. This review will justify the selection of design methodologies that can enhance the safety of the IWT system.

RQ2: *How to identify a robust and control-oriented maneuvering model of marine vessels under realistic operating conditions?*

Model-based design is the core foundation of this thesis. Accurate maneuvering models provide reliable predictions of the vessel dynamics, facilitating the design of guidance and control systems for autonomous navigation. However, real-world conditions introduce significant uncertainties due to sensor noise, environmental disturbances and model mismatch. Therefore, it is crucial to account for these uncertainties by quantifying uncertainty bounds in the identification procedure. This will yield robust vessel maneuvering models that enhance navigation safety. Maintaining the physical interpretability enables the design of model-based control systems.

RQ3: *How to design and evaluate control systems that ensure safe navigation of autonomous vessels in confined waterways?*

Safely navigating confined waterways requires addressing unique challenges posed by hydrodynamic phenomena, such as shallow-water effects and those resulting from proximity to channel walls. These factors significantly influence vessel maneuverability and steering dynamics, making conventional control strategies inadequate. An advanced control approach, namely the nonlinear model predictive control (NMPC), is explored to enable the design of autopilot/control systems that incorporate these hydrodynamic effects. To evaluate control performance, new key performance indices (KPIs) are designed that account for navigation challenges in inland waterways.

RQ4: *How to detect and isolate multiple sensor faults affecting the navigational sensors on autonomous surface vessels?*

Faults in navigational sensors can severely compromise safety-critical operations, making their timely diagnosis essential. The key challenge is detecting and isolating multiple sensor faults across diverse vessel configurations, sensor setups and environmental conditions. Residual signals should be generated as deviations from the expected behavior,

using models that represent the vessel's navigation and are sensitive to one or more sensor faults. Additionally, thresholds must be calculated to bound these residuals while ensuring robustness against uncertainties in vessel dynamics and sensor noise. This approach does not lead to false positives and enhances the reliability of the fault diagnosis method.

RQ5: *How can the risk of grounding and collision of autonomous vessels in inland waterways be modelled and mitigated?*

The vessel's internal factors, such as machinery faults and failures, compounded by external influences like dense traffic and adverse weather conditions, can compromise its GNC system operation, leading to hazardous situations, including grounding and collisions. Incorporating risk monitoring and mitigation into the autonomy stack enables the fail-safe operation of autonomous vessels, thereby preventing hazardous situations. An intelligent supervisory system must be designed to continuously manage risk and provide high-level fallback decisions when the risk exceeds a threshold.

1.5 Contributions

The main contributions of this thesis are summarised as follows:

1. A robust system identification method is proposed for marine vessels using the set- membership method. Unlike existing methods that yield unbounded parameter estimates, the proposed framework enables robust, bounded parameter estimation by explicitly accounting for uncertainties, including sensor noise and external disturbances. The identification problem is reformulated as a quadratic program, ensuring computational efficiency and convergence. The identified model facilitates the design of robust control and fault-diagnosis systems. This work has also been published in [25].

2. A multiple sensor FDI scheme is presented for the navigational sensors of an ASV. The proposed scheme utilises a bank of monitoring modules with structurally sensitive residuals tailored for different vessel types and sensor setups. Adaptive thresholds are computed to bound the residuals, thereby improving fault detectability by eliminating false positives. Furthermore, fault isolation is performed using a combinatorial fault decision logic, enabling the isolation of multiple sensor faults. This work has also been published in [26, 27].

3. The design and analysis of an NMPC scheme for path-following control of an IWV in confined waterways is presented. The dynamics of the IWV are modeled using an improved maneuvering model that accounts for hydrodynamic effects, including water depth, river currents, and bank effects. Furthermore, the evaluation of the vessel's steering performance is conducted using KPIs proposed for inland waterway navigation. The proposed control scheme is validated through an extensive case study involving diverse and complex inland waterway scenarios. This work has also been published in [28, 29].

4. A dynamic risk-mitigation method is proposed, based on a Bayesian Belief Network (BBN) for risk modelling and a Partially Observable Markov Decision Process (POMDP) for decision-making. When the vessel encounters a complex failure, the proposed method

serves as a fallback system by providing a high-level control strategy and preventing hazardous situations. This work has also been published in [30].

1.6 Thesis Outline

Figure 1.5 visualises the outline of this thesis. In Chapter 2, Research Question **RQ1** is addressed by performing a systematic literature review of the state-of-the-art. In Chapter 3, the model identification problem for marine vessels is discussed to address the Research Question **RQ2**. Hence, a systematic approach for identifying a three-degrees-of-freedom (3-DOF) model of a full-scale vessel using the Set-Membership Identification (SMI) method is presented. In Chapter 4, the vessel's control system design problem is considered to address the Research Question **RQ3**. To accomplish this, an NMPC for the path-following of IWVs in confined waterways is presented. Therefore, Chapters 3 and 4 address the research questions related to *autonomous navigation under uncertain operational conditions* for ASVs through modelling, identification, and control design.

Chapters 5 and 6 consider the *autonomous navigation under abnormal operational conditions*. Through these chapters, Research Questions **RQ4** and **RQ5** are respectively addressed. In Chapter 5, the problem of sensor monitoring for an ASV is discussed. To accomplish this, a multiple-sensor FDI scheme is presented for the navigational sensors of an ASV. In Chapter 6, the risk modelling and mitigation problem for IWVs is considered through the design of a higher-level safe control strategy (SCS). Finally, in Chapter 7, the conclusions are presented to address the main research question of this thesis. Furthermore, future research directions are proposed to improve the proposed methods and address related topics to enhance the safety of the IWT system.

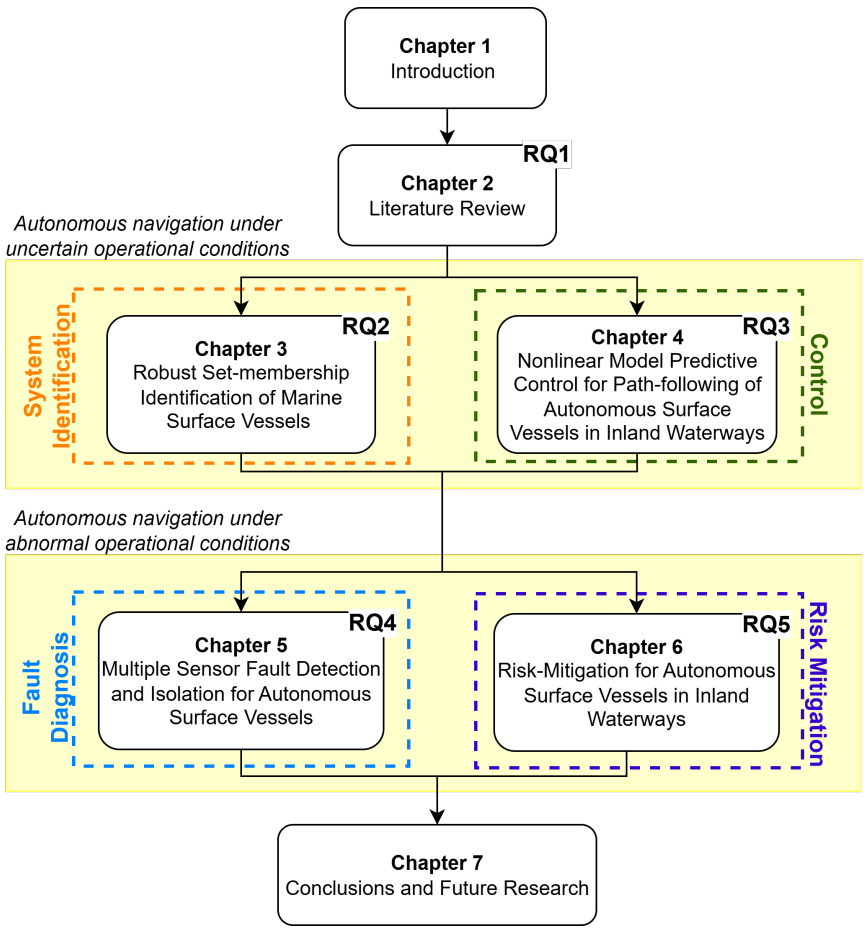

Figure 1.5: The outline of this thesis.

Chapter 2

Literature Review

Since we cannot know all that there is to be known about anything,
we ought to know a little about everything.

-Blaise Pascal

In this chapter, a literature review of the state-of-the-art is presented, covering the four main topics related to the safe autonomous navigation of IWVs, namely: 1) maneuvering modelling and robust identification, 2) path-planning and control, 3) sensor fault diagnosis, and 4) risk-aware decision-making. With that, this chapter addresses the first research question **RQ1:** *What are the state-of-the-art and research gaps regarding the safe navigation of autonomous vessels in inland waterways?*

This chapter is organised as follows: Section 2.1 reviews the literature on the identification of a maneuvering model for marine vessels. Section 2.2 reviews the path-following control literature for IWVs, and is divided into two sections, namely, the IWV maneuvering modelling, and vessel path-following control. Section 2.3 reviews the literature on fault diagnosis, covering firstly, the model-based fault diagnosis methods, and subsequently, the fault diagnosis of ASVs. Section 2.4 reviews the literature on the risk-aware decision making for ASVs. Finally, the conclusions are presented in Section 2.5 by identifying the research gaps.

Table 2.1: Categorisation of studies on full-scale vessel identification

Reference	Vessel and Type	Identification Method	Model Identified	Model Accuracy	Computational Complexity
[34]	Trimaran ferry	Nonlinear prediction error method, Unscented Kalman filter	4-DOF model (including roll dynamics)	Moderate-High	High
[35]	Ribcraft, Inflatable boat	Least squares method	First-order speed and yaw-rate models	Moderate-High	Low
[36]	Telemetron, Leisure boat	Linear regression	First-order speed and yaw-rate models	Moderate-High	Low
[37]	MilliAmpere, ferry	Grey-box modelling	3-DOF fully-coupled and surge-decoupled models	Moderate-High	Moderate-High
[38, 39]	Multratug 32, Tugboat	Model-based estimation	Linear 3-DOF model	Moderate-High	Low
[40]	Yukun, Training ship	Support vector regression, Modified grey wolf optimiser	3-DOF black-box model	High	High
[41]	Yukun, Training ship	Multi-innovation least squares method	4-DOF model (including roll dynamics)	Moderate-High	Moderate
[42]	Inflatable boat	Support vector regression	3-DOF model	Moderate-High	Moderate
[43]	Gunnerus, Research vessel	Hybrid neural network model	3-DOF hybrid model	High	High
[44]	Gunnerus, Research vessel	Neural network with multistep constraints	3-DOF black-box model	High	High
[45]	Maverick, Catamaran	Nonlinear least squares method	Decoupled surge and yaw-rate models	Moderate-High	Moderate

2.1 Maneuvering Model Identification of Marine Vessels

To obtain accurate maneuvering models, a combination of model-scale free-running experiments (using a scaled model of the vessel) and mathematical model-based methods is often employed [31]. Free-running experiments, including turning circles, zig-zag and spiral maneuvers, provide realistic measurements of the vessel's behaviour in environments such as towing tanks, lakes, or the open seas. Based on these experiments, model-based system identification methods estimate key physical parameters of the vessel, including the hydrodynamic coefficients. The resulting models facilitate precise predictions of the vessel's maneuvering performance, making them suitable for applications such as autopilot control design, route planning, collision avoidance and fault diagnosis algorithms [27, 29].

Model-scale tests and simulations require extrapolation to full scale (conforming to the vessel's actual size), which introduces significant uncertainties from scale effects and environmental variations [32]. As a result, further validation using full-scale experiments is necessary. For vessels already in service, such tests are typically preferred for system identification. However, identification from full-scale data must particularly address significant modelling and measurement uncertainties [31]. Moreover, some parameters are inherently challenging to identify due to their dependence on specific operations and environmental conditions. In particular, multicollinearity among hydrodynamic terms can make strongly correlated coefficients difficult to distinguish and accurately identify [33].

Recent studies have explored a range of data-driven and model-based approaches for full-scale vessel identification (see Table 2.1). In Wang et al. [44], a neural-network model with multistep constraints was used to capture the dynamics of a full-scale offshore research vessel. Zhang et al. [40] employed a support vector regression method combined with a modified grey wolf optimiser to predict the states of the full-scale vessel *Yukun*. Although these methods achieve good predictive performance, they are purely data-driven and yield parameters that

lack physical interpretability, limiting their usefulness for physics-based modelling and control design. To address this limitation, Wang et al. [43] proposed a hybrid approach that combines a known vessel model with a neural network-based calibrator. However, the procedure for identifying the physical model parameters remains unspecified. Alternatively, several studies have adopted white-box or grey-box modelling approaches to preserve the link to the physical parameters. For instance, Pedersen [37] applied grey-box identification to identify a simplified model of the fully-actuated ferry *MilliAmpere*. Sonnenburg and Woolsey [35] applied the least squares method to identify a set of linear first-order models, including a Nomoto (steering) model, a sideslip lag model, a speed model, and a bilinear thruster model for a rigid hull inflatable vessel *Ribcraft*. Eriksen and Breivik [36] proposed a simple 2-DOF model for an agile leisure boat, the *Telemetron*, identified using linear regression and full-scale identification experiments. Wu et al. [42] employ a support vector regression algorithm to identify linear and nonlinear hydrodynamic coefficients, as well as the damping coefficients for pitch and roll motions, through sea trials and simulations. Song et al. [41] proposed a multi-innovation least squares algorithm to identify the 4-DOF vessel dynamics, and demonstrated its application to full-scale trial data from the *Yukun* training ship. Herrero and González [34] presented an unscented Kalman filtering approach for parameter identification of marine vessels, and applied it to identify the parameters of a high-speed trimaran ferry. Hahn et al. [39] presented an estimation approach for identifying a full-scale tugboat model using measurement data from regular operation. Zhang et al. [45] performed an experimental identification of the decoupled dynamics of a catamaran ferry, focusing on surge and yaw motions, using a bounded nonlinear least-squares algorithm. Most existing full-scale identification studies either focus on simplified or decoupled system dynamics or estimate only a few parameters. Only a few works, such as [34, 41], consider the complete nonlinear dynamics.

Epistemic uncertainties arising from imperfectly known system parameters and initial conditions can significantly affect identification performance, thereby necessitating robustness considerations in the identification process [46]. Conventional identification methods, such as stochastic approaches, provide a probabilistic treatment of uncertainties; however, the identified parameters often remain statistically unbounded, especially in nonlinear settings. This can reduce confidence in the obtained estimates, as the optimisation may converge to local minima. Furthermore, the assumptions about the distributions of random variables (e.g., Gaussian with known mean and standard deviation) are often strict.

In contrast to this approach, a bounded-error characterisation of uncertainties, while more conservative, avoids assumptions related to the noise distribution model and the independence of the underlying random variables. The SMI framework utilises this principle to compute parameter sets consistent with the data and the assumed uncertainty bounds, such as measurement noise and external disturbances [47]. Consequently, SMI provides not only the nominal parameter estimates but also bounds that enclose the true parameters. This formulation supports robust prediction and control design, ensuring the model's validity within explicitly defined uncertainty sets. Furthermore, online identification/update of the system parameters and states facilitates real-time gain scheduling, state estimation and fault detection [48]. Applying SMI to full-scale vessel system identification becomes particularly attractive, as it can further facilitate adaptive and robust control design, ensuring safe operation under uncertain or variable operating conditions [49, 50].

2.2 Path-Following Control of IWVs

Operating IWVs in confined waterways is challenging as they are constrained by factors such as canal width, infrastructure, dynamic water levels, river currents and riverbed variations. Water depth, especially the impact of shallow waters, significantly affects a vessel's motion and maneuverability [51–56]. Furthermore, IWVs must frequently sail close to one side of the bank to clear the way for other vessels, thereby approaching the channel wall. This can result in flow acceleration between the gap, generating additional hydrodynamic forces on the hull, which poses challenges to vessel steering and handling, the so-called bank effect [57, 58]. Figure 2.1 visualises the impact of these phenomena on an inland vessel's maneuvering motion. Shallow water and bank effects are also suspected as factors responsible for several grounding accidents, including the infamous 2021 Suez Canal obstruction [59]. Therefore, a precise and robust mathematical model is critical for ensuring the operational safety of full-scale autonomous vessels, as it facilitates accurate prediction of the vessel's motion in confined waterways under these hydrodynamic effects. In addition, effective control techniques must be developed to safely and precisely follow the desired track while minimising the effort required from the propulsion and steering systems. By reducing unnecessary maneuvers and optimising steering commands, the vessel can mitigate wear and tear across the whole system and reduce energy consumption, which is essential, e.g., for an electrified vessel, to maintain operational efficiency over longer distances without frequent recharging.

2.2.1 IWV Maneuvering Modelling

Vessel maneuvering is a critical research topic that has been continuously developed during the past decades. The existing studies on maneuvering can be classified into two categories: (i) free running tests, by directly conducting model tests and full-scale trails with acting propeller and rudder to analyse the vessel's steering ability; (ii) mathematical model-based methods, focusing on solving equations of vessel's motion as rigid body dynamics to update its states based on the speed and rudder inputs. Due to the high cost of free-running experiments and the difficulty of predicting vessel maneuvering during construction, most research has been conducted using mathematical maneuvering models, which can generate fast, accurate predictions. Some typical maneuvering models, such as the linear Nomoto model and other nonlinear models [60–62], have been widely used in the maritime domain to meet various application requirements. Nevertheless, these models are developed for open-water applications using the profiles of classical commercial vessels, reducing their applicability to inland waterways, where vessels must navigate in shallow, confined waterways most of the time. Kijima and Nakiri [52] proposed the popular maneuvering modelling group (MMG)-based model with corrections in the hydrodynamic derivatives for shallow water. These corrections were provided using semi-empirical formulas derived from model tests and lifting surface theory for classical seagoing vessels. Yoshimura [56] used the MMG model to predict the maneuvering of a car carrier under various water-depth conditions. The simulation results show good agreement with the experimental data but also emphasise the shortcomings of calculated hydrodynamic coefficients, which are vessel-specific, limiting their application to IWVs as the hull types may differ significantly. In addition to model tests, several researchers [63–66] used computational fluid dynamics (CFD) to quantify the impact of shallow water on vessel maneuvering, but the focus was still on correcting

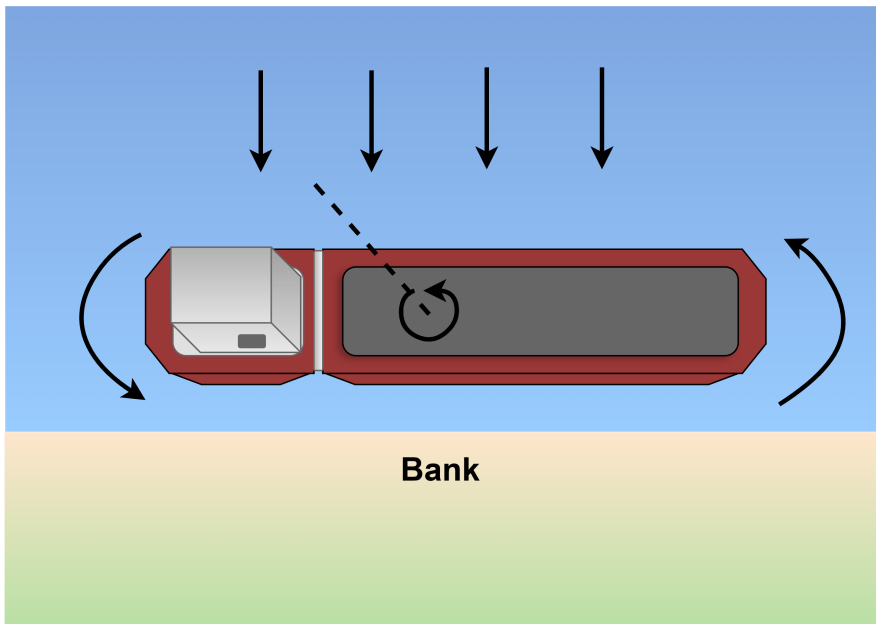

(a) Bank effect (top view)

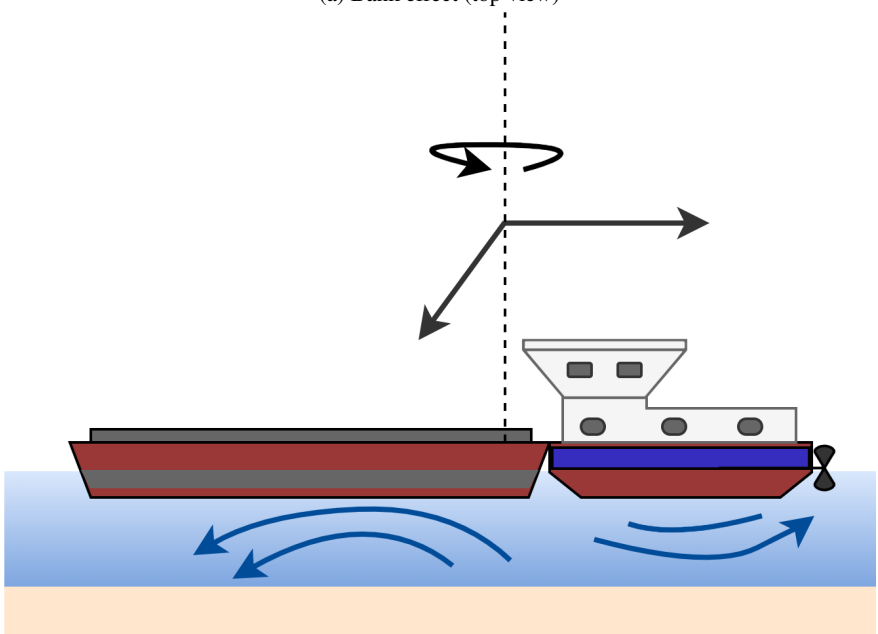

(b) Shallow water effect (side view)

Figure 2.1: Visualisation of the (a) bank effect and (b) shallow water effect, acting on an IWV.

the hydrodynamic coefficients of an individual vessel type rather than proposing a generic maneuvering model. Liu et al. [67] proposed a holistic maneuvering model, specifically for inland vessels, utilising the MMG model as the baseline and incorporating modifications tailored for the twin-propeller configuration, along with a rudder model developed using two-dimensional CFD simulations. However, the study focused only on navigation in the Yangtze River in China, which has greater water depth and wider channel width than European inland waterways in general; therefore, the water depth and other confinement effects were neglected.

Based on the existing literature, it can be concluded that to enhance the accuracy of IWV dynamics predictions, a suitable maneuvering model must be derived and applied to confined waterway scenarios. One related work was conducted by Yang and Moctar [68]. Using massive captive model tests at varying water depths, a new Abkowitz-type model was developed to account for the shallow-water effect on maneuvering forces and moments, and the results were successfully validated against experimental and full-scale trials of an inland vessel. From a different perspective, Zhang et al. [69] proposed a modified MMG model that incorporated additional terms for the bank effect; the shallow-water effect was modelled using hydrodynamic derivatives across various water depths. The model was validated using turning test data from a pusher barge model [70].

2.2.2 Vessel Path-following Control

In addition to vessel maneuvering modelling, research efforts to enhance vessel motion control have also been witnessed during the past decade, focusing on the vessel path-following problem. Path-following control system design can be further categorised into linear path-following or course-keeping, which involves controlling the vessel to maintain a straight-line trajectory, and curved path-following, which involves intricate steering mechanisms to navigate the bends in the pathway. Curved path following is a comparatively complex task due to the need to counteract the vessel's lateral drift, which primarily results from its inertia and hydrodynamic disturbances [71]. To account for modelling uncertainties and the limited knowledge of environmental forces such as wind and currents, a robust control law must be designed to counteract their effects on the vessel; see, for example, [72–75]. Model-based robust control algorithms aim at estimating and eliminating the impact of these disturbances on vessel navigation, applying techniques such as active disturbance-rejection [74], neural networks [76, 77], model-predictive control [78, 79], feedback linearisation [72], reinforcement learning [80, 81], and sliding-mode control [82], to name a few. However, most of these proposed methods focus only on the environmental disturbances that dominate the open sea, while maintaining sea-going vessel characteristics (single-propeller, single-rudder designs). This is due to the limited existing literature on the modelling of the characteristics of inland waterways using physical laws. As a result, these algorithms are inadequate in providing good control performance in inland waterway conditions. Motion control in restricted waterways, such as rivers and port areas, has recently been a focus in some works [75, 83]; however, further research on control design is needed.

Navigating in inland waterways introduces additional constraints, such as the bank and shallow-water effect, which can significantly impact the performance of traditional controllers [84, 85], making the control synthesis problem more complex. Current maritime navigation systems, such as track pilots, are often based on a Proportional-Integral-Derivative (PID) con-

trol law or its variants due to their simplicity and ease of implementation [86, 87]. However, the performance and robustness of such track pilots at river confluences and in the presence of river currents are insufficient, leading to large cross-track errors [28]. This is partly due to nonlinear effects, which are more pronounced during complex maneuvers and cannot be compensated for by the model-free PID controller. Furthermore, the controller's performance must be analyzed for inland navigation. Finally, modelling waterways while considering the impact of bank geometry is not addressed in the existing literature, thereby failing to fully represent a real inland waterway. These factors necessitate the development of sophisticated model-based control algorithms to ensure safe navigation.

Model Predictive Control (MPC) has been a widely popular control technique for the path-following control design of ASVs [78, 88, 89]. By employing a prediction model, MPC can anticipate and accommodate changes in the system's future behaviour. This makes it an attractive choice for vessel navigation applications, where proactive decision-making is crucial due to the vessel's large inertia and limited maneuverability. Furthermore, MPC can explicitly take into account the constraints on the vessel inputs and states, facilitating the constrained control requirements of inland navigation. Since the performance of the MPC algorithm greatly relies on the model's accuracy, a detailed maneuvering model is a foremost requirement for control design. Many existing works have addressed the path-following control problem for autonomous vessels using linear MPC [79, 89–91]). These methods use models obtained by successive linearisation around the operation point, which may change significantly. However, a wide range of operating conditions (e.g., varying water depths, variable proximity to channel wall, sharp turns) cannot be effectively represented by a single linear maneuvering model around a fixed point. As a result, for long prediction times, this leads to significant model mismatch and, therefore, large tracking errors [89]. Unlike open-sea navigation, where ample space allows for gradual course corrections, the confined and dynamic nature of inland waterways demands high-fidelity modelling of the aforementioned effects to ensure safe navigation. NMPC utilises the complete vessel model, ensuring that various nonlinear effects and varying operating conditions in inland waterways are accounted for. However, NMPC is known to have a high computational burden, which may lead to implementation issues, as the underlying optimisation problem may not converge in a timely manner. Several methods have been proposed in the literature to address this issue, including explicit MPC [92], direct multiple shooting [93], and real-time iteration [94], among others. The direct multiple-shooting method has also been employed for vessel path-tracking control applications, see [95–97].

2.3 Fault Diagnosis

2.3.1 Model-based Fault Diagnosis Methods

In the existing literature, it is occasionally assumed that the impact of a fault on the vessel's performance is not safety-critical and can be circumvented by employing a robust controller. This approach of achieving fault tolerance is often referred to as passive FTC. On the other hand, in active FTC, such a limiting assumption is discarded. Active FTC schemes include monitoring modules that detect, isolate, and estimate faults as they occur, and thereafter accommodate their impact to maintain the stability and performance of a system. Therefore, active FTC schemes

can offer fault tolerance for a broader range of faults and failures, and can generally do so more effectively.

Model-based methods for fault diagnosis are based on an explicit mathematical model of the system functioning in a nominal/healthy condition. These methods typically employ a residual generator that compares the expected behaviour of the system with the observed behaviour to detect a fault. Under healthy conditions and considering uncertainties, the residual is bounded by a known threshold. However, when the system is subject to a fault, the residual magnitude may exceed this threshold, thereby detecting the fault. Model-based residual generation methods can be broadly classified as follows [98]:

1. Observer-based methods: These methods are based on the system's state-space model, and use the output estimation error of an observer to generate the residuals. Several approaches have been proposed for observer-based fault detection, using Luenberger observers [99], unknown input observers [100, 101], Kalman filters [102], etc.

2. Parity space approach [103]: The parity space approach is based on an input-output model or a state-space model of the system. Unlike an observer, the parity space approach uses the so-called parity relations between the inputs and outputs of a system, obtained by rearranging the system's model via linear transformations to decouple disturbances and faults. Their limitation, compared to observer-based methods, is that they assume the model's structure and parameters to be precisely known.

3. System identification methods [98, Chapter 9]: This category of fault diagnosis methods is based on identifying a model of the system by using the input and output signals, which can be used to detect a fault, e.g., by associating the possible faults with specific parameters that the identification algorithm estimates.

In model-based fault diagnosis methods, a fault is detected when an analytical redundancy relation (ARR), an expression relating the residual to its threshold, is violated. Subsequently, the goal is to locate the fault in the system, i.e., isolate the faulty component. Fault isolation can be performed at both the residual generation and evaluation steps. There is a significant body of literature focused on isolating faults during residual generation, aiming for perfect isolation, i.e., each residual is affected by only a single fault. Various methods for achieving this have been proposed, such as those based on input decoupling, directional residuals, and using a bank of observers [104]. However, it should be noted that in many practical cases, perfect fault isolation may not be possible due to the system's structural limitations [105]. On the other hand, fault isolation during the residual evaluation phase is based on formulating a decision logic that compares the decisions of the affected system states (observed fault patterns) with theoretical fault signatures derived from the set of residuals. Two common ways of performing this consistency test during decision-logic design are row reasoning and column reasoning [106].

2.3.2 Fault Diagnosis of ASVs

Faults in sensor systems may arise from signal degradation due to environmental conditions or from a physical breakdown and can be either temporary or permanent. For example, a temporary fault might occur when GNSS positional accuracy degrades due to obstacles such as buildings,

bridges, or mountains that hinder satellite connectivity, even though there is no physical breakdown. GNSS multipath effects can also introduce bias and significantly reduce measurement accuracy [107]. Various methods have been proposed in the literature to mitigate these issues; see, for example, [108, 109]. Additionally, signal spoofing and jamming, which are categorised as cyberattacks, pose serious safety risks. For example, a malicious agent might intercept and manipulate GNSS data, jeopardising the system's nominal operation. On the other hand, permanent faults may result from physical issues such as short circuits in sensor circuitry, Ethernet failure, or sensor wear and tear.

Table 2.2: Categorisation of literature on the fault diagnosis of surface vessels. The abbreviations stand for the following terms: PF: Path following, TT: Trajectory tracking, DP: Dynamic positioning, SK: Station keeping.

References	Application scenario			Type of Fault			Fault Detection/Estimation Method
	PF/ TT	DP	Mooring/ SK	Actuator/Effector	Sensor	Structure	
[110]*			✓	✓	✓		Structural Analysis
[111–113]			✓			✓	Structural Analysis
[114]	✓				✓		Structural Analysis
[115]	✓			✓	✓		Particle Filter
[116]	✓			✓	✓		Deep Auto-encoders
[117]	✓			✓	✓		Neural Network Observer
[118]	✓			✓	✓		Extended State Observer
[119]	✓			✓			Nonlinear Observer
[120]	✓				✓		Nonlinear Observer
[121]	✓			✓			Nonlinear Observer
[122]	✓			✓			Unknown Input Observer
[123]	✓			✓			Nonlinear Observer
[124]	✓			✓			Adaptive Extended Kalman filter
[125]	✓				✓		Adaptive Kalman filter
[126, 127]		✓		✓			Parity Space Approach and Nonlinear Observer
[128]		✓		✓			Nonlinear Observer
[129]		✓		✓			Linear Observer
[130]		✓		✓			Convolutional Neural Network
[131, 132]		✓			✓		Nonlinear Observer

**Either actuator or sensor faults can be diagnosed*

Table 2.2 categorises the existing literature on the fault diagnosis of marine surface vessels, based on the application scenario, the affected component, and the proposed fault detection or estimation method. A broad majority of the literature employs model-based FDI schemes, which involve designing observers to generate residual signals indicative of potential faults. Many of these works propose approaches for diagnosing faults impacting the actuators; see, for example, [119, 121–124, 126–129]. Wang et al. [119] proposed an online fault estimator for ASVs affected by unknown faults and disturbances. The estimator can achieve finite-time convergence of the tracking error in the presence of actuator bias and partial loss-of-effectiveness faults. Park and Yoo [121] proposed a robust fault detection observer and an adaptive fault accommodation scheme for saturated actuator faults affecting underactuated surface vessels. Cristofaro and Johansen [122] proposed an actuator and effector FDI and control reconfiguration scheme for overactuated systems using unknown input observers. The scheme is further verified by a case study on an overactuated vessel. In Tsolakis et al. [123], an active isolation approach is proposed for an overactuated vessel with thruster faults, which can be integrated with a traffic-rule-compliant trajectory optimisation algorithm. Bhagavathi et al. [124] pro-

posed a digital twin-driven scheme for detecting and estimating faults in the vessel's propellers using an adaptive extended Kalman filter. Zhou et al. [129] proposed an actuator fault diagnosis observer and a fault-tolerant controller for ASVs in a network environment with delays, packet dropouts and packet disordering. In Benetazzo et al. [126, 127] and Lin et al. [128], the problem of thruster fault diagnosis for the dynamic positioning (DP) of vessels is addressed following the parity space and observer-based approaches.

In addition to actuator fault diagnosis, addressing the sensor FDI problem is equally crucial, given the extensive number of sensors required for perception, situational awareness and state estimation. Furthermore, the harsh marine environment, characterised by salt spray and high moisture levels, can accelerate sensor degradation [19]. Table 2.3 summarises the commonly used sensors for vessel navigation, along with the respective data processing methods and the parameters obtained. Some sensor FDI approaches, including those proposed by references [114, 125, 131, 132], rely on simple kinematic models. Blanke [114] proposed a structural analysis method that uses analytical redundancy relations (ARRs) to diagnose sensor faults and provide fault tolerance via sensor data fusion. The structural analysis technique is also applied to position-moored vessels under the conditions of the loss of a moving line buoyancy element, mooring line breakage, and faults occurring in the vessel actuators and sensors [111–113]. Rogne et al. [131, 132] presented a sensor FDI scheme that relies on multiple nonlinear observers for vessels performing DP tasks. However, the aforementioned schemes do not account for the impact of external disturbances acting on the vessel. These factors can significantly impact diagnostic performance, leading to false alarms. Asfihani et al. [125] proposed an adaptive Kalman filter-based method for sensor fault detection and estimation. The fault estimation, however, fails in some cases when the states linked to the sensor fault are not persistently excited.

On the other hand, sensor FDI schemes employing detailed dynamical models of the vessel have also been proposed [115, 118, 120]. Zhang et al. [115] proposed an adaptive particle filter to ensure the robust navigation of unmanned vessels affected by faults in the navigational sensors and the propeller. A switching-mode hidden Markov model is used to describe the vessel model affected by possible fault modes. However, this approach lacks a theoretical verification of the estimation and diagnosis performance. In Zhang et al. [120], a nonlinear observer is proposed for sensor fault estimation in conjunction with a fault-tolerant model reference reinforcement learning control method that ensures stable tracking for ASVs affected by a sensor fault. A limitation of the proposed scheme is that it assumes the occurrence of a single fault. In Wang et al. [118], an active fault-tolerant control scheme for ASVs is proposed for simultaneous sensor and actuator faults. The proposed method utilises a modified extended-state observer and an adaptive output-feedback control strategy, focusing on position-heading sensor faults. However, faults are modelled as a multiplicative factor with known bounds, limiting their scope of application.

External disturbances such as winds, waves, and currents can significantly impact vessel navigation, and their effects can lead to erroneous diagnostic results if not considered. In ports and inland waterways, wind forces are among the dominant external forces [133]. Likewise, the vessel's motion and maneuverability are highly sensitive to water depth, which can vary in inland waterways and canals [53, 134]. Depth limitations impact the vessel's behaviour in various ways: they are perceptible in medium-deep water, highly significant in shallow water, and dominant in extremely shallow water [135]. These factors, however, are neglected in existing

Table 2.3: Typically used sensors on vessels for localisation and state estimation, along with their corresponding measurements and the monitored parameters. These parameters are obtained post-processing using data processing methods as summarised below.

Sensor	**Measured Parameter(s)**	**Data Processing Methods**	**Monitored Parameter(s) for Navigation**
GNSS	Position (latitude, longitude, altitude)	Kalman Filtering, Low-pass Filtering, Sensor Fusion (e.g. with IMU)	Position in NED frame (x_p, y_p)
Dual-Antenna GNSS	Heading	Kalman Filtering, Sensor Fusion (e.g., with IMU)	Vessel heading (ψ)
IMU (accelerometer, gyroscope)	Linear accelerations and angular rates	Kalman Filtering, Sensor Fusion	Velocities in body frame (u, v, r)
Gyrocompass	Heading (true north reference)	Low-pass Filtering	Vessel heading (ψ)
Magnetic Compass	Heading (magnetic north reference)	Low-pass Filtering, Sensor Fusion (e.g. with gyrocompass)	Vessel heading (ψ)
Doppler Velocity Log (DVL)	Velocity through water or over ground in surge, sway directions	Kalman Filtering, Sensor Fusion (e.g. with GNSS)	Translational velocities in body frame (u, v)
Speed Log	Speed through water along the longitudinal axis (surge)	Low-pass Filtering, Sensor Fusion	Surge velocity in body frame (u)
AIS (Automatic Identification System)	Own vessel's speed over ground (SOG), course over ground (COG) and position (if integrated with onboard GNSS)	Low-pass Filtering, Sensor Fusion	Speed over ground (U), course over ground (χ) and position in NED frame (x_p, y_p)

model-based fault diagnosis schemes. Another key aspect that varies across vessels is the configuration of actuators and onboard sensors, which determines the dynamical model employed for residual generation in model-based FDI schemes.

2.4 Risk-aware Decision Making for ASVs

Hazard identification and risk assessment analysis are essential steps in the design of engineering systems to ensure their safe and reliable operation. In the context of autonomous vessels, techniques such as Systems Theoretic Process Analysis (STPA) have been widely explored in the literature for safety assessment and verification (see, for e.g., [136, 137] and references therein). Additionally, providing the analysis results as inputs to the control system during system operation can further enhance the decision-making capabilities of autonomous vessels [138].

Arguably, one of the most critical decision-making tasks is identifying a hazardous situation and preventing an accident by bringing the system to an MRC. According to DNV GL, an MRC is defined as *"a temporary as-safe-as-possible state that the vessel enters when it experiences situations which, if continued, involve operating outside the safe operating envelope"* [139]. These situations can arise from unsafe actions taken during vessel operation, originating from factors such as sensor faults, communication delays, or harsh weather conditions, and can potentially disrupt nominal operations. In this context, Lefebvre et al. [140] presented a hierarchical path-planning method for autonomous underwater vehicles that integrates collision risk using a "risk map". Bremnes et al. [141] performed hazard identification for autonomous underwater vehicles and used the results to construct a dynamic Bayesian network for risk-based decision-making. In Utne et al. [142], a framework for online risk modeling and control of autonomous ships, known as supervisory risk control, is proposed. Risk is evaluated during the operation using a BBN designed based on the results of the STPA hazard analysis.

One limitation of using a scalar risk variable in decision-making (as in Bayesian-based approaches) for control is the quantification, which inevitably leads to a loss of information [143]. Furthermore, it can lead to a situation in which a very low-consequence scenario receives the same risk value as a very unlikely but high-consequence scenario [144]. To tackle this limitation, GLAS DNV proposed a risk-based assessment tool where the risk probability is replaced with another metric called the "effectiveness of risk mitigation", which can be considered along with the risk severity [145]. Further, Johansen and Utne [146] extended the work of Utne et al. [142] to develop a supervisory risk controller that considers both risks and operational costs in the online risk model. Rothmund et al. [147] present an approach to model and infer the intentions of other ships by using a Dynamic Bayesian Network (DBN), which is based on various intention variables such as safe distance, COLREGs situation, etc. Thieme et al. [138] detail various approaches for integrating risk analysis methods into the control systems of autonomous systems.

POMDPs, on the other hand, are decision-theoretic models that can explicitly represent the effect of actions taken on the system's state in their framework. Furthermore, POMDPs support online planning algorithms for selecting actions based on the current belief state, rather than requiring a precomputed policy. Unlike static Bayesian networks, POMDPs model the sequential consequences of actions under uncertainty, making them suitable for dynamic risk-mitigation

tasks. However, the use of POMDPs for post-failure risk mitigation in ASVs remains unexplored in the literature, although it has been applied in other domains, such as mobile robots, underwater vehicles, and EMI resilience (e.g., see [148–150]). A few limitations have generally restricted the adoption of POMDPs in this setting. Firstly, the number of states and their associated properties in POMDPs can rapidly proliferate, which could significantly increase the computational cost of real-time evaluation. Secondly, the belief states of POMDP represent abstractions of the vessel states that are less intuitive to a human operator than the semantically meaningful nodes of a Bayesian network. Finally, determining the transition function for the POMDP model is non-trivial, as it requires conditional probabilities for every state-action pair. These factors are a key consideration favoring the adoption of Bayesian networks [143, 151].

A hybrid BBN-POMDP pipeline may directly alleviate the aforementioned limitations. In such an architecture, the BBN provides an interpretable, evidence-driven representation of risk factors, whereas its inferred probabilities can be systematically mapped to POMDP transition probabilities. Subsequently, the POMDP model provides tractable online planning capabilities. To the best of our knowledge, such an architecture has not been explored in the literature for ASV risk mitigation.

2.5 Conclusions

This chapter reviews the literature on the safe autonomous navigation of IWVs and addresses the research question **RQ1:** *What are the state-of-the-art and research gaps regarding the safe navigation of autonomous vessels in inland waterways?*

For the vessel maneuvering model identification problem, least-squares regression and stochastic methods such as Kalman filtering are most commonly employed in the literature. However, these methods yield unbounded parameter estimates and/or impose stricter assumptions on the uncertainties (e.g., the noise distribution), thereby limiting the robustness of the estimates and reducing their confidence. Furthermore, the complexity of the identified model varies significantly in terms of the model order, nonlinearity, DOF coupling, etc. This affects the model's accuracy and the computational complexity of the identification algorithm. A detailed categorisation for the same is provided in Table 2.1.

The majority of existing literature on the path-following control problem focuses on open-sea navigation, and modelling of the environmental characteristics and hydrodynamic phenomena in inland waterways is lacking. Therefore, existing model-based control methods perform poorly when the vessel experiences bank and shallow-water effects in confined waterways. Furthermore, evaluating the controller's performance in inland navigation is not considered in the existing literature.

Next, the literature on model-based fault diagnosis is reviewed, considering both fundamental research and applications to ASVs. Observer-based methods are most commonly employed across vessels operating under different scenarios, and actuator faults are the commonly considered type of faults. An overview of the literature across various categories (application scenario, fault type, etc.) is provided in Table 2.2. Sensor faults are identified as a critical area of research, especially given the very limited research on their detection under external disturbances and on multiple-sensor fault isolation. The primary sensors of interest are presented in Table 2.3, along

with their measured variables and processing techniques.

For risk-aware decision-making, designing a risk control framework has been a recent area of interest, where balancing the complexity of dynamic risk modelling with real-time decision-making remains a challenge. Existing works focus on Bayesian networks for online risk modelling, providing posterior probabilities that must be paired with a control system for decision-making. However, dynamic decision-making methods that directly output control policies, such as POMDPs, have not been explored for autonomous vessels, despite their potential for real-time risk mitigation.

Overall, it can be concluded that the research gaps on the autonomous navigation of IWVs include a) methods for robust and bounded parameter identification, b) path-following control considering the confined waterways environment, c) multiple sensor-fault diagnosis methods considering external disturbances and sensor noise, and d) dynamic risk-mitigation methods for decision-making and control of IWVs. Based on these findings, the upcoming chapters (Chapters 3-6) propose methods for system identification, fault diagnosis, control, and risk mitigation for autonomous navigation of IWVs.

Chapter 3

Robust Set-membership Identification of Marine Surface Vessels

Models are a matter of inspiration, not deduction.

- Jan C. Willems

Considering the research gaps determined in Section 2.1 of the previous chapter, this chapter presents a systematic approach for identifying a nonlinear 3-DOF maneuvering model for a full-scale vessel using the SMI method. It also demonstrates the practical application of the SMI method to real-world experimental data, establishing its effectiveness for full-scale identification under uncertain operating conditions. Therefore, the following research question is answered **RQ2:** *How to identify a robust and control-oriented maneuvering model of marine vessels under realistic operating conditions?*

This chapter is organised as follows: In Section 3.1, the vessel's nonlinear maneuvering model and thrusters model are introduced, along with the key parameters to be identified. Section 3.2 provides a detailed description of the proposed SMI method, which involves computing the feasible parameter set (FPS) that is guaranteed to include the true parameters. In Section 3.3, the proposed method is validated through parameter identification of a catamaran-type passenger ferry by utilising logged data from multiple maneuvers performed during river trials. The method yields both optimal point estimates and bounded parameter sets, providing robust uncertainty quantification. Validation using synthetic data is performed to benchmark the algorithm's performance under idealised conditions. Additionally, sensitivity analysis is performed to determine the most crucial parameters for accurate identification. Finally, in Section 3.4, the conclusions and key findings are summarised.

The contents of this chapter have been published in (Dhyani et al., 2026[1]).

[1]**Dhyani, A.**, Tsolakis A., van der El, K., Negenborn, R.R. and Reppa, V., 2026. Robust vessel maneuvering modelling using set-membership identification. Control Engineering Practice, 173, p.106936.

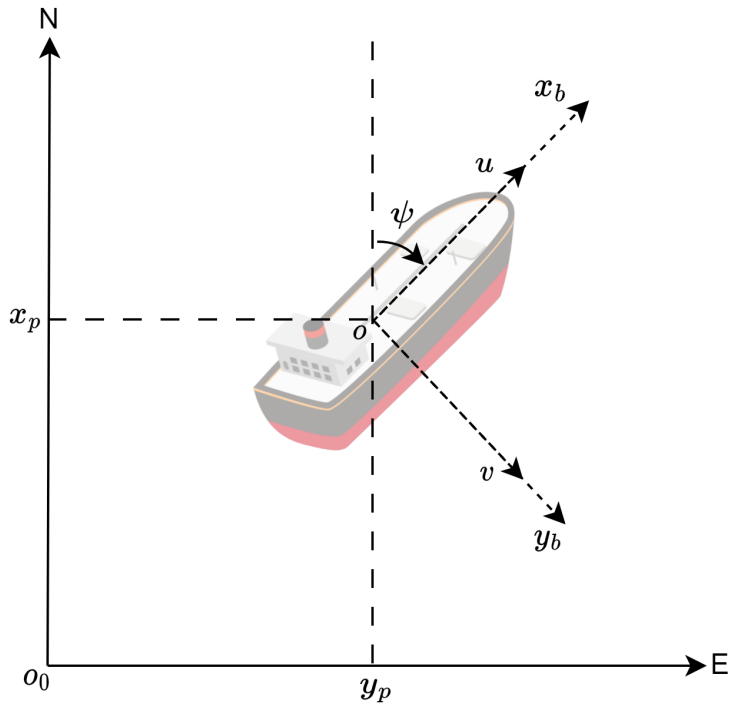

Figure 3.1: The coordinate system of a surface vessel. The variables (x_p, y_p) represent the coordinates of the vessel's position in the o_0 frame. u, v and ψ are the surge, sway velocities and the heading angle, respectively.

3.1 Vessel Maneuvering Model

Figure 3.1 illustrates the coordinate system of a vessel in 3-DOF with the North-East-Down reference frame ($o_0 - NED$) and the body-fixed reference frame ($o - x_b y_b z_b$) (the D- and z_b-axes are not shown). Its detailed kinetic and kinematic model are described in the following subsections.

3.1.1 3-Degrees of Freedom (DOF) Maneuvering Model

The 3-DOF dynamical model of the vessel can be expressed by

$$\dot{\eta} = R(\psi)\nu, \tag{3.1a}$$

$$M\dot{\nu} + C(\nu)\nu + D(\nu)\nu = \tau + \tau_d, \tag{3.1b}$$

where $\eta = \begin{bmatrix} x_p & y_p & \psi \end{bmatrix}^T$ is the generalised coordinate vector in the NED frame, and $\nu = \begin{bmatrix} u & v & r \end{bmatrix}^T$ is the generalised velocity vector in the body-fixed frame, with u, v denoting the linear velocities in surge and sway, and r denoting the angular velocity (yaw rate). The variable $\tau = \begin{bmatrix} \tau_u & \tau_v & \tau_r \end{bmatrix}^T$ represents the controlled input force vector and $\tau_d \in \mathbb{R}^3$ represents the added

force vector, which comprises unknown forces acting on the vessel due to various external factors such as wind, currents, forces from the towing system, etc ([152]). The terms M and $R(\psi)$ represent the inertia and rotation matrices respectively, having a 3×3 dimension, with

$$M = \begin{bmatrix} m-X_{\dot{u}} & 0 & 0 \\ 0 & m-Y_{\dot{v}} & mx_G-Y_{\dot{r}} \\ 0 & mx_G-N_{\dot{v}} & I_{z_p}-N_{\dot{r}} \end{bmatrix}, \text{ and,} \tag{3.2}$$

$$R(\psi) = \begin{bmatrix} \cos(\psi) & -\sin(\psi) & 0 \\ \sin(\psi) & \cos(\psi) & 0 \\ 0 & 0 & 1 \end{bmatrix}. \tag{3.3}$$

Here, m is the vessel's mass, I_{z_p} is the moment of inertia about the z_p- axis, and, $X_{\dot{u}}$, $Y_{\dot{v}}$, $Y_{\dot{r}}$, $N_{\dot{v}}$ and $N_{\dot{r}}$ are hydrodynamic parameters that account for the added mass. Further, x_G represents the coordinate of the vessel's centre of gravity along the x_b- axis. The terms $C(\nu), D(\nu)$ are the Coriolis-centripetal and damping matrices, respectively, and are given by

$$\begin{aligned} C(\nu) &= \begin{bmatrix} 0 & 0 & c_{13}(\nu) \\ 0 & 0 & c_{23}(\nu) \\ -c_{13}(\nu) & -c_{23}(\nu) & 0 \end{bmatrix}, \\ D(\nu) &= \begin{bmatrix} d_{11}(\nu) & 0 & 0 \\ 0 & d_{22}(\nu) & d_{23}(\nu) \\ 0 & d_{32}(\nu) & d_{33}(\nu) \end{bmatrix}, \end{aligned} \tag{3.4}$$

with $c_{13}(\nu) = -m(x_G r+v)+Y_{\dot{v}}v+Y_{\dot{r}}r$, $c_{23}(\nu) = mu-X_{\dot{u}}u$, $d_{11}(\nu) = -X_u - X_{|u|u}|u| - X_{uuu}|u^2|$, $d_{22}(\nu) = -Y_v - Y_{|v|v}|v| - Y_{|r|v}|r|$, $d_{23}(\nu) = -Y_r - Y_{|v|r}|v| - Y_{|r|r}|r|$, $d_{32}(\nu) = -N_v - N_{|v|v}|v| - N_{|r|v}|r|$, and $d_{33}(\nu) = -N_r - N_{|v|r}|v| - N_{|r|r}|r|$. The terms X_u, $X_{|u|u}$, X_{uuu}, Y_v, $Y_{|v|v}$, $Y_{|r|v}$, Y_r, $Y_{|v|r}$, $Y_{|r|r}$, N_v, $N_{|v|v}$, $N_{|r|v}$, N_r, $N_{|v|r}$ and $N_{|r|r}$, are the hydrodynamic parameters that account for the damping forces within the second-order modulus model representation ([153, 154]).

3.1.2 Thrusters Modelling

For a twin azimuth-thruster configuration, the controlled input force vector can be defined as

$$\tau = \begin{bmatrix} \tau_u \\ \tau_v \\ \tau_r \end{bmatrix} = \begin{bmatrix} X_{pr,1}+X_{pr,2} \\ Y_{pr,1}+Y_{pr,2}+Y_{\text{bow}} \\ N_{pr,1}+N_{pr,2}+N_{\text{bow}} \end{bmatrix}, \tag{3.5}$$

where, $X_{pr,i}$, $Y_{pr,i}$ and $N_{pr,i}$ are the generalised force components for the $i-$th thruster, $i \in \{1,2\}$, such that ([155])

$$\begin{aligned} X_{pr,i} &= F_{t,i}\cos(\delta_{c,i}) - F_{d,i}\cos(\beta_i) - F_{l,i}\sin(\beta_i) \\ Y_{pr,i} &= F_{t,i}\sin(\delta_{c,i}) - F_{d,i}\sin(\beta_i) + F_{l,i}\cos(\beta_i)\,. \\ N_{pr,i} &= x_R Y_{pr,i} - y_{R,i}X_{pr,i} \end{aligned} \tag{3.6}$$

Here, $F_{t,i}$, $F_{d,i}$ and $F_{l,i}$ represent forces due to the $i-$th thruster acting in the propeller direction, in the relative fluid velocity direction and perpendicular to the relative fluid velocity, respectively. Further, $\delta_{c,i}$ and β_i are the azimuth and flow orientation angles for the $i-$th thruster,

respectively. Finally, x_R and $y_{R,i}$ are the longitudinal and lateral coordinates of the thruster's location. The thruster force can be defined using the following quadratic relation:

$$F_{t,i} = C_{t,i}\omega_{c,i}^2, \quad i \in \{1,2\}, \tag{3.7}$$

where, $C_{t,i}$ represents the thrust force coefficient and $\omega_{c,i}$ represents the propeller revolutions in rad/s. Furthermore, the force components $F_{d,i}$ and $F_{l,i}$ can be defined as

$$\begin{aligned} F_{d,i} &= 0.5\rho A_R(C_{d,0} + C_{d,1}|\phi_i|)V_i^2 \\ F_{l,i} &= 0.25\rho A_R C_{l,1}\sin(2\phi_i)V_i^2, \quad i \in \{1,2\}, \end{aligned} \tag{3.8}$$

where, the terms ρ represents the fluid density, A_R the reference area, $\phi_i = \delta_{c,i} - \beta_i$ is the relative fluid angle of attack and V_i is the total fluid flow velocity. The constants $C_{d,0}, C_{d,1}$ represent the base drag coefficient and its variation w.r.t. ϕ, respectively, whereas constant $C_{l,1}$ represents the variation in the lift coefficient w.r.t. ϕ.

Remark 3.1 Notably, in this study, we focus solely on the vessel's high-speed maneuvering; therefore, the bow tunnel thrusters are not employed, resulting in Y_{bow} and N_{bow} having zero values. □

The parameters vector $\theta \in \mathbb{R}^{n_\theta}$, $n_\theta = 27$, comprising the parameters in the vessel maneuvering model (Equations (3.1),(3.5)) to be determined, is given by :

$$\theta = \begin{bmatrix} \theta_1 & \theta_2 & \theta_3 \end{bmatrix}^T, \tag{3.9}$$

where

$$\begin{aligned} \theta_1 &= \begin{bmatrix} I_{z_p} & X_{\dot{u}} & Y_{\dot{v}} & Y_{\dot{r}} & N_{\dot{v}} & N_{\dot{r}} & X_u & X_{|u|u} & X_{uuu} \end{bmatrix}, \\ \theta_2 &= \begin{bmatrix} Y_v & Y_{|v|v} & Y_{|r|v} & Y_r & Y_{|v|r} & Y_{|r|r} & N_v & N_{|v|v} & N_{|r|v} \end{bmatrix}, \\ \theta_3 &= \begin{bmatrix} N_r & N_{|v|r} & N_{|r|r} & C_{t,1} & C_{t,2} & C_{l,1} & C_{d,0} & C_{d,1} & A_R \end{bmatrix}. \end{aligned} \tag{3.10}$$

The initial values and bounds for these parameters are determined using empirical formulas, standardised full-scale tests, such as bollard-pull tests, and/or expert knowledge.

The objective of this study is to estimate the aforementioned parameters of a 3-DOF nonlinear maneuvering model using the SMI method, while providing their guaranteed bounds. The proposed method is described in detail in the following section.

3.2 Set-Membership Identification (SMI)

SMI enables the identification of unknown system parameters under the assumption of bounded noise and disturbances, thereby avoiding the need for a stochastic treatment for these uncertainties. It requires that the system is linear in the parameters of interest, even if the maneuvering model given by Equation (3.1) and the thruster model given by Equations (3.5), (3.6) are inherently nonlinear with respect to the system states and control inputs. The nonlinear entry of these parameters into the system dynamics also makes the system identification task difficult, as it leads to a nonconvex objective function. This can further lead to the optimisation solver

converging to a local minima. Consequently, the identified parameters may not accurately represent the true underlying vessel dynamics. To address these issues, the model is transformed and discretised to obtain a discrete-time linear-in-parameters (DT-LIP) model, given by

$$x(k+1) = G(x(k),u(k))\xi \tag{3.11a}$$
$$y(k) = x(k) + n(k), \tag{3.11b}$$

where $G \in \mathbb{R}^{n \times n_\xi}$ denotes a nonlinear basis function in states $x(k) \in \mathbb{R}^n$ and controlled inputs $u(k) \in \mathbb{R}^p$, with $n = 6$ and $p = 4$, respectively, and $y(k)$ is the output, which is a function of $x(k)$ and the measurement noise $n(k)$. The vessel's states $x(k)$ and the controlled inputs $u(k)$ are respectively defined by

$$\begin{aligned} x(k) &= \begin{bmatrix} \eta(k) & \nu(k) \end{bmatrix}^T \\ u(k) &= \begin{bmatrix} \delta_{c,1}(k) & \delta_{c,2}(k) & \omega_{c,1}(k) & \omega_{c,2}(k) \end{bmatrix}^T. \end{aligned} \tag{3.12}$$

Further, the vector $\xi \in \mathbb{R}^{n_\xi}$, $n_\xi = 78$, represents the transformed parameters vector to be identified, and is given by

$$\xi = \begin{bmatrix} \xi_1 & \xi_2 & \xi_3 \end{bmatrix}^T, \tag{3.13}$$

with

$$\xi_1 = \frac{1}{(X_{\dot{u}} - m)} \begin{bmatrix} -X_u \\ 0 \\ 0 \\ 0 \\ 0 \\ (Y_{\dot{v}} - m) \\ -X_{|u|u} \\ 0 \\ 0 \\ 0 \\ 0 \\ (Y_{\dot{r}} - mx_G) \\ -X_{uuu} \\ -C_{t,1} \\ -C_{t,2} \\ -a_2 \\ -a_2 \\ -a_3 \\ -a_3 \\ -a_4 \\ -a_4 \\ 0 \\ 0 \\ 0 \\ 0 \\ 0 \end{bmatrix}^T, \quad \xi_2 = \frac{1}{a_5} \begin{bmatrix} 0 \\ -(I_{z_p} Y_v - N_{\dot{r}} Y_{\dot{v}} + N_{\dot{v}} Y_{\dot{r}} - N_{\dot{v}} m x_G) \\ -(I_{z_p} Y_r + N_{\dot{r}} Y_{\dot{v}} - N_{\dot{r}} Y_{\dot{r}} - N_{\dot{r}} m x_G) \\ ((X_{\dot{u}} - Y_{\dot{v}})(Y_{\dot{r}} - m x_G)) \\ -(I_{z_p} X_{\dot{u}} + m^2 x_G^2 - N_{\dot{r}} X_{\dot{u}} - I_{z_p} m + N_{\dot{r}} m + Y_{\dot{r}}^2 - 2 Y_{\dot{r}} m x_G) \\ 0 \\ 0 \\ -(I_{z_p} Y_{vv} - N_{\dot{r}} Y_{vv} + N_{vv} Y_{\dot{r}} - N_{vv} m x_G) \\ -(I_{z_p} Y_{rr} - N_{\dot{r}} Y_{rr} + N_{rr} Y_{\dot{r}} - N_{rr} m x_G) \\ -(I_{z_p} Y_{rv} - N_{\dot{r}} Y_{rv} + N_{rv} Y_{\dot{r}} - N_{rv} m x_G) \\ -(I_{z_p} Y_{vr} - N_{\dot{r}} Y_{vr} + N_{vr} Y_{\dot{r}} - N_{vr} m x_G) \\ 0 \\ 0 \\ (C_{t,1} Y_r (Y_{\dot{r}} - m x_G)) \\ (C_{t,2} Y_r (Y_{\dot{r}} - m x_G)) \\ (a_2 Y_r (Y_{\dot{r}} - m x_G)) \\ -(a_2 Y_r (Y_{\dot{r}} - m x_G)) \\ (a_3 Y_r (Y_{\dot{r}} - m x_G)) \\ -(a_3 Y_r (Y_{\dot{r}} - m x_G)) \\ (a_4 Y_r (Y_{\dot{r}} - m x_G)) \\ -(a_4 Y_r (Y_{\dot{r}} - m x_G)) \\ -(C_{t,1}(a_7)) \\ -(C_{t,2}(a_7)) \\ -(a_2(a_7)) \\ -(a_3(a_7)) \\ -(a_4(a_7)) \end{bmatrix}^T, \quad \xi_3 = \frac{1}{a_5} \begin{bmatrix} 0 \\ (N_{\dot{v}} Y_{\dot{v}} - N_{\dot{v}} Y_{\dot{v}} - N_{\dot{r}} m + Y_{\dot{r}} m x_G) \\ (N_{\dot{r}} Y_{\dot{v}} - N_{\dot{v}} Y_{\dot{r}} - N_{\dot{r}} m + Y_{\dot{r}} m x_G) \\ -((X_{\dot{u}} - Y_{\dot{v}})(Y_{\dot{v}} - m)) \\ -(N_{\dot{v}} X_{\dot{u}} - Y_{\dot{r}} Y_{\dot{v}} - N_{\dot{v}} m + Y_{\dot{r}} m - X_{\dot{u}} m x_G + Y_{\dot{v}} m x_G) \\ 0 \\ 0 \\ -(N_{\dot{v}} Y_{vv} - N_{vv} Y_{\dot{v}} + N_{vv} m - Y_{vv} m x_G) \\ (N_{rr} Y_{\dot{v}} - N_{\dot{v}} Y_{rr} - N_{rr} m + Y_{rr} m x_G) \\ (N_{rv} Y_{\dot{v}} - N_{\dot{v}} Y_{rv} - N_{rv} m + Y_{rv} m x_G) \\ -(N_{\dot{v}} Y_{vr} - N_{vr} Y_{\dot{v}} + N_{vr} m - Y_{vr} m x_G) \\ 0 \\ 0 \\ -(C_{t,1} Y_r (Y_{\dot{v}} - m)) \\ -(C_{t,2} Y_r (Y_{\dot{v}} - m)) \\ -(a_2 Y_r (Y_{\dot{v}} - m)) \\ (a_2 Y_r (Y_{\dot{v}} - m)) \\ -(a_3 Y_r (Y_{\dot{v}} - m)) \\ (a_3 Y_r (Y_{\dot{v}} - m)) \\ -(a_4 Y_r (Y_{\dot{v}} - m)) \\ (a_4 Y_r (Y_{\dot{v}} - m)) \\ -(C_{t,1}(a_6)) \\ -(C_{t,2}(a_6)) \\ -(a_2(a_6)) \\ -(a_3(a_6)) \\ -(a_4(a_6)) \end{bmatrix}^T \tag{3.14}$$

where $a_2 = 0.5\rho A_R C_{d,0}$, $a_3 = 0.5\rho A_R C_{d,1}$, $a_4 = 0.5\rho A_R (0.9 C_{l,1})$, $a_5 = I_{z_p} Y_{\dot{v}} + m^2 x_G^2 - N_{\dot{r}} Y_{\dot{v}} + N_{\dot{v}} Y_{\dot{r}} - I_{z_p} m + N_{\dot{r}} m - N_{\dot{v}} m x_G - Y_{\dot{r}} m x_G$, $a_6 = N_{\dot{v}} - Y_{\dot{v}} x_R + m x_R - m x_G$, $a_7 = I_{z_p} - N_{\dot{r}} + Y_{\dot{r}} x_R - m x_R x_G$. Note that ξ differs from the physical parameters in θ due to the transformation of the system dynamics into the DT-LIP form, with the transformation function represented by $f : \mathbb{R}^{n_\theta} \to \mathbb{R}^{n_\xi}$. Carrying out this transformation involves formulating ξ by separating the unknown parameters from the known states and inputs and vectorising them, and obtaining G by converting the original nonlinear function in Equation (3.1) into a block-matrix form (see, for e.g., [156, 157]).

The bounded noise assumption can be stated as follows:

Assumption 1 *The noise is unknown and bounded by a known upper and lower bound, i.e.,*

$$|n(k)| \leq \bar{n} \Leftrightarrow n(k) \in \mathcal{N}(k) = \{n(k) \in \mathbb{R}^n, Hn(k) \leq h_n\}, \tag{3.15}$$

where

$$\begin{aligned} H &= \begin{bmatrix} I_n & -I_n \end{bmatrix}^T \in \mathbb{R}^{2n\times n}, \\ h_n &= \begin{bmatrix} \underline{n} & \overline{n} \end{bmatrix} \in \mathbb{R}^{2n}, \end{aligned} \tag{3.16}$$

with I_n denoting an identity matrix of dimension n.

The proposed SMI algorithm can be summarised as follows: Firstly, a DDPS, $\Delta(k) \subseteq \mathbb{R}^{n_\xi}$ must be computed, using the DT-LIP description of the system dynamics (Equation 3.11), the noise bound (Equation 3.15) and the input-output measurements. The input-output measurements could correspond to logged data or real-time measurements, depending on whether the identification is offline or online. Next, the FPS, $\Pi(k) \subseteq \mathbb{R}^{n_\xi}$, is computed, using the DDPS and the previous estimate of the FPS $\Pi(k-1)$. A parameter estimate $\hat{\theta}^\star$ is obtained by solving a QP over $\bar{\Pi}(k)$, using the DDPS as a constraint. The QP is formulated in terms of the original parameter vector θ instead of the transformed parameter vector ξ, to avoid the need for a non-linear transformation to invert the system dynamics. Finally, the parameter bounds are obtained by solving a minimisation/maximisation linear program over the DDPS polytope. In the case of online identification, both the optimal parameter vector estimate and the bounds must be computed at each iteration. The steps to compute the DDPS are described in the next section.

3.2.1 Data-driven Parameter Set (DDPS) Computation

For the DT-LIP system represented by Equations (3.11), the DDPS refers to the set of all parameters that is consistent with the model structure, measurement data and the noise and disturbance bounds at each time-step k. The DDPS can be approximated as a polytope computed by firstly combining the equations (3.11a), (3.11b), such that

$$y(k+1) = \mathfrak{g}(k) + n(k+1), \tag{3.17}$$

where the term $\mathfrak{g}(k) \in \mathbb{R}^n$ is given by

$$\mathfrak{g}(k) = G(y(k) - n(k), u(k))\xi, \tag{3.18}$$

and depends on the output $y(k)$ and the control input $u(k)$, which are known; however, the noise signal $n(k)$ is unknown. For computing the DDPS, we require computing a polytopic bound for this term, which can be obtained via interval analysis. Firstly, a bound on the states can be computed as

$$\begin{aligned} &\underline{x}(k) = y(k) - \bar{n} \leq y(k) - n(k) \leq y(k) + \bar{n} = \bar{x}(k), \\ \Leftrightarrow\ &x(k) \in [\underline{x}(k), \bar{x}(k)] = [x(k)]. \end{aligned} \tag{3.19}$$

The interval $[x(k)]$ can be updated online for each new measurement. Using equation (3.19) and interval arithmetic, we can further compute a time-varying interval bound for the nonlinear basis function $G(y(k) - n(k), u(k))$, as in [158], such that

$$[\underline{G}(k), \overline{G}(k)] \supseteq G([x(k)], u(k)). \tag{3.20}$$

As a result, Equation (3.20) yields the polytopic bounds given by

$$\begin{aligned} &\mathfrak{g}(k) \in \mathcal{G}, \\ &\mathcal{G} = \{\mathfrak{g}(k) \in \mathbb{R}^n | H\mathfrak{g}(k) \leq h_g(y(k), u(k))\}, \end{aligned} \tag{3.21}$$

where the upper-bound $h_g(y(k),u(k)) \in \mathbb{R}^{2n}$ is calculated using

$$h_g(y(k),u(k)) = \begin{bmatrix} \Delta y(k) + G_r(k)\bar{\xi} \\ -\Delta y(k) + G_r(k)\bar{\xi} \end{bmatrix}. \tag{3.22}$$

Here, $\Delta y(k)$ is the one-step difference equal to $(y(k+1) - y(k))$, $G_r(k)$ is the radius of the interval matrix $G([x(k)],u(k))$ and $\bar{\xi}$ is a component-wise upper bound vector for ξ. Since the inequalities in (3.15) and (3.21) are pre-multiplied by the matrix H, these can be added together, resulting in the following inequality

$$H(\mathfrak{g}(k) + n(k+1)) \leq h_g(y(k),u(k)) + h_n. \tag{3.23}$$

Note that to obtain the above inequality, the noise bound in (3.15) is shifted forward by one timestep. Finally, substituting the relations in (3.18) and (3.15) into the LHS of the above equation results in the DDPS given by

$$\begin{aligned} \Delta(k) = \{\xi \in \mathbb{R}^{n_\xi} | & HG([x(k)],u(k))\xi \leq \\ & h_g(y(k),u(k)) + 2h_n\}. \end{aligned} \tag{3.24}$$

The above equation can be rewritten in a simplified form as

$$\Delta(k) = \{\xi \in \mathbb{R}^{n_\xi} | H_\Delta(k)\xi \leq h_\Delta(k)\}, \tag{3.25}$$

where $H_\Delta(k) = HG([x(k)],u(k)) \in \mathbb{R}^{2n \times n_\xi}$ and $h_\Delta(k) = h_g(y(k),u(k)) + 2h_n \in \mathbb{R}^{2n}$.

To ensure that the physical parameters can be directly obtained from the parameter identification procedure, the DDPS must be reformulated in terms of the physical parameter vector θ. To carry out this re-formulation, firstly, the nonlinear mapping from the physical parameters to the transformed parameters is linearised as

$$\xi = \xi_0 + J(\delta\theta), \tag{3.26}$$

where ξ_0 is the initial transformed parameter vector computed by using the initial parameter vector θ_0, and $J = \partial\xi/\partial\theta|_{\theta_0} \in \mathbb{R}^{n_\xi \times n_\theta}$ is the Jacobian computed by finite differences. Rewriting Equation (3.24) using the relation in Equation (3.26), we obtain

$$\begin{aligned} \Delta_\theta(k) = \{\delta\theta \in \mathbb{R}^{n_\theta} | & HG([x(k)],u(k))J\delta\theta \leq \\ & -HG([x(k)],u(k))\xi_0 + h_g(y(k),u(k)) + 2h_n\}, \end{aligned} \tag{3.27}$$

which can be rewritten in a simplified form as

$$\Delta_\theta(k) = \{\delta\theta \in \mathbb{R}^{n_\theta} | H_{\Delta_\theta}(k)\delta\theta \leq h_{\Delta_\theta}(k)\}, \tag{3.28}$$

where $H_{\Delta_\theta}(k) = HG([x(k)],u(k))J \in \mathbb{R}^{2n \times n_\theta}$ and $h_{\Delta_\theta}(k) = -HG([x(k)],u(k))\xi_0 + h_g(y(k),u(k)) + 2h_n \in \mathbb{R}^{2n}$.

3.2.2 Feasible Parameter Set Computation

The set of all feasible parameters must be computed by recursively updating it using the DDPS, starting from an initial bounded parameter estimate. For the transformed parameters vector ξ, it can be represented using polytopes as

$$\Pi(k) = \{\xi \in \mathbb{R}^{n_\xi} | H_\xi(k)\xi \leq h_\xi(k)\}, \tag{3.29}$$

where $H_\xi(k) \in \mathbb{R}^{2n_\xi \times n_\xi}$ and $h_\xi(k) \in \mathbb{R}^{2n_\xi}$. Starting from an initial estimate of $H_\xi(0) = \begin{bmatrix} I_{n_\xi} & -I_{n_\xi} \end{bmatrix}^T$ and $h_\xi(0) = \begin{bmatrix} \bar{\xi} & \bar{\xi} \end{bmatrix}^T$, the FPS update at each time-step k is performed such that

$$\Pi(k) = \Pi(k-1) \cap \Delta(k), \forall k = 1, \ldots, N. \tag{3.30}$$

This intersection of the two polytopic sets results in a new set defined by the inequality in (3.29), with the new pair $(H_\xi(k), h_\xi(k))$ given by

$$H_\xi(k) = \begin{bmatrix} H_\xi(k-1) \\ H_\Delta(k) \end{bmatrix}, \; h_\xi(k) = \begin{bmatrix} h_\xi(k-1) \\ h_\Delta(k) \end{bmatrix}. \tag{3.31}$$

As new measurements are incorporated, the polytope can quickly explode in size and must be kept bounded to avoid computational burden.

The parameter identification problem is formulated as a QP in the physical parameter increment vector given by $\delta\theta \in \mathbb{R}^{n_\theta}$, around an initial anchor θ_0. Defining $\Phi = H_\xi(N)$ and $\mu = h_\xi(N)$ as the final stacked pair representing the FPS at the N-th timestep, the constrained QP can be stated as the following minimisation problem

$$\min_{\delta\theta} \frac{1}{2}\|\Phi(\xi_0 + J(\delta\theta)) - \mu\|_2^2 + \frac{\lambda}{2}\|\delta\theta\|_2^2 \tag{3.32a}$$

$$\text{s.t. } \underline{\theta} \leq \theta_0 + \delta\theta \leq \bar{\theta}, \tag{3.32b}$$

$$H_{\Delta_\theta}\delta\theta \leq h_{\Delta_\theta}. \tag{3.32c}$$

The variable λ represents the regularisation factor to prevent overfitting. Further, the Equation (3.32b) represents a box constraint on the physical parameters. The inequality constraint (3.32c) enforces the DDPS, where $H_{\Delta_\theta}, h_{\Delta_\theta}$ denote a stacked pair obtained by vertical concatenation, i.e.,

$$\begin{aligned} H_{\Delta_\theta} &= \begin{bmatrix} H_{\Delta_\theta}(1) & \ldots H_{\Delta_\theta}(N-1) \end{bmatrix}^T \in \mathbb{R}^{2n(N-1)\times n_\theta}, \\ h_{\Delta_\theta} &= \begin{bmatrix} h_{\Delta_\theta}(1) & \ldots h_{\Delta_\theta}(N-1) \end{bmatrix}^T \in \mathbb{R}^{2n(N-1)}, \end{aligned} \tag{3.33}$$

leading to the compact DDPS representation in $\delta\theta$ given by

$$\Delta_\theta = \{\delta\theta \in \mathbb{R}^{n_\theta} | H_{\Delta_\theta}\delta\theta \leq h_{\Delta_\theta}\}. \tag{3.34}$$

The resulting solution $\delta\theta^\star$ is the smallest parameter increment that is consistent with both measured input-output data and the FPS. The identified optimal parameters vector is given by

$$\hat{\theta}^\star = \theta_0 + \delta\theta^\star. \tag{3.35}$$

Using the above relation, the parameter bounds can also be directly inferred by solving a componentwise min/max problem over the compact DDPS polytope, such that

$$\begin{aligned} \underline{\theta}_i^\star &= \theta_{0,i} + \min_{\delta\theta \in \Delta_\theta} \delta\theta_i \\ \bar{\theta}_i^\star &= \theta_{0,i} + \max_{\delta\theta \in \Delta_\theta} \delta\theta_i, \end{aligned} \tag{3.36}$$

with $\underline{\theta}_i$ and $\bar{\theta}_i$ denoting the lower and upper bounds for the $i-$th parameter, respectively, for all $i \in \{1, \ldots, n_\theta\}$. The overall architecture of the SMI method is illustrated in Figure 3.2.

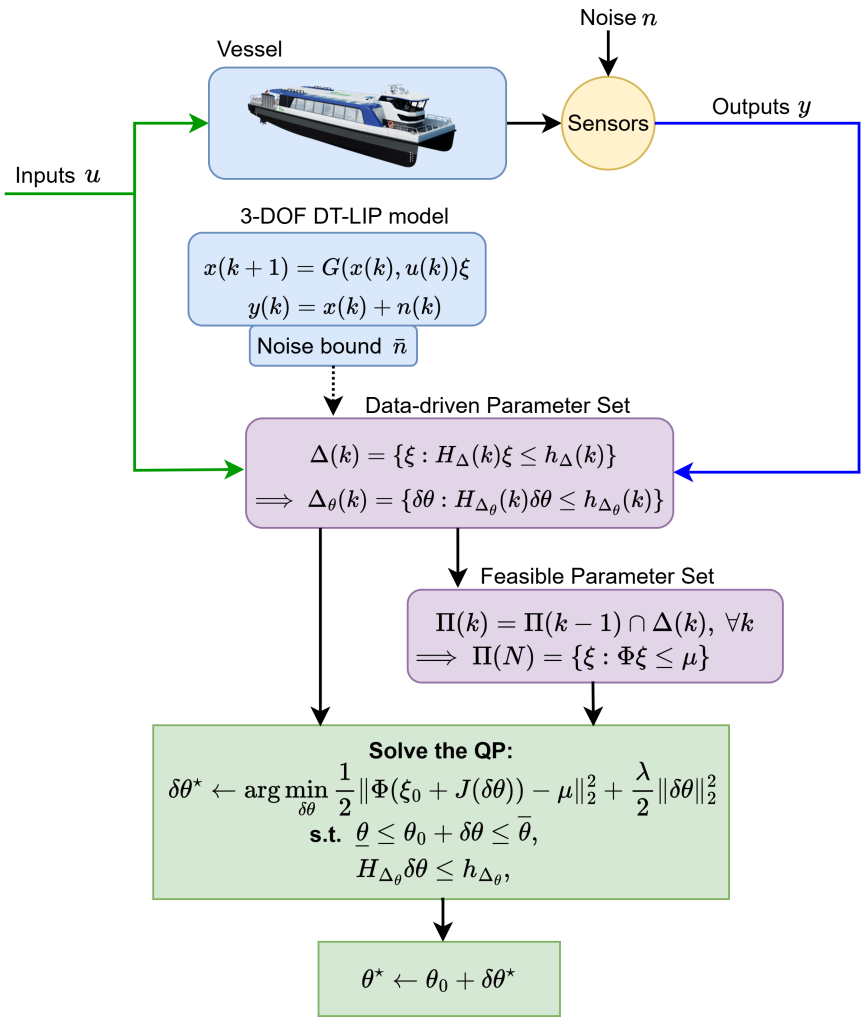

Figure 3.2: Architecture of the proposed SMI method.

Table 3.1: Parameters related to the DAMEN waterbus 2907 shuttle

Parameter	Description	Value	Unit
L_{oa}	Overall length	28.65	m
b	Beam	7.50	m
m	Mass	45000	kg
x_R	Thruster's x-coordinate	-12	m
$y_{R,i}$	Thruster's y-coordinate	$\pm$ 3.175	m

Table 3.2: The measurement noise bounds

Element	Value	Unit	Element	Value	Unit
$\bar{n}(1)$	2	m	$\bar{n}(4)$	0.5	m/s
$\bar{n}(2)$	2	m	$\bar{n}(5)$	0.5	m/s
$\bar{n}(3)$	0.05	rad	$\bar{n}(6)$	0.05	rad/s

3.3 System Identification: DAMEN Waterbus 2907 Vessel

In this section, the validation results are presented by applying the proposed method to the Waterbus 2907, a hybrid (diesel and battery) powered water shuttle designed by Damen Shipyards ([159]), equipped with two azimuth thrusters and two bow thrusters. Its main parameters, related to its dimensions and mass, are mentioned in Table 3.1. The vessel's maneuvering model is identified using logged data, including sensor measurements from the onboard global navigation satellite system (GNSS) and inertial navigation system (INS), as well as the propulsion system, during various maneuvers performed on the Merwede River. The controlled inputs correspond to the azimuth thrusters' angles and revolution speeds, whereas the bow thrusters are not employed, as only high-speed maneuvers are considered.

The data correspond to tests performed at full speed, including the zig-zag tests (at thruster angles of +20/-20, +10/-10, and +5/-5 degrees) and the turning test, and comprise a total of 3101 data points collected at a sampling rate of 10 Hz. As a result, the total dataset length and the sampling time are $N_{\text{total}} = 3101$ and $T_s = 0.1$ seconds, respectively. These tests provide sufficient persistence of excitation for the input signals, enabling reliable parameter identification for the given speed profile. The GNSS measurements are collected with real-time kinematic (RTK) positioning enabled, providing centimeter-level precision. Furthermore, the onboard INS provides filtered velocity measurements by fusing raw data from GNSS and IMU sensors. The tests were performed in calm waters, with water currents estimated at 3 km/h along the direction of the river. Further, wind speeds corresponding to a Beaufort Number of 2 were observed. The noise bound vector $\bar{n}$ is obtained using technical specifications for the onboard sensors, and its elements are given in Table 3.2.

3.3.1 Identification Procedure

Algorithm 3.1 summarises the overall system identification procedure using the proposed SMI method. For each maneuvering experiment $j = 1, \ldots, n_j$, the inputs $u_j \in \mathbb{R}^{N_j \times 4}$, and the measured outputs $y_j \in \mathbb{R}^{N_j \times 6}$ are employed in the identification procedure, where $N_{\text{total}} = N_j \cdot n_j$. Further, noise bounds $\bar{n} \in \mathbb{R}^n$ and the initial physical parameter bounds $[\underline{\theta}, \overline{\theta}]$ are utilised, based on technical datasheets and expert knowledge. At each trial, an initial guess on the parameters, θ_0, is randomly selected inside the parameter bounds. Using θ_0, a transformed parameter vector ξ_0 is obtained by using the transformation function f. In the for-loop (Lines 9-15), the DDPS and FPS are computed for each data point. The DT-LIP representation (Equation (3.11a)) is employed to compute the DDPS, using the relation in Equation (3.25) (Lines 10-11). In addition, the DDPS is transformed into $\delta\theta$-space in lines 12-13. Finally, the FPS is computed in Line 14, represented by a polytope defined by the pair $(H_\xi(k), h_\xi(k))$. Starting from an initialisation at the transformed bounds $[\underline{\xi}, \overline{\xi}]^T$, it is updated by intersecting it with the DDPS $\Delta(k)$, defined by

Figure 3.3: The Waterbus 2907 vessel (Courtesy: Damen Shipyards).

the pair $(H_\Delta(k), h_\Delta(k))$.

The compact DDPS polytope, represented by the pair $(H_{\Delta_\theta}, h_{\Delta_\theta})$, is obtained by vertically stacking the pairs obtained for each time step. The QP is formulated with respect to $\delta\theta$, to obtain the optimal $\delta\theta^\star$ value (Lines 18-19). Finally, the optimal physical parameter vector $\theta^\star$, and the optimal parameter bounds are obtained. For each experiment, the estimated states can be obtained by simulating the model using the optimal parameter vector $\theta^\star$.

It is noteworthy that Algorithm 3.1 can also be implemented for online parameter updating, since the DDPS and FPS are recursively updated. However, computational burden in real-time applications must be reduced, particularly for the intersection operation described by Equations (3.30) and (3.31). Many approaches have been suggested in the literature to address this issue, for example, outer-approximating the FPS at each iteration using predefined normal directions (see [158]).

3.3.2 Identification Results

The parameters of the 3-DOF model of the vessel obtained by using Algorithm 3.1 are summarised in Table 3.3. These correspond to the inertia- and added-mass-related parameters, the hydrodynamic derivatives, and the actuation-related parameters. The identified parameters are further validated by estimating the vessel's states, as described in the following subsections.

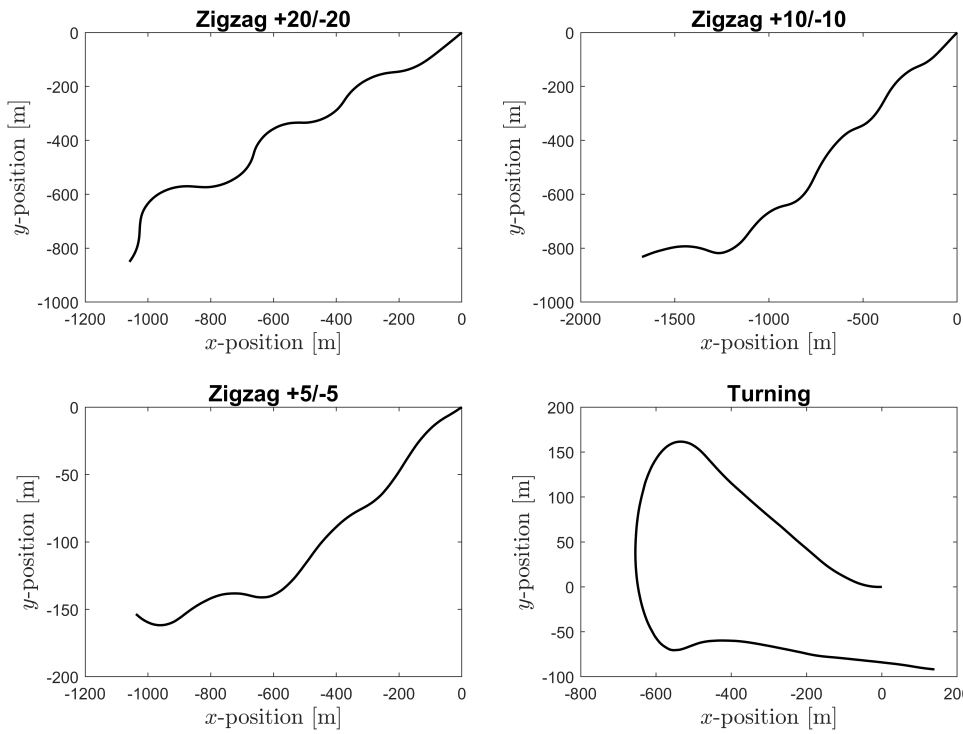

Figure 3.4: The vessel's motion trajectories in its x- and y- positions, corresponding to various maneuvering tests performed at full speed.

Algorithm 3.1 The proposed SMI algorithm

Input: $\{(u_j(k), y_j(k))\}_{j=1}^{n_\mathrm{j}}$ for $k = \{1, \ldots, N_\mathrm{j}\}$

Parameters: sample time T_s, noise bound $\bar{n} \in \mathbb{R}^n$, initial parameter bounds $\theta \in [\underline{\theta}, \overline{\theta}]$

Output: Optimal parameters per-experiment $\theta_j^\star$, Bounds $[\underline{\theta}_j^\star, \bar{\theta}_j^\star]$

for $j = 1$ **to** n_j **do**
  succ $\leftarrow 0$
  while succ $< N_\mathrm{starts}$ **do**
    $h_n \leftarrow \begin{bmatrix} \underline{n} & \overline{n} \end{bmatrix}$
    $\theta_0 \sim \mathcal{U}\big([\underline{\theta}, \overline{\theta}]\big)$, $\xi_0 \leftarrow f\big(\theta_0\big)$ ▷ random restart
    $J \leftarrow \partial\xi / \partial\theta|_{\theta_0}$ ▷ Jacobian
    $\begin{bmatrix} \underline{\xi}, & \overline{\xi} \end{bmatrix} \leftarrow f([\underline{\theta}, \overline{\theta}])$ ▷ transformed bounds
    $H_\xi(0) \leftarrow \begin{bmatrix} I_{n_\xi} & -I_{n_\xi} \end{bmatrix}^T$, $h_\xi(0) \leftarrow \begin{bmatrix} \underline{\xi} & \overline{\xi} \end{bmatrix}^T$ ▷ initial FPS
    for $k = 1$ **to** $N_j - 1$ **do**
      $H_\Delta(k) \leftarrow HG([x_j(k)], u_j(k))$
      $h_\Delta(k) \leftarrow h_g(y_j(k), u_j(k)) + 2h_n$
      $H_{\Delta_\theta}(k) \leftarrow H_\Delta(k)J$
      $h_{\Delta_\theta}(k) \leftarrow -HG([x_j(k)], u_j(k))\xi_0 + h_\Delta(k)$
      $H_\xi(k) \leftarrow \begin{bmatrix} H_\xi(k-1) \\ H_\Delta(k) \end{bmatrix}$, $h_\xi(k) \leftarrow \begin{bmatrix} h_\xi(k-1) \\ h_\Delta(k) \end{bmatrix}$
    end for
    Build stacked $H_{\Delta_\theta} \in \mathbb{R}^{2n(N_j-1)\times n_\theta}$ and $h_{\Delta_\theta} \in \mathbb{R}^{2n(N_j-1)}$ from $\{H_{\Delta_\theta}(k), h_{\Delta_\theta}(k)\}$
    $\Phi \leftarrow H_\xi(N) \in \mathbb{R}^{(2n_\xi + 2n(N_j-1))\times n_\xi}$ and $\mu \leftarrow h_\xi(N) \in \mathbb{R}^{2n_\xi + 2n(N_j-1)}$
    Solve the QP described in Equation (3.32).
    $\theta_j^\star \leftarrow \theta_0 + \delta\theta_j^\star$
    $\underline{\theta}_{i,j}^\star = \theta_{0,i} + \min_{\delta\theta\in\Delta_\theta} \delta\theta_i; \bar{\theta}_{i,j}^\star = \theta_{0,i} + \max_{\delta\theta\in\Delta_\theta} \delta\theta_i$, for $i \in \{1, \ldots, n_\theta\}$
    succ $\leftarrow$ succ $+ 1$
  end while
end for

Table 3.3: Identified parameters of the DAMEN waterbus 2907 shuttle

Parameter	I_{z_p}	$X_{\dot{u}}$	$Y_{\dot{v}}$	$Y_{\dot{r}}$	$N_{\dot{v}}$	$N_{\dot{r}}$	X_u	$X_{\|u\|u}$	X_{uuu}
Value	2.7 $\times 10^6$	-1945.16	-28921.48	-34885.49	-27909.24	-197285.14	-0.00	-642.59	-0.00
Unit	kgm^2	kg	kg	kgm	kgm	kgm^2	kg/s	kg/m	kgs^2/m^2
Parameter	Y_v	$Y_{\|v\|v}$	$Y_{\|r\|v}$	Y_r	$Y_{\|v\|r}$	$Y_{\|r\|r}$	N_v	$N_{\|v\|v}$	$N_{\|r\|v}$
Value	-12.93	-24921.71	-95742.81	256.50	-929504.91	496954.14	444.81	213501.59	-70223.26
Unit	kg/s	kg/m	kg	kgm	kg	kgm/rad	kgm	kgm	kgm^2
Parameter	N_r	$N_{\|v\|r}$	$N_{\|r\|r}$	$C_{t,1}$	$C_{t,2}$	$C_{l,1}$	$C_{d,0}$	$C_{d,1}$	A_R
Value	-0.19	-355262.69	-37454.15	1.25	1.06	0.1	0.1	0.1	8
Unit	kg m^2/s	kgm^2	kgm^2	Ns^2/rad^2	Ns^2/rad^2	-/rad	-	-/rad	m^2

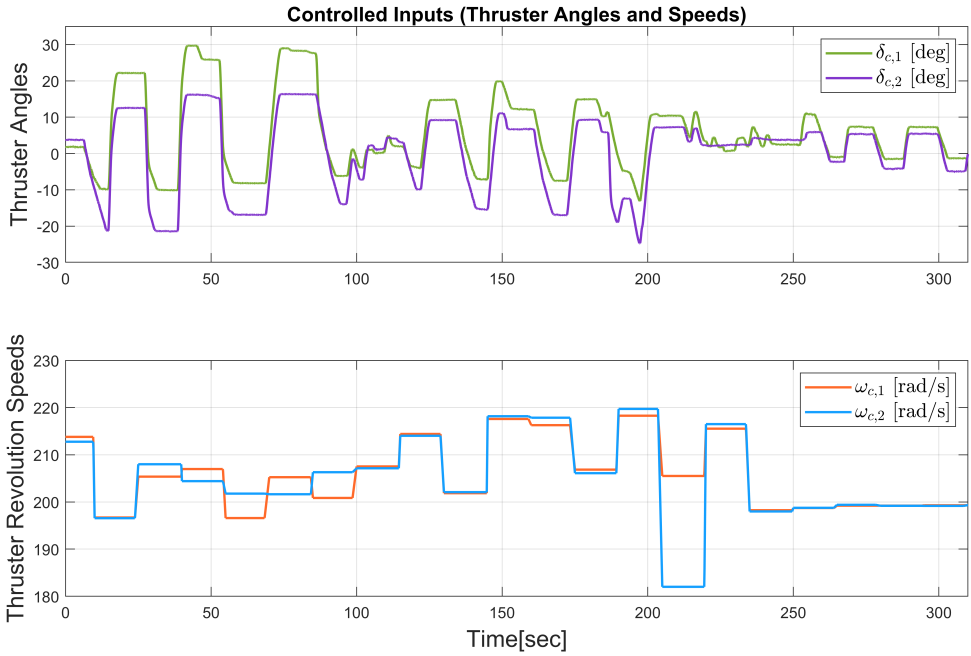

(a) Controlled inputs including the angles and revolution speeds for the port-side and starboard thrusters, respectively.

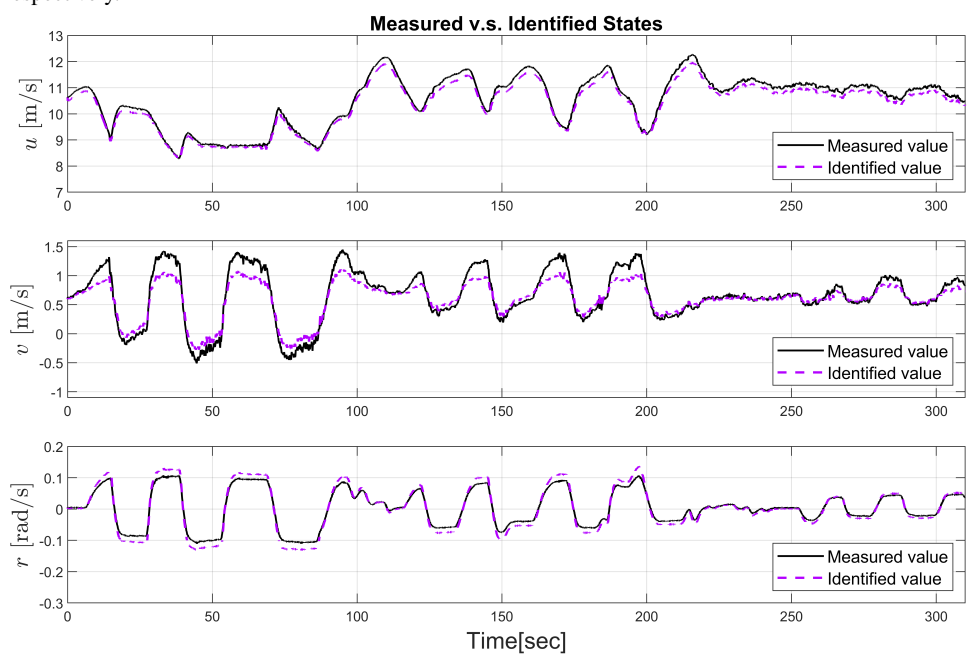

(b) Comparison between the vessel's measured linear and angular velocities and the corresponding simulated values.

Figure 3.5: The controlled inputs and the corresponding outputs, including the measured and simulated states. The simulated states are obtained using the vessel's identified model.

Table 3.4: Comparison between the average values of the percentage fit and computational time metrics corresponding to each test maneuver.

	Zig-zag $(-20/20)$	**Zig-zag** $(-10/10)$	**Zig-zag** $(-5/5)$	**Turning**
	Average J_{fit} value			
MATLAB's `nlgreyest`	81.45	76.11	61.54	81.49
SMI (Algorithm 3.1)	**86.04**	**83.59**	**88.08**	**86.49**
	Average J_{comp} value [sec]			
MATLAB's `nlgreyest`	0.0184	0.0228	0.0156	0.0273
SMI (Algorithm 3.1)	**0.0023**	**0.0030**	**0.0008**	**0.0029**

Validation using Simulations

The identified model is further validated by predicting the vessel's linear velocities and yaw rate, and comparing these predictions with the measurements. Figure 3.5 shows the controlled inputs, namely the azimuth angles and the propeller revolutions, and the corresponding states predicted using the identified model. The predicted trajectories closely match the measured data, demonstrating that the identified model accurately captures the vessel's dynamic behaviour across diverse maneuvers. The slight offset observed in the sway and yaw velocities is likely due to a combination of two related factors. First, the model assumes still water conditions, i.e., the relative velocity due to currents is not taken into account. However, during the tests, a mild river current was observed (at an estimated speed of 3 km/h), contributing to the vessel's sideslip and yaw moment. Secondly, wind speeds during the tests, although small in magnitude (estimated to be between 4-6 knots), can lead to time-varying sway forces and yaw moments, with their signs depending on the vessel's heading. To eliminate these errors and achieve higher prediction accuracy, incorporating a disturbance model for wind and current or including bounded disturbances in the DDPS can be beneficial.

Subsequently, the prediction accuracy and computational times are quantitatively evaluated using two performance metrics. Firstly, the percentage fit metric (J_{fit}) is calculated for each state as

$$J_{\text{fit}} = \max\left(0, 100\left(1 - \frac{\|y_x - \hat{x}\|}{\max(y_{\text{ref}}, \varepsilon)}\right)\right), \tag{3.37}$$

where y_x and $\hat{x}$ represent the measured and predicted states, respectively, and y_{ref} is the reference value, equal to the initial measurement. Next, the computational time metric J_{comp} is calculated to underline the feasibility of real-time application of the identification procedure. This metric is calculated as

$$J_{\text{comp}} = \frac{t_{\text{CPU}}}{N_{\text{total}}}, \tag{3.38}$$

where t_{CPU} is calculated by using MATLAB's `tic` and `toc` functions, at the beginning and end of the identification algorithm. The average values obtained for the aforementioned metrics are presented in Table 3.4 for each test maneuver. Across all maneuvers, the proposed SMI algorithm achieves a higher average J_{fit} value than MATLAB's `nlgreyest` algorithm, further confirming its accuracy and generalisability. In addition, the average J_{comp} value is at least one order of magnitude lower, supporting the case for online implementation of the SMI algorithm.

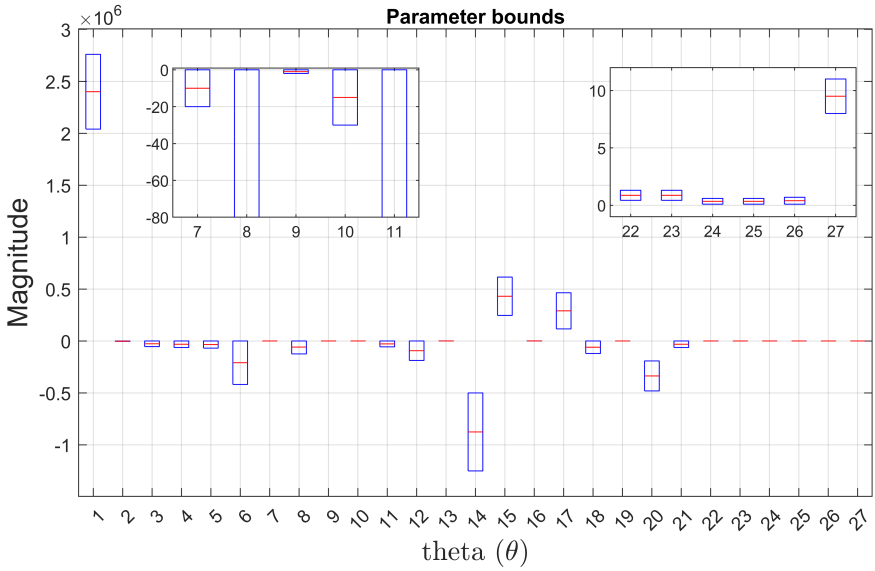

Figure 3.6: Box plot showcasing the lower and upper bounds on the parameters' magnitudes. The parameters are arranged in the x-axis according to the corresponding element's index in Equation (3.9).

Optimal Parameter Bounds

For each identified parameter, optimal bounds are computed by solving the pair of linear programs in Equation (3.36) over the DDPS polytope. The resulting intervals are visualised in the box plot as shown in Figure 3.6, with their respective numerical values listed in Table 3.5. Most parameters exhibit narrow intervals, indicating that they are tied to directions well excited by the data. The intervals are expected to shrink as more informative data are added to the DDPS set and to widen when the noise bounds are expanded. Importantly, the intervals remain non-empty and physically interpretable across all runs, indicating that the data are free of anomalies.

3.3.3 Validation using Synthetic Data

Validation using synthetic data provides a controlled benchmark for evaluating the proposed algorithm's accuracy. In this setting, the synthetic dataset is generated using a known model structure and parameter set, allowing direct comparison between the identified and true parameters. This enables the assessment of the algorithm's ability to accurately recover the physical parameters under idealised and controlled noise conditions. The synthetic data comprises controlled inputs and outputs for various simulated maneuvers of the vessel. Sensor noise is simulated using the bounds described in Table 3.2. The resulting magnitudes of the identified parameters using synthetic data are shown in Figure 3.7. As shown, the identified parameters are plotted for three scenarios: noiseless synthetic data (yellow markers), noisy synthetic data (blue markers), and real-world experimental data (green markers). The parameters identified from real-world

Parameter	Lower Bound	Upper Bound	Parameter	Lower Bound	Upper Bound
I_{z_p}	2.04 $\times 10^6$	2.76 $\times 10^6$	$Y_{\|r\|r}$	246031.5	615078.75
$X_{\dot{u}}$	-4120	0	N_v	0	790
$Y_{\dot{v}}$	-54370	0	$N_{\|v\|v}$	115993	463972
$Y_{\dot{r}}$	-63150	0	$N_{\|r\|v}$	-120462	0
$N_{\dot{v}}$	-68942	0	N_r	-0.45	0
$N_{\dot{r}}$	-418910	0	$N_{\|v\|r}$	-481073.75	-192429.5
X_u	-20	0	$N_{\|r\|r}$	-63174	0
$X_{\|u\|u}$	-128706.92	0	$C_{t,1}$	0.44	1.31
X_{uuu}	-2.00	0	$C_{t,2}$	0.44	1.31
Y_v	-30.00	0	$C_{l,1}$	0.1	0.6
$Y_{\|v\|v}$	-56668	0	$C_{d,0}$	0.1	0.6
$Y_{\|r\|v}$	-187748	0	$C_{d,1}$	0.1	0.7
Y_r	0	462	A_R	8	11
$Y_{\|v\|r}$	-1251352.5	-500541			

Table 3.5: The lower and upper bound values obtained for the identified parameters.

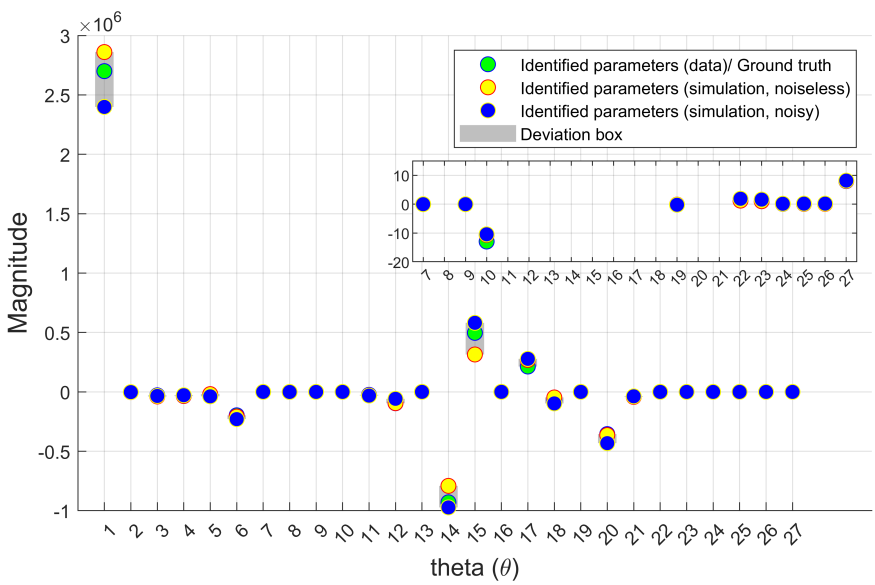

Figure 3.7: Comparison of various parameter magnitudes identified from simulations and real data, along with their ground truth values.

data also serve as the ground truth. It can be observed that the identified parameters lie within the same range as the ground truth and within the previously obtained parameter bounds. Importantly, the parameter sign consistency is maintained across all cases. This indicates that the identification method generalises well beyond idealised simulations and results in physically reliable results.

3.3.4 Sensitivity Analysis

Next, we evaluate the identified model's sensitivity by propagating parameter uncertainty through the predicted vessel states. This helps determine the impact of parameter variation on prediction accuracy. Firstly, a total of 500 parameter vector samples $\theta^{(s)} \in \mathbb{R}^{n_\theta}$ were uniformly generated within the obtained parameter bounds, such that,

$$\underline{\theta}_i^\star \leq \theta_i^{(s)} \leq \bar{\theta}_i^\star, \quad i \in \{1, \ldots, n_\theta\}. \tag{3.39}$$

For each sample, the nonlinear state update is performed using the available control inputs, resulting in multiple predicted trajectories over the full horizon (N_{total}). Further, prediction uncertainty bands are obtained by calculating the minimum and maximum values at each time instant across samples. The resulting plots, including predictions using the nominal and median parameter vectors ($\theta^\star, \tilde{\theta}$, respectively), the prediction band for each velocity component, are compared with the measured values, and visualised in Figure 3.8. As observed, a tight prediction uncertainty band is obtained that closely follows the measurements, with the nominal and median parameter vectors offering similar prediction accuracies within the band.

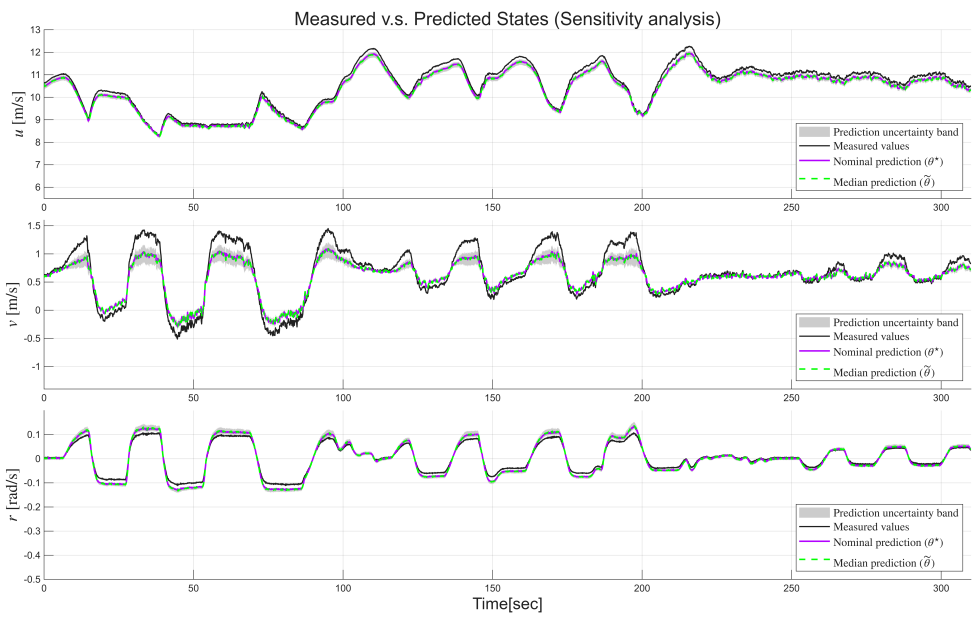

Figure 3.8: Plots of the vessel's measured linear and angular velocities and the corresponding predicted values obtained at the nominal (optimal) parameter ($\theta^\star$), the median parameter ($\tilde{\theta}$) in the parameter bounds, and the uncertainty band representing the minimum and maximum state predictions.

To quantify model accuracy for each sampled parameter vector $\theta^{(s)}$, a root mean squared error (RMSE)-based performance metric J_{RMSE} is defined, and is given by

$$J_{\text{RMSE}}(\theta^{(s)}) = \sum_{k=1}^{N_{\text{total}}} (y_x(k) - \hat{x}(\theta^{(s)}, k))^2, \tag{3.40}$$

where $y_x(k)$ represents the measured state at the k-th time-instant, and $\hat{x}(\theta^{(s)}, k)$ represents the predicted state value at the k-th time-instant obtained using sample $\theta^{(s)}$. To determine the parameter-wise sensitivity and the most crucial parameters for predictive accuracy, the Spearman rank correlation between each parameter θ_i^s and J_{RMSE} is computed across the samples. The Spearman coefficient, denoted by $\rho_s(\theta_i, J_{\text{RMSE}})$, correlates the ranks of the sampled values, and returns a correlation factor $\rho \in [-1, 1]$, with a ± 1 indicating strong correlation between the parameter θ_i and J_{RMSE}, whereas values close to zero indicating small correlation over the range of samples ([160]). Figure 3.9 plots the bar graphs for all parameters with their corresponding Spearman coefficients arranged in a descending order of their magnitudes. Notably, the moment of inertia parameter I_{z_p}, the yaw cross-coupling resistance parameter $N_{|v|r}$, and the second-order surge resistance parameter $X_{|u|u}$ obtain the highest values, implying that their variation within the parameter bound range is consistently related to the changes in the prediction quality. On the other hand, the third-order surge resistance parameter X_{uuu}, as well as the sway resistance parameters $Y_{|v|r}$, $Y_{\dot{r}}$, have the least impact on J_{RMSE}, or their effect is masked by interactions with other parameters.

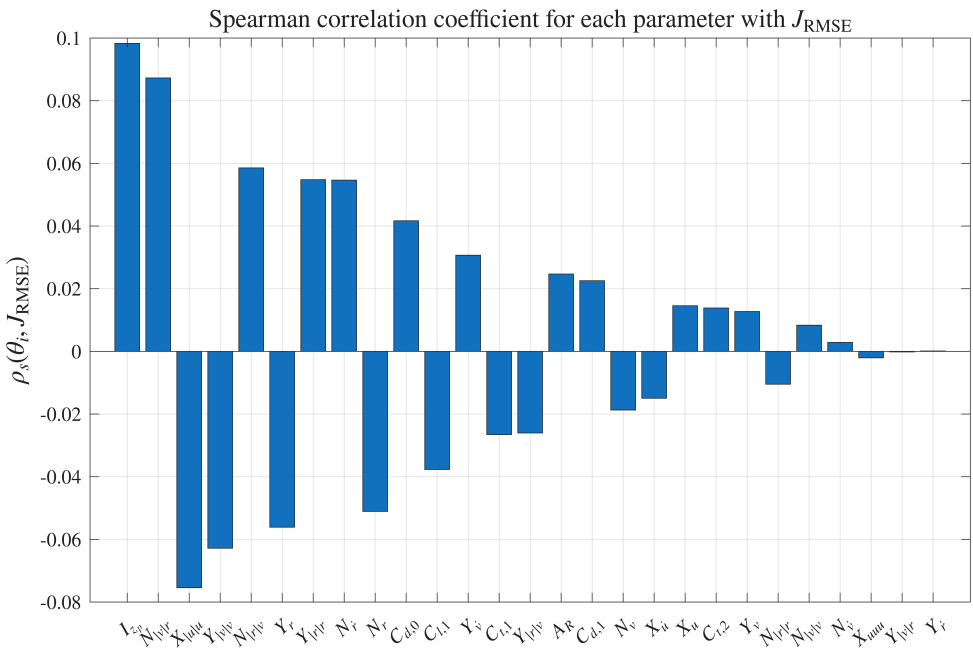

Figure 3.9: Spearman rank correlation coefficient for each parameter across the samples, with the prediction error metric J_{RMSE}.

3.4 Conclusions

This chapter proposed an SMI method for parameter identification of a full-scale 3-DOF vessel maneuvering model, thereby answering the research question **RQ2:** *How to identify a robust*

and control-oriented maneuvering model of marine vessels under realistic operating conditions?

The method relies on unknown but bounded descriptions for sensor noise and disturbances to deliver both nominal parameters and their bounds via the solution of convex programs. Validation using data from experimental trials with a full-scale catamaran ferry demonstrated that the proposed method yields parameters while requiring up to one order of magnitude less computational time per sample and achieving improved state prediction accuracy. Compared with MATLAB's built-in grey-box identification method, the prediction accuracy improved by up to 26.5%. Furthermore, the identified parameters were consistently obtained within definite bounds across all experimental and synthetic data validation. The obtained bounds facilitate the derivation of explicit guarantees for robustness and safety. Finally, through sensitivity analysis, the impact of parameter variation on the predicted trajectories was evaluated, and the most crucial parameters were identified.

Chapter 4

Nonlinear Model Predictive Control for Path-following of Autonomous Surface Vessels in Inland Waterways

To reach a port we must set sail –
Sail, not tie at anchor
Sail, not drift.

- Franklin D. Roosevelt

While Chapter 3 provides a method for obtaining robust vessel maneuvering models, autonomous navigation under uncertain conditions requires utilising these models to achieve accurate control predictions. This objective aligns with the following research question: **RQ3:** *How to design and evaluate control systems that ensure safe navigation of autonomous vessels in confined waterways?* To answer this question, an NMPC design for path-following control of an IWV is presented in this chapter. The dynamics of the IWV are modelled using an improved MMG maneuvering model, specifically designed for inland waterways and based on physical laws to effectively capture the unique hydrodynamic effects arising from water depths, river currents, and bank effects. Furthermore, an extensive case study is conducted to validate the performance of the proposed control design across diverse and complex inland waterway conditions, including navigating river bends and intersections. New key performance metrics are also proposed to evaluate the control performance on inland waterways.

This chapter is structured as follows: Section 4.1 introduces the modified MMG model and highlights the modified terms for the hydrodynamic effects in confined waterways. Section 4.2 describes the design of the NMPC path-following controller for an IWV. Section 4.3 presents the key performance metrics proposed for evaluating the controller's performance. Section 4.4 presents the simulation results for various scenarios considered with the vessel navigating in confined waterways. Finally, Section 4.5 presents the main conclusions of this chapter.

The contents of this chapter have been published in (Zhang et al., 2025[1] ; Zhang et al., 2024[2]).

4.1 Maneuvering Model for Inland Waterway Vessels

The maneuvering model follows the architecture in [69], where the effect of shallow water was modelled by two parts: (i) increasing resistance, especially the viscous pressure coefficient, is predicted using the methods from [161], and (ii) surge force and moments during steering in shallow water were calculated straightforwardly using hydrodynamic derivatives from the experiment. In addition, the bank effect is a critical factor for navigation in narrow fairways, which is calculated using the method from [58], where the lateral force and the yaw moment are modelled based on the vessel-bank distance, the water depth, and the bank geometry.

4.1.1 Equations of motion

IWVs typically operate at a steady, low speed and therefore do not frequently encounter high waves or strong winds. Consequently, the maneuvering model in this study focuses on two-dimensional (2D) planar ship motion with 3-DOF, considering only surge, sway, and yaw motions. The equations of rigid body dynamics for IWVs operating in confined waterways are obtained by modifying the MMG formulation given by Equation (5.13) in Chapter 4, and are represented as

$$\begin{aligned}
&(m + m_x)\,\dot{u} - (m+m_y)\,v_m r - x_G m r^2 = X_H + X_P + X_R + X_B \\
&(m + m_x)\,\dot{v}_m + (m + m_x)\,ur + x_G m\dot{r} = Y_H + Y_R + Y_B \\
&\left(I_{z_p} + x_G^2\, m + J_{z_p}\right)\dot{r} + x_G m\,(\dot{v}_m + ur) = N_H + N_R + N_B
\end{aligned} \tag{4.1}$$

where v_m is the sway velocity at midship. The right-hand side is the summation of the surge force X, sway force Y, and yaw moment N, and the subscripts H, P, R, and B represent the individual effect from the hull, propeller, rudder, and bank effect, respectively.

4.1.2 Hydrodynamic force on vessel hull

Hydrodynamic forces on the vessel hull are dimensionless according to the following equation

[1]Zhang, C.*, **Dhyani, A.***, Ringsberg, J.W., Thies, F., Negenborn, R.R. and Reppa, V., 2025. Nonlinear model predictive control for path following of autonomous inland vessels in confined waterways. Ocean Engineering, 334, p.121592.

[2]Zhang, C.*, **Dhyani, A.***, Ringsberg, J.W., Thies, F., Reppa, V. and Negenborn, R.R., 2024, June. Manoeuvring modelling and control design of autonomous vessels on inland waterways. In International Conference on Offshore Mechanics and Arctic Engineering (Vol. 87820, p. V05AT06A046). American Society of Mechanical Engineers.

*Equal contribution. The author of the thesis contributed to the systematic literature review, the design and analysis of the GNC system (Section 4.2), formulation of the key performance metrics (Section 4.3), and the simulations (Section 4.4).

$$\begin{aligned}
\frac{X_H}{(0.5\rho LTU^2)} &= -R_0^{'} + X_{\beta\beta}^{'}\beta_m^2 + X_{\beta r}^{'}\beta_m r^{'} + X_{rr}^{'}r^{'2} + X_{\beta\beta\beta\beta}^{'}\beta_m^4 \\
\frac{Y_H}{(0.5\rho LTU^2)} &= Y_{\beta}^{'}\beta_m + Y_r^{'}r^{'} + Y_{\beta\beta\beta}^{'}\beta_m^3 + Y_{\beta\beta r}^{'}\beta_m^2 r^{'} + Y_{\beta rr}^{'}\beta_m r^{'2} + Y_{rrr}^{'}r^{'3} \\
\frac{N_H}{(0.5\rho L^2TU^2)} &= N_{\beta}^{'}\beta_m + N_r^{'}r^{'} + N_{\beta\beta\beta}^{'}\beta_m^3 + N_{\beta\beta r}^{'}\beta_m^2 r^{'} + N_{\beta rr}^{'}\beta_m r^{'2} + N_{rrr}^{'}r^{'3}
\end{aligned} \tag{4.2}$$

where ρ is the freshwater density, L is the vessel length, T is the draught, and U is the vessel's total speed, $R_0^{'}$ is the resistance coefficient in shallow water [161], β_m is the drift angle at midship, if there is no current, this is calculated by $\beta_m = -\tan^{-1}\left(\frac{v_m}{u}\right)$; $X_{\beta\beta}^{'}$, $X_{\beta r}^{'}$, …, $N_{rrr}^{'}$ are the so-called hydrodynamic derivatives by regression analysis from the captive model test, $r^{'}$ is the non-dimensional yaw speed $\left(r^{'} = \frac{rL}{U}\right)$. It should be noted that u, v_m must be modified based on the speed and direction of the water flow if the current effect is included.

4.1.3 Propeller thrust

IWVs are typically equipped with twin propellers. The total longitudinal force delivered from a twin-propeller configuration can be expressed by

$$X_P = (1 - t)\left(T_P^P + T_P^S\right) \tag{4.3}$$

where t is the thrust deduction factor and T_P^P, T_P^S represent the thrust generated from the portside and starboard propellers, respectively, which are computed as

$$T_P^P = T_P^S = \rho n_P^2 D_P^4 K_T(J). \tag{4.4}$$

Here, n_P is the propeller revolution speed, D_P is the propeller diameter, and $K_T(J)$ is the function of the thrust coefficient derived from the open water test under various advanced ratios J. The advanced ratio is given by

$$J = u(1 - w_P)/(n_P D_P) \tag{4.5}$$

where u is the surge velocity and w_P represents the wake fraction at the propeller in maneuvering, computed as

$$w_P/w_{P0} = \exp\left(-4\,\beta_P^2\right) \tag{4.6}$$

where w_{P0} is the effective wake in a straight motion. Furthermore, β_P represents the inflow angle at the propeller, which includes the drift angle β_m and yaw speed $r^{'}$, and is given by

$$\beta_P = \beta_m - \left(\frac{x_P}{L}\right) r' \tag{4.7}$$

where x_P is the position of the propeller in the longitudinal direction. The propulsive coefficients, such as thrust deduction t and wake fraction w_{P0} are regarded as identical for each propeller. This is because of the challenge of analysing the unsymmetrical inflow fields during maneuvering motions; the crossflow can alter the wake field, and oblique movement might result in more complicated interactions. To understand this, sophisticated experimental measurements [162], such as Particle Image Velocimetry (PIV), or extensive CFD simulations are required, which are beyond the scope of the present work.

4.1.4 Rudder steering force and moment

Rudder steering forces and moments are another crucial component in the maneuvering model, as they directly influence the vessel's maneuverability. IWVs are typically equipped with twin or multiple rudders for improved steering. In this work, the rudder forces are computed as follows

$$\begin{aligned} X_R &= -(1 - t_R)\left(F_N^P + F_N^S\right)\sin\delta \\ Y_R &= -(1 + \alpha_H)\left(F_N^P + F_N^S\right)\cos\delta \\ N_R &= -(x_R + \alpha_H x_H)\left(F_N^P + F_N^S\right)\cos\delta \end{aligned} \tag{4.8}$$

where t_R is the empirical correction factor to rudder surge force during steering [163]; F_N^P and F_N^S denotes the rudder normal force on the port side and starboard, respectively; δ represents the rudder angle; α_H is the rudder force increase factor; x_R is the relative position of rudders in the longitudinal direction, and x_H is the position where additional lateral force is acting. As in the propeller force calculation, the interaction between multiple rudders was neglected in this work. Therefore, the rudder normal force is assumed to be identical with the same inflow angle, and is given by

$$F_N = 0.5\rho A_R U_R^2 \left(\frac{6.13\Lambda}{\Lambda + 2.25}\sin\alpha_R\right) \tag{4.9}$$

where A_R is the rudder area, U_R is the resultant inflow velocity at the rudder ($U_R = \sqrt{u_R^2 + v_R^2}$), Λ is the rudder aspect ratio. Further, α_R is the effective inflow angle at the rudder given by

$$\alpha_R = \delta - tan^{-1}\left(\frac{v_R}{u_R}\right) \tag{4.10}$$

where u_R and v_R represent the longitudinal rudder inflow velocity and the transverse rudder inflow velocity, respectively. These individual velocities are computed as

$$\begin{aligned} v_R &= U\gamma_R\left(\beta_m - l_R^{'} r^{'}\right) \\ u_R &= \frac{\varepsilon u_P}{1-s}\sqrt{1 - 2(1 - \eta\,\kappa)s + \{1 - \eta\,\kappa\,(2 - \kappa)\}s^2} \end{aligned} \tag{4.11}$$

where γ_R is the flow straightening coefficient; $l_R^{'}$ is a constant derived from experiments which denotes the acting point of v_R; s is the propeller slip ratio; η is a ratio of propeller diameter to rudder span $\left(\eta = \frac{D_P}{B_R}\right)$; κ is an experimental constant; and ε is the ratio of the wake fraction at the rudder and propeller positions given by

$$\varepsilon = \frac{(1 - w_R)}{(1 - w_P)}. \tag{4.12}$$

Here, w_R is the wake coefficient at the rudder position.

4.1.5 Bank-induced effect

The bank effect is another important factor that affects vessel handling in inland waterways. In this work, the hydrodynamic forces and bow-out moment are calculated through the methods

from [58]. A key feature of their mathematical model is that it also decomposes bank-induced force and moment into individual components, which can be easily incorporated into the MMG model.

4.1.6 River current

The effect of current, especially in sharp river bends or narrow fairways, makes maneuvering in inland waterways more complex. The currents in this work follow a near-parabolic distribution along the lateral direction, meaning that the flow is faster near the center of the waterway and nearly zero near the banks. The equation is given by

$$\begin{aligned} u_r &= u - U_C \cos(\beta_{\text{cur}} - \psi) \\ v_{rm} &= v_m - U_C \sin(\beta_{\text{cur}} - \psi) \end{aligned} \tag{4.13}$$

where β_{cur} is the incoming current angle in the earth-fixed coordinate system. Hence, the drift angle at midship, which accounts for the difference between the vessel's course and heading, is now given by $\beta_m = -\tan^{-1}\left(\frac{v_{rm}}{u_r}\right)$. Further, the total ship speed U is calculated by using $U = \sqrt{{u_r}^2 + {v_{rm}}^2}$. Note that the equations of motion are updated using the vessel's speed through water.

4.2 Guidance, Navigation and Control for Inland Navigation

4.2.1 Navigation system

The guidance and control systems rely on the continuous availability of the vessel's position, heading and velocities in 3-DOF. This is made possible by the multiple sensors that typically form a part of the navigation system and facilitate sensor fusion, redundancy and fault diagnosis. Typically, GPS/GNSS, gyrocompass and accelerometers are employed for the same. The navigation system of an IWV can be differentiated from that of a seagoing vessel by the requirement for additional sensors measuring water depth and currents, which must be incorporated into a closed-loop control system for autonomous navigation. The vessel's distance from the bank must also be available and can be measured using Electronic Chart Display and Information System (ECDIS) data [16]. Additionally, in major rivers and canals, bank infrastructure is increasingly being installed to provide precise localisation relative to fairway boundaries. Such infrastructure includes fixed beacons and transponders that communicate with the vessel's systems to provide constant updates on its relative position. Advanced navigation systems may further integrate Automatic Identification System (AIS) data and satellite-based augmentation system (SBAS) to improve positioning accuracy and situational awareness.

4.2.2 Guidance system

The IWV path-following problem can be posed as a heading control problem using an appropriate guidance law. This requires transforming the desired position coordinates to the desired

heading angles. This is a typical approach followed for vessel control, using steering laws such as Line-Of-Sight (LOS) [164], or their improved variants [75, 165]. The primary objective of such guidance laws is to adjust the vessel's heading angle to minimise the cross-track error, i.e., the lateral deviation from the desired path. As shown in the next section, focusing on heading control can greatly simplify the control design procedure without trading off the path-following performance.

The guidance system employs a path-planning algorithm to calculate reference heading angles for a predetermined path defined by a set of waypoints. In this work, a lookahead-based Line-of-Sight (LOS) algorithm is employed [164], as visualised in Figure 4.1. Firstly, the cross-track error $XTE(t)$ is defined by

$$XTE(t) = \sqrt{\left(x_p(t) - x_{\mathrm{cl}}(t)\right)^2 + \left(y_p(t) - y_{\mathrm{cl}}(t)\right)^2} \tag{4.14}$$

where x_{cl} and y_{cl} are the points at the closest distance from the vessel on the desired path. Similarly, signed XTE (SXTE(t)) can be defined as

$$\mathrm{SXTE}(t) = \begin{cases} \mathrm{XTE}(t), & |\widetilde{\pi}| < 0 \\ -\mathrm{XTE}(t), & \textit{Otherwise} \end{cases} \tag{4.15}$$

where $\widetilde{\pi}$ is the cross product between the waypoint vector and the ship's position vector, and is equal to

$$\widetilde{\pi} = \left(x_{wp,k+1} - x_{wp,k}\right)\left(y_p - y_{wp,k}\right) - \left(y_{wp,k+1} - y_{wp,k}\right)\left(x_p - x_{wp,k}\right) \tag{4.16}$$

Using the current position of the vessel and the positions of the waypoints, the reference heading is computed as

$$\psi^{ref}(t) = \psi_{wp}(t) \; - \; \psi_{cross}(t) \tag{4.17}$$

where $\psi_{\mathrm{wp}}(t)$ represents the reference heading angle component corresponding to the slope of the line formed by two consecutive waypoints, i.e.,

$$\psi_{wp}(t) = \mathrm{atan2}\left(y_{wp,k+1} - y_{wp,k}, x_{wp,k+1} - x_{wp,k}\right) \tag{4.18}$$

Further, $\psi_{\mathrm{cross}}(t)$ is the reference heading angle component that minimises the cross-track error $\mathrm{XTE}(t)$ and is given by:

$$\psi_{cross}(t) = \mathrm{atan2}\left(\mathrm{SXTE}(t),\, X_D\right) \tag{4.19}$$

where X_D is a predefined lookahead distance value corresponding to the reaction distance of the IWV, which depends on the vessel type and its dimensions. In this work, it is selected as a constant positive value.

Since the path is approximated by straight-line segments connected by waypoints, a switching criterion is needed to transition between them. In this work, the along-track distance-based waypoint switching criterion is employed, where a switch is made when the vessel reaches a predefined distance away from the upcoming waypoint [164].

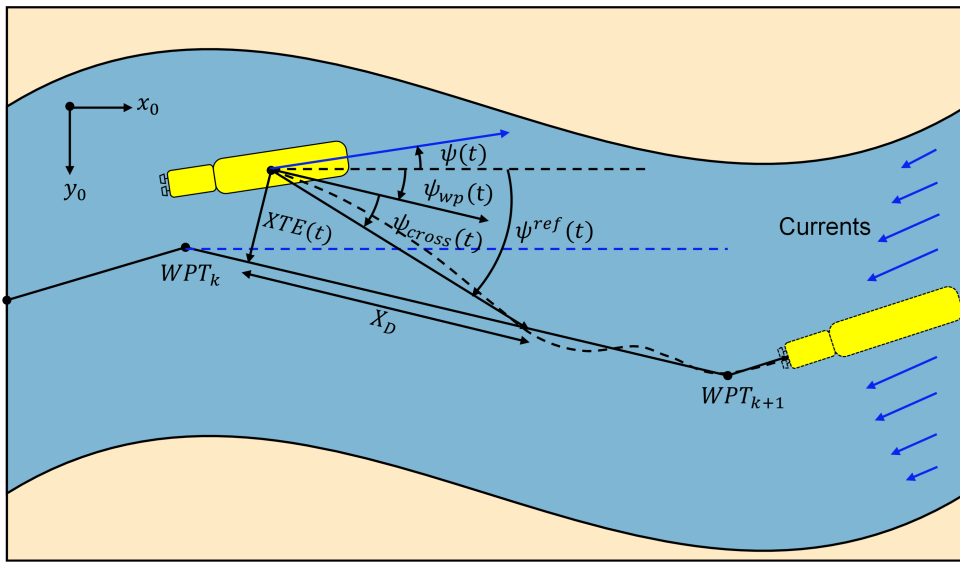

Figure 4.1: Guidance law for the IWV heading control.

Remark 4.1 Path segment/waypoint switching using a constant distance or a circular radius can cause sharp changes in the reference heading, leading to rudder angle oscillations [166]. These oscillations can be reduced by carefully selecting the lookahead and along-track distances. Furthermore, a smoother LOS steering law or switching criteria can significantly reduce this effect [167–169]. □

4.2.3 PID control design

Figure 4.2 shows a block diagram representation of the resulting closed-loop system with a PID controller for the IWV heading control. The PID reference tracking control law was designed to update δ_c at each time step, such that:

$$\delta_c(t) = K_p\left(\psi_e(t) + T_d\left(\psi_e(t) - \psi_e(t-1)\right) + \frac{1}{T_i}\left(\sum_{l=0}^{t}\psi_{e_l}\right)\right) \tag{4.20}$$

where, $\psi_e(t)$ represents the error in the heading angle at the time step t, K_p is the controller's proportional gain and T_d and T_i are the derivative and integral time constants, respectively. To select an optimal value for these control gains, the Ziegler-Nichols method [170] was employed to ensure a minimal heading error and acceptable overshooting and settling times for the resulting path.

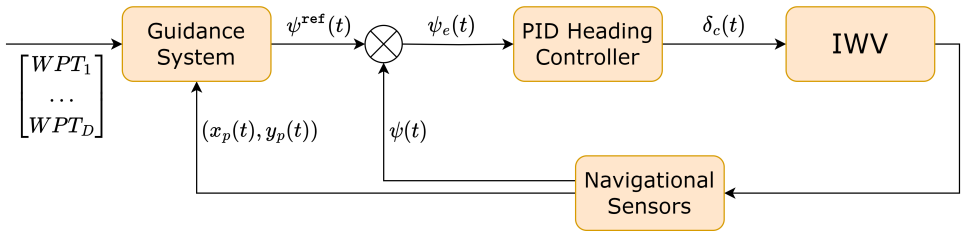

Figure 4.2: Block diagram representation of the IWV heading control using the PID controller.

4.2.4 Nonlinear Model-Predictive Control (NMPC): IWV model

To formulate the NMPC design problem, the IWV dynamics are presented in the state-space notation as:

$$\dot{q}(t) = f(q(t)) + g_1(q(t), \mathfrak{u}(t)) + g_2(q(t)) \tag{4.21}$$

where, $q(t)$ denotes the vessel's states and $\mathfrak{u}(t)$ is the control input, given by:

$$\begin{aligned} q(t) &= \begin{bmatrix} q_1(t) & q_2(t) & q_3(t) & q_4(t) & q_5(t) & q_6(t) \end{bmatrix}^T \\ &= \begin{bmatrix} x_p(t) & y_p(t) & \psi(t) & u(t) & v_m(t) & r(t) \end{bmatrix}^T \\ \mathfrak{u}(t) &= \delta(t) \end{aligned} \tag{4.22}$$

Further, the function of vessel states $f(q(t))$, $g_2(q(t))$, and of the states and control input $g_1(q(t), u(t))$ are given by:

$$\begin{aligned} f(q(t)) &= \begin{bmatrix} R(q_3(t))\,\nu(t) \\ -M^{-1}(D - \tau_e) \end{bmatrix}, g_1(q(t), \mathfrak{u}(t)) = \begin{bmatrix} \mathbf{0} \\ M^{-1}\tau_c \end{bmatrix}, \\ g_2(q(t)) &= \begin{bmatrix} \mathbf{0} \\ M^{-1}\tau_o \end{bmatrix}. \end{aligned} \tag{4.23}$$

where:

$$M = \begin{bmatrix} (m+m_x) & 0 & 0 \\ 0 & (m+m_x) & x_G m \\ 0 & x_G m & \left(I_{z_p} + x_G^2 m + J_{z_p}\right) \end{bmatrix}, D = \begin{bmatrix} -(m+m_y)\,q_5(t) q_6(t) - x_G m q_6(t)^2 \\ -(m+m_x)\,q_4(t) q_6(t) \\ x_G m q_4(t) q_6(t) \end{bmatrix},$$

$$\tau_e = \begin{bmatrix} X_H + X_B \\ Y_H + Y_B \\ N_H + N_B \end{bmatrix}, \tau_c = \begin{bmatrix} X_R \\ Y_R \\ N_R \end{bmatrix}, \tau_o = \begin{bmatrix} X_P \\ 0 \\ 0 \end{bmatrix}, R(q_3(t)) = \begin{bmatrix} \cos(q_3(t)) & -sin(q_3(t)) & 0 \\ \sin(q_3(t)) & \cos(q_3(t)) & 0 \\ 0 & 0 & 1 \end{bmatrix},$$

and η and ν represent the generalised position and generalised velocity vectors, given by:

$$\begin{aligned}\eta(t) &= \begin{bmatrix} q_1(t) & q_2(t) & q_3(t) \end{bmatrix}^T \\ &= \begin{bmatrix} x_p(t) & y_p(t) & \psi(t) \end{bmatrix}^T, \\ \nu(t) &= \begin{bmatrix} q_4(t) & q_5(t) & q_6(t) \end{bmatrix}^T \\ &= \begin{bmatrix} u(t) & v_m(t) & r(t) \end{bmatrix}^T \end{aligned} \tag{4.24}$$

As shown, τ_e comprises the hull forces and bank effect forces, whereas τ_c comprises the controlled rudder forces. Further, note that to simplify the control design process, the propeller rotation speed n_P is uncontrolled and assumed to remain constant during the heading control phase. This assumption is commonly used for path following in inland waterways, as overtaking is rare due to narrow channels, thereby minimising the speed variations. Instead, speed is often optimised as part of the voyage optimisation, see for example [171].

Equation (4.21) must be further discretised for a given sampling time to incorporate it as a prediction model within the finite time horizon of the NMPC OCP formulation. Therefore, upon discretisation, the IWV model is derived by the following discrete-time dynamics:

$$q_c(k+1) = f_c\left(q_c(k)\right) + g_{1c}\left(q_c(k), u_c(k)\right) + g_{2c}(q_c(k)) \tag{4.25}$$

where the subscript $(.)_c$ is used to represent the variables used in the IWV prediction model, and k is the discrete time step. Notice that Equation (4.25) is highly nonlinear and non-affine in control. Next, the constraints on the state variables and the control inputs are presented through the following inequalities:

$$\begin{aligned} \psi_{\min} \leq q_{3c}(k) \leq \psi_{\max} \\ u_{\min} \leq q_{4c}(k) \leq u_{\max} \\ v_{\min} \leq q_{5c}(k) \leq v_{\max} \\ r_{\min} \leq q_{6c}(k) \leq r_{\max} \end{aligned} \tag{4.26}$$

$$\delta_{\min} \leq u_c(k) \leq \delta_{\max} \tag{4.27}$$

Furthermore, to avoid rudder damage due to excessive actuation, the rate of change of the rudder angle can be limited by enforcing the following inequality:

$$|u_c(k+1) - u_c(k)| \leq \Delta_{\max} \tag{4.28}$$

where, $\Delta_{\max}$ is the maximum allowed change in the rudder angle in one time step. Finally, the fairway constraints can also be better modelled by using polyhedrons in terms of the constraints on the $x-$ and $y-$ coordinates of the vessel, which results in the following inequality constraint:

$$A_{fw} \begin{bmatrix} q_{1c}(k) & q_{2c}(k) \end{bmatrix}^T \leq b_{fw} \tag{4.29}$$

where, $A_{fw} \in \mathbb{R}^{N_{fw} \times 2}$ and $b_{fw} \in \mathbb{R}^{N_{fw}}$ represent the polyhedron in the H-representation.

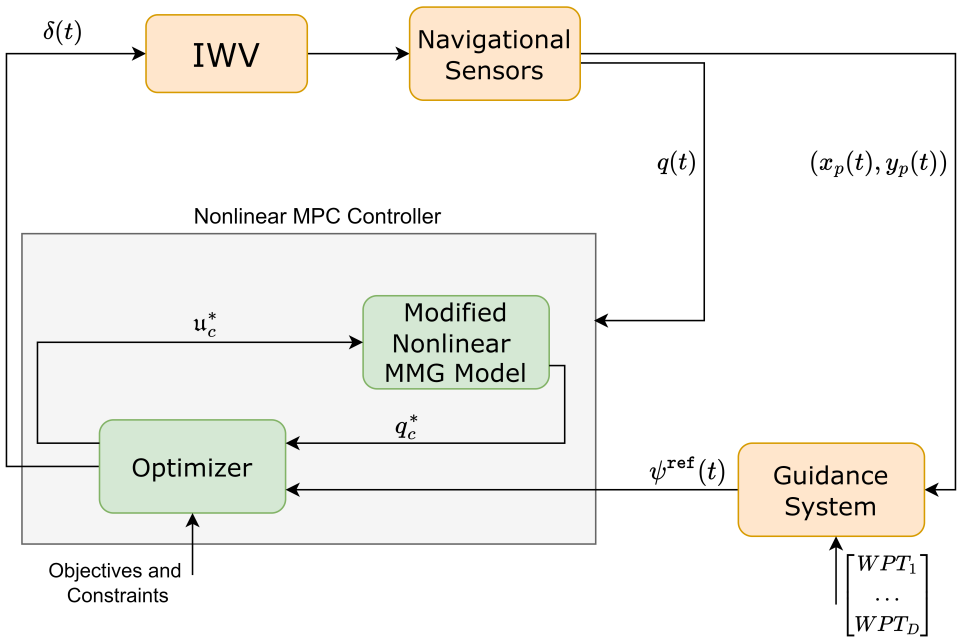

Figure 4.3: Block diagram representation of the IWV heading control using NMPC.

4.2.5 NMPC optimal control problem (OCP) formulation

An MPC-based control system computes a finite sequence of optimal control actions online by solving a finite-horizon optimisation problem. Out of the computed sequence, only the first control action is provided to the system, and this process is repeated at each time step. Figure 4.3 represents the overall closed-loop system resulting from the implementation of the NMPC system.

The NMPC OCP is formulated as a nonlinear programming (NLP) problem using the multiple shooting method over a finite prediction horizon N_h, where at each time step k, the following

optimisation problem is solved:

$$
\begin{aligned}
&NMPC\left(q_{3c}(k),\psi^{ref}(k)\right) = \\
&\arg\min_{q_{3c},\mathfrak{u}_c}\left(q_{3c}(N_h|k)-\psi^{ref}(N_h|k)\right)^2 p_m + \sum_{h=0}^{N_h-1}\frac{1}{2}\left(q_{3c}(h|k)-\psi^{ref}(h|k)\right)^2 q_m \\
&\qquad + {\mathfrak{u}_c}^2(h|k)\, r_m \\
&\quad s.t. \quad q_c(0|k) = q(k), \\
&\qquad q_c(h+1|k) = f_c(q_c(h|k)) + g_{1c}(q_c(h|k),u_c(h|k)) + g_{2c}(q_c(h|k)),\ \forall h\in\{0,\ldots,N_h-1\} \\
&\qquad \psi_{\min} \le q_{3c}(h|k) \le \psi_{\max},\ \forall h\in\{0,\ldots,N_h\} \\
&\qquad u_{\min} \le q_{4c}(h|k) \le u_{\max},\ \forall h\in\{0,\ldots,N_h\} \\
&\qquad v_{\min} \le q_{5c}(h|k) \le v_{\max},\ \forall h\in\{0,\ldots,N_h\} \\
&\qquad r_{\min} \le q_{6c}(h|k) \le r_{\max},\ \forall h\in\{0,\ldots,N_h\} \\
&\qquad \delta_{\min} \le u_c(h|k) \le \delta_{\max}, \forall h\in\{0,\ldots,N_h-1\} \\
&\qquad |u_c(h+1|k)-u_c(h|k)| \le \Delta_{\max},\ \forall h\in\{0,\ldots,N_h-2\} \\
&\qquad A_{fw}\begin{bmatrix} q_{1c}(h|k) & q_{2c}(h|k)\end{bmatrix}^T \le b_{fw},\ \forall h\in\{0,\ldots,N_h\}.
\end{aligned}
\tag{4.30}
$$

Here, p_m, q_m, and r_m are scalar values representing the controller weights. Further, h represents a time step over the prediction horizon, such that, $0 \le h \le N_h - 1$. Therefore, $h|k$ represents the prediction of the respective variable at the prediction step h, performed at the time step k. The objective function comprises a running cost and a terminal cost component that minimises the heading error. In addition, a running-cost component also minimises the required rudder movements. The solution of the NMPC OCP at the k^{th} time step is the pair of optimal rudder angle sequence and the corresponding sequence of the vessel's states, given by:

$$
(u_c^*, q_{3c}^*) = NMPC\left(q_{3c}(k),\psi^{ref}(k)\right) \tag{4.31}
$$

Finally, the first input rudder angle in the sequence is applied to the vessel, such that:

$$
\delta(k) = \mathfrak{u}_c^*(0|k) \tag{4.32}
$$

A unique feature of the multiple shooting method is that it divides the time horizon into smaller segments and generates the state trajectory at each time interval, by solving an independent initial value problem. This is unlike the single shooting method, which propagates the state trajectory from a single initial condition over the entire prediction horizon. This, in turn, improves the convergence speed of the solution and makes the optimisation more robust to errors in the initial values [95].

4.2.6 Closed-loop stability and recursive feasibility

The vessel's dynamical model is nonlinear, non-affine, and highly coupled, making it challenging to formally establish closed-loop stability. For this class of NMPC, selecting a suitable

Lyapunov function is difficult, and restrictive assumptions may fail to hold in operational conditions. Although the OCP given by Equation (4.30) includes a terminal cost term, it only serves as a tracking penalty and does not provide a control-Lyapunov terminal cost paired with a terminal invariant set [172]. Consequently, stability is only argued empirically from the case study results in Section 4.4. Likewise, recursive feasibility is not enforced through a terminal invariant set. However, Equation (4.29) provides a structural mitigation by considering a clearance margin relative to the physical waterway boundary. As shown later in Section 4.4, no infeasibility events were observed across the simulation scenarios.

A future direction to address both the stability and the recursive feasibility gap is to use computational methods to construct a suitable polytopic terminal set and a terminal cost term, as proposed by Lazar and Tetteroo [173]. This method works by linearising the nonlinear dynamics at the equilibrium point of interest and computing a stabilising local LQR controller for the linearised system.

4.3 Key Performance Metrics

The IWV heading control involves the satisfaction of multiple objectives. Typically, the controller's performance is evaluated by using the cross-track error and rudder angle error measures [20]. In this section, we propose some key performance metrics specifically focussing on evaluating the performance of path-following controllers for IWVs. While some of these metrics are based on commonly used metrics for control analysis, others are focused on evaluating the safety and robustness of inland navigation.

- Maximum Absolute Cross-Track Error (MAXTE): The minimisation of cross-track error (XTE) is the primary objective of IWV heading control. The satisfaction of this objective can be evaluated by using the MAXTE metric, which is given by:

$$\text{MAXTE} = \max_k XTE(k) = \max_k \sqrt{(x_p(k) - x_{cl}(k))^2 + (y_p(k) - y_{cl}(k))^2} \tag{4.33}$$

  Note that (x_{cl}, y_{cl}) maybe different from the waypoints and correspond to the closest point at a straight-line distance from the vessel. For a pusher connected to multiple barges, it is important to take into account the cumulative width when calculating the MAXTE, and the coordinates (x_p, y_p) must be modified accordingly.

- Average Absolute Cross-Track Error (AAXTE): While MAXTE indicates the maximum deviation from the desired path, AAXTE is concerned with the mean XTE accumulated over the time horizon until the vessel reaches its destination. This metric is also directly related to the running state cost of the NMPC OCP formulation.

$$\text{AAXTE} = \frac{1}{T_f} \sum_{k=0}^{T_f - 1} \sqrt{(x_p(k) - x_{cl}(k))^2 + (y_p(k) - y_{cl}(k))^2} \tag{4.34}$$

- Safe Inland Navigation Metric (SINM): Assuming two-way traffic on the waterway, it is desired to ensure that the vessel does not deviate too far in the port side direction.

For a constant width of the river channel, this corresponds to the vessel not crossing the waterway axis. At the same time, it must have a minimal XTE. These constraints can be simultaneously evaluated by using the SINM metric given as

$$\text{SINM} = \frac{1}{T_f}\sum_{k=0}^{T_f-1}\left(\sigma_1\frac{\max\left(0, XTE(k) - XTE_{\max}\right)}{XTE_{\max}} + \sigma_2\frac{\max\left(0, d_{cl,\min} - d_{cl}(k)\right)}{d_{cl,\min}}\right) \tag{4.35}$$

where, $XTE(k)$ is the cross-track error at the time step k, $XTE_{\max}$ is the maximum allowable cross-track error, $d_{cl}(k)$ is the distance of the vessel from the centreline at the k^{th} timestep, and $d_{cl,\min}$ is the minimum allowable distance from the centreline. The terms σ_1 and σ_2 are scalars used to assign weights to the importance of XTE and d_{cl}.

- Average Absolute Control Effort (AACE): The AACE metric computes the average control effort expanded by the control system throughout the duration of the course. It is a crucial metric from the energy consumption point of view. Similar to AAXTE, AACE considers the time-varying profile of the commanded rudder angles δ. This metric is expressed as:

$$\text{AACE} = \frac{1}{T_f}\sum_{k=0}^{T_f-1}|\delta(k)|^2 \tag{4.36}$$

- Inland Waterway Robustness Index (IWRI): As river currents, shallow-water effect and bank effect are some of the most significant sources of external disturbances impacting the IWV maneuvering, it is crucial to ensure that the designed controller is sufficiently robust against them. The IWRI is calculated by measuring the impact of these disturbances on performance metrics such as the cross-track error and the heading error, by comparing it to a nominal baseline scenario. It is calculated as:

$$\text{IWRI} = \frac{1}{T_f}\sum_{k=0}^{T_f-1}\left(\frac{XTE_k - XTE_{bl}}{XTE_{bl}} + \frac{\psi_{e,k} - \psi_{ebl}}{\psi_{ebl}}\right) \tag{4.37}$$

where XTE_k and $\psi_{e,k}$ are the cross-track errors and the heading errors at the k^{th} time-step, whereas XTE_{bl} and ψ_{ebl} are the corresponding baseline errors under nominal conditions. The baseline errors can be calculated by estimating the achievable errors under no water current, shallow-water and bank effect conditions.

- Estimated Time of Arrival (ETA): The vessel's ETA can vary significantly despite it maintaining a constant propeller rpm due to environmental factors such as currents, wind, and hydrodynamic disturbances. The controller's ability to effectively predict and counteract these factors plays a crucial role in determining the actual sailing time. For simplicity, the ETA is calculated while assuming no traffic congestion and the vessel being able to maintain a constant propeller speed throughout its journey.

$$\text{ETA} = \frac{D}{v} + \sum_{i=1}^{n}\left(\frac{\Delta d_i}{v - \Delta v_i}\right) \tag{4.38}$$

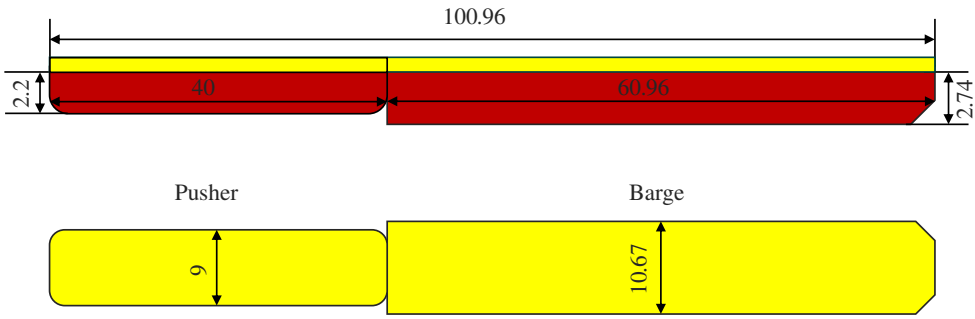

Figure 4.4: Geometry of pusher-barge convoy; dimensions in meters.

Here, n distance segments are considered where speed deviations are caused by various factors. D and v denote the total distance to be covered and the constant nominal speed of the vessel, whereas Δd_i, Δv_i denote the $i-$th distance segment with speed variation, and the variation in speed, respectively.

Ideally, these performance metrics should have the lowest possible values. For SINM, the ideal value is zero, whereas for IWRI, a negative value indicates that the controller outperforms the nominal case. In the following subsections, various simulation scenarios are presented to further evaluate the proposed controller's performance against these metrics.

4.4 Simulation Results

This section presents simulations of pusher-barge trajectories with the designed controllers. The modified MMG model is utilised as the basis for predicting vessels' dynamics under inland waterways with current effects. The simulation scenarios cover three typical operational modes of IWVs: (i) navigation along one side of the bank in the straight canal, (ii) turning in waterway interactions confluence, and (iii) track-pilot along river bends. The performance and robustness of the proposed control methods are evaluated using deviations in course (cross-track error) and rudder effort, as well as the proposed key performance metrics.

4.4.1 Vessel model

The vessel considered in this work is a pusher-barge convoy, where a rake barge connects to a pusher to formulate the 11BP system, as shown in Figure 4.4. The geometry of the convoy is listed in Table 4.1. Note that the midship position for the vessel is defined at the longitudinal and latitudinal coordinate representing the centre of the entire convoy, i.e., $(50.48,\ 0)$ m. The pusher has twin ducted propellers and four rudders to generate adequate maneuverability. The profile of the propeller and rudder is shown in Table 4.2. The hydrodynamic derivatives are selected based on experimental data from [70]. The model test was conducted on various water depth conditions, including depth-to-draught ratio (H/T) of 1.5 for medium shallow water and 1.2 for shallow water conditions (see the Table 4.3).

Table 4.1: Dimensions of the pusher-barge convoy in full-scale.

Parameters	Pusher	Rake-barge	Pusher-barge convoy
Length, L [m]	40.00	60.96	100.96
Ship Beam, B [m]	9.00	10.67	10.67
Draught, T [m]	2.20	2.74	2.74
Displacement, ∇ [m^3]	494.7	1646.2	2140.9
Block coefficient, C_B [-]	0.633	0.924	0.725

Table 4.2: Profile of rudder and propeller equipped on the pusher.

Parameters	Values
Propeller diameter, D_p [m]	1.8
Revolution speed, n_P [rpm]	300
Rudder span, B_R [m]	2.0
Rudder chord length, C_R [m]	2.0

4.4.2 Control parameters

The simulation scenarios are implemented based on the controller parameters listed in Table 4.4. For the NMPC, the state constraints are derived from the practical physical limits of the IWV. A prediction horizon equal to 25 secs is selected based on the full-scale vessel's characteristic time-scale and a computational requirement that enables for real-time application. Furthermore, the OCP is formulated using the Casadi toolbox [174] and solved using IPOPT ([175]). The NLP formulation of the OCP is performed using the multiple-shooting method in MATLAB to ensure improved efficiency and numerical stability.

4.4.3 Straight channel simulation

The straight channel is designed to have a width of W_C=100 m, and a rectangular cross-section with a constant water depth of H/T=1.2, representing extreme shallow water conditions that might pose challenges to steering handling. The currents are near parabolic and distributed along the canal with the maximum current speed at the waterway centre ($U_{C\mathrm{MAX}}$ = 0.5 m/s). The vessel is desired to keep a constant lateral vessel-bank distance of y_s= 25, which is a typical operational condition to ensure safety in confined canals to clear the way for upcoming or overtaking vessels. Under this circumstance, the heading controller is responsible for compensating the disturbances due to complex hydrodynamic effects from waterway, such as shallow water effect, bank effect and currents, to track and maintain the desired course with minimum error and control effort.

Figure 4.5 showcases the vessel trajectory with PID controller and NMPC under the influence of water currents. For upstream sailing, it can be observed in Figure 4.5 (a) that both controllers show good performance as the trajectories are fairly close to the reference path. Under downstream conditions in Figure 4.5 (b), the heading controller can maintain the path effectively while a slight course deviation can be noticed. This is due to the decrease of rudder

Table 4.3: Hydrodynamic derivatives of the pusher-barge model in shallow water.

Symbol	$H/T = 1.5$	$H/T = 1.2$	**Symbol**	$H/T = 1.5$	$H/T = 1.2$
$X'_{\beta\beta}$	-0.1749	-0.3637	ε	1.189	1.823
X'_{rr}	0.0792	0.1055	ℓ'_R	-0.538	-1.113
$X'_{\beta r}$	-0.0888	-0.248	t	0.249	0.326
Y'_{β}	0.6354	1.2375	α_H	0.089	0.418
Y'_{r}	-0.0227	-0.113	γ_R	0.357	0.293
$Y'_{\beta\beta\beta}$	2.5333	4.2245	w_{P0}	0.493	0.576
$Y'_{\beta\beta r}$	0.7413	3.6005			
$Y'_{\beta rr}$	0.286	0.7129			
Y'_{rrr}	-0.0836	-0.2003			
N'_{β}	0.1988	0.4435			
N'_{r}	-0.0654	0.0811			
$N'_{\beta\beta\beta}$	0.5665	1.1277			
$N'_{\beta\beta r}$	-0.6547	-0.2249			
$N'_{\beta rr}$	-0.0528	-0.0561			
N'_{rrr}	0.0097	-0.0522			

Table 4.4: Parameters of the controllers.

Controller	**Parameter**	**Value**
PID	K_p	5
	T_I	10
	T_D	25
	Time interval [sec]	0.5
NMPC	Prediction horizon N_h [sec]	2.5
	Interval [sec]	0.5
	Terminal cost weight p_m	4500
	Running cost weights $q_m\, r_m$	$q_m = 150,\ r_m = 1 \times 10^{-4}$
	Rudder angle limits [degrees]	$-45 \leq u_c(k) \leq 45$
	Heading angle limits [degrees]	$-90 \leq q_{3c}(k) \leq 90$
	Surge velocity limits [m/s]	$0 \leq q_{4c}(k) \leq 5$
	Sway velocity limits [m/s]	$-1.5 \leq q_{5c}(k) \leq 1.5$
	Yaw velocity limits [degrees/s]	$-5 \leq q_{6c}(k) \leq 5$
	Rudder angle change rate Δ_{max} [degrees/s]	7.2

incoming flow speed at downstream navigation for lower steering force. This phenomenon can be clearly seen in Figure 4.6, where the rudder effort is obviously lower in the upcoming current (Figure 4.6 (a)) as compared to downstream sailing, as shown in Figure 4.6 (b). The comparison of rudder effort also emphasises an important feature of NMPC: optimisation of the control effort. The controller can effectively utilise its predictions over the future horizon to adjust the rudder instead of correcting only based on the vessel's states, as in the case of PID control. The cross-track error is shown in Figure 4.6 (c) and (d), and in general, the time plot shows both controllers have good tracking performance, with the NMPC having an even smaller cross-track

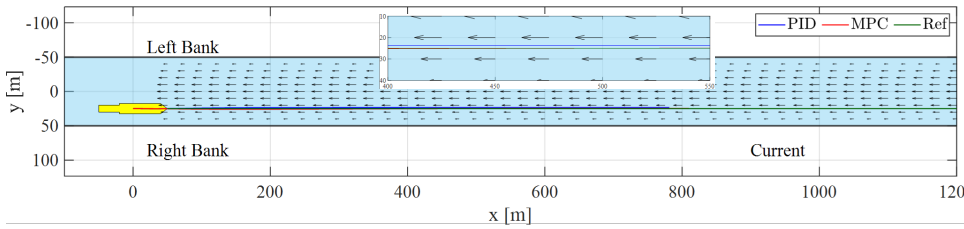

(a) Trajectory of upstream sailing.

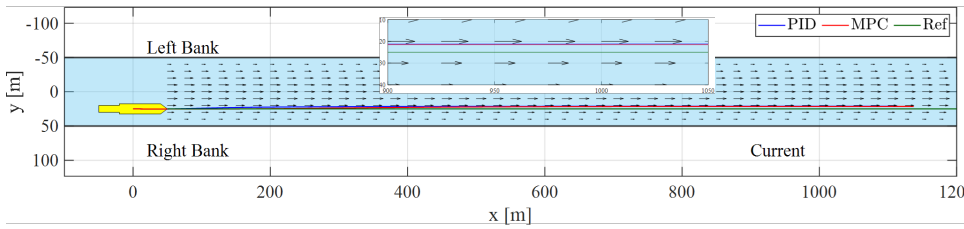

(b) Trajectory of downstream sailing.

Figure 4.5: Trajectories in a straight channel under heading control.

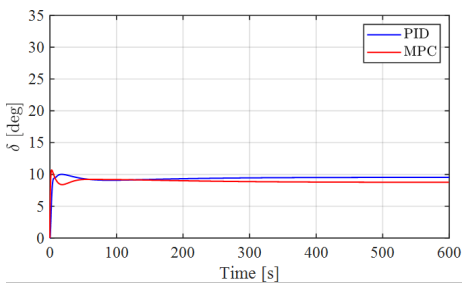

(a) Rudder angle (upstream).

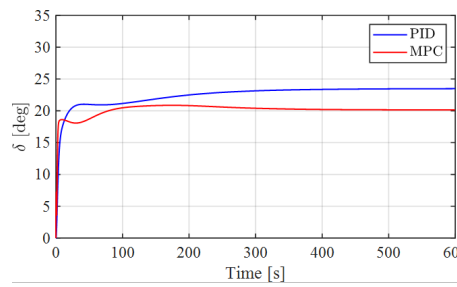

(b) Rudder angle (downstream).

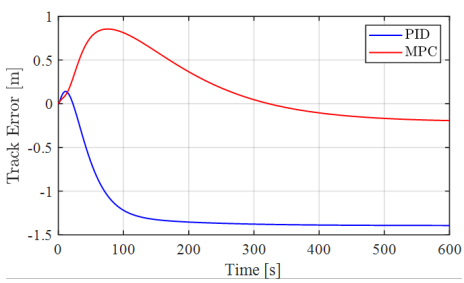

(c) SXTE (upstream).

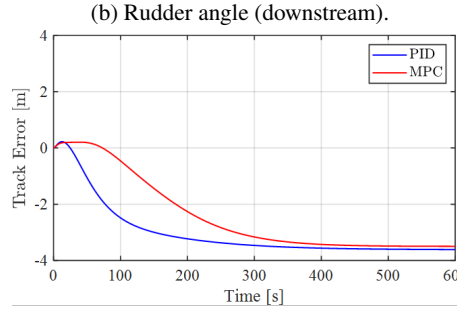

(d) SXTE (downstream).

Figure 4.6: The rudder angles and signed cross-track errors (SXTE) over time with PID controller and NMPC for the vessel sailing upstream and downstream, respectively.

error. Especially in upstream conditions, the lateral course deviation converges to within 0.5 m of the desired track. When navigating in narrow fairways, such as locks or small canals, precise motion control and track-keeping are critical for ensuring navigational safety.

4.4.4 T-junction simulation

Inland waterways have many intersections that connect river branches, canals, and ports to form complex transport networks. Navigating a vessel through this waterway confluence faces unique challenges, such as tight maneuvers or sharp turning. Unlike sea-going vessels, the operational spaces of IWVs are limited by such waterways. Therefore, advanced heading control is critically important when steering vessels in these intersections. To evaluate the tracking performance of the designed controllers, a waterway intersection with a "T-junction" shape is established in this section. The main channel has a relatively higher current speed (U_{CMAX}=0.5 m/s), and the tributary has a lower current speed (U_{CMAX}=0.1 m/s). It should be noted that the hydrodynamic behaviour of flow at the confluence point, such as vortices, is neglected in this work as it requires CFD simulation with accurate turbulence models. To execute a sharp turn in confined water, the vessel must initiate the maneuver well in advance. This implies that the waypoint generation should take the vessel's turning behaviour into consideration. In this scenario, the starting point for turning was selected based on the vessel's advance distance, which is equal to 2.5 times the vessel's length [69].

Figure 4.7 illustrates the trajectories resulting from the turning simulation under different current directions in the main channel, where attitudes of the vessel have been plotted in different colours to show its turning dynamics along the corresponding trajectory. To ensure turning safety, the vessel maintains a relatively low constant propulsion speed of 100 rpm, meaning that the speed changes dynamically only according to the vessel's location and current directions, as shown in Figure 4.8. The trajectories indicate that the NMPC achieves a near-perfect tracking performance under both conditions. In the downstream current as depicted in Figure 4.7 (a), the difference between the PID controller and NMPC is relatively minor, as the incoming current increases the rudder load and generates more maneuvering force, although some course deviation from the PID controller is still observable. In contrast, when applied to the downstream current scenario (see Figure 4.7 (b)), a clear difference between the two control methods can be seen. The PID controller exhibits a significantly higher tracking error compared to the NMPC, with the maximum tracking error even exceeding 20 m during the turning simulation, as shown in Figure 4.9. Another important factor that should be noted is that while the tracking performance of the PID controller is inferior to the more advanced NMPC, it still enables the system to generate fast responses to dynamic environmental impacts. As shown in Figure 4.7 (b), when the vessel completes the turn and enters the tributary, the PID controller's heading control can quickly steer the vessel back to the desired track, highlighting the controller's ability to adapt swiftly to changing conditions.

The corresponding rudder control effort is summarised in Figure 4.10. The rudder angle indicates a clear difference between the PID controller and NMPC. The NMPC's objective function explicitly considers reducing control effort, resulting in smoother and more consistent rudder angles over time. As seen in the NMPC simulations, the rudder angle does not show sudden changes during most of the operational period. However, relatively large deflections are observed in a short period when the vessel enters the near-bank track in the tributary due to the need for the heading controller to compensate for newly encountered hydrodynamic disturbances and maintain the vessel's course. On the contrary, the PID heading controller results in large deflections under both current directions. This difference highlights the potential of the NMPC to reduce frequent changes in the steering system, which is crucial for energy conservation and the stability of autonomous systems, especially as future IWVs may be fully electrified.

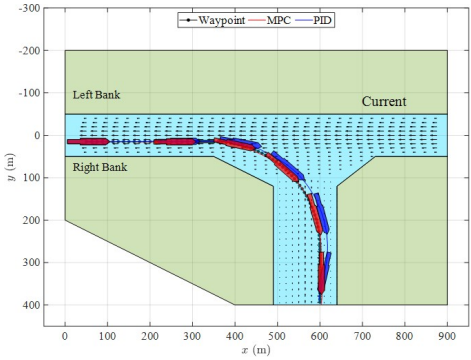

(a) Trajectory under upstream current.

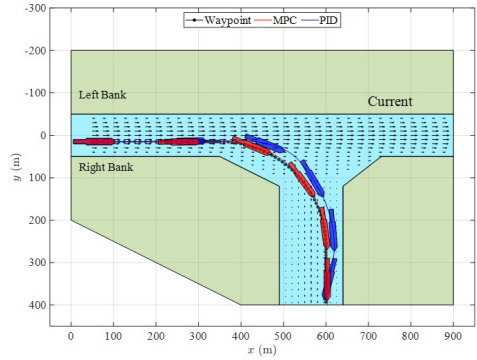

(b) Trajectory under downstream current.

Figure 4.7: Comparison of trajectories in T-junction-shaped waterways with a consistent water depth condition of H/T=1.2. The vessel keeps a constant propulsion speed of 100 rpm.

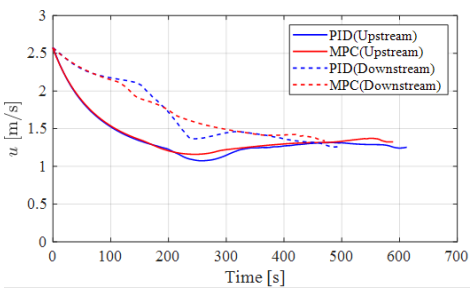

(a) Surge velocity u.

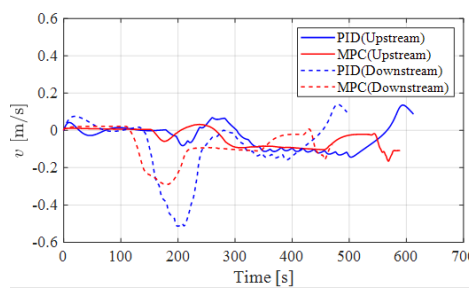

(b) Sway velocity v.

Figure 4.8: Comparison of the surge velocity u, sway velocity v during vessel turning, for PID controller and NMPC.

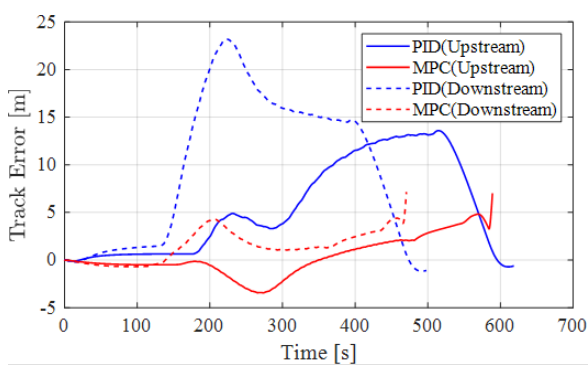

Figure 4.9: The signed cross-track errors with PID controller and NMPC for the vessel sailing upstream and downstream, respectively.

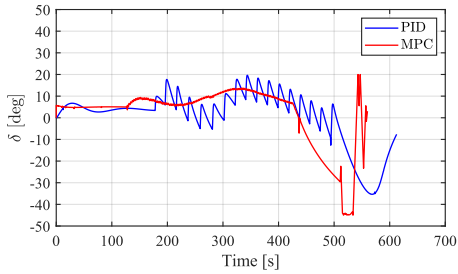

(a) Rudder execution for upstream case.

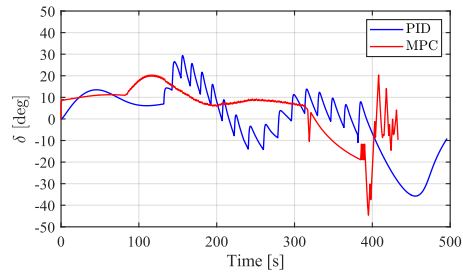

(b) Rudder execution for downstream case.

Figure 4.10: The rudder angles over time with PID controller and NMPC for the vessel sailing upstream and downstream, respectively.

Additionally, in this work, the vessel follows a constant rpm since vessels typically do not frequently change speed while navigating in a straight line. Implementing speed control within a certain range during sharp turns could potentially enhance the controller's performance in course tracking. However, this approach would also increase the complexity of the control design. Both controllers would require more parameter tuning due to the introduction of additional control variables. Furthermore, the computational demand will be higher when solving the NMPC optimisation problem online, necessitating more advanced hardware to ensure real-time performance.

4.4.5 River bends simulation

The final simulation scenario is navigation over river bends, which is the most prevalent environment for natural rivers. In this section, a river with near-wave-shaped bends is defined. The channel has a constant width of 150 m and a uniform water depth (H/T=1.2), which corresponds to the shallow water condition described in Section 4.4.4. The current flow follows the direction of the waterway, reaching its maximum speed in the centreline. Figure 4.11 depicts the trajectories obtained from the vessel's closed-loop simulations in river bends. The vessel begins at an initial vessel-bank distance (y_s) of 55 m and maintains a constant propulsion speed of 100 rpm. The control objective is to steer the vessel towards a predefined route at a lateral distance of 35 m from the bank. Overall, the results suggest that both control methods provide good tracking performance, as the vessel effectively follows the course. It is noteworthy that, in this scenario, the PID controller outperforms the NMPC at the start of the simulation, as it can steer the vessel faster toward the track. This aligns with the findings in Section 4.4.4, demonstrating the PID controller's capability to react quickly. Because current fields become more complex near river bends, the NMPC must account for these additional dynamic disturbances within the same prediction time step. This can explain its initial struggle at optimisation, especially in the downstream case with reduced rudder capacity (see Figure 4.11 (b)). Once the interaction increases, the NMPC follows the course while providing a good tracking performance. This is evident in the time plot of the cross-track error, which shows that NMPC can effectively reduce course deviation (see Figure 4.12). At the second river bend, where x spans from 800 to 1200 m, the XTE from NMPC remained steady at less than 5 m, whereas the PID controller had nearly twice the value. Similarly, the rudder angle oscillations are also significantly larger for

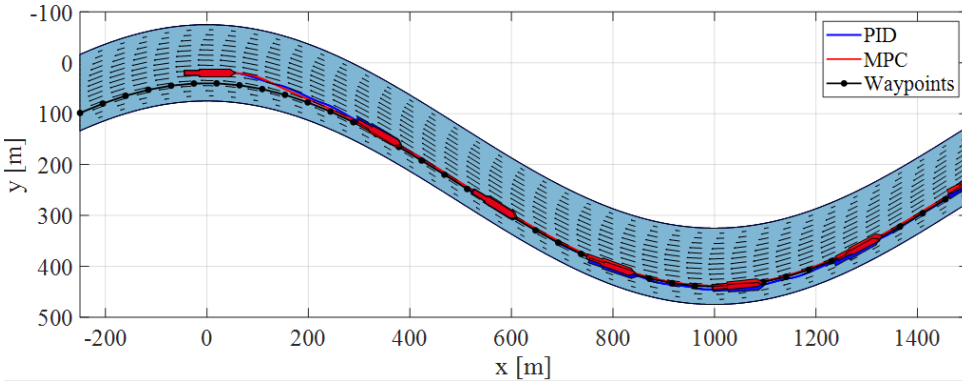

(a) Trajectory of upstream sailing.

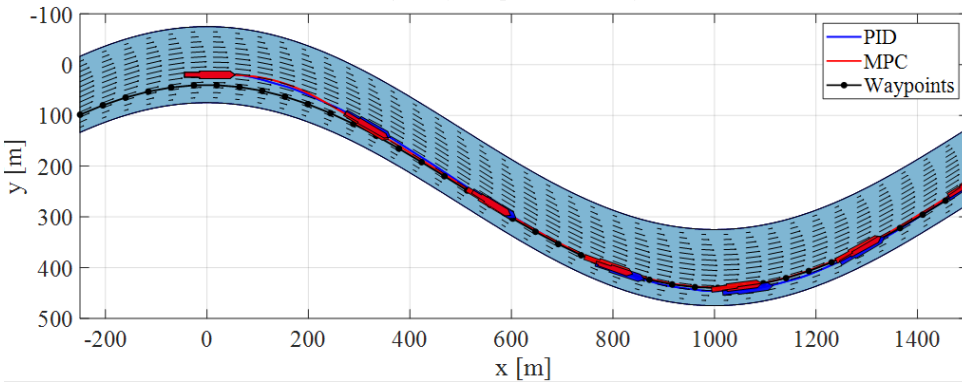

(b) Trajectory of downstream sailing.

Figure 4.11: Trajectories of control simulations on river bends.

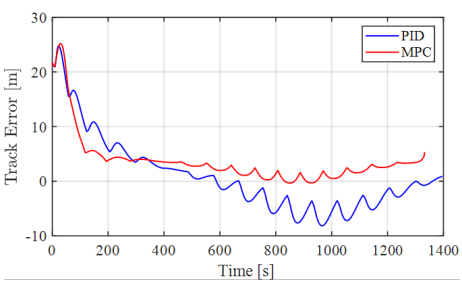

(a) SXTE for upstream sailing case.

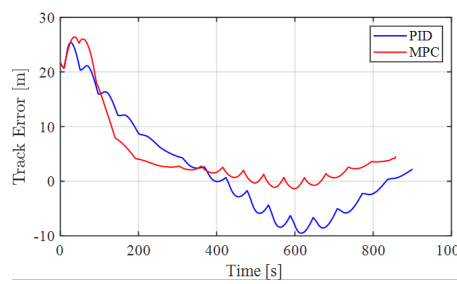

(b) SXTE for downstream sailing case.

Figure 4.12: Comparison of signed cross-track errors with PID controller and NMPC for the vessel sailing upstream and downstream, respectively.

the PID controller for both upstream and downstream sailing cases (Figure 4.13), even reaching its maximum angle limit of 45 degrees.

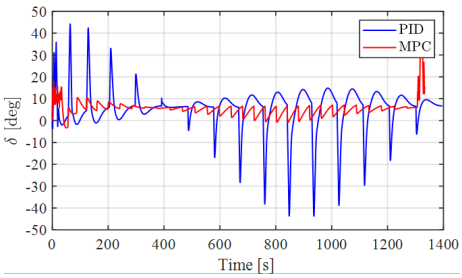

(a) Rudder angles for upstream sailing case.

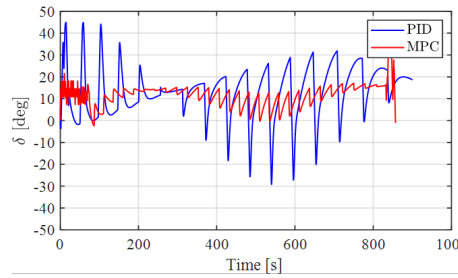

(b) Rudder angles for downstream sailing case.

Figure 4.13: Rudder angle plots for river bend navigation for the vessel sailing upstream and downstream, respectively.

Impact of ship-bank distances

IWVs frequently need to sail close to riverbanks to facilitate the passage of other vessels. However, vessels may experience significant hydrodynamic effects when navigating very close to the banks. The impact of bank effects is investigated under different ship-bank distances to evaluate the performance of the control design. Figure 4.14 showcases the trajectories under two ship-bank distance conditions. The vessel is expected to follow the designated path with heading control to maintain its course despite disturbances caused by increasing bank effects. The NMPC can effectively control the heading deviation at a medium ship-bank distance (y_s=30). However, it is important to note that the closer the vessel is to the bank, the more pronounced the bow-out moment acting on it becomes, see Figure 4.14 (b). When the route is extremely close to the bank, both controllers struggle to steer the vessel back to the desired track. It can be observed from the rudder angle plots (Figure 4.15) that the PID controller expends higher control effort in the form of large rudder deviations to maintain the reference trajectory, whereas the NMPC makes smaller but more frequent rudder deviations.

Considering the vessel's response time, such scenarios of navigating very close to riverbanks are particularly challenging. Future research should focus on developing more refined control designs, such as reducing speed while ensuring sufficient rudder steering force.

Impact of propulsion speeds

In this subsection, the impact of shaft speed on control performance is analysed for three different RPMs: 100, 125 and 150. The initial simulation setup was kept consistent with the aforementioned conditions. The cross-track errors of the two algorithms at different speeds are presented in Figure 18. The results indicate that increasing speed can reduce the tracking error by utilising higher rudder force, as shown in Figure 4.16 (a). However, in the case of the PID controller, increasing speed does not improve the vessel's tracking performance; instead, it introduces higher deviations. This may be attributed to the characteristics of the NMPC, which incorporates a prediction model. This is crucial for allocating the control inputs appropriately based on anticipated vessel behaviour in future steps. In contrast, the increased rudder load does not yield the expected benefits with the PID controller, as the rudder may oversteer due to shorter reaction times at higher speeds. Additionally, it is noteworthy that the NMPC can

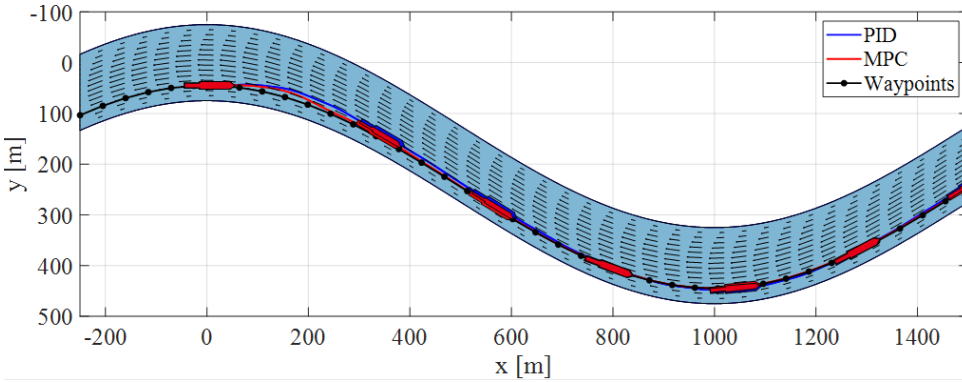

(a) Trajectory under y_s=30.

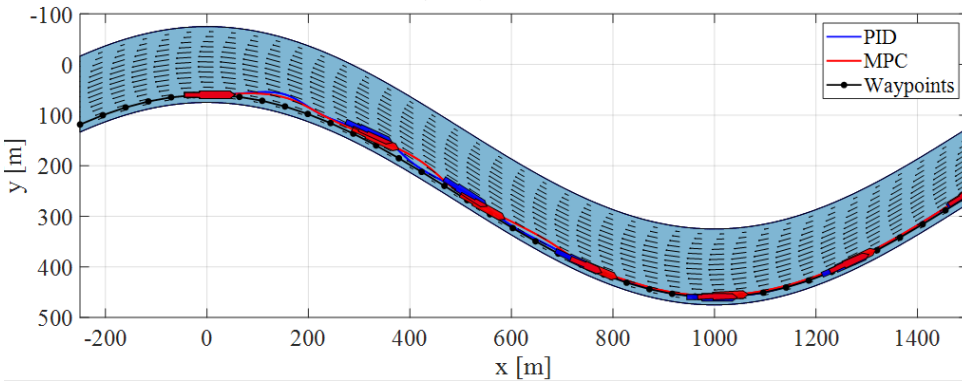

(b) Trajectory under y_s=15.

Figure 4.14: Trajectories under different ship-bank distances.

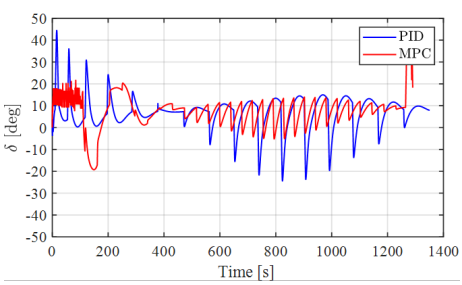

(a) Rudder angle under y_s=30.

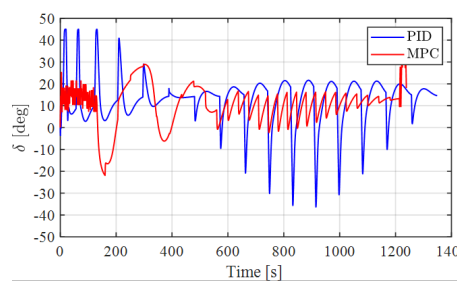

(b) Rudder angle under y_s=15.

Figure 4.15: Rudder angle plots under different ship-bank distances.

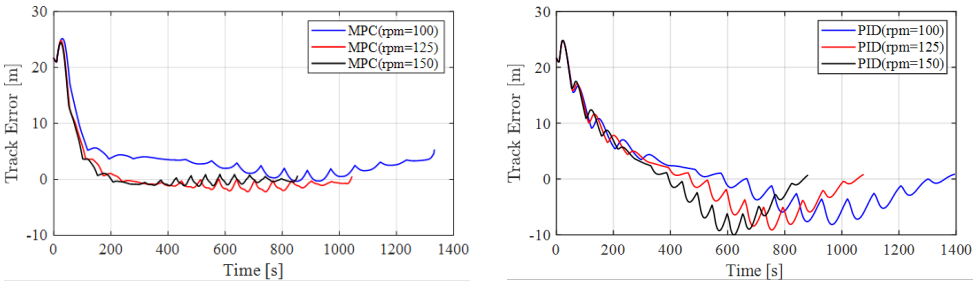

(a) SXTE of NMPC.

(b) SXTE of PID.

Figure 4.16: The impact of propulsion speeds on the signed cross-track error with PID controller and NMPC. The vessel is sailing upstream in these scenarios.

align the vessel with the reference trajectories with minimal track error, significantly reducing the sailing time while ensuring minor course deviations. For instance, the blue line (100 rpm) indicates that the NMPC saves almost 200 seconds of operation time as compared to the PID controller. This is crucial for reducing the ETA and saving energy, especially during long-term operations.

Impact of river cross-section shapes

In previous sections, the channel has a rectangular-shaped cross-section. In natural inland waterways, the fairway has different bank geometry with varying slopes. A typical cross-section shape is trapezoidal, with a constant slope from the bottom up to the free surface. In this section, the impact of the cross-section shape is analysed and quantified with three bank slopes. The channel's top width is 150 m, and the bottom width varies from 120 m to 80 m. The maximum water depth is 1.5 times the vessel's draught (H/T=1.5) to represent medium shallow water, and it decreases near both sides of the banks. The cross-sectional shape and waterway generated from the top view are illustrated in Figure 4.17. The control objective for the vessel is to keep a constant distance of 40 m from the bank ($y_s = 40$). This suggests that the narrower the bottom width, the more confined the waterways are and the stronger the hydrodynamic force (bank-effect) acting on the vessel. Under this scenario, the initial rpm is set to 100 according to the speed's impact on the performance of both controllers in Subsection 4.4.5.2.

In the case of a relatively wider bottom, as shown in Figure 4.18a, some deviations between the two controllers have been noticed. The PID controller exhibits higher course deviations initially, but the error gradually converges, yielding good tracking performance over time (blue line). It is clear that the PID controller shows difficulties in course tracking due to the bank effect. For NMPC simulation, as illustrated by the blue line, the vessel is also subject to a bow-out effect at the beginning; however, proactive heading control effectively mitigates the course deviation, and the trajectory exhibits minimal oscillation behaviour. When the waterway becomes more constrained, the channel wall exerts a stronger hydrodynamic force and moment on the vessel, resulting in worse tracking performance with the PID controller, as evident from the obvious deviations. The NMPC is also affected by stronger bank effects, but its trajectory remains more stable and continues to follow the desired track, as shown in Figure 21 and Figure

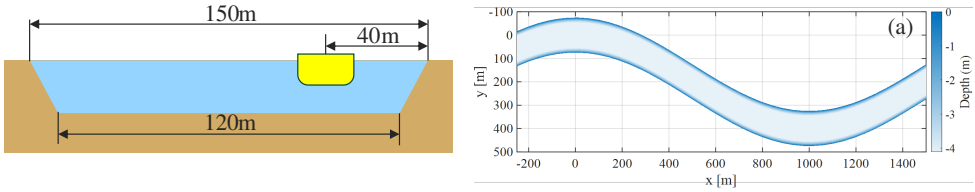

(a) Slope 1: w_{CB}=120.

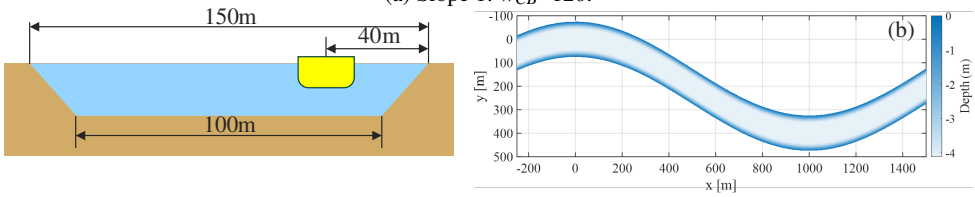

(b) Slope 2: w_{CB}=100.

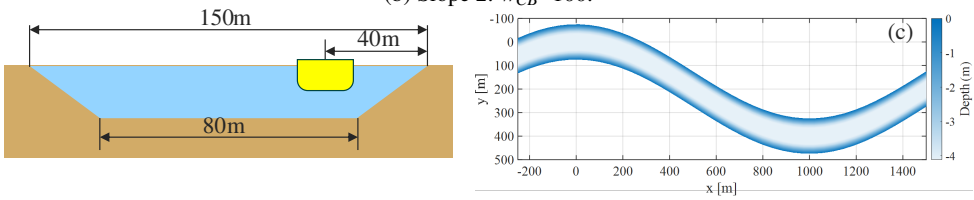

(c) Slope 3: w_{CB}=80.

Figure 4.17: Waterway generation with different cross-section shapes.

4.18c. A quantitative analysis of the signed cross-track error and the rudder angles is presented in Figures 4.19 and 4.20, respectively, which compare the performance of each controller for the considered cases. The NMPC demonstrates excellent tracking ability with reduced rudder efforts under a variety of waterway constraints. The increasing bank effect results in slightly increased tracking error, but the heading control can limit deviations to a very promising range (below 5 m) in all instances. In contrast, the PID controller has a considerable steady cross-track error at the second bend, which is almost twice that of the MPC. Such a value is considered a significant course deviation, as the vessel may risk losing maneuverability when approaching channel banks.

4.4.6 Comparison of key performance metrics

In this subsection, the performance of the proposed NMPC is further analysed and compared with that of the traditional PID controller using the key performance metrics proposed in subsection 2.3. For the SINM metric, the parameters σ_1 and σ_2 are set to 0.5. Further, $XTE_{\max}$ and $d_{cl,min}$ are selected as 1.7, 10 meters for the straight channel and 2.5, 5 meters for the T-junction and river bends scenario, respectively. For the IWRI metric, the XTE_{bl} and ψ_{ebl} are selected as 0.15 meters, 0.01 radians for the straight channel, and 1.5 meters, 0.07 radians for the T-junction and river bends scenarios, respectively.

As seen in Table 4.5, the values obtained for NMPC are significantly lower than the ones for the PID controller for most metrics in both upstream and downstream cases. The PID controller

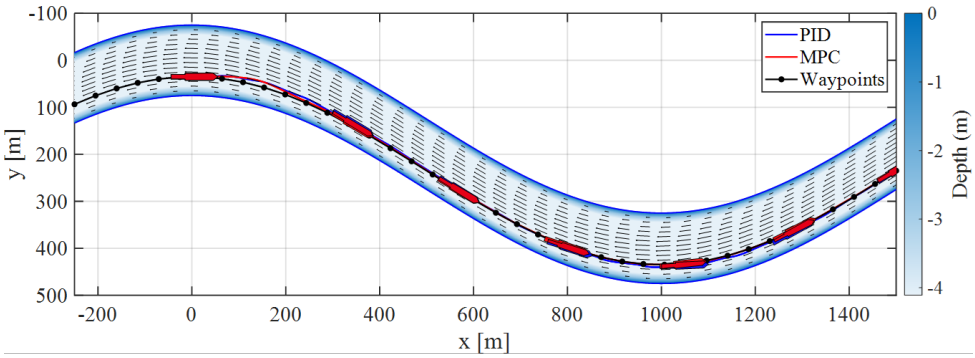

(a) Trajectories in river bends with a bottom width of w_{CB}=120m.

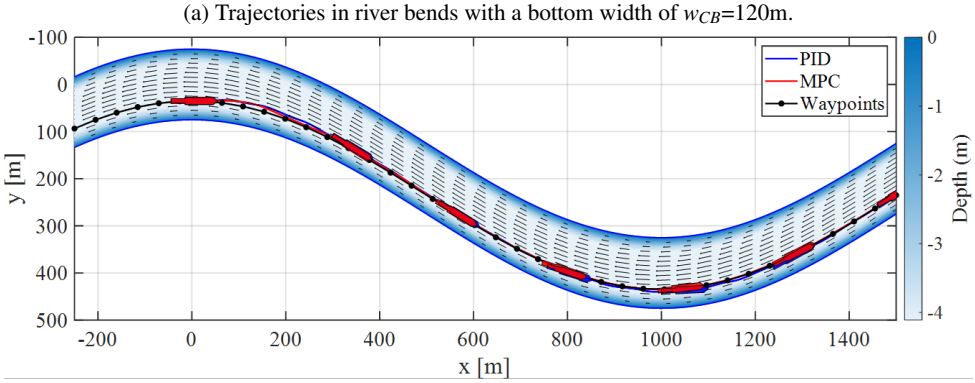

(b) Trajectories in river bends with a bottom width of w_{CB}=100m.

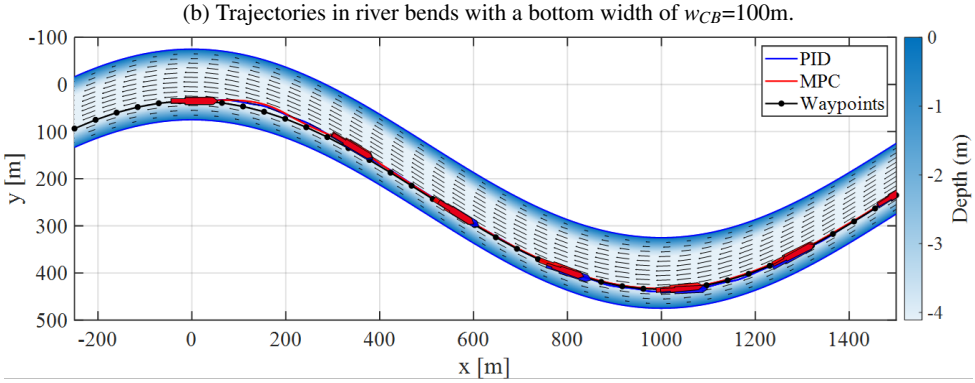

(c) Trajectories in river bends with a bottom width of w_{CB}=80m.

Figure 4.18: Trajectories under different bottom widths of the waterway.

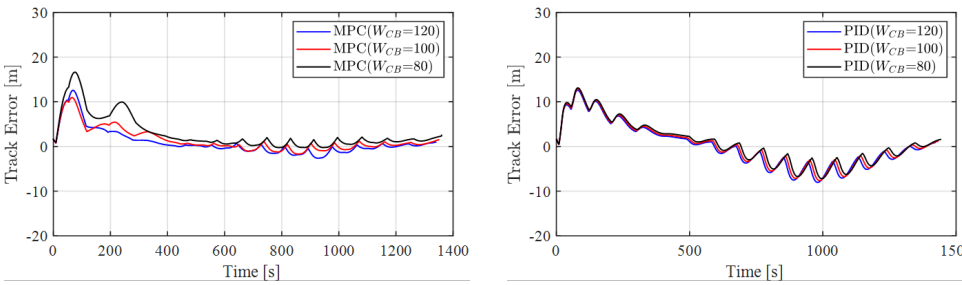

(a) SXTE of NMPC. (b) SXTE of PID.

Figure 4.19: Signed cross-track error comparison with PID controller and NMPC under varying width of the river bottom.

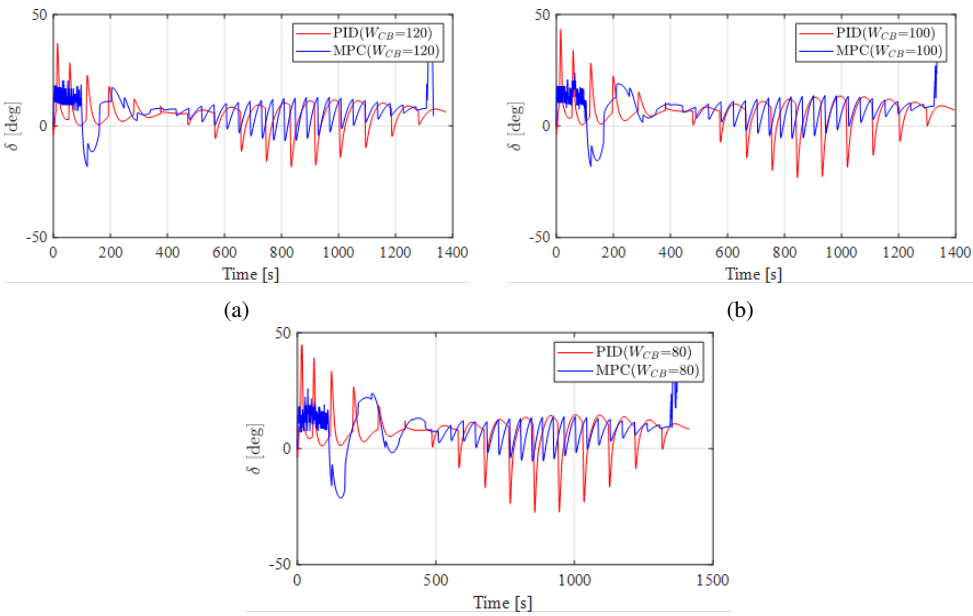

(a) (b)

(c)

Figure 4.20: Rudder angles for the PID controller and NMPC under varying width of channel bottom.

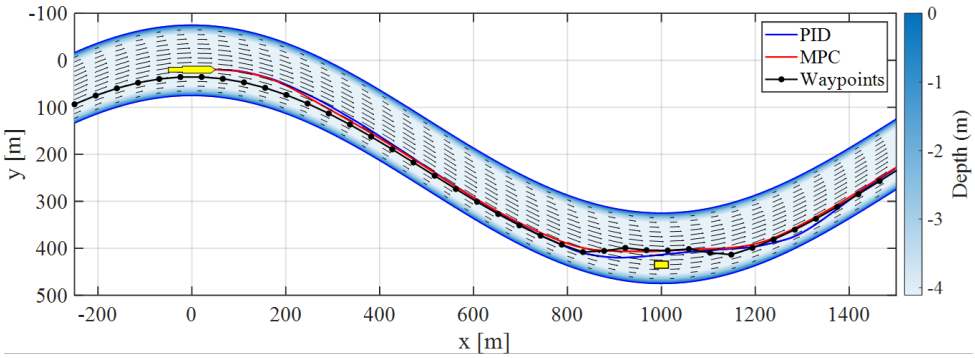

Figure 4.21: Trajectories in the river bend with a static obstacle (x=1000 m).

outperforms NMPC only in the AACE metric in the straight channel and river bends simulation, and in the MAXTE metric in the river bends case. However, the higher MAXTE value for NMPC is due to a sharper initial heading it computes for steering the vessel. This ultimately leads to a smaller average XTE, as indicated by the AAXTE metric. Interestingly, the IWRI metric is negative in the T-junction scenario for downstream sailing with NMPC, highlighting its robustness relative to the baseline. The NMPC also takes significantly less time to reach the destination in all three scenarios, as captured by the ETA metric.

4.4.7 Discussion on the impact of static obstacles

In addition to its path-following capabilities, the NMPC can also improve the vessel's collision-avoidance performance. Consider static obstacles such as buoys, a standstill vessel, or a permanent fixture. These obstacles can be incorporated into the planned path or detected in real time, allowing the guidance system to dynamically update the vessel's trajectory. The following simulations consider manually modifying the waypoints without employing a collision avoidance algorithm. Preliminary results, as shown in Figure 4.21, visualise the resulting path followed by the IWV with a static obstacle along its route. The obstacle is located at the coordinates $(1000, 435)$ and has a length and width of 30 m and 15 m, respectively. The NMPC can handle sharp changes in the reference trajectory by effectively mitigating cross-track errors without causing instability. On the other hand, the PID controller takes a longer time to steer the vessel back towards the reference trajectory. Furthermore, it avoids the static obstacle with only a small margin. This again emphasises the advantage of employing predictive control, which is crucial for sharp-turn scenarios. To further enhance the tracking performance, a variable speed control may be employed in this case.

4.5 Conclusions

This chapter focused on the design and analysis of an improved model-predictive heading control method for the path-following of IWVs. The rigid body dynamics of the vessel were modelled using a modified MMG model incorporating specific hydrodynamic impacts of inland

Table 4.5: The values of the key performance metrics for the considered simulation scenarios. For each scenario, the minimum values obtained are highlighted in bold.

Scenario	**Current stream**	**PID**						**NMPC**					
		MAXTE	AAXTE	SINM	AACE	IWRI	ETA (s)	MAXTE	AAXTE	SINM	AACE	IWRI	ETA (s)
Straight channel	Up	1.393	1.244	0	**161.242**	8.097	600	**0.854**	0.292	0	9.53×10^4	**0.515**	586
	Down	3.609	3.019	0.424	**920.526**	21.268	600	**3.494**	2.438	0.312	4.85×10^5	17.132	**578.5**
T-junction	Up	13.634	5.455	0.736	2.30×10^5	2.255	630	9.319	3.112	0.335	1.24×10^5	0.607	529.5
	Down	22.031	9.497	1.539	2.28×10^5	5.251	497	7.148	1.731	0.056	1.40×10^5	-0.039	**470.5**
River bend	Up	**24.747**	4.873	0.670	**63.795**	1.625	1396	25.162	3.737	0.461	8.25×10^4	0.747	1332.5
	Down	**25.358**	7.278	1.140	**124.01**	3.294	900.5	26.407	**5.160**	**0.794**	2.38×10^5	**1.884**	**857**

waterways, including shallow water, river current and bank effects. The performance of the proposed NMPC was evaluated against a standard PID controller using cross-track error and control effort metrics across various inland waterway scenarios. Additionally, key performance metrics were proposed to evaluate control performance against navigation requirements specific to inland waterways. Therefore, a thorough investigation of the following research question was performed **RQ3:** *How to design and evaluate control systems that ensure safe navigation of autonomous vessels in confined waterways?*

Simulations were conducted for a straight channel and a river confluence with a sharp turn, where the NMPC exhibited smaller tracking errors and fewer rudder efforts in both upstream and downstream sailing conditions. While the PID controller exhibited significant course deviations (even exceeding 20 meters at times), the NMPC controller, apart from the final steering, maintained the tracking error below 5 meters. Furthermore, simulations were conducted considering the impact of propulsion speeds and bank geometries at different bank slopes in a river bend. Interestingly, increasing the vessel's speed reduces the tracking error in the NMPC case, yet leads to the opposite behaviour in the PID controller's case. This is because increasing speed shortens the vessel's reaction time for the PID controller, even though the rudder steering force increases at higher propulsion speeds. In contrast, NMPC can anticipate the vessel's future behaviour and optimally allocate control input.

A decrease in the waterway bottom width significantly affected the PID controller's performance, as the vessel experienced a stronger bank effect. On the contrary, NMPC experienced minor disturbances and demonstrated good tracking performance. The performance of NMPC was also found to be significantly better than that of the PID controller across the proposed key performance metrics. Finally, a sharply changing reference trajectory resulting from a collision-avoidance scenario was also simulated, in which, unlike the PID controller, the NMPC maintained an acceptable error margin and avoided unstable maneuvers.

Chapter 5

Multiple Sensor Fault Detection and Isolation for Autonomous Surface Vessels

It ain't what you don't know that gets you into trouble.
It's what you know for sure that just ain't so.

- Mark Twain

Until this point in the thesis, normal operating conditions were assumed in the design of the proposed methods, i.e., faults or system-level failures were not considered. However, Chapters 5, 6 will focus on autonomous navigation under abnormal operating conditions. In this chapter, the following research question is addressed: **RQ4:** *How to detect and isolate multiple sensor faults affecting the navigational sensors on autonomous surface vessels?* To do so, a model-based FDI scheme for ASVs affected by multiple sensor faults is proposed.

This chapter is structured as follows: Section 5.1 presents the modelling of the vessel's maneuvering dynamics and the external forces and moments acting on the vessel. In Section 5.2, the design of the proposed sensor FDI scheme is detailed. In Section 5.3, the proposed scheme is verified through simulation studies involving two vessel types: a pusher-barge inland vessel model and a catamaran-type ferry. Sensor FDI for these two vessels, which have different available models, sensors, and actuator configurations, is performed by utilising an appropriate selection of residuals. Finally, the conclusions are reported in Section 5.4.

The contents of this chapter have been published in (Dhyani et al., 2026[1] ; Dhyani et al., 2024 [2]).

[1] **Dhyani, A.**, Van Der El, K., Negenborn, R.R. and Reppa, V., 2026. Multiple sensor fault diagnosis for safe navigation of autonomous surface vessels. Control Engineering Practice, 168, p.106673.

[2] **Dhyani, A.**, Negenborn, R.R. and Reppa, V., 2024. A multiple sensor fault diagnosis scheme for autonomous surface vessels. 12th IFAC Symposium on Fault Detection, Supervision and Safety for Technical Processes (SAFEPROCESS). IFAC-PapersOnLine, 58(4), pp.31-36.

5.1 Modelling for Sensor Fault Diagnosis

Vessels are typically equipped with multiple redundant sensors for localisation and state estimation, complemented by processing methods to derive specific vessel states. A GNSS sensor determines the vessel's position $p = \begin{bmatrix} x_p & y_p \end{bmatrix}^T$, whereas the IMU, typically comprising an accelerometer, gyroscope/rate sensor, etc., provides the velocities ($\nu \in \mathbb{R}^3$). A gyrocompass measures the vessel's heading angle (ψ), and may be complemented by a magnetic compass. In some smaller vessels, a gyrocompass is replaced by a dual-antenna GNSS setup, as it allows for a sufficiently accurate heading angle estimation at a cheaper cost [176]. The aforementioned parameters are obtained from raw sensor outputs using sensor fusion and estimation methods, such as Kalman filtering, that are part of navigation devices, such as an inertial navigation system (INS) or an attitude heading reference system (AHRS). Further, Doppler velocity log (DVL) and speed log (or electromagnetic log) measure the vessel's speed through water (or ground) by making use of the Doppler effect and electromagnetic induction principles, respectively. The automatic identification system (AIS) integrates a GNSS antenna and can provide the vessel's position, speed and course information, in addition to its other functions. GNSS-IMU sensor systems are ideal for vessel localisation due to their small size, low cost, and low energy consumption [19].

The sensor's outputs can be described by

$$\begin{aligned} S_{\text{pos}} &: y_{\text{pos}} = p + n_p + f_p \\ S_{\psi} &: y_{\psi} = \psi + n_{\psi} + f_{\psi} \\ S_{\nu} &: y_{\nu} = \nu + n_{\nu} + f_{\nu} \\ S_{\chi} &: y_{\chi} = \chi + n_{\chi} + f_{\chi}, \end{aligned} \tag{5.1}$$

where, $y_{\text{pos}} \in \mathbb{R}^2, y_{\psi} \in \mathbb{R}$, $y_{\nu} \in \mathbb{R}^3$ and $y_{\chi} \in \mathbb{R}$ correspond to the position p, heading angle ψ, velocities ν, and the course angle χ, respectively. The vectors n and f represent the noise and fault(s) affecting these measurements.

We consider permanent, persistent faults in this work. A sensor fault f_z occurring at a time instant T_{f_z} is modelled according to [177]. Furthermore, the characteristics of a fault, defined by the fault function, the time of occurrence, and the evolution rate, are all treated as unknown in the design of the proposed scheme.

5.1.1 Vessel Maneuvering Models

Vessel manoeuvring models can vary significantly in terms of complexity for a specific application. The availability of an accurate manoeuvring model with hydrodynamic characteristics is the foundation for model-based FDI. This section explores various models that can be used for generating residuals for FDI using the available sensor measurements and actuator/thrust information.

Kinematic Model

A vessel in motion satisfies kinematic constraints, which can provide information about the vessel's position and its heading, and have applications in target tracking [178] and path-following

[179]. The kinematic constraints describe the relation of the vessel's velocities in the NED frame with its heading angle by

$$\begin{aligned} \dot{x}_p &= u\cos(\psi) - v\sin(\psi) \\ \dot{y}_p &= u\sin(\psi) + v\cos(\psi). \end{aligned} \tag{5.2}$$

In the amplitude-phase form, the above equations can be expressed as

$$\begin{aligned} \dot{x}_p &= U\cos(\psi + \beta_c) \\ \dot{y}_p &= U\sin(\psi + \beta_c), \end{aligned} \tag{5.3}$$

where $U = \sqrt{u^2 + v^2}$ is the speed in the horizontal plane and β_c is the crab angle. The course angle χ can be determined by filtering the position measurements, such as by employing a Kalman filter [179], due to the relation

$$\chi = \tan^{-1}\left(\frac{\dot{y}_p}{\dot{x}_p}\right). \tag{5.4}$$

Similarly, the crab angle β_c can be calculated using the surge and sway velocities as

$$\beta_c = \tan^{-1}\left(\frac{v}{u}\right). \tag{5.5}$$

Finally, the heading angle can be expressed as

$$\psi = \chi - \beta_c. \tag{5.6}$$

Remark 5.1 It must be noted that the heading angle estimated using Equation (5.6) is accurate only for a moving vessel. This is because the horizontal crab angle formula (5.5) is numerically ill-conditioned for small values of surge and sway velocities. To address this issue, a numerically stable implementation is required, where crab angle calculations are discarded at low speeds. □

3-DOF Maneuvering Model

For many applications, the motion in a horizontal plane can be approximated by the following 3-DOF hydrodynamic model:

$$\begin{bmatrix} \dot{\eta} \\ \dot{\nu} \end{bmatrix} = \begin{bmatrix} R(\psi)\nu \\ f(\nu, \tau) \end{bmatrix} + \begin{bmatrix} \mathbf{0} \\ \Delta(\eta, \nu) \end{bmatrix}, \tag{5.7}$$

where $\eta = \begin{bmatrix} x_p & y_p & \psi \end{bmatrix}^T$ is the generalised coordinate vector in the North-East-Down (NED) frame, and $\nu = \begin{bmatrix} u & v & r \end{bmatrix}^T$ is the generalised velocity vector in the body-fixed frame, with u, v denoting the linear velocities in surge and sway, and r denoting the angular velocity (yaw rate). The variable $\tau = \begin{bmatrix} \tau_u & \tau_v & \tau_r \end{bmatrix}^T$ represents the controlled input force vector. The term $R(\psi)$ represents the rotation matrix, described as

$$R(\psi) = \begin{bmatrix} \cos(\psi) & -\sin(\psi) & 0 \\ \sin(\psi) & \cos(\psi) & 0 \\ 0 & 0 & 1 \end{bmatrix}. \tag{5.8}$$

Further, $f(\nu, \tau), \Delta(\eta, \nu) \in \mathbb{R}^3$ comprise the known and unknown nonlinear terms, respectively, described in two ways:

- In the Abkowitz model [180, 181] it is

$$\begin{aligned} f(\nu,\tau) &= M^{-1}(-C(\nu)\nu - D(\nu)\nu + \tau) \\ \Delta(\eta,\nu) &= M^{-1}\tau_d, \end{aligned} \tag{5.9}$$

where $\tau_d \in \mathbb{R}^3$ represents the added force vector, which models the impact of unknown forces acting on the vessel due to various external factors such as wind, currents and forces from the towing system [152, 182]. The term M represents the inertia matrix, which, under the assumption that the ship is port-starboard symmetric, can be described as

$$M = \begin{bmatrix} m + X_{\dot{u}} & 0 & 0 \\ 0 & m - Y_{\dot{v}} & mx_G - Y_{\dot{r}} \\ 0 & mx_G - N_{\dot{v}} & I_{z_p} - N_{\dot{r}} \end{bmatrix}. \tag{5.10}$$

Here m is the vessel's mass, I_{z_p} is the moment of inertia about the z_p- axis, and, $X_{\dot{u}}$, $Y_{\dot{v}}$, $Y_{\dot{r}}$, $N_{\dot{v}}$ and $N_{\dot{r}}$ are hydrodynamic parameters that account for the added mass. Further, x_G represents the x-coordinate of the vessel's centre of gravity. The terms $C(\nu), D(\nu)$ are the Coriolis-centripetal and damping matrices given by

$$C(\nu) = \begin{bmatrix} 0 & 0 & -m(x_G r + v) + Y_{\dot{v}} v + Y_{\dot{r}} r \\ 0 & 0 & mu - X_{\dot{u}} u \\ m(x_G r + v) - Y_{\dot{v}} v - Y_{\dot{r}} r & -mu + X_{\dot{u}} u & 0 \end{bmatrix} \tag{5.11}$$

$$D(\nu) = \begin{bmatrix} -X_u - X_{|u|u}|u| - X_{uuu}|u^2| & 0 & 0 \\ 0 & -Y_v - Y_{|v|v}|v| - Y_{|r|v}|r| & -Y_r - Y_{|v|r}|v| - Y_{|r|r}|r| \\ 0 & -N_v - N_{|v|v}|v| - N_{|r|v}|r| & -N_r - N_{|v|r}|v| - N_{|r|r}|r| \end{bmatrix}. \tag{5.12}$$

Here, X_u, $X_{|u|u}$, X_{uuu}, Y_v, $Y_{|v|v}$, $Y_{|r|v}$, Y_r, $Y_{|v|r}$, $Y_{|r|r}$, N_v, $N_{|v|v}$, $N_{|r|v}$, N_r, $N_{|v|r}$ and $N_{|r|r}$, are the hydrodynamic parameters that account for the damping forces within the second-order modulus model representation [153, 154].

- In the Maneuvering Modeling Group (MMG) model, [163, 183] it is

$$\begin{aligned} f(\nu,\tau) &= M'^{-1}(-D'(\nu) + \tau) \\ \Delta(\eta,\nu) &= M'^{-1}\tau_d. \end{aligned} \tag{5.13}$$

Here, the matrices M' and $D'(\nu)$ are given as

$$\begin{aligned} M' &= \begin{bmatrix} (m + m_x) & 0 & 0 \\ 0 & (m + m_y) & -x_G m_y \\ 0 & x_G m & (I_{z_p} + J_{z_p}) \end{bmatrix} \\ D'(\nu) &= \begin{bmatrix} -(m + m_y) vr + x_G m_y r^2 \\ (m + m_x) ur \\ x_G mur \end{bmatrix}, \end{aligned} \tag{5.14}$$

where, m_x, m_y are the added masses in the x_p - and y_p - directions and J_{z_p} is the added moment of inertia for yaw motion. The assumption of port-starboard symmetry is applied again to obtain the matrix M' in this form.

Unlike the Abkowitz model in (5.9), where the hydrodynamic forces and moments are aggregated into the damping and Coriolis matrices (5.11),(5.12), in the MMG model, the hydrodynamic forces are decomposed into individual terms arising from the hull, propeller, and rudder. This approach is often more suitable for assessing the impact of these different components on the vessel's maneuverability. However, it is based on the assumption that the vessel has a conventional propeller and rudder configuration.

The vessel's actuation system is directly responsible for controlling its maneuvering motion. Therefore, its dynamics and configuration must be accurately modelled to simulate realistic vessel behaviour. For a twin azimuth-thruster configuration, the controlled input force vector can be defined by Equation (3.5). For the rudder-propeller configuration, the controlled input force vector is given by

$$\tau = \begin{bmatrix} \tau_1 \\ \tau_2 \\ \tau_3 \end{bmatrix} = \begin{bmatrix} X_P + X_R \\ Y_R \\ N_R \end{bmatrix}, \tag{5.15}$$

where, X_R represents the forward force, Y_R the lateral force, and N_R the yaw moment component due to the rudder. Further, X_P represents the forward force component from the ship's propeller.

Steering Model

The steering or KT model, attributed to [184], is a popular linear modelling approach that can sufficiently capture the turning and course-keeping behaviour of the vessel. This work focuses on its second-order form, which is a common variant that supports overshooting behaviour and has a higher accuracy as compared to the first-order form. For an azimuth-type twin-thruster configuration, it can be described by

$$\begin{gathered} \ddot{r} + a_1 \dot{r} + a_2 r = b_1 (b_2 \dot{\delta}_p + \delta_p) + b_3 (b_4 \dot{\delta}_s + \delta_s) \\ \dot{\psi} = r,\ \dot{u} = 0,\ \dot{v} = 0, \end{gathered} \tag{5.16}$$

where δ_p and δ_s are the thruster angles for the port and starboard sides, and $a_{(.)}$, $b_{(.)}$ represent the parameters related to yaw rate and thruster angles, respectively. These parameters can be determined using the vessel's operational data from free-running tests involving zigzag and/or turning circle maneuvers. It is worth noting that the steering model is a 1-DOF model that assumes constant surge and sway velocities; therefore, it is not a complete replacement of the aforementioned 3-DOF hydrodynamic models.

5.1.2 External Forces and Moments

In this work, two types of external/environmental forces and moments acting on the vessel are considered: 1) forces due to wind and 2) hydrodynamic forces acting on the vessel's hull, including the forces due to the shallow-water effect.

Wind Forces

The effect of wind forces acting on the vessel can be modelled by using the following expression, under the assumption that the ship is symmetrical about the $x_p z_p$ and $y_p z_p$ planes [181]

$$\tau_w = \begin{bmatrix} X_W \\ Y_W \\ N_W \end{bmatrix} = \frac{1}{2} P_a V_r^2 \begin{bmatrix} -c_x \cos(\gamma_r) A_F \\ c_y \sin(\gamma_r) A_L \\ c_n \sin(2\gamma_r) A_L L_{oa} \end{bmatrix}, \tag{5.17}$$

where

$$\begin{aligned} V_r &= \sqrt{u_r^2 + v_r^2} \\ \gamma_r &= -\text{atan2}(v_r, u_r). \end{aligned} \tag{5.18}$$

Here, atan2 is a 2-argument inverse tangent function. The notation P_a denotes the air density; V_r is the relative wind speed; γ_r the relative wind angle of attack; c_x, c_y and c_n the wind coefficients for the horizontal plane motions; A_F, A_L the frontal and lateral projected areas of the vessel above the water, respectively; L_{oa} the overall length of the vessel. u_r and v_r are the relative velocity components of V_r in the x_p and y_p directions, such that

$$\begin{aligned} u_r &= u - V\cos(\beta_V - \psi) \\ v_r &= v - V\sin(\beta_V - \psi). \end{aligned} \tag{5.19}$$

The wind speed $V \in \mathbb{R}$ and direction $\beta_V \in \mathbb{R}$ can be measured in real-time by an anemometer and a weather vane, respectively. Furthermore, the coefficients c_x, c_y, and c_n can be empirically calculated [181]. In this work, the wind forces acting on the vessel are treated as unknown.

Hull Forces

While the Abkowitz model (Equation (5.9)) considers the hydrodynamic forces and moments acting on the vessel's hull as part of the known nonlinear dynamics, in this work, these forces are considered unknown for the MMG model. The vector $\tau_H = \begin{bmatrix} X_H & Y_H & N_H \end{bmatrix}^T$ represents these forces and moments and forms a part of the unknown force vector τ_d for Equation (5.13). For inland waterway vessels, this includes the resistance due to the shallow-water effect, which is a predominant factor impacting the vessel's motion. The generalised hydrodynamic forces acting on the vessel hull are formulated as:

$$\begin{aligned} X_H &= 0.5\rho L_{\text{oa}} T U^2 X'_H \\ Y_H &= 0.5\rho L_{\text{oa}} T U^2 Y'_H \\ N_H &= 0.5\rho L_{\text{oa}}^2 T U^2 N'_H, \end{aligned} \tag{5.20}$$

where ρ is defined as the density of freshwater, U is the vessel's speed, and T is the vessel's draught. X'_H, Y'_H and N'_H are dimensionless quantities given by

$$\begin{aligned} X'_H &= -R'_0 \cos^2\beta_m + X'_{\beta\beta}\beta_m^2 + X'_{\beta r}\beta_m r' + X'_{rr} r'^2 + X'_{\beta\beta\beta\beta}\beta_m^4 \\ Y'_H &= Y'_\beta \beta_m + Y'_r r' + Y'_{\beta\beta\beta}\beta_m^3 + Y'_{\beta\beta r}\beta_m^2 r' + Y'_{\beta rr}\beta_m r'^2 + Y'_{rrr} r'^3 \\ N'_H &= N'_\beta \beta_m + N'_r r' + N'_{\beta\beta\beta}\beta_m^3 + N'_{\beta\beta r}\beta_m^2 r' + N'_{\beta rr}\beta_m r'^2 + N'_{rrr} r'^3, \end{aligned} \tag{5.21}$$

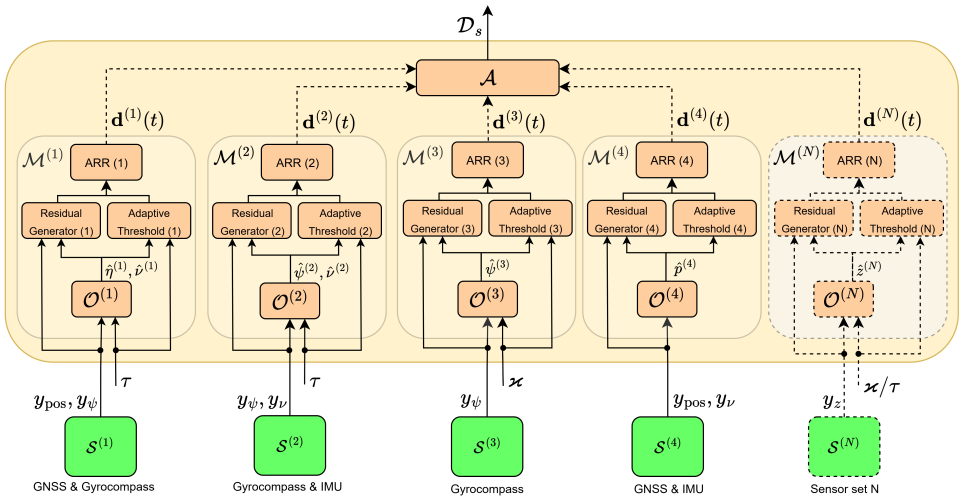

Figure 5.1: Proposed architecture of the sensor fault detection and isolation scheme.

where $X'_{\beta\beta}, X'_{\beta r}, \ldots, N'_{rrr}$ are the hydrodynamic derivatives in the MMG modelling approach, β_m is the midship drift angle, and r' is the non-dimensional yaw rate which is equal to rL_{oa}/U. The expression for the resistance coefficient, R'_0, modified to include the impact of shallow water effect on the vessel, is given by [161]:

$$\begin{aligned} R'_0 &= \frac{R_{\text{Sh}}}{(0.5\rho L_{\text{oa}} T U^2)} \\ R_{\text{Sh}} &= 0.5\rho S_W U^2 \left(C_F \ \left(1 + \left(k + \bar{k}\right)\right) + C_W\right), \end{aligned} \tag{5.22}$$

where, S_W represents the ship's wetted surface area; C_F, C_W are the frictional resistance and the wave-making resistance coefficients, k is the ship's form factor in deep water and $\bar{k}$ is the additional viscous resistance in shallow water.

The objective of this work is to design a multiple-sensor FDI scheme for ASVs, accounting for the effects of external disturbances, sensor noise, and variations in sensor and actuator configurations. The details of the proposed approach are presented in the following section.

5.2 Sensor Fault Detection and Isolation Scheme

In this section, the design of the proposed multiple-sensor FDI scheme is discussed in detail. Firstly, to enable the isolation of multiple sensor faults, the considered sensors are decomposed into N sensor sets $\mathcal{S}^{(I)}, I = 1, \ldots, N$ [177]. A monitoring module $\mathcal{M}^{(I)}$ is employed, composed of an observer to estimate the measurements corresponding to each sensor set. Further, every monitoring module contains a set of analytical redundancy relations (ARRs) that detect the occurrence of faults. Designing monitoring modules for the isolation of multiple faulty sensors is particularly challenging, as it requires that each monitoring module be selectively sensitive to a subset of possible sensor faults. This can introduce challenges in the observer design due to

a potential loss of observability. To overcome this issue and enhance isolability, the sensor sets are designed to be overlapping, i.e., some sensors belong to more than one sensor set.

As shown in Figure 5.1, the monitoring module $\mathcal{M}^{(I)}$ comprises observers denoted by $O^{(I)}$, which are used to generate the residuals. A residual is a signal that describes the difference between observed system behaviour (using sensors) and the expected one (using observers). Within each module, the ARRs are computed and subsequently, the decisions $\mathbf{d}^{(I)}$, which are binary vectors representing the fault detection results. Adaptive thresholds are derived to compute the ARRs while accounting for sensor noise, as well as external factors described in Section 5.1.2. Finally, the decisions obtained based on the satisfaction or violation of the ARRs are provided to the aggregator module $\mathcal{A}$, which computes the set of possibly occurring (multiple) fault(s) $\mathcal{D}_s$, thereby isolating the faulty sensor(s).

In this work, the decomposition of sensors is performed such that $N = 4$. The resulting sensor sets are defined by

$$\begin{aligned}
\mathcal{S}^{(1)} &= \{\mathcal{S}^{(1,1)}, \mathcal{S}^{(1,2)}\} = \{S_{\text{pos}}, S_{\psi}\} \\
\mathcal{S}^{(2)} &= \{\mathcal{S}^{(2,1)}, \mathcal{S}^{(2,2)}\} = \{S_{\psi}, S_{\text{v}}\} \\
\mathcal{S}^{(3)} &= \{\mathcal{S}^{(3,1)}\} = \{S_{\psi}\} \\
\mathcal{S}^{(4)} &= \{\mathcal{S}^{(4,1)}\} = \{S_{\text{pos}}, S_{\text{v}}\}.
\end{aligned} \tag{5.23}$$

This decomposition facilitates designing observers that are selectively sensitive to sensor faults, as shown in the consecutive sections. The corresponding monitoring modules are given by $\mathcal{M}^{(1)} - \mathcal{M}^{(4)}$, respectively, and are responsible for (a) GNSS and gyrocompass, (b) gyrocompass and IMU, (c) gyrocompass only, and (d) GNSS sensors only. While the monitoring modules $\mathcal{M}^{(1)} - \mathcal{M}^{(3)}$ employ observers based on both the sensor measurements and controlled inputs (generalised forces/thruster angles) for residual generation, the observer in module $\mathcal{M}^{(4)}$ utilises only the sensor measurements. Depending on the sensor setup, a sensor set and the corresponding monitoring module may be discarded, or additional monitoring modules may be integrated for residual generation. For example, using an available, more "reliable" redundant sensor can help improve fault isolability [131, 185].

5.2.1 Observer Design

This subsection details the design of a bank of Luenberger-type observers for performing sensor FDI. The design enables structured sensitivity against the set of possible faults. Firstly, the monitoring module $\mathcal{M}^{(1)}$ is considered for monitoring the GNSS and gyrocompass sensors, having the observer dynamics given by

$$O^{(1)} : \begin{cases} \dot{\hat{\eta}}^{(1)} = R(\hat{\psi}^{(1)})\hat{\nu}^{(1)} + K_1\tilde{\eta}^{(1)} \\ \dot{\hat{\nu}}^{(1)} = f(\hat{\nu}^{(1)}, \tau) + K_2 R^T(\hat{\psi}^{(1)})\tilde{\eta}^{(1)}, \end{cases} \tag{5.24}$$

where, $\hat{\eta}^{(1)}$, $\hat{\nu}^{(1)}$ and $\hat{\psi}^{(1)}$ denote the estimations of $\eta = \begin{bmatrix} p & \psi \end{bmatrix}^T$, ν and ψ, respectively, and $\tilde{\eta}^{(1)} = y_\eta - \hat{\eta}^{(1)}$, where $y_\eta = \begin{bmatrix} y_{\text{pos}} & y_\psi \end{bmatrix}^T$. The term $f(\hat{\nu}^{(1)}, \tau)$ is given by Equation (5.9) or (5.13), according to the selected modelling approach. The observer gains K_1 and $K_2 \in \mathbb{R}^{3\times 3}$ are positive diagonal matrices.

The monitoring module $\mathcal{M}^{(2)}$, designed for the gyrocompass and IMU, comprises the observer $O^{(2)}$, given by

$$O^{(2)}: \begin{cases} \dot{\hat{\psi}}^{(2)} = \hat{r}^{(2)} + k_3 \tilde{\psi}^{(2)} \\ \dot{\hat{\nu}}^{(2)} = f(\hat{\nu}^{(2)}, \tau) + K_4 \tilde{\nu}^{(2)}, \end{cases} \tag{5.25}$$

where, $\tilde{\psi}^{(2)} = y_\psi - \hat{\psi}^{(2)}$ and $\tilde{\nu}^{(2)} = y_\nu - \hat{\nu}^{(2)}$ are the output estimation errors for ψ and ν, respectively. Here, $k_3 \in \mathbb{R}$, and $K_4 \in \mathbb{R}^{3\times 3}$ is a diagonal gain matrix.

Remark 5.2 Note that the observers $O^{(1)}$ and $O^{(2)}$ are independent of the sensor measurements y_ν and y_{pos}, respectively. As a result, the residuals computed in the monitoring modules $\mathcal{M}^{(1)}$ and $\mathcal{M}^{(2)}$ are structurally sensitive only to a desired subset of faults. □

The monitoring module $\mathcal{M}^{(3)}$ is based on a linear observer $O^{(3)}$, which is derived from the second-order steering model given by (5.16). The observer dynamics are given as

$$O^{(3)}: \left\{ \begin{bmatrix} \dot{\hat{\psi}}^{(3)} \\ \ddot{\hat{\psi}}^{(3)} \\ \dddot{\hat{\psi}}^{(3)} \end{bmatrix} = \begin{bmatrix} 0 & 1 & 0 \\ 0 & 0 & 1 \\ 0 & -a_2 & -a_1 \end{bmatrix} \begin{bmatrix} \hat{\psi}^{(3)} \\ \hat{r}^{(3)} \\ \dot{\hat{r}}^{(3)} \end{bmatrix} + \begin{bmatrix} 0 & 0 & 0 & 0 \\ 0 & 0 & 0 & 0 \\ b_1 & b_1 b_2 & b_3 & b_3 b_4 \end{bmatrix} \begin{bmatrix} \delta_p \\ \dot{\delta}_p \\ \delta_s \\ \dot{\delta}_s \end{bmatrix} + \begin{bmatrix} k_5 \\ 0 \\ 0 \end{bmatrix} \tilde{\psi}^{(3)} \right. \tag{5.26}$$

where $\tilde{\psi}^{(3)} = y_\psi - \hat{\psi}^{(3)}$ is the output estimation error for ψ, $a_{(.)}$ and $b_{(.)}$ are the identified parameters of the steering model, and $k_5 \in \mathbb{R}$ is the observer gain. Note that unlike the observers $O^{(1)}$ and $O^{(2)}$, $O^{(3)}$ takes the thruster angles and their derivatives as inputs, represented by $\varkappa = \begin{bmatrix} \delta_p & \dot{\delta}_p & \delta_s & \dot{\delta}_s \end{bmatrix}^T$.

Remark 5.3 For the rudder-propeller configuration, the observer $O^{(3)}$ can be given by

$$O^{(3)}: \left\{ \begin{bmatrix} \dot{\hat{\psi}}^{(3)} \\ \ddot{\hat{\psi}}^{(3)} \\ \dddot{\hat{\psi}}^{(3)} \end{bmatrix} = \begin{bmatrix} 0 & 1 & 0 \\ 0 & 0 & 1 \\ 0 & -\frac{1}{T_1 T_2} & -\frac{T_1+T_2}{T_1 T_2} \end{bmatrix} \begin{bmatrix} \hat{\psi}^{(3)} \\ \hat{r}^{(3)} \\ \dot{\hat{r}}^{(3)} \end{bmatrix} + \frac{K}{T_1 T_2} \begin{bmatrix} 0 & 0 \\ 0 & 0 \\ 1 & T_3 \end{bmatrix} \begin{bmatrix} \delta \\ \dot{\delta} \end{bmatrix} + \begin{bmatrix} k_5 \\ 0 \\ 0 \end{bmatrix} \tilde{\psi}^{(3)}, \right. \tag{5.27}$$

and the input of the monitoring module $\mathcal{M}^{(3)}$ becomes $\varkappa = \begin{bmatrix} \delta & \dot{\delta} \end{bmatrix}^T$. Here, the terms T_1, T_2, and T_3 denote the time constants, and K denotes the gain factor. □

Finally, the monitoring module $\mathcal{M}^{(4)}$ is designed by using the GNSS (or AIS) and IMU measurements only. Firstly, the vessel's heading angle is calculated as a function of its course and crab angles, and it is given by

$$y_\psi = y_\chi - \tan^{-1}\left(\frac{y_v}{y_u}\right), \tag{5.28}$$

where y_u, y_v are the surge and sway velocity measurements and y_χ is the course angle measurement provided by the GNSS or the AIS. Using the heading angle measurement (y_ψ), and the velocity measurements (y_u, y_v), the observer dynamics $O^{(4)}$ can be described by

$$O^{(4)}: \begin{cases} \dot{\hat{x}}_p^{(4)} = y_u \cos(y_\psi) - y_v \sin(y_\psi) + k_{61} \tilde{x}_p^{(4)} \\ \dot{\hat{y}}_p^{(4)} = y_u \sin(y_\psi) + y_v \cos(y_\psi) + k_{62} \tilde{y}_p^{(4)}, \end{cases} \tag{5.29}$$

where, $\tilde{x}_p^{(4)} = y_{x_p} - \hat{x}_p^{(4)}$, $\tilde{y}_p^{(4)} = y_{y_p} - \hat{y}_p^{(4)}$, with y_{x_p} and y_{y_p} denoting the position measurements, and $k_{61}, k_{62} \in \mathbb{R}$.

5.2.2 Fault Detector Design

Using the observers defined in the previous subsection, we proceed to generate the residuals and compute their corresponding adaptive thresholds within the respective monitoring modules. Let us define $z^{(I)}, I = 1,\ldots,4$, to be vectors consisting of the vessel states such that $z^{(1)} = \begin{bmatrix} p & \psi & \nu \end{bmatrix}^T$, $z^{(2)} = \begin{bmatrix} \psi & \nu \end{bmatrix}^T$, $z^{(3)} = \psi$ and $z^{(4)} = \begin{bmatrix} p & \nu \end{bmatrix}^T$. The residual vector $\varepsilon_{y_z}^{(I)} \in \mathbb{R}^{N_I}$ is defined by

$$\varepsilon_{y_z}^{(I)} = y_z^{(I)} - \hat{z}^{(I)}, \tag{5.30}$$

where, $y_z^{(I)}$ and $\hat{z}^{(I)}$ represent the measurements and estimations of the vectors $z^{(I)}$ in the $I-$th monitoring module, respectively. The superscript $\{.\}^{(j)}$ will be used to signify that the residual corresponds to the $j-$th sensor, $j \in \{1,\ldots,m_I\}$, where m_I denotes the no. of sensors in the $I-$th sensor set. In this work, $m_I = 2$, for the sensor sets $\mathcal{S}^{(1)}, \mathcal{S}^{(2)}$, and $m_I = 1$, for the sensor sets $\mathcal{S}^{(3)}$ and $\mathcal{S}^{(4)}$, respectively. The corresponding residual vectors are given by

$$\begin{aligned}
\varepsilon_{y_z}^{(1)} &= \begin{bmatrix} \varepsilon_{y_z}^{(1,1)} \\ \varepsilon_{y_z}^{(1,2)} \end{bmatrix} = \begin{bmatrix} y_{\text{pos}} \\ y_\psi \end{bmatrix} - \begin{bmatrix} \hat{z}^{(1,1)} \\ \hat{z}^{(1,2)} \end{bmatrix} \\
\varepsilon_{y_z}^{(2)} &= \begin{bmatrix} \varepsilon_{y_z}^{(2,1)} \\ \varepsilon_{y_z}^{(2,2)} \end{bmatrix} = \begin{bmatrix} y_\psi \\ y_\nu \end{bmatrix} - \begin{bmatrix} \hat{z}^{(2,1)} \\ \hat{z}^{(2,2)} \end{bmatrix} \\
\varepsilon_{y_z}^{(3)} &= \varepsilon_{y_z}^{(3,1)} = y_\psi - \hat{z}^{(3,1)} \\
\varepsilon_{y_z}^{(4)} &= \varepsilon_{y_z}^{(4,1)} = y_{\text{pos}} - \hat{z}^{(4,1)},
\end{aligned} \tag{5.31}$$

where $\begin{bmatrix} \hat{z}^{(1,1)} & \hat{z}^{(1,2)} \end{bmatrix}^T = \begin{bmatrix} \hat{p} & \hat{\psi} \end{bmatrix}^T$, $\begin{bmatrix} \hat{z}^{(2,1)} & \hat{z}^{(2,2)} \end{bmatrix}^T = \begin{bmatrix} \hat{\psi} & \hat{\nu} \end{bmatrix}^T$, $\hat{z}^{(3,1)} = \hat{\psi}$ and $\hat{z}^{(4,1)} = \hat{p}$ are generated by the observers $O^{(1)}$,..., $O^{(4)}$, respectively. Under healthy conditions (absence of faults), the residual components $\varepsilon_{y_z H}^{(I,j)}$ are described by

$$\varepsilon_{y_z H}^{(I,j)} = y_{z_j H} - \hat{z}_H^{(I,j)}, \tag{5.32}$$

with $y_{z_j H}$ denoting the healthy sensor measurement of the state $z^{(I,j)}$. The $j-$th adaptive threshold is defined by $\bar{\varepsilon}_{y_z}^{(I,j)}$, for $I \in \{1,\ldots,4\}$ and $j \in \{1,\ldots,m_I\}$, respectively. Under healthy conditions, it is denoted by $\bar{\varepsilon}_{y_z H}^{(I,j)}$ and must be computed such that

$$|\varepsilon_{y_z H}^{(I,j)}| \leq \bar{\varepsilon}_{y_z H}^{(I,j)}. \tag{5.33}$$

The following design criteria are adopted to compute the adaptive thresholds $\bar{\varepsilon}_{y_z}^{(I,j)}$ and subsequently, the ARRs:

1. The thresholds must be robust to uncertainties, thereby ensuring that no false alarms occur, i.e., if $\mathcal{S}^{(I)}$ is not affected by faults, then the corresponding set of ARRs must always be satisfied.

2. The ARRs must be structurally sensitive to the occurrence of one or more sensor faults, i.e., if at any time instant t, the set of ARRs is not satisfied, then the occurrence of at least one sensor fault in $\mathcal{S}^{(I)}$ must be guaranteed.

To compute adaptive thresholds that satisfy these criteria, firstly, $\varepsilon_{y_zH}^{(I,j)}$ can be expressed in terms of the state estimation error under healthy conditions $\varepsilon_{zH}^{(I,j)}$ as

$$\varepsilon_{y_zH}^{(I,j)} = \varepsilon_{zH}^{(I,j)} + n_z^{(I,j)}, \tag{5.34}$$

with, $\varepsilon_{zH}^{(I,j)} = z^{(I,j)} - \hat{z}_H^{(I,j)}$. Under healthy conditions, the following assumptions regarding the vessel dynamics and sensor noise are considered:

Assumption 2 *The input force τ remains bounded before and after the occurrence of multiple sensor faults, i.e., there exist some compact stability region $\mathcal{R}^{\tau} \subset \mathbb{R}^3$ such that $\tau \in \mathcal{R}^{\tau}$, for all $t \geq 0$.*

Assumption 3 *The unknown noise affecting the $j-th$ sensor $(n_z^{(I,j)})$ is uniformly bounded, i.e., $|n_{z_k}^{(I,j)}| \leq \bar{n}_{z_k}^{(I,j)}$, for all k elements of $n_z^{(I,j)}$, with $\bar{n}_{z_k}^{(I,j)}$ representing a known bound.*

These assumptions represent realistic system behaviour under healthy conditions while ensuring the convergence of the residual signals. As a result, the magnitudes of the residual components are bounded by

$$\begin{aligned}
\begin{bmatrix} |\varepsilon_{y_zH}^{(1,1)}| \\ |\varepsilon_{y_zH}^{(1,2)}| \end{bmatrix} &\leq \begin{bmatrix} |\varepsilon_{zH}^{(1,1)}| \\ |\varepsilon_{zH}^{(1,2)}| \end{bmatrix} + \begin{bmatrix} \bar{n}_z^{(1,1)} \\ \bar{n}_z^{(1,2)} \end{bmatrix} \\
\begin{bmatrix} |\varepsilon_{y_zH}^{(2,1)}| \\ |\varepsilon_{y_zH}^{(2,2)}| \end{bmatrix} &\leq \begin{bmatrix} |\varepsilon_{zH}^{(2,1)}| \\ |\varepsilon_{zH}^{(2,2)}| \end{bmatrix} + \begin{bmatrix} \bar{n}_z^{(2,1)} \\ \bar{n}_z^{(2,2)} \end{bmatrix} \\
|\varepsilon_{y_zH}^{(3,1)}| &\leq |\varepsilon_{zH}^{(3,1)}| + \bar{n}_z^{(3,1)} \\
|\varepsilon_{y_zH}^{(4,1)}| &\leq |\varepsilon_{zH}^{(4,1)}| + \bar{n}_z^{(4,1)},
\end{aligned} \tag{5.35}$$

where $|\varepsilon_{zH}^{(I,j)}|$ are the estimation error magnitudes for the states in the vectors $z^{(I)}$, respectively.

Further, the dynamics governing the state estimation error of the observer $O^{(1)}$ can be described by

$$\begin{aligned}
\dot{\varepsilon}_{zH}^{(1)} = \begin{bmatrix} \dot{\varepsilon}_{zH}^{(1,1)} \\ \dot{\varepsilon}_{zH}^{(1,2)} \\ \dot{\varepsilon}_{zH}^{(1,3)} \end{bmatrix} &= \begin{bmatrix} -K_{11} & \mathbf{0} & \mathbf{0} \\ \mathbf{0} & -k_{12} & \mathbf{0} \\ \mathbf{0} & \mathbf{0} & -K_2 \end{bmatrix} \begin{bmatrix} \varepsilon_{zH}^{(1,1)} \\ \varepsilon_{zH}^{(1,2)} \\ \varepsilon_{zH}^{(1,3)} \end{bmatrix} + \begin{bmatrix} \tilde{\gamma}_{1H}^{(1)} \\ \tilde{\gamma}_{2H}^{(1)} \end{bmatrix} \\
&+ \begin{bmatrix} \mathbf{0} \\ \Delta(\eta,\nu) + K_2\nu \end{bmatrix} + \begin{bmatrix} -K_{11} & \mathbf{0} & \mathbf{0} \\ \mathbf{0} & -k_{12} & \mathbf{0} \\ \mathbf{0} & \mathbf{0} & -K_2 \end{bmatrix} \begin{bmatrix} n_z^{(1,1)} \\ n_z^{(1,2)} \\ R^T(\hat{\psi}_H^{(1)}) y_\eta \end{bmatrix},
\end{aligned} \tag{5.36}$$

where $K_1 = \text{diag}(\begin{bmatrix} K_{11} & k_{12} \end{bmatrix})$, $\tilde{\gamma}_{1H}^{(1)} = R(\psi)\nu - R(\hat{\psi}_H^{(1)})\hat{\nu}_H^{(1)}$, $\tilde{\gamma}_{2H}^{(1)} = f(\nu,\tau) - f(\hat{\nu}_H^{(1)},\tau)$, and $\mathbf{0}$

denotes a matrix/vector of zeroes, having a suitable dimension. Solving (5.36) results in

$$\begin{aligned}\varepsilon_{zH}^{(1)} = \begin{bmatrix}\varepsilon_{zH}^{(1,1)}\\ \varepsilon_{zH}^{(1,2)}\\ \varepsilon_{zH}^{(1,3)}\end{bmatrix} &= \begin{bmatrix}e^{-K_{11}t} & \mathbf{0} & \mathbf{0}\\ \mathbf{0} & e^{-k_{12}t} & \mathbf{0}\\ \mathbf{0} & \mathbf{0} & e^{-K_2 t}\end{bmatrix}\begin{bmatrix}\varepsilon_{zH}^{(1,1)}(0)\\ \varepsilon_{zH}^{(1,2)}(0)\\ \varepsilon_{zH}^{(1,3)}(0)\end{bmatrix}\\ &+\int_0^t \begin{bmatrix}e^{-K_1(t-\mathrm{t})} & \mathbf{0}\\ \mathbf{0} & e^{-K_2(t-\mathrm{t})}\end{bmatrix}\left(\begin{bmatrix}\tilde{\gamma}_{1H}^{(1)}(\mathrm{t})\\ \tilde{\gamma}_{2H}^{(1)}(\mathrm{t})+\Delta(\eta,\nu)\end{bmatrix}\right.\\ &\left.+\begin{bmatrix}-K_1 n_\eta\\ -K_2 R^T(\hat{\psi}_H^{(1)}(\mathrm{t}))n_\eta + K_2(\nu(\mathrm{t})-R^T(\hat{\psi}_H^{(1)}(\mathrm{t}))\eta(\mathrm{t}))\end{bmatrix}\right)d\mathrm{t},\end{aligned} \tag{5.37}$$

where $n_\eta = \begin{bmatrix}n_z^{(1,1)} & n_z^{(1,2)}\end{bmatrix}^T$. Using the above equation and the relation in (5.34), the residuals in $\varepsilon_{y_z}^{(1)}$ under healthy conditions can be expressed by

$$\begin{bmatrix}\varepsilon_{y_zH}^{(1,1)}\\ \varepsilon_{y_zH}^{(1,2)}\end{bmatrix} = e^{-K_1 t}\begin{bmatrix}\varepsilon_{zH}^{(1,1)}(0)\\ \varepsilon_{zH}^{(1,2)}(0)\end{bmatrix} + \begin{bmatrix}n_z^{(1,1)}\\ n_z^{(1,2)}\end{bmatrix} + \int_0^t e^{-K_1(t-\mathrm{t})}\left(\tilde{\gamma}_{1H}^{(1)}(\mathrm{t}) - K_1 n_\eta\right)d\mathrm{t}. \tag{5.38}$$

A bound on $|\varepsilon_{zH}^{(1)}|$ satisfies the inequality

$$\begin{aligned}|\varepsilon_{zH}^{(1)}| &\le \begin{bmatrix}|e^{-K_1 t}| & \mathbf{0}\\ \mathbf{0} & |e^{-K_2 t}|\end{bmatrix}\begin{bmatrix}|\varepsilon_{zH}^{(1,1)}(0)|\\ |\varepsilon_{zH}^{(1,2)}(0)|\\ |\varepsilon_{zH}^{(1,3)}(0)|\end{bmatrix}\\ &+\int_0^t\left(\begin{bmatrix}|e^{-K_1(t-\mathrm{t})}| & \mathbf{0}\\ \mathbf{0} & |e^{-K_2(t-\mathrm{t})}|\end{bmatrix}\begin{bmatrix}|\tilde{\gamma}_{1H}^{(1)}(\mathrm{t})|\\ |\tilde{\gamma}_{2H}^{(1)}(\mathrm{t})|+|\Delta(\eta,\nu)|+\end{bmatrix}\right.\\ &\left.\begin{bmatrix}|-K_2 R^T(\hat{\psi}_H^{(1)}(\mathrm{t}))n_\eta| + |-K_2(R^T(\hat{\psi}_H^{(1)}(\mathrm{t}))\eta(\mathrm{t})-\nu(\mathrm{t}))|\end{bmatrix}\right.\\ &\left.+\begin{bmatrix}|-K_1 e^{-K_1(t-\mathrm{t})}| & \mathbf{0}\\ \mathbf{0} & |-K_2 e^{-K_2(t-\mathrm{t})}|\end{bmatrix}\begin{bmatrix}|n_\eta|\\ \mathbf{0}\end{bmatrix}\right)d\mathrm{t}.\end{aligned} \tag{5.39}$$

In addition to the Assumptions 2 and 3, the following assumption regarding the uncertainties is considered:

Assumption 4 *The unknown added force vector τ_d is uniformly bounded, i.e., $|\tau_{d_i}| \le \bar{\tau}_{d_i}$, with $i \in \{1,2,3\}$ representing the elements of the vector and $\bar{\tau}_{d_i}$ representing a known bound.*

Assumption 4 provides a bound to distinguish the uncertainties from the faults. Under this assumption, a bound on each term constituting the inequality (5.39) is determined and is given by

5.39a. $$\begin{bmatrix}|\varepsilon_{zH}^{(1,1)}(0)| & |\varepsilon_{zH}^{(1,2)}(0)| & |\varepsilon_{zH}^{(1,3)}(0)|\end{bmatrix}^T = \begin{bmatrix}\bar{p}^{(1)} & \bar{\Psi}^{(1)} & \bar{\nu}^{(1)}\end{bmatrix}^T = \bar{z}^{(1)T},$$

5.39b. $$\begin{bmatrix}|e^{-K_1 t}| & \mathbf{0}\\ \mathbf{0} & |e^{-K_2 t}|\end{bmatrix} \le \rho^{(1)} e^{-\xi^{(1)} t} = \Phi^{(1)}(t),$$

5.39c. $\begin{bmatrix} |-K_1 e^{-K_1 t}| & \mathbf{0} \\ \mathbf{0} & |-K_2 e^{-K_2 t}| \end{bmatrix} \leq \rho_d^{(1)} e^{-\xi_d^{(1)} t},$

5.39d. $|n_\eta| \leq \begin{bmatrix} \bar{n}_z^{(1,1)} & \bar{n}_z^{(1,2)} \end{bmatrix}^T,$

5.39e. $|\tilde{\gamma}_{1H}^{(1)}| = |R(\psi)\nu - R(\hat{\psi}_H^{(1)})\hat{\nu}_H^{(1)}| \leq \lambda_{\gamma_1^{(1)}} \begin{bmatrix} |\varepsilon_{zH}^{(1,1)}| & |\varepsilon_{zH}^{(1,2)}| \end{bmatrix}^T,$
$|\tilde{\gamma}_{2H}^{(1)}| = |f(\nu,\tau) - f(\hat{\nu}_H^{(1)},\tau)| \leq \lambda_{\gamma_2^{(1)}} |\varepsilon_{zH}^{(1,3)}|,$
$|\Delta(\eta,\nu)| = \tilde{\tau}_d \leq \bar{\tilde{\tau}}_d$, and,

5.39f. $|-K_2 R^T(\hat{\psi}_H^{(1)}) n_\eta| \leq \begin{bmatrix} k_{21}(\bar{n}_{z_1}^{(1,1)} + \bar{n}_{z_2}^{(1,1)}) \\ k_{22}(\bar{n}_{z_1}^{(1,1)} + \bar{n}_{z_2}^{(1,1)}) \\ k_{23}(\bar{n}_z^{(1,2)}) \end{bmatrix} = \bar{\tilde{n}}_\eta,$
$|-K_2(R^T(\hat{\psi}_H^{(1)})\eta - \nu)| \leq (\tilde{\eta} - \tilde{\nu})$, with,
$|-K_2 R^T(\hat{\psi}_H)\eta| \leq \begin{bmatrix} k_{21}(\bar{x}_p + \bar{y}_p) & k_{22}(\bar{x}_p + \bar{y}_p) & k_{23}(\bar{\psi}) \end{bmatrix}^T = \tilde{\eta},$
$|K_2 \nu| \in [\underline{\nu}, \tilde{\nu}], \eta \in [\underline{\eta}, \bar{\eta}] \in [\begin{bmatrix} \underline{x} & \underline{y} & \underline{\psi} \end{bmatrix}^T, \begin{bmatrix} \bar{x} & \bar{y} & \bar{\psi} \end{bmatrix}^T],$

and where, $\lambda_{\gamma_1^{(1)}}, \lambda_{\gamma_2^{(1)}}$ are the respective Lipschitz constants. Upon substituting the above equations into (5.39), the state estimation error under healthy conditions $\varepsilon_{zH}^{(1)}$ satisfies

$$|\varepsilon_{zH}^{(1)}| \leq \Phi^{(1)}(t) \begin{bmatrix} \bar{p}^{(1)} \\ \bar{\psi}^{(1)} \\ \bar{\nu}^{(1)} \end{bmatrix} + \int_0^t \left(\rho_d^{(1)} e^{-\xi_d^{(1)}(t-\mathfrak{t})} \begin{bmatrix} \bar{n}_z^{(1,1)} \\ \bar{n}_z^{(1,2)} \\ \mathbf{0} \end{bmatrix} + \Phi^{(1)}(t-\mathfrak{t}) \begin{bmatrix} \lambda_{\gamma_1^{(1)}} |\varepsilon_{zH}^{(1,1)}(\mathfrak{t})| \\ \lambda_{\gamma_1^{(1)}} |\varepsilon_{zH}^{(1,2)}(\mathfrak{t})| \\ \lambda_{\gamma_2^{(1)}} |\varepsilon_{zH}^{(1,3)}(\mathfrak{t})| + \bar{\tilde{\tau}}_d + \bar{\tilde{n}}_\eta + (\tilde{\eta} - \tilde{\nu}) \end{bmatrix} \right) d\mathfrak{t}. \tag{5.40}$$

Applying the Bellman-Gronwall lemma to Equation (5.40) and by using the relation in (5.35), the $j-$th component of the adaptive threshold $(j \in \{1,2\})$ for the sensor faults in $\mathcal{S}^{(1)}$ can be expressed as [177]

$$\bar{\varepsilon}_{y_z}^{(1,j)}(t) = E^{(1,j)}(t) + \rho^{(1,j)} \Lambda_1 \int_0^t Z^{(1,j)}(\mathfrak{t}) e^{-\xi^{(1,j)}(t-\mathfrak{t})} d\mathfrak{t} + \bar{n}_z^{(1,j)}, \tag{5.41}$$

where

$$\begin{aligned} E^{(1)}(t) &= \rho^{(1)} e^{-\xi^{(1)} t} \bar{z}^{(1)} + \frac{\rho_d^{(1)} \bar{n}_z^{(1)}}{\xi_d^{(1)}} (1 - e^{-\xi_d^{(1)} t}) \\ &+ \int_0^t \rho^{(1)} e^{-\xi^{(1)}(t-\mathfrak{t})} \begin{bmatrix} \mathbf{0} \\ \bar{\tilde{\tau}}_d + \bar{\tilde{n}}_\eta + (\tilde{\eta} - \tilde{\nu}) \end{bmatrix} d\mathfrak{t} \\ Z^{(1)}(t) &= E^{(1)}(t) + \rho^{(1)} \Lambda_1 \int_0^t E^{(1)}(\mathfrak{t}) e^{(\rho^{(1)}\Lambda_1 - \xi^{(1)})(t-\mathfrak{t})} d\mathfrak{t}. \end{aligned} \tag{5.42}$$

For the observer $O^{(2)}$, the state estimation error dynamics are given by

$$\dot{\varepsilon}_{zH}^{(2)} = \begin{bmatrix} \dot{\varepsilon}_{zH}^{(2,1)} \\ \dot{\varepsilon}_{zH}^{(2,2)} \end{bmatrix} = \begin{bmatrix} -k_3 & \mathbf{0} \\ \mathbf{0} & -K_4 \end{bmatrix} \begin{bmatrix} \varepsilon_{zH}^{(2,1)} \\ \varepsilon_{zH}^{(2,2)} \end{bmatrix} + \begin{bmatrix} \tilde{\gamma}_{1H}^{(2)} \\ \tilde{\gamma}_{2H}^{(2)} + \Delta(\eta,\nu) \end{bmatrix} + \begin{bmatrix} -k_3 & \mathbf{0} \\ \mathbf{0} & -K_4 \end{bmatrix} \begin{bmatrix} n_z^{(2,1)} \\ n_z^{(2,2)} \end{bmatrix}, \tag{5.43}$$

where $\tilde{\gamma}_{1H}^{(2)} = r - \hat{r}_H$, and $\tilde{\gamma}_{2H}^{(2)} = f(\nu,\tau) - f(\hat{\nu}_H^{(2)},\tau)$. The resulting residuals in $\varepsilon_{y_z}^{(2)}$ under healthy conditions can be expressed by

$$\begin{aligned}\begin{bmatrix}\varepsilon_{y_zH}^{(2,1)}\\ \varepsilon_{y_zH}^{(2,2)}\end{bmatrix} &= \begin{bmatrix}e^{-k_3 t} & \mathbf{0}\\ \mathbf{0} & e^{-K_4 t}\end{bmatrix}\begin{bmatrix}\varepsilon_{zH}^{(2,1)}(0)\\ \varepsilon_{zH}^{(2,2)}(0)\end{bmatrix} + \begin{bmatrix}n_z^{(2,1)}\\ n_z^{(2,2)}\end{bmatrix} + \\ &\int_0^t \begin{bmatrix}e^{-k_3(t-\mathfrak{t})} & \mathbf{0}\\ \mathbf{0} & e^{-K_4(t-\mathfrak{t})}\end{bmatrix}\left(\begin{bmatrix}\tilde{\gamma}_{1H}^{(2)}(\mathfrak{t}) - k_3 n_z^{(2,1)}\\ \tilde{\gamma}_{2H}^{(2)}(\mathfrak{t}) + \Delta(\eta,\nu) - K_4 n_z^{(2,2)}\end{bmatrix}\right) d\mathfrak{t}.\end{aligned} \tag{5.44}$$

Further, similar to Equation (5.40), a bound on the magnitude of the state estimation error under healthy conditions $|\varepsilon_{zH}^{(2)}|$ is computed and is given by

$$|\varepsilon_{zH}^{(2)}| \leq \Phi^{(2)}(t)\begin{bmatrix}\bar{\Psi}^{(2)}\\ \bar{\nu}^{(2)}\end{bmatrix} + \int_0^t \left(\Phi^{(2)}(t-\mathfrak{t})\begin{bmatrix}\lambda_{\gamma_1^{(2)}}|\varepsilon_{zH}^{(2,1)}(\mathfrak{t})|\\ \lambda_{\gamma_2^{(2)}}|\varepsilon_{zH}^{(2,2)}(\mathfrak{t})| + \bar{\bar{\tau}}_d\end{bmatrix} + \rho_d^{(2)} e^{-\xi_d^{(2)}(t-\mathfrak{t})}\begin{bmatrix}\bar{n}_z^{(2,1)}\\ \bar{n}_z^{(2,2)}\end{bmatrix}\right) d\mathfrak{t}, \tag{5.45}$$

where,

5.45a. $\begin{bmatrix}|\varepsilon_{zH}^{(2,1)}(0)| & |\varepsilon_{zH}^{(2,2)}(0)|\end{bmatrix}^T = \begin{bmatrix}\bar{\Psi}^{(2)} & \bar{\nu}^{(2)}\end{bmatrix}^T = \bar{z}^{(2)T}$,

5.45b. $\begin{bmatrix}|e^{-k_3 t}| & \mathbf{0}\\ \mathbf{0} & |e^{-K_4 t}|\end{bmatrix} \leq \rho^{(2)} e^{-\xi^{(2)} t} = \Phi^{(2)}(t)$,

5.45c. $\begin{bmatrix}|-k_3 e^{-k_3 t}| & \mathbf{0}\\ \mathbf{0} & |-K_4 e^{-K_4 t}|\end{bmatrix} \leq \rho_d^{(2)} e^{-\xi_d^{(2)} t}$,

5.45d. $\begin{bmatrix}|n_z^{(2,1)}| & |n_z^{(2,2)}|\end{bmatrix}^T \leq \begin{bmatrix}\bar{n}_z^{(2,1)} & \bar{n}_z^{(2,2)}\end{bmatrix}^T$,

5.45e. $|r - \hat{r}_H^{(2)}| = |\tilde{\gamma}_{1H}^{(2)}| \leq \lambda_{\gamma_1^{(2)}}|\varepsilon_{zH}^{(2,1)}|$,
$|f(\nu,\tau) - f(\hat{\nu}_H^{(2)},\tau)| = |\tilde{\gamma}_{2H}^{(2)}| \leq \lambda_{\gamma_2^{(2)}}|\varepsilon_{zH}^{(2,2)}|$,
$|\Delta(\eta,\nu)| = \tilde{\tau}_d \leq \bar{\bar{\tau}}_d$,

where, $\lambda_{\gamma_1^{(2)}}$ and $\lambda_{\gamma_2^{(2)}}$ are the respective Lipschitz constants. Further, let us define $\rho^{(I,j)}$, $\xi^{(I,j)}$, $\rho_d^{(I,j)}$, $\xi_d^{(I,j)}$ as positive constants satisfying $|e^{-K_p t}| \leq \rho^{(I)} e^{-\xi^{(I)} t}$ and $\xi^{(I)} > \Lambda_I \rho^{(I)}$, $p \in \{1,\ldots,4\}$; $\Lambda_1 = \lambda_{\gamma_1^{(1)}}$, $\Lambda_2 = \begin{bmatrix}\lambda_{\gamma_1^{(2)}} & \mathbf{0}\\ \mathbf{0} & \lambda_{\gamma_2^{(2)}} + \lambda_{\bar{\bar{\tau}}_d}\end{bmatrix}$. Applying the Bellman-Gronwall lemma to Equation (5.45) and by using the relation in (5.35), for the faults occurring in the sensor set $\mathcal{S}^{(2)}$, the $j-$th adaptive threshold ($j \in \{1,2\}$) is expressed as

$$\bar{\varepsilon}_{y_z}^{(2,j)}(t) = E^{(2,j)}(t) + \rho^{(2,j)}\Lambda_2^{(j)} \int_0^t Z^{(2,j)}(\mathfrak{t}) e^{-\xi^{(2,j)}(t-\mathfrak{t})} d\mathfrak{t} + \bar{n}_z^{(2,j)}, \tag{5.46}$$

where

$$\begin{aligned}E^{(2)}(t) &= \rho^{(2)} e^{-\xi^{(2)} t}\bar{z}^{(2)} + \frac{\rho_d^{(2)}\bar{n}_z^{(2)}}{\xi_d^{(2)}}(1 - e^{-\xi_d^{(2)} t}) + \int_0^t \rho^{(2)} e^{-\xi^{(2)}(t-\mathfrak{t})}\begin{bmatrix}0\\ \bar{\bar{\tau}}_d\end{bmatrix} d\mathfrak{t}\\ Z^{(2)}(t) &= E^{(2)}(t) + \rho^{(2)}\Lambda_2 \int_0^t E^{(2)}(\mathfrak{t}) e^{(\rho^{(2)}\Lambda_2 - \xi^{(2)})(t-\mathfrak{t})} d\mathfrak{t}.\end{aligned} \tag{5.47}$$

Next, the adaptive threshold corresponding to the residual in $\mathcal{M}^{(3)}$ is derived. The state estimation error for the observer $O^{(3)}$ can be described under healthy conditions by

$$\dot{\varepsilon}_{zH}^{(3,1)} = -k_5\varepsilon_{zH}^{(3,1)} + \dot{\psi}_H + \frac{1}{a_2}\dddot{\psi}^{(3)} + \frac{a_1}{a_2}\ddot{\psi}^{(3)} - \frac{b_1}{a_2}(b_2\dot{\delta}_p + \delta_p) - \frac{b_3}{a_2}(b_4\dot{\delta}_s + \delta_s) - k_5 n_z^{(3,1)}. \tag{5.48}$$

The resulting residual under healthy conditions ($\varepsilon_{y_zH}^{(3,1)}$) is expressed by

$$\begin{aligned}\varepsilon_{y_zH}^{(3,1)} &= e^{-k_5 t}\varepsilon_{zH}^{(3,1)}(0) + n_z^{(3,1)} + \int_0^t e^{-k_5(t-\mathfrak{t})}\Bigg(\dot{\psi}_H + \\ &\frac{1}{a_2}\dddot{\psi}^{(3)} + \frac{a_1}{a_2}\ddot{\psi}^{(3)} - \frac{b_1}{a_2}(b_2\dot{\delta}_p + \delta_p) - \frac{b_3}{a_2}(b_4\dot{\delta}_s + \delta_s) - k_5 n_z^{(3,1)}\Bigg)d\mathfrak{t}.\end{aligned} \tag{5.49}$$

Computing an upper bound on the magnitude of $\varepsilon_{zH}^{(3,1)}$, we obtain

$$|\varepsilon_{zH}^{(3,1)}| \leq \Phi^{(3,1)}(t)\bar{\psi}^{(3,1)} + \int_0^t \left(\Phi^{(3,1)}(t-\mathfrak{t})\Lambda_\gamma^{(3,1)} + \rho_d^{(3,1)} e^{-\xi_d^{(3,1)}(t-\mathfrak{t})}\bar{n}_z^{(3,1)}\right)d\mathfrak{t}, \tag{5.50}$$

where,

5.50a. $|\varepsilon_{zH}^{(3,1)}(0)| = \bar{\psi}^{(3,1)} = \bar{z}^{(3,1)}$,

5.50b. $|e^{-k_5 t}| \leq \rho^{(3,1)} e^{-\xi^{(3,1)}t} = \Phi^{(3,1)}(t)$,

5.50c. $|-k_5 e^{-k_5 t}| \leq \rho_d^{(3,1)} e^{-\xi_d^{(3,1)}t}$,

5.50d. $\Lambda_\gamma^{(3,1)} = \lambda_{\gamma_1^{(3)}} + |\frac{1}{a_2}|\lambda_{\gamma_3^{(3)}} + \frac{|a_1|}{|a_2|}\lambda_{\gamma_2^{(3)}} - \frac{|b_1||b_2|}{|a_2|}\bar{\dot{\delta}}_p - \frac{|b_1|}{|a_2|}\bar{\delta}_p - \frac{|b_3||b_4|}{|a_2|}\bar{\dot{\delta}}_s - \frac{|b_3|}{|a_2|}\bar{\delta}_s$,

5.50e. $|n_z^{(3,1)}| \leq \bar{n}_z^{(3,1)}$,

and $\lambda_{\gamma_1^{(3)}}, \lambda_{\gamma_2^{(3)}}$, and $\lambda_{\gamma_3^{(3)}}$ are the Lipschitz constants corresponding to ψ, r and $\dot{r}$, respectively; $(\bar{\delta}_p, \bar{\delta}_s)$ and $(\bar{\dot{\delta}}_p, \bar{\dot{\delta}}_s)$ are the upper limits on the respective thruster angles and their angular rates, respectively. The resulting adaptive threshold can be expressed by

$$\begin{aligned}\bar{\varepsilon}_{y_z}^{(3,1)}(t) &= \rho^{(3,1)} e^{-\xi^{(3,1)}t}\bar{z}^{(3,1)} + \rho^{(3,1)}\Lambda_\gamma^{(3,1)} \\ &\int_0^t e^{-\xi^{(3,1)}(t-\mathfrak{t})}d\mathfrak{t} - \frac{\rho_d^{(3,1)}\bar{n}_z^{(3,1)}}{\xi_d^{(3,1)}}(1 - e^{-\xi_d^{(3,1)}t}) + \bar{n}_z^{(3,1)}.\end{aligned} \tag{5.51}$$

Finally, for the observer $O^{(4)}$, the state estimation error dynamics under healthy conditions can be described by

$$\begin{aligned}\dot{\varepsilon}_{zH}^{(4,1)} &= -K_6\varepsilon_{zH}^{(4,1)} + \begin{bmatrix} u(\cos\psi - \cos y_\psi^{(4)}) + v(-\sin\psi + \sin y_\psi^{(4)}) \\ u(\sin\psi - \sin y_\psi^{(4)}) + v(\cos\psi - \cos y_\psi^{(4)}) \end{bmatrix} \\ &+ \begin{bmatrix} -\cos y_\psi^{(4)} & \sin y_\psi^{(4)} & 0 \\ -\sin y_\psi^{(4)} & -\cos y_\psi^{(4)} & 0 \end{bmatrix} n_z^{(4,2)} - K_6 n_z^{(4,1)},\end{aligned} \tag{5.52}$$

where $K_6 = \text{diag}(\begin{bmatrix} k_{61} & k_{62} \end{bmatrix})$ and $n_z^{(4,2)} = n_v$. The resulting residual under healthy conditions ($\varepsilon_{y_z H}^{(4,1)}$) is expressed by

$$\begin{aligned} \varepsilon_{y_z H}^{(4,1)} &= e^{-K_6 t} \varepsilon_{zH}^{(4,1)}(0) + \int_0^t e^{-K_6(t-\mathfrak{t})} \\ &\left(\begin{bmatrix} \cos\psi & -\sin\psi \\ \sin\psi & \cos\psi \end{bmatrix} \begin{bmatrix} u \\ v \end{bmatrix} - \begin{bmatrix} \cos y_\psi & -\sin y_\psi \\ \sin y_\psi & \cos y_\psi \end{bmatrix} \begin{bmatrix} y_u \\ y_v \end{bmatrix} - K_6 n_z^{(4,1)} \right) d\mathfrak{t}. \end{aligned} \tag{5.53}$$

A bounded magnitude of the state estimation error under healthy conditions, $|\varepsilon_{zH}^{(4,1)}|$, can be described by

$$|\varepsilon_{zH}^{(4,1)}| \leq \Phi^{(4,1)}(t)\bar{p}^{(4,1)} + \int_0^t \left(\Phi^{(4,1)}(t-\mathfrak{t})\Lambda_\gamma^{(4,1)} - \rho_d^{(4,1)} e^{-\xi_d^{(4,1)}(t-\mathfrak{t})} \bar{n}_z^{(4,1)} \right) d\mathfrak{t}, \tag{5.54}$$

where,

5.54a. $|\varepsilon_{zH}^{(4,1)}(0)| = \bar{p}^{(4,1)} = \bar{z}^{(4,1)}$,

5.54b. $|e^{-K_6 t}| \leq \rho^{(4,1)} e^{-\xi^{(4,1)} t} = \Phi^{(4,1)}(t)$,

5.54c. $|-K_6 e^{-K_6 t}| \leq \rho_d^{(4,1)} e^{-\xi_d^{(4,1)} t}$,

5.54d. $\Lambda_\gamma^{(4,1)} = \begin{bmatrix} 2(\bar{u}+\bar{v}) + \bar{n}_u + \bar{n}_v \\ 2(\bar{u}+\bar{v}) + \bar{n}_u + \bar{n}_v \end{bmatrix}$, such that $z^{(4,2)} \leq \begin{bmatrix} \bar{u} & \bar{v} & \bar{r} \end{bmatrix}^T$ and $\bar{n}_z^{(4,2)} = \begin{bmatrix} \bar{n}_u & \bar{n}_v & \bar{n}_r \end{bmatrix}^T$,

5.54e. $|n_z^{(4,1)}| \leq \bar{n}_z^{(4,1)}$.

Based on these computed bounds, the adaptive threshold can be expressed by

$$\begin{aligned} \bar{\varepsilon}_{y_z}^{(4,1)}(t) &= \rho^{(4,1)} e^{-\xi^{(4,1)} t} \bar{z}^{(4,1)} + \rho^{(4,1)} \Lambda_\gamma^{(4,1)} \\ &\int_0^t e^{-\xi^{(4,1)}(t-\mathfrak{t})} d\mathfrak{t} - \frac{\rho_d^{(4,1)} \bar{n}_z^{(4,1)}}{\xi_d^{(4,1)}} (1 - e^{-\xi_d^{(4,1)} t}) + \bar{n}_z^{(4,1)}. \end{aligned} \tag{5.55}$$

5.2.3 Combinatorial Fault Decision Logic

In this subsection, the design of a combinatorial fault decision logic that enables the isolation of multiple sensor faults is presented. Firstly, the aggregator module receives a decision on the fault detection from the various monitoring modules based on a set of ARRs composed of residuals and adaptive thresholds. Specifically, for the monitoring module $\mathcal{M}^{(I)}$, the set of ARRs $\mathcal{E}_{y_z}^{(I)}$ is defined for detecting faults in the sensor set $\mathcal{S}^{(I)}$, as

$$\mathcal{E}_{y_z}^{(I)} = \bigcup_j \mathcal{E}_{y_z}^{(I,j)}, \tag{5.56}$$

where, for $I \in \{1, \ldots, 4\}$, the $j-$th ARR $\mathcal{E}_{y_z}^{(I,j)}$ is given by

$$\mathcal{E}_{y_z}^{(I,j)} : |\varepsilon_{y_z}^{(I,j)}(t)| - \bar{\varepsilon}_{y_z}^{(I,j)}(t) \leq 0, \quad j \in \{1, \ldots, m_I\}. \tag{5.57}$$

As per the design criterion (2), a violation of the $j-$th ARR implies the occurrence of at least one sensor fault in the corresponding sensor set $\mathcal{S}^{(I)}$. Define $T_D^{(I,j)}$ to be the first instance of violation of the $j-$th ARR $\mathcal{E}_{y_z}^{(I,j)}$ in $\mathcal{M}^{(I)}$, i.e.,

$$T_D^{(I,j)} = \begin{cases} \min\{t \in \mathbb{R}^+ : |\varepsilon_{y_z}^{(I,j)}(t)| > \bar{\varepsilon}_{y_z}^{(I,j)}(t)\}, & \neg\mathcal{E}_{y_z}^{(I,j)} \\ \infty, & \text{otherwise.} \end{cases} \tag{5.58}$$

$T_D^{(I,j)}$ indicates the first instance of fault detection in the corresponding sensor within $\mathcal{S}^{(I)}$. The output of the monitoring module $\mathcal{M}^{(I)}$ is the $I-$th decision $\mathbf{d}^{(I)}(t) = \left[\mathbf{d}^{(I,1)}(t), \quad \ldots, \quad \mathbf{d}^{(I,m_I)}(t)\right]^T$, where,

$$\mathbf{d}^{(I,j)}(t) = \begin{cases} 0, & \text{if } t < T_D^{(I,j)} \\ 1, & \text{otherwise} \end{cases}. \tag{5.59}$$

Under the exoneration assumption [186] which considers that $\mathcal{S}^{(I)}$ is functioning properly before the time instant $T_{FD}^{(I)}$, $\mathbf{d}^{(I)}(t) = \mathbf{0}$ implies that no fault has occurred in the sensor set $S^{(I)}$. Upon receiving the decisions $\mathbf{d}^{(I)}(t)$ from each monitoring module in the aggregator module $\mathcal{A}$, an aggregated decision vector $\mathbf{d}(t)$ is formed by combining these individual decisions, i.e.,

$$\mathbf{d}(t) = \texttt{vcat}(\mathbf{d}^{(I)}(t)), \tag{5.60}$$

where $\texttt{vcat}()$ represents a vertical concatenation function.

Remark 5.4 Unlike in some multi-level FDI schemes (e.g., see [186]), instead of aggregating the individual sensor fault decisions $\mathbf{d}^{(I,j)}(t)$ into a boolean function, the aggregated decision vector $\mathbf{d}(t)$ composed of $\mathbf{d}^{(I,j)}(t)$ is directly used for consistency checking. Since each sensor set may have multiple sensors, such a combinatorial logic can isolate multiple sensor faults, as shown later. □

The aggregator module includes the FSM, comprising zeros, ones or an '*' as its elements. Fault isolation involves conducting a consistency test between $\mathbf{d}(t)$ and the FSM, represented by F. The matrix F consists of a maximum of l rows, $l = \sum_I m_I$, with each row corresponding to the $j-$th ARR $\mathcal{E}_{y_z}^{(I,j)}$. Further, F consists of $N_c = 2^{\mathfrak{s}} - 1$ columns, with $\mathfrak{s}$ representing the total no. of monitored sensors. Each column F_q, $q \in \{1, \ldots, N_c\}$, represents a theoretical sensor fault pattern. An entry $F_{pq} = 1$ (where $p \in \{1, \ldots, l\}$) indicates that at least one sensor fault within the combination $\mathcal{F}_{c_q}$ is responsible for the violation of the ARR $\mathcal{E}_{y_z}^{(I,j)}$, thereby impacting $\mathcal{S}^{(I)}$. An entry $F_{pq} =$'*' is used instead of '1' to distinguish a possible violation due to the weak sensitivity of the ARR $\mathcal{E}_{y_z}^{(I,j)}$ to a sensor fault included in $\mathcal{F}_{c_q}$. Otherwise, F_{pq} is taken to be zero. The observed fault pattern in $\mathbf{d}(t)$ is considered consistent with a theoretical pattern F_q when $\mathbf{d}_p(t) = F_{pq}$ for all $p \in \{1, \ldots, l\}$.

The final diagnostic output, denoted as the diagnosis set $\mathcal{D}_s(t)$, is obtained from the aggregator module and includes all possible fault combinations $\mathcal{F}_{c_q}$ that pass the consistency test. It is important to note that, as the elements of $\mathbf{d}(t)$ can fluctuate over time, the cardinality of the diagnosis set may also change. This allows the diagnosis set to reflect the evolving fault conditions as the system operates. Given the assumption that the faults are permanent, the cardinality can only increase.

Table 5.1: Sensor fault signature matrix (FSM) for the designed ARRs.

	$\mathcal{F}_{c_1}$	$\mathcal{F}_{c_2}$	$\mathcal{F}_{c_3}$	$\mathcal{F}_{c_4}$	$\mathcal{F}_{c_5}$	$\mathcal{F}_{c_6}$	$\mathcal{F}_{c_7}$	$\mathcal{F}_{c_8}$	$\mathcal{F}_{c_9}$	$\mathcal{F}_{c_{10}}$	$\mathcal{F}_{c_{11}}$	$\mathcal{F}_{c_{12}}$	$\mathcal{F}_{c_{13}}$	$\mathcal{F}_{c_{14}}$	$\mathcal{F}_{c_{15}}$
$\mathcal{E}_{y_z}^{(1,1)}$	1	*	0	0	1	1	1	*	*	0	1	1	*	1	1
$\mathcal{E}_{y_z}^{(1,2)}$	0	1	0	0	1	0	0	1	1	0	1	1	1	0	1
$\mathcal{E}_{y_z}^{(2,1)}$	0	1	1	0	1	1	0	1	1	1	1	1	1	1	1
$\mathcal{E}_{y_z}^{(2,2)}$	0	0	1	0	0	1	0	1	0	1	1	0	1	1	1
$\mathcal{E}_{y_z}^{(3,1)}$	0	1	0	0	1	0	0	1	1	0	1	1	1	0	1
$\mathcal{E}_{y_z}^{(4,1)}$	1	0	*	*	1	1	1	*	*	*	1	1	*	1	1

Remark 5.5 The selection of monitoring modules in the proposed FDI scheme should be based on the sensors that are to be monitored. Accordingly, the observer design, adaptive thresholds computation and the FSM must be updated to accommodate the new sensor configuration and additional model uncertainties. □

5.2.4 Sensitivity Analysis

While the structural sensitivity to the sensor faults can be directly inferred from the residual expressions, it may be difficult to infer the weak sensitivity. A sensitivity analysis is subsequently performed to realise the smaller impacts of the faults on the residuals (and subsequently the ARRs). For the sensors considered in this work, the following sensor fault/fault combinations are possible: $\mathcal{F}_{c_1} = \{f_p\}$, $\mathcal{F}_{c_2} = \{f_\psi\}$, $\mathcal{F}_{c_3} = \{f_v\}$, $\mathcal{F}_{c_4} = \{f_\chi\}$, $\mathcal{F}_{c_5} = \{f_p, f_\psi\}$, $\mathcal{F}_{c_6} = \{f_p, f_v\}$, $\mathcal{F}_{c_7} = \{f_p, f_\chi\}$, $\mathcal{F}_{c_8} = \{f_\psi, f_v\}$, $\mathcal{F}_{c_9} = \{f_\psi, f_\chi\}$, $\mathcal{F}_{c_{10}} = \{f_v, f_\chi\}$, $\mathcal{F}_{c_{11}} = \{f_p, f_\psi, f_v\}$, $\mathcal{F}_{c_{12}} = \{f_p, f_\psi, f_\chi\}$, $\mathcal{F}_{c_{13}} = \{f_\psi, f_v, f_\chi\}$, $\mathcal{F}_{c_{14}} = \{f_v, f_\chi, f_p\}$, and $\mathcal{F}_{c_{15}} = \{f_p, f_\psi, f_v, f_\chi\}$. A Jacobian block matrix is computed for the residuals derived in Section 5.2 5.2.2. w.r.t. single faults (f_p, f_ψ, f_v and f_χ), and is given by

$$\nabla\varepsilon_{y_z}(f_z) = \begin{bmatrix} \partial\varepsilon_{y_z}^{(1,1)}(f_p) & \partial\varepsilon_{y_z}^{(1,1)}(f_\psi) & \partial\varepsilon_{y_z}^{(1,1)}(f_v) & \partial\varepsilon_{y_z}^{(1,1)}(f_\chi) \\ \partial\varepsilon_{y_z}^{(1,2)}(f_p) & \partial\varepsilon_{y_z}^{(1,2)}(f_\psi) & \partial\varepsilon_{y_z}^{(1,2)}(f_v) & \partial\varepsilon_{y_z}^{(1,2)}(f_\chi) \\ \partial\varepsilon_{y_z}^{(2,1)}(f_p) & \partial\varepsilon_{y_z}^{(2,1)}(f_\psi) & \partial\varepsilon_{y_z}^{(2,1)}(f_v) & \partial\varepsilon_{y_z}^{(2,1)}(f_\chi) \\ \partial\varepsilon_{y_z}^{(2,2)}(f_p) & \partial\varepsilon_{y_z}^{(2,2)}(f_\psi) & \partial\varepsilon_{y_z}^{(2,2)}(f_v) & \partial\varepsilon_{y_z}^{(2,2)}(f_\chi) \\ \partial\varepsilon_{y_z}^{(3,1)}(f_p) & \partial\varepsilon_{y_z}^{(3,1)}(f_\psi) & \partial\varepsilon_{y_z}^{(3,1)}(f_v) & \partial\varepsilon_{y_z}^{(3,1)}(f_\chi) \\ \partial\varepsilon_{y_z}^{(4,1)}(f_p) & \partial\varepsilon_{y_z}^{(4,1)}(f_\psi) & \partial\varepsilon_{y_z}^{(4,1)}(f_v) & \partial\varepsilon_{y_z}^{(4,1)}(f_\chi) \end{bmatrix}. \tag{5.61}$$

Here, each block of the matrix represents the partial derivative of the corresponding residual vector elements with respect to a sensor fault. Computing the Jacobian matrix results in

$$\nabla\varepsilon_{y_z}(f_z) = \begin{bmatrix} \mathbf{1} & \partial\varepsilon_{y_z}^{(1,1)}(f_\psi) & \mathbf{0} & \mathbf{0} \\ 0 & 1 & 0 & 0 \\ 0 & 1 & 1 & 0 \\ \mathbf{0} & \mathbf{0} & \mathbf{1} & \mathbf{0} \\ 0 & 1 & 0 & 0 \\ \mathbf{1} & \mathbf{0} & \partial\varepsilon_{y_z}^{(4,1)}(f_v) & \partial\varepsilon_{y_z}^{(4,1)}(f_\chi) \end{bmatrix}, \tag{5.62}$$

where, **1**, **0** represent an all-ones matrix and a null matrix of appropriate dimensions, respectively. The ones and zeros confirm or refute the existence of a structural relationship, respectively, whereas the following weak sensitivities are also observed:

- $\partial\varepsilon_{y_z}^{(1,1)}(f_\psi)$: A fault in the heading angle measurement enters the residual $\varepsilon_{y_z}^{(1,1)}$ directly through the heading angle estimate $\hat{\psi}^{(1)}$ and indirectly through the velocity vector estimate $\hat{\mathbf{v}}^{(1)}$, resulting in a Jacobian given by

$$\begin{bmatrix} \frac{\hat{u}^{(1)}\sin\hat{\psi}^{(1)}+\hat{v}^{(1)}\cos\hat{\psi}^{(1)}}{|\hat{r}^{(1)}|}\left(k_{23}\mathcal{J}_1+k_{12}\mathcal{J}_2\right) \\ \frac{\hat{u}^{(1)}\cos\hat{\psi}^{(1)}-\hat{v}^{(1)}\sin\hat{\psi}^{(1)}}{|\hat{r}^{(1)}|}\left(k_{23}\mathcal{J}_3+k_{12}\mathcal{J}_4\right) \end{bmatrix}, \tag{5.63}$$

  where, $k_{12}, k_{23} \in \mathbb{R}$ are observer gains such that $K_1 = \text{diag}(\begin{bmatrix} K_{11} & k_{12} \end{bmatrix})$ and $K_2 = \text{diag}(\begin{bmatrix} k_{21} & k_{22} & k_{23} \end{bmatrix})$. Further, $\mathcal{J}_1$, $\mathcal{J}_2$, $\mathcal{J}_3$ and $\mathcal{J}_4$ represent polynomial functions of the observer's states $\hat{u}^{(1)}, \hat{v}^{(1)}$ and $\hat{r}^{(1)}$. By tuning the gains k_{12}, k_{23}, a balance between the fault sensitivity of the residual and observer convergence rate can be achieved. Specifically, the gains should be selected high enough to ensure fast convergence of the estimation errors but not amplify the propagation of heading angle fault into the position residual.

- $\partial\varepsilon_{y_z}^{(4,1)}(f_v)$: The Jacobian elements are given by

$$\begin{bmatrix} -\cos(y_\chi)\cos\left(\tan^{-1}\left(\frac{y_v}{y_u}\right)\right) & -\cos(y_\chi)\sin\left(\tan^{-1}\left(\frac{y_v}{y_u}\right)\right) & 0 \\ -\sin(y_\chi)\cos\left(\tan^{-1}\left(\frac{y_v}{y_u}\right)\right) & -\sin(y_\chi)\sin\left(\tan^{-1}\left(\frac{y_v}{y_u}\right)\right) & 0 \end{bmatrix}. \tag{5.64}$$

  It can be observed that each element is bounded in the range of $[-1, 1]$, and is independent of the observer's gains. This prevents an arbitrarily large variation in the residual's value due to a fault in the velocity measurements.

- $\partial\varepsilon_{y_z}^{(4,1)}(f_\chi)$: The Jacobian elements are given by

$$\begin{bmatrix} U_y\sin(y_\chi) \\ -U_y\cos(y_\chi) \end{bmatrix}, \tag{5.65}$$

  where $U_y = \sqrt{y_u^2 + y_v^2}$. The weak sensitivity of $\varepsilon_{y_z}^{(4,1)}$ to faults in course angle measurements is attributed to the faults appearing in the domain of sine and cosine functions, which return values in a small range $[-1, 1]$. When multiplied by the ship's measured speed U_y, a bounded sensitivity in the $[-U_y, U_y]$ range is obtained. Therefore, the sensitivities are small at low speeds, however, it is non-negligible at higher speeds.

Based on the above sensitivity analysis results, the FSM for the ARRs designed in this work is determined and is given in Table 5.1. The weak sensitivity of an ARR to sensor fault(s) is denoted by a '*' symbol.

5.3 Simulation Results

The proposed FDI scheme is further verified in this section using simulation examples that involve two different vessel types: a pusher-barge inland vessel and a catamaran-type ferry.

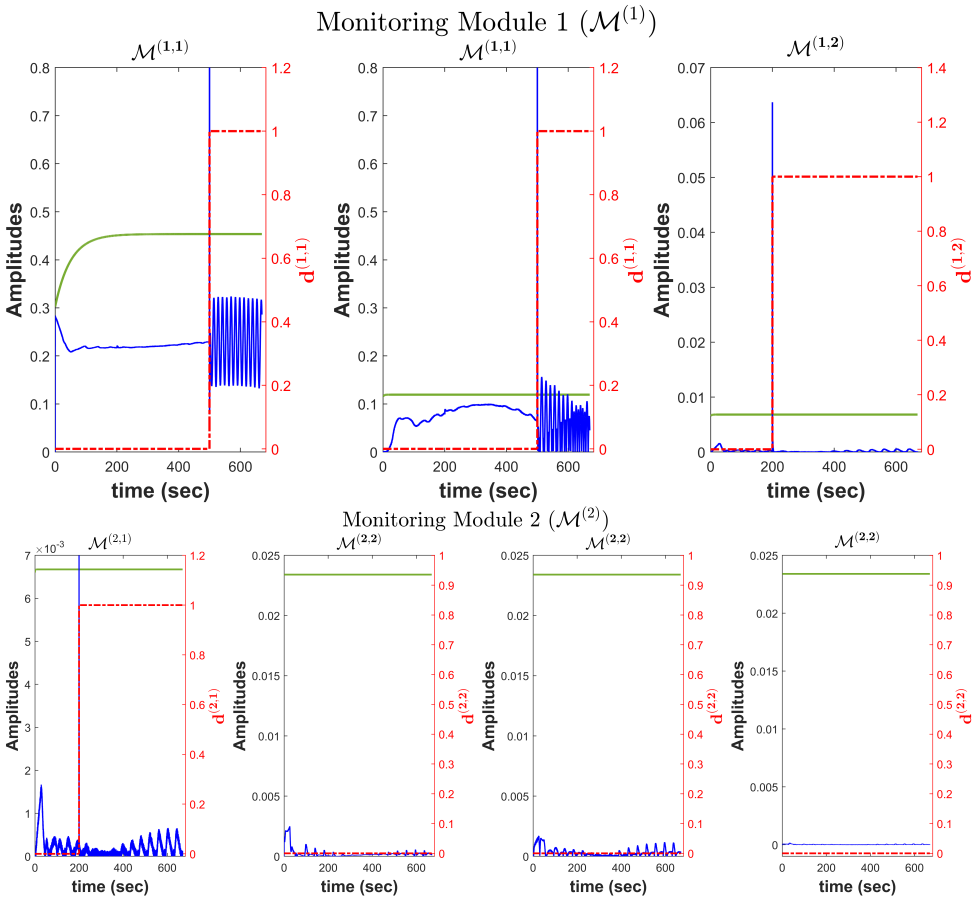

Figure 5.2: Simulation results from Example 1 with the magnitude of residual signals (blue curve), the corresponding adaptive thresholds (green curve), and the decisions (dashed red curve) for the corresponding monitoring modules.

5.3.1 Example 1: TPQR Pusher-Barge System

This section presents simulation results for an 11BP pusher-barge system as studied in [70]. The vessel has full-scale dimensions and is modified to have a twin-propeller and quad rudder (TPQR) actuator configuration for improved maneuverability. Its MMG model parameters, including the hydrodynamic coefficients, are provided in [70, 187].

The vessel is simulated to follow a predefined path in an inland waterway, emulating the practical conditions in a canal with medium-shallow water. Wind conditions are modelled with a velocity of $V = 17$ m/s, corresponding to a value of 7 in the Beaufort scale, and at an angle of $\beta_V = 45°$, coming from the southwest direction. Additionally, the total forward resistance, including the effects of shallow water, is modelled by considering a water depth-to-draft ratio of 1.5. Therefore, the magnitude of the unknown force vector τ_d is equal to $|\tau_d| = (|\tau_w| + |\tau_H|) \leq \bar{\tau}_d$. Three sensors, namely the GNSS, gyrocompass and IMU, are considered on the vessel.

Table 5.2: Parameters for designing the adaptive thresholds for each residual.

Example 1	
Parameters	**Values**
$\rho^{(1,1)}, \rho^{(1,2)}, \rho^{(2,1)}, \rho_d^{(1,1)}, \rho_d^{(1,2)}, \rho_d^{(2,1)}$	0.01
$\xi^{(1,1)}, \xi^{(1,2)}, \xi^{(2,1)}, \xi_d^{(1,1)}, \xi_d^{(1,2)}, \xi_d^{(2,1)}$	0.3
$\rho^{(2,2)}, \rho_d^{(2,2)}$	0.0001
$\xi^{(2,2)}, \xi_d^{(2,2)}$	45
Example 2	
Parameters	**Values**
$\rho^{(1,1)}, \rho^{(2,2)}$	1
$\rho_d^{(1,1)}, \rho_d^{(2,2)}$	10
$\rho_d^{(2,2)}$ *	5
$\xi^{(1,1)}$	1
$\xi_d^{(1,1)}$	9
$\xi^{(2,2)}, \xi_d^{(2,2)}$	5
$\rho^{(4,1)}$	0.01
$\rho_d^{(4,1)}$	1
$\xi^{(4,1)}$	0.3
$\xi_d^{(4,1)}$	0.9

* Corresponding to yaw-rate measurement.

Each sensor is assumed to be corrupted by Gaussian white noise having an amplitude within 3% of the mean absolute value of the noiseless sensor measurement.

For residual generation, the sensor sets $\mathcal{S}^{(1)}$ and $\mathcal{S}^{(2)}$ are considered, with $\mathcal{S}^{(1)}$ containing the GNSS and gyrocompass and $\mathcal{S}^{(2)}$ containing the gyrocompass and IMU. Two monitoring modules $\mathcal{M}^{(I)}, I \in \{1,2\}$, are subsequently designed, based on the measurements obtained from the corresponding sensor sets, the input force vector, and using ARRs as given by Equation (5.57). The fault detection observer gain matrices K_1, K_2, K_4 are taken to be equal to a diagonal matrix diag($\begin{bmatrix}100, & 100, & 100\end{bmatrix}$), and k_3 is equal to 100. Further, the design parameters for the adaptive thresholds in each monitoring module are given in Table 5.2. The theoretical fault signatures used in the aggregator module are provided in Table 5.3, where, $\mathcal{F}_{c_1} = \{f_p\}$, $\mathcal{F}_{c_2} = \{f_\psi\}$, $\mathcal{F}_{c_3} = \{f_v\}$, $\mathcal{F}_{c_4} = \{f_p, f_\psi\}$, $\mathcal{F}_{c_5} = \{f_p, f_v\}$, $\mathcal{F}_{c_6} = \{f_\psi, f_v\}$ and $\mathcal{F}_{c_7} = \{f_p, f_\psi, f_v\}$. An edge case is observed when the aggregated decision vector $\mathbf{d}(t) = \begin{bmatrix}0 & 1 & 1 & 1\end{bmatrix}^T$ is obtained. The resulting diagnosis set is equal to $\mathcal{D}_s(t) = \{\mathcal{F}_{c_6}, \mathcal{F}_{c_7}\}$, implying that the faults f_ψ, f_v have occurred, and that the fault f_p may or may not have occurred. This ambiguity is eliminated when $\mathbf{d}(t) = \begin{bmatrix}1 & 1 & 1 & 1\end{bmatrix}^T$, leading to $\mathcal{D}_s(t) = \mathcal{F}_{c_7}$, thereby isolating all the occurred faults.

A fault scenario is simulated to further verify the proposed FDI method. The simulation is carried out for a total duration of 670 seconds. Permanent faults in the gyrocompass and GNSS sensors are considered to have occurred at $T_{f_\psi} = 200$ secs and $T_{f_p} = 500$ secs, respectively. The

Table 5.3: Example 1 - Sensor fault signature matrix for the aggregator $\mathcal{A}$.

	$\mathcal{F}_{c_1}$	$\mathcal{F}_{c_2}$	$\mathcal{F}_{c_3}$	$\mathcal{F}_{c_4}$	$\mathcal{F}_{c_5}$	$\mathcal{F}_{c_6}$	$\mathcal{F}_{c_7}$
$\mathcal{E}_{y_z}^{(1,1)}$	1	*	0	1	1	*	1
$\mathcal{E}_{y_z}^{(1,2)}$	0	1	0	1	0	1	1
$\mathcal{E}_{y_z}^{(2,1)}$	0	1	1	1	1	1	1
$\mathcal{E}_{y_z}^{(2,2)}$	0	0	1	0	1	1	1

respective fault functions are given by

$$\begin{aligned} f_\psi &= \cup(t - T_{f_\psi})(\mathfrak{a}_{f_\psi} + (1 - e^{-(t-T_{f_\psi})})) \\ f_p &= \cup(t - T_{f_p})(\mathfrak{a}_{f_p} + \sin(0.45t)), \end{aligned} \tag{5.66}$$

where $\cup(t)$ denotes a unit step function, and, $\mathfrak{a}_{f_\psi}$, $\mathfrak{a}_{f_p}$ are fault amplitudes ranging between $1-2$ times the mean absolute values of the noiseless sensor measurement. The time plots of the fault functions and the respective sensor measurements (under healthy and faulty conditions) are shown in Figures 5.4a and 5.4c, respectively. The resulting residual signals and the corresponding adaptive thresholds for the j^{th} sensor monitored by $\mathcal{M}^{(I)}$ are plotted under $\mathcal{M}^{(I,j)}$ in Figure 5.2. As shown, the residuals corresponding to the gyrocompass (in $\mathcal{M}^{(1,2)}$ and $\mathcal{M}^{(2,1)}$), the residuals corresponding to the GNSS (in $\mathcal{M}^{(1,1)}$) exceed the respective thresholds. The fault detection time, which is expressed by (5.58), is equal to $T_D^{(1,1)} = 500.1$ secs, $T_D^{(1,2)} = 200$ secs and $T_D^{(2,1)} = 200.1$ secs, respectively.

For $t < 200$ secs, the aggregated decision vector $\mathbf{d}(t)$'s elements remain zero, and the diagnosis set corresponds to a null set. For $200 \leq t < 500$ secs, the occurrence of the first fault is detected by the residual exceeding the adaptive threshold, resulting in $\mathbf{d}(t) = \begin{bmatrix} 0 & 1 & 1 & 0 \end{bmatrix}^T$. For $t \geq 500$ secs, the second fault is detected, leading to $\mathbf{d}(t) = \begin{bmatrix} 1 & 1 & 1 & 0 \end{bmatrix}$. At the end of the simulation, a consistency test is performed by comparing the observed pattern $\mathbf{d}(t)$ to the theoretical patterns $\mathcal{F}_{c_q}$, which results in a diagnosis set $\mathcal{D}_s(t) = \{\mathcal{F}_{c_2}, \mathcal{F}_{c_4}\} = \{\{f_\psi\}, \{f_p, f_\psi\}\}$, thereby isolating the faulty sensors.

In this section, we consider an example of a catamaran-type passenger ferry to showcase and verify the design of the proposed FDI scheme. The vessel, namely, the Waterbus 2907, is a fully electric water shuttle designed by Damen Shipyards [159], equipped with two azimuth thrusters as well as two bow thrusters (see Figure 3.3). The vessel's maneuvering model is identified using logged data, which includes sensor measurements from onboard GNSS/INS and the propulsion system in various maneuvers performed on the Merwede River. The dynamical model of the vessel and the actuation forces can be expressed using equations (5.7), (5.9), and (3.5), respectively, and its main parameters are mentioned in Table 3.1. For this example, the unknown added force vector is modelled as $\tau_d = \tau_w$, and the wind conditions are considered the same as in Example 1.

The vessel is equipped with an IMU and uses dual GNSS antennas instead of a gyrocompass for heading angle estimation. The fault combinations are given as $\mathcal{F}_{c_1} = \{f_p\}$, $\mathcal{F}_{c_2} = \{f_v\}$, $\mathcal{F}_{c_3} = \{f_\chi\}$, $\mathcal{F}_{c_4} = \{f_p, f_v\}$, $\mathcal{F}_{c_5} = \{f_p, f_\chi\}$, $\mathcal{F}_{c_6} = \{f_v, f_\chi\}$, and $\mathcal{F}_{c_7} = \{f_p, f_v, f_\chi\}$. Further, three residuals are considered, resulting in a fault signature matrix given in Table 5.4. The observer gain matrices are given by the diagonal matrices $K_1 = \text{diag}(\begin{bmatrix} 10 & 10 \end{bmatrix})$, $K_4 = \text{diag}(\begin{bmatrix} 10 & 5 & 5 \end{bmatrix})$,

Table 5.4: Example 2 - Sensor fault signature matrix for the aggregator $\mathcal{A}$.

	$\mathcal{F}_{c_1}$	$\mathcal{F}_{c_2}$	$\mathcal{F}_{c_3}$	$\mathcal{F}_{c_4}$	$\mathcal{F}_{c_5}$	$\mathcal{F}_{c_6}$	$\mathcal{F}_{c_7}$
$\mathcal{E}_{y_z}^{(1,1)}$	1	0	0	1	1	0	1
$\mathcal{E}_{y_z}^{(2,2)}$	0	1	0	1	0	1	1
$\mathcal{E}_{y_z}^{(4,1)}$	1	*	*	1	1	*	1

and $K_6 = \text{diag}(\begin{bmatrix}2 & 10\end{bmatrix})$, respectively. The design parameters for the adaptive thresholds are given in Table 5.2.

The vessel is simulated to perform various maneuvers, including zig-zag and turning, for a duration of 310 secs. A *sensor disconnection* fault is considered, which causes new sensor measurements to be lost, with static measurements received in their place. Such a fault can occur due to an Ethernet failure and can be difficult to distinguish from a stationary or stopping vessel [188]. In this example, a sensor disconnection fault affecting the velocity measurements is simulated at time $T_{f_\nu} = 150$ secs, with the fault evolution function given by

$$f_\nu(t) = \begin{cases} 0 & \text{if } t < T_{f_\nu} \\ \nu(T_{f_\nu}) - \nu(t) & \text{if } t \geq T_{f_\nu} \end{cases}. \tag{5.67}$$

Figure 5.4b shows the time plot of the above fault function. Its impact on the sensor measurements is visualised in Figure 5.4d. The obtained diagnosis results, including the residual signals, adaptive thresholds, and decisions, are shown in Figure 5.3. The fault detection time, which is equal to the instance of violation of the ARR $\mathcal{E}_{y_z}^{(2,2)}$, is given by $T_D^{(2,2)} = 163$ secs and results in an aggregated decision vector equal to $\mathbf{d}(t) = \begin{bmatrix}0 & 1 & 0\end{bmatrix}^T$. Ultimately, the outcome of the consistency test is a diagnosis set $\mathcal{D}_s(t) = \{\mathcal{F}_{c_2}, \mathcal{F}_{c_6}\} = \{\{f_\nu\}, \{f_\nu, f_\chi\}\}$, which leads to the isolation of the faulty IMU sensor. Therefore, the faulty IMU sensor is isolated, whereas a possible fault f_χ is indicated.

5.4 Conclusions

This chapter presented an observer-based FDI scheme for diagnosing multiple faults in the navigational sensors of an ASV. Therefore, the following research question was satisfactorily addressed: **RQ4:** *How to detect and isolate multiple sensor faults affecting the navigational sensors on autonomous surface vessels?*

The proposed scheme effectively addresses challenges associated with modelling complexities, variations in sensor and actuator configurations, and environmental disturbances impacting the ASV. By employing a bank of monitoring modules with structurally sensitive residuals tailored to different vessel dynamics and sensor measurement models, the scheme can diagnose multiple sensor faults. Furthermore, an aggregator module equipped with a combinatorial fault decision logic was designed, enabling the isolation of faulty sensors. Adaptive thresholds were also derived for residual bounding, thereby eliminating false positives and improving diagnostic reliability. Extensive simulations with two different vessel types and sensor setups verify the effectiveness of the proposed scheme, demonstrating that the faults can be isolated across various scenarios.

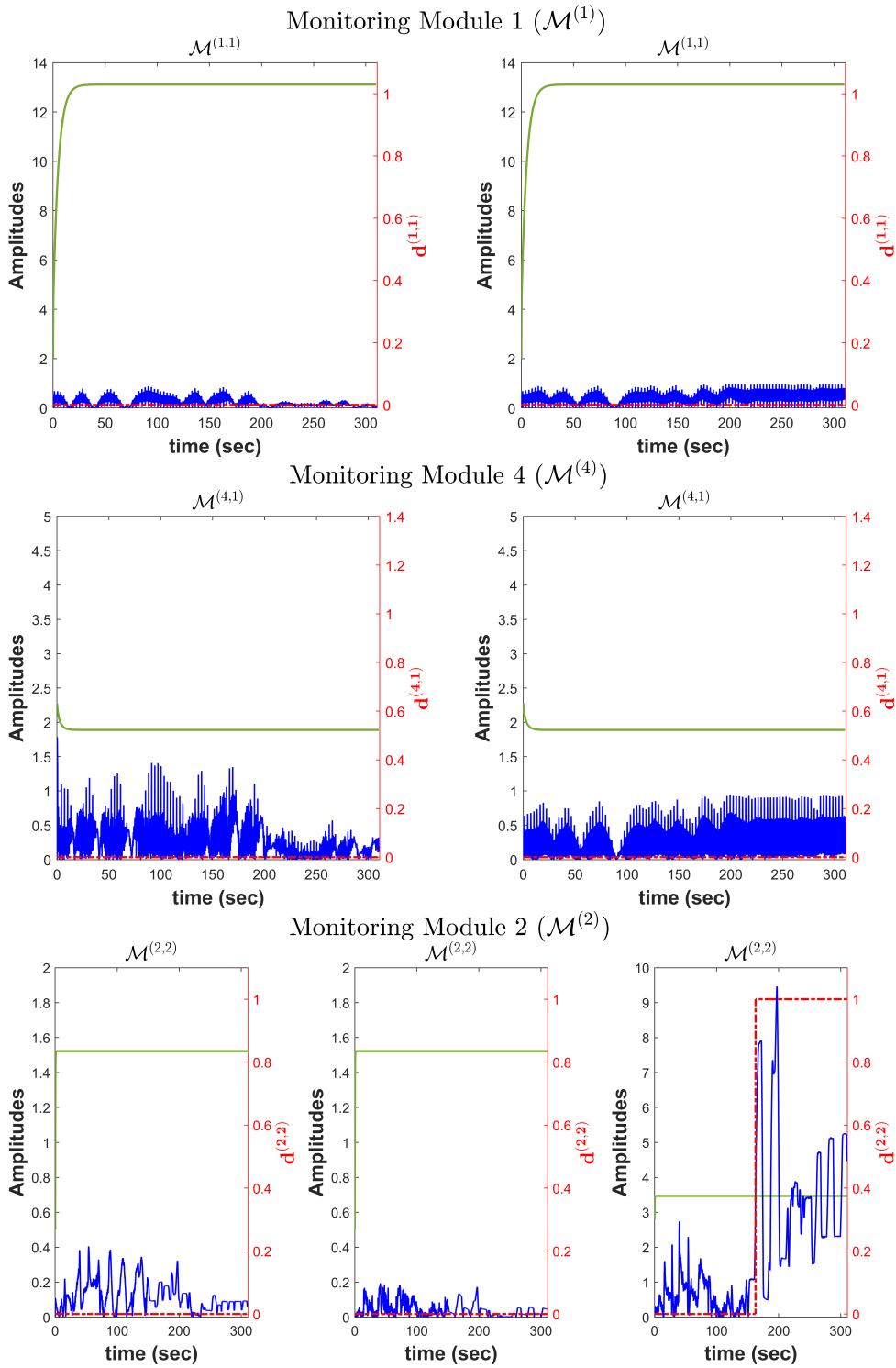

Figure 5.3: Simulation results from Example 2 of the residual signals (blue curve), the corresponding adaptive thresholds (green curve), and the decisions (dashed red curve) for the corresponding monitoring modules.

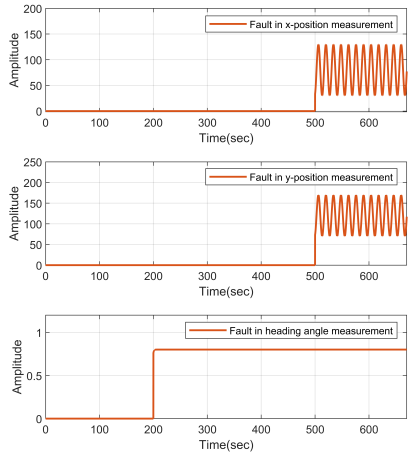

(a) The GNSS and gyrocompass faults in Example 1 (Equation (5.66)).

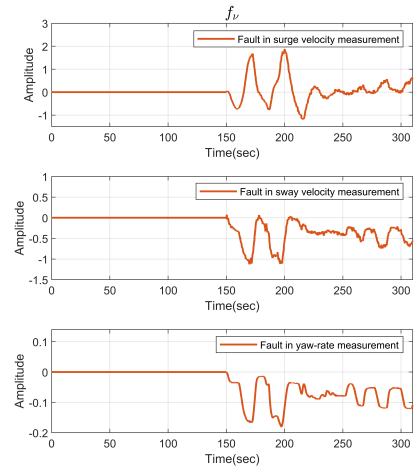

(b) The IMU fault in Example 2 (Equation (5.67)).

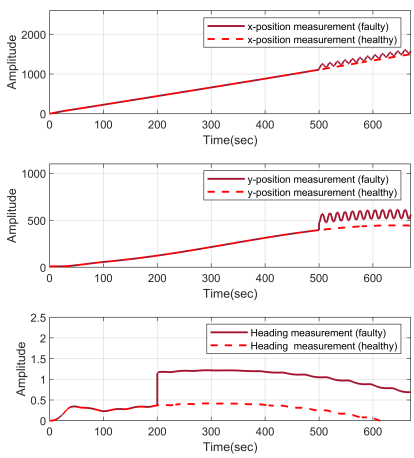

(c) The healthy and faulty sensor measurements in Example 1.

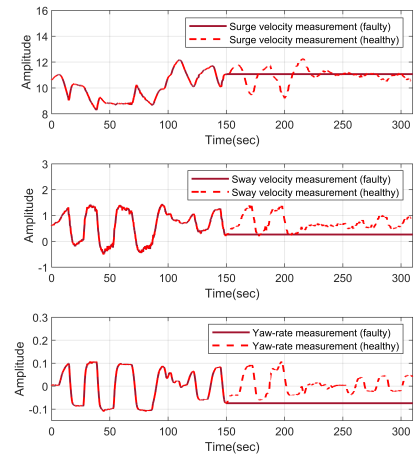

(d) The healthy and faulty sensor measurements in Example 2.

Figure 5.4: Visualisation of the fault functions and the resulting measurements corresponding to Examples 1 and 2.

Chapter 6

Risk-Mitigation for Autonomous Surface Vessels in Inland Waterways

Mathematical rigour is like clothing: in its style it ought to suit the occasion, and it diminishes comfort and restricts freedom of movement if it is either too loose or too tight.

- George F. Simmons

While Chapter 5 addressed the sensor fault diagnosis problem, this chapter considers compounded failures that can compromise the overall system's safety by leading to hazardous situations. A POMDP-based risk-mitigation method for the guidance and control system of an autonomous vessel operating in inland waterways is proposed. This chapter addresses the last research question: **RQ5:** *How can the risk of grounding and collision of autonomous vessels in inland waterways be modelled and mitigated?*

It is organised as follows: In Section 6.1, the ASV risk mitigation problem is formulated. In Section 6.2, the proposed method is described by first modeling the BBN from the STPA hazard analysis results which is used for computing the POMDP state-transition probabilities. Thereafter, the POMDP model is constructed, which computes a safe control strategy (SCS) by complementing unsafe control actions with specific recovery control actions that guide the vessel to a safe state, i.e., a state with minimum risk. In Section 6.3, a case study is presented for an autonomous vessel in an inland waterway scenario. Finally, the conclusions are reported in Section 6.4.

The contents of this chapter have been published in (Dhyani et al., 2024[1]).

[1]**Dhyani, A.**, Wang, Y., Verbeke, M., Pissoort, D. and Reppa, V., 2024. A POMDP model-based online risk mitigation method for autonomous inland vessels. 15th IFAC Conference on Control Applications in Marine Systems, Robotics and Vehicles (CAMS). IFAC-PapersOnLine, 58(20), pp.335-340.

6.1 ASV Risk Mitigation Problem

We consider an inland vessel at automation level 3, as defined by the CCNR, where the vessel's autonomous system is primarily responsible for navigation. However, the human operator *"will be receptive to requests to intervene and to system failures and will respond appropriately"* [189]. The main objective of the POMDP model-based method is to provide risk mitigation support in the form of an SCS. The SCS is updated to avoid two hazardous situations, namely, *collision with another vessel or fixed obstacle* and *grounding of the vessel while navigating in shallow water.*

Firstly, we define the states of the vessel, categorised into three sets: the safe states (S_s), the unsafe states (S_u), and the recovery states (S_r). The safe states S_s refer to vessel states in which there are no hazardous situations. This conforms with the ISO/IEC Guide 51:2014, which defines safety as *freedom from risk which is not tolerable* [190]. On the other hand, unsafe states S_u correspond to states with a high risk of a hazardous situation. The recovery states S_r correspond to the intermediary set of states resulting from applying a corrective measure to eliminate the risk of a hazardous situation. Similarly, we define three sets of actions performed by the vessel's control system, namely the safe (A_s), unsafe (A_u), and recovery (A_r) control actions. A_s is defined as the set of actions that constitute the vessel control system's primary function(s) (often referred to as the "control responsibilities" in the STPA terminology), and ensure that the vessel stays in a safe state. When the control system executes an unsafe action A_u, it increases the level of risk as the system transitions to an unsafe state. Finally, A_r corresponds to the recovery control actions applied to bring the system from an unsafe state to a safe state. In this work, we define the safe control action/control responsibility as:
A_{s_1} : Provide the rudders and thruster (R & T) commands for the steering and propulsion of the vessel to execute the planned path.

With regard to A_{s_1}, the following states of the vessel are of interest:

1. Safe states:
   (a) S_{s_1} : The navigational plan is successfully obtained
   (b) S_{s_2} : Vessel follows the desired path
2. Unsafe states:
   (a) S_{u_1} : Vessel does not follow the desired path
   (b) S_{u_2} : Vessel violates the safety margin
   (c) S_{u_3} : Vessel enters a shallow water-depth area
   (d) S_{u_4} : Desired control is not achieved / collision or grounding risk is not averted
3. Recovery states:
   (a) S_{r_1} : Updated control action corrects the vessel's path and averts the risk
   (b) S_{r_2} : A human supervisor corrects the vessel's path

When the action A_{s_1} is executed, it leads the vessel to the safe state S_{s_2}. Subsequently, by performing an STPA, the unsafe actions (A_u) that could lead the vessel to an unsafe state

Table 6.1: Unsafe control actions (A_u) originating from the control responsibility A_{s_1}

Control responsibility provided	**Control responsibility not provided**	**Control responsibility provided too early /too late**
A_{u_1}: R&T commands provided based on incorrect vessel's navigational states	A_{u_2}: R&T commands are not provided as the vessel's navigational states are unknown	A_{u_3} : R&T commands are provided too late as the guidance system provides a path update too late
A_{u_4} : R&T commands provided cannot be followed due to insufficient available power	A_{u_5} : R&T commands are not provided as there are no feasible path options	
A_{u_6} : R&T commands are provided without considering the effect of external disturbance, such as wind, water depth, etc.		
A_{u_7} : R&T commands provided violate vessel's give-way obligations		

are identified. These actions are obtained by considering A_{s_1} together with four generic types of unsafe control actions, and are described in Table 6.1. Unlike traditional hazard analysis methods, STPA's systems-thinking approach can help capture emerging risks from complex interactions among system components [191].

Finally, the recovery control actions (A_r) are defined, constituting the set of possible SCSs to direct the vessel to an MRC. These actions correspond to either the fail-safe or fail-operational actions and must be selected based on the vessel's assessment of the existing risk. Based on class guidelines recommended by classification societies such as DNV [139], ClassNK [192], and similar fallback strategies proposed in the literature (for example, in [193]), a total of six recovery control actions are identified, as mentioned below:

1. A_{r_1} : Limp home
2. A_{r_2} : Fault-tolerant control strategy is selected
3. A_{r_3} : Keep position
4. A_{r_4} : Human supervision is requested
5. A_{r_5} : Move away from the quay and other vessels
6. A_{r_6} : Vessel's speed is reduced

These actions can be further categorised as follows:

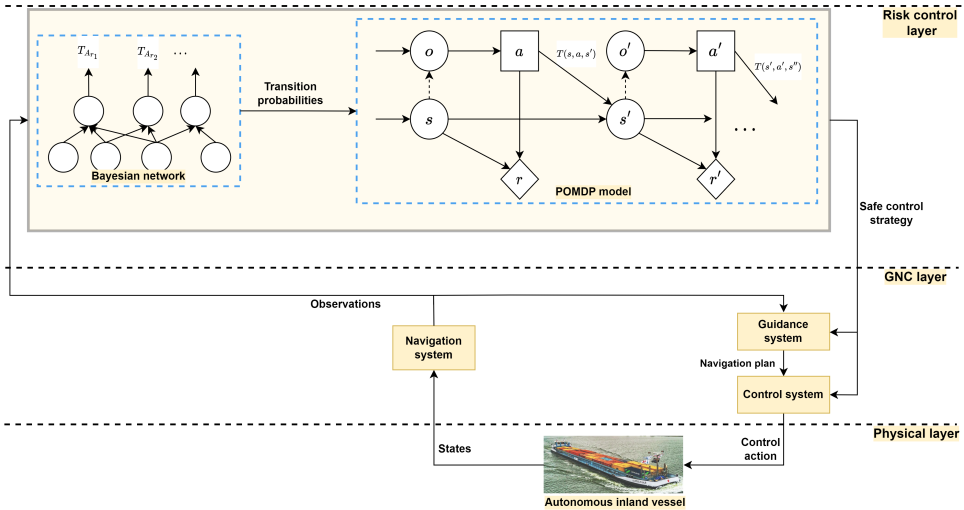

Figure 6.1: Block diagram representation of the proposed online risk mitigation method for ASVs. For the BBN, the observations comprise the inputs from various onboard sensors, devices, metocean services, etc. (see Table 6.2 for the complete list of input sources). Further, the POMDP model receives noisy vessel states as observations, along with the transition probabilities from the BBN. The output of the BBN-POMDP risk mitigation method is a Safe Control Strategy (SCS), selected from the set of recovery control actions (A_r).

1. Fail-operational strategies: A_{r_2}, A_{r_4}, and A_{r_6}
2. Fail-safe strategies: A_{r_1}, A_{r_3}, and A_{r_5}

The fail-operational strategies provide path planning and control updates that enable the vessel to maintain operations, albeit with possibly reduced performance. In contrast, the fail-safe strategies guide the vessel to a safe state and cease its operations. The selection of the SCS is performed by the proposed risk-mitigation method, which is described in the next section.

6.2 Risk Mitigation Method

Figure 6.1 provides an overview of the proposed risk mitigation method for ASVs. The vessel's control system can execute any one of the unsafe actions (A_u) identified in Table 6.1. These unsafe actions form part of the set of actions of the POMDP model, along with the set of recovery control actions (A_r). Additionally, the vessel's states (S_s, S_u, S_r) are used to construct the POMDP model's states. The transition probabilities for the model are calculated from the BBN output and the posterior probabilities, which it infers from various input sources. The output of the POMDP model is the appropriate SCS to mitigate the risk of a hazardous situation. The overall steps involved in the proposed risk mitigation method are summarised in Algorithm 6.1. The steps 1–3 of the algorithm, which involve the BBN, are detailed next.

Algorithm 6.1 Computation of the safe control strategy (SCS) for ASV risk mitigation.

Input: BBN inputs, Observations $\mathscr{O}$, Rewards $\mathscr{R}$
Parameters: Discount factor γ, Initial belief b_0, Maximum iterations N_{sim}, Particle count, UCB exploration coefficient C
Bayesian Belief Network:
Compute the probabilities of input RIFs based on the BBN inputs.
Compute the recovery action activation probabilities (using equation (6.1)) and the hazard risk indicators (using equations (6.2), (6.3)) by propagating through the BBN layers.
Calculate the transition function $\mathscr{T}$ using the BBN outputs and hazard risk indicators.
POMDP Model Initialisation:
Initialise the state space $\mathscr{S}$, action space $\mathscr{A}$, observations $\mathscr{O}$, and rewards $\mathscr{R}$.
Set the discount factor γ, particle count, UCB exploration coefficient C, and initial belief b_0.
Online Planning (MCTS Algorithm):
Initialize the tree with the current belief as the root node.
while no. of iterations $< N_{\text{sim}}$, **do**
Select the optimal node using the UCB formula, given by equation (6.4).
Expand the selected node by adding a child node.
Simulate a random playout from the child node.
Backpropagate the result of the playout through the tree to update the Q-value.
end while
SCS Calculation:
Compute the SCS by using equation (6.5).
Output: SCS $\in \{A_{r_1}, \ldots, A_{r_6}\}$

6.2.1 Bayesian Belief Network (BBN)

A BBN is a graphical method that employs a directed acyclic graph for probabilistic reasoning. It comprises various nodes representing the variables of interest, for which the respective probabilities are computed using Bayesian reasoning. The BBN is designed to compute transition probabilities for the POMDP model using inputs from various meteorological and communication sources, including onboard sensors, AIS, electronic navigational charts (ENC), metocean services, and sensor monitoring modules. The BBN structure follows the supervisory risk control (SRC) framework of [142, 194], extended to cover both grounding and collisions. The overall structure is visualised in Figure 6.2. It comprises 36 nodes organised into four hierarchical layers: (i) input nodes, (ii) input risk influence factors (RIFs), (iii) derived RIFs, and (iv) recovery actions. A total of 17 input nodes (I1-I17) were identified. These nodes are described in Table 6.2, along with their states and the sources used to determine them. The nodes I1-I7 cover the vessel's sensing and maneuvering capacity and assume that the health of the underlying equipment can be determined in real time using monitoring modules, sensor metadata, etc. The nodes I8-I11 and I15 capture environmental characteristics crucial for safe navigation in inland waterways. Further, nodes I12 and I13 capture the nearby vessel traffic, using AIS and/or Radar data. Notably, two collision metrics, namely the Time to Closest Point of Approach (TCPA) and the Closest Point of Approach (CPA), are also included as input nodes (I16, I17). TCPA measures the time remaining until the vessel pair reaches its geometrically closest approach, whereas CPA is the minimum distance between two vessels at any instant if neither changes its course. Together, these two metrics help identify a collision course and ensure that an action is taken in ample time [195].

The second layer of the BBN consists of nodes representing the input RIFs, each of which is associated with a conditional probability table (CPT) computed from the aforementioned input

Table 6.2: The input nodes of the BBN, with their respective states and input sources

Input Node	States	Source
I1: GNSS Health	Reliable / Degraded / Failed	GNSS Dilution of Precision (DOP), Active Satellites, Carrier-to-Noise Density ratio (C/N0), Fault and Integrity Monitor
I2: IMU Health	Reliable / Degraded / Failed	IMU Consistency Check, Fault and Integrity Monitor
I3: Depth Sensor Health	Reliable / Failed	Echo Sounder Health Monitor
I4: AIS Health	Reliable / Failed	AIS Health Monitor
I5: Communication Link	Healthy / Broken	Link Status Monitor
I6: Thruster State	Ok / Degraded / Failed	Thruster Feedback Monitor
I7: Steering State	Ok / Failed	Rudder Feedback Monitor
I8: Weather	Light / Moderate / Rough	Anemometer, Metocean Data
I9: Current Velocity	Low / Medium / High	Current Sensor, Metocean Data
I10: Water Depth	Safe ($>2\times$draft) / Moderate ($1-2\times$ draft) / Shallow ($<1\times$ draft)	ENC, Echo Sounder
I11: Distance to Shallow Waters	Far (>500 m) / Moderate ($100-500$ m) / Near (<100 m)	ENC
I12: Traffic Density	Low / Medium / High	AIS, Radar
I13: Number of Obstacles	Few / Moderate / Many	AIS, Radar (within 1400 m radius)
I14: Vessel Speed	Low (<3 kn) / Medium ($3-8$ kn) / High (>8 kn)	IMU, Speed Log
I15: Waterway Geometry	Open / Moderate / Confined	ENC
I16: TCPA	Safe (>5 min) / Moderate ($1-5$ min) / Critical (<1 min)	AIS, GNSS, IMU
I17: CPA	Safe (>200 m) / Near-Miss ($50-200$ m) / Danger (<50 m)	AIS, GNSS, IMU

Table 6.3: The input RIFs with their respective parent nodes and states

Input RIFs	Parents	States
INT1: Sensor Fusion Quality	I1, I2, I4	Good / Sufficient / Poor
INT2: Propulsion Availability	I6, I7	Full / Degraded / Failed
INT3: Environmental Severity	I8, I9	Low / Medium / High
INT4: Navigational Complexity	I10, I11, I12, I13, I14, I15	Low / Medium / High
INT5: Collision Threat	I16, I17, I12, I13	Low / Medium / High
INT6: Grounding Threat	I10, I11, I15	Low / Medium / High

Table 6.4: The derived RIFs with their respective parent nodes and states

Derived RIFs	Parents	States
D1: Connectivity	I5	Ok / Failed
D2: Safe Navigational Options	INT3, INT4	Available / Limited / None
D3: State Estimation Quality	INT1, INT3	Correct / Imprecise / Incorrect
D4: Trajectory Tracking Performance	INT1, INT2, INT3, I14	Good / Sufficient / Poor
D5: Propulsion Capacity	INT2	Full / Degraded / Failed
D6: Grounding Risk	INT6, I3	Low / Medium / High
D7: Collision Risk	INT5, INT1	Low / Medium / High

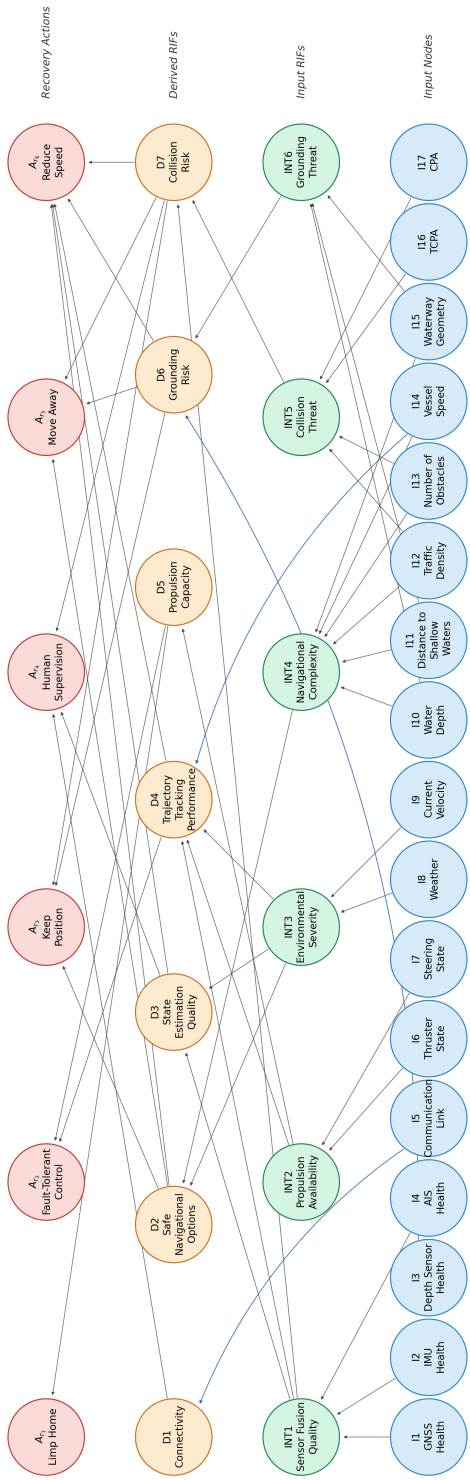

Figure 6.2: Proposed structure of the BBN for computing the POMDP model's transition probabilities.

nodes. By aggregating functionally related input nodes, these input RIFs reduce the complexity of CPTs for the downstream nodes. In this work, we consider six input RIFs (INT1–INT6), namely, Sensor Fusion Quality, Propulsion Availability, Environmental Severity, Navigational Complexity, Collision Threat, and Grounding Threat. The states and parent nodes for each of these nodes are listed in Table 6.3. Similarly, the third layer contains seven nodes (D1-D7) representing the derived RIFs, namely, Connectivity, Safe Navigational Options, State Estimation Quality, Trajectory Tracking Performance, Propulsion Capacity, Grounding Risk, and Collision Risk. These nodes represent the vessel's functional risk state along distinct causal dimensions. Table 6.4 lists the parents corresponding to each node in this layer and their various states.

Finally, the derived RIFs are mapped to the output layer, which comprises six recovery action nodes $(A_{r_1} - A_{r_6})$, where each node outputs an activation probability $P_{A_{r_i}}$ such that

$$P_{A_{r_i}} = P(A_{r_i} = \text{High}), \quad A_{r_i} \in A_r;\ i = 1, \ldots, 6. \tag{6.1}$$

An edge exists between the nodes in these two layers if the corresponding recovery action can lead to a transition to a safe state for the derived RIF. Unlike many existing BBN risk models that terminate at a loss node (e.g., [141, 196, 197]), the proposed model terminates at multiple recovery nodes, thereby preserving distinguishable actions rather than collapsing into a single quantity. From the BBN's derived RIF posteriors, the following hazard risk indicators can also be defined:

$$\rho_{\text{grd}} = P(\text{D6} = \text{High}) \quad \text{(Grounding Risk)} \tag{6.2}$$

$$\rho_{\text{col}} = P(\text{D7} = \text{High}) \quad \text{(Collision Risk)} \tag{6.3}$$

These indicators quantify the relative likelihood of the two hazardous situations when a recovery action fails.

Prior Probabilities Selection

The prior probabilities are selected using a combination of the following sources: (i) equipment reliability databases, (ii) empirical vessel encounter and collision statistics, (iii) operational area statistics, and (iv) expert elicitation where published data is insufficient. The selected values reflect the operational profile of European inland waterways, and the thresholds for state-discretisation are based on regulatory standards (such as those of CCNR). For the input nodes, the prior probability distributions represent the unconditional probabilities for each observed variable and are summarised in Table 6.5, including their primary references. For nodes representing onboard equipment health (I1-I7), the primary sources are reliability databases from SINTEF/DNV GL [198]. Further, the environmental, bathymetric and traffic priors (I8-I15) are based on expert elicitation for the Rhine/Danube operational profile. Finally, for encounter frequencies and thresholds used to determine the nodes I16 and I17, published statistics are utilised [146, 194].

To construct the CPTs of the input and derived RIF layer nodes, a combination of sources is employed. For the nodes with many parent combinations (INT4, INT5, INT6, D4), a weighted-risk-score approach is used, where a scalar risk score is computed as a weighted sum of the normalised parent states [141, 199]. This value is further mapped to a probability distribution through a sigmoid transition function. This approach significantly reduces the elicitation burden to a small set of weights and transition thresholds. In the recovery actions layer, the node A_{r_6}

Table 6.5: Prior probability distributions for the input nodes

Input Node	State 1	State 2	State 3	Primary References
I1: GNSS Health	0.93 (Reliable)	0.05 (Degraded)	0.02 (Failed)	[198]; [146]; [201]
I2: IMU Health	0.95 (Reliable)	0.04 (Degraded)	0.01 (Failed)	[198]; [146]; [201]
I3: Depth Sensor Health	0.97 (Reliable)	0.03 (Failed)	—	[198]; [201]
I4: AIS Health	0.95 (Reliable)	0.05 (Failed)	—	[146]
I5: Communication Link	0.95 (Healthy)	0.05 (Broken)	—	[146]
I6: Thruster State	0.985 (OK)	0.012 (Degraded)	0.003 (Failed)	[198]; [146]
I7: Steering State	0.998 (OK)	0.002 (Failed)	—	[198]; [146]
I8: Weather	0.50 (Light)	0.35 (Moderate)	0.15 (Rough)	Expert judgement
I9: Current Velocity	0.45 (Low)	0.40 (Medium)	0.15 (High)	Expert judgement
I10: Water Depth	0.70 (Safe)	0.20 (Moderate)	0.10 (Shallow)	Expert judgement; [194]
I11: Distance to Shallow Waters	0.60 (Far)	0.25 (Moderate)	0.15 (Near)	Expert judgement; [194]
I12: Traffic Density	0.40 (Low)	0.40 (Medium)	0.20 (High)	[194]
I13: Number of Obstacles	0.50 (Few)	0.35 (Moderate)	0.15 (Many)	[194]
I14: Vessel Speed	0.30 (Low)	0.50 (Medium)	0.20 (High)	Operational profile assumption
I15: Waterway Geometry	0.40 (Open)	0.35 (Moderate)	0.25 (Confined)	Expert judgement; [194]
I16: TCPA	0.70 (Safe)	0.25 (Moderate)	0.05 (Critical)	[146]
I17: CPA	0.82 (Safe)	0.15 (Near-Miss)	0.03 (Danger)	[194]

is the most broadly applicable recovery action with five parent nodes. It is therefore modelled using a noisy-OR structure, where any parent with elevated risk can independently trigger speed reduction [200]. The CPT construction for all the remaining non-input nodes relies on direct elicitation and uses the references [136, 141, 146, 194, 201]. The CPT elicitation method for all non-input nodes, including their primary references, is summarised in Table 6.6.

6.2.2 Partially Observable Markov Decision Process (POMDP) Modeling

This section describes the finite-state, discrete POMDP model, which is constructed to represent the states and actions relevant for the risk mitigation of an ASV. The POMDP framework facilitates sequential decision-making in an environment characterised by noise and uncertainty, where only a partial view of the system's state is available. Instead of having access to precise state information, the model can deal with potentially imperfect observations. The model is defined as a tuple $\mathcal{P} = \langle \mathcal{S}, \mathcal{A}, \mathcal{T}, \mathcal{R}, \Omega, \mathcal{O}, \gamma \rangle$, where $\mathcal{S}$ denotes the state space of the POMDP model given by $\mathcal{S} = \{s_1, s_2, \ldots, s_n\}$, for n vessel states. The state space is further partitioned into the previously identified set of states, such that $\mathcal{S} = \{S_u, S_r\}$. To simplify the POMDP model, we consider only the unsafe and recovery states, since only these are involved in the risk mitigation process. An action space can be defined as a finite set, given by $\mathcal{A} = \{a_1, a_2, \ldots, a_m\}$, with m representing the total number of actions. It corresponds to the actions performed by the vessel control system that lead the vessel to another state. To highlight the new state resulting from performing a specific action, a similar partitioning of the action space is performed such that $\mathcal{A} = \{A_u, A_r\}$. Further, $\mathcal{T}$ represents the transition function, which comprises the probability of transitioning to a state given the current state and an action, defined as $\mathcal{T} : \mathcal{S} \times \mathcal{A} \times \mathcal{S} \to [0,1]$. $\mathcal{R}$ represents the reward function used to favor certain actions over others, defined as $\mathcal{R} : \mathcal{S} \times \mathcal{A} \times \mathcal{S} \to \mathbb{R}$. $\mathcal{O}$ is the finite set of observations, and Ω is an observation function that is used to capture the uncertainty in determining the current

Table 6.6: Method used for CPT elicitation for the non-input nodes

Node	**CPT Method**	**Primary References**
INT1: Sensor Fusion Quality	Direct elicitation	[141]; [146]
INT2: Propulsion Availability	Direct elicitation	Design rule; [146]
INT3: Environmental Severity	Direct elicitation	Expert judgement; [146]
INT4: Navigational Complexity	Weighted-risk-score	[141]; [194]
INT5: Collision Threat	Weighted-risk-score	[146]; [194]
INT6: Grounding Threat	Weighted-risk-score	[141]
D1: Connectivity	Direct elicitation	Design rule
D2: Safe Navigational Options	Direct elicitation	[146]
D3: State Estimation Quality	Direct elicitation	[146]; [141]
D4: Trajectory Tracking Performance	Weighted-risk-score	[146]; [194]
D5: Propulsion Capacity	Direct elicitation	Design rule
D6: Grounding Risk	Direct elicitation	[201]; [141]
D7: Collision Risk	Direct elicitation	[201]; [141]; [146]
A_{r_1}	Direct elicitation	[146]
A_{r_2}	Direct elicitation	[146]
A_{r_3}	Direct elicitation	[146]
A_{r_4}	Direct elicitation	[146]; [136]
A_{r_5}	Direct elicitation	[146]; [136]
A_{r_6}	Noisy-OR	[141]

state, defined as $\Omega : \mathscr{S} \times \mathscr{A} \times \mathscr{O} \to [0,1]$. Finally, $\gamma \in [0,1]$ is the discount factor used to consider the importance of future rewards. The initialisation of the aforementioned properties of the POMDP model and other simulation-related parameters forms steps 4-5 of Algorithm 6.1.

Throughout the decision-making process, a posterior distribution over the potential states is maintained and continually updated by utilising the actions taken and observations gathered, referred to as the belief state $b(s)$. In the MCTS algorithm, a tree of possible actions and the resulting observations is constructed, guided by the Upper Confidence Bound (UCB) formula given by

$$\text{UCB} = Q(b,a) + C\sqrt{\frac{\ln N(b)}{n(b,a)}}, \tag{6.4}$$

where for each belief node b in the tree, $N(b)$ is the total visit count, $n(b,a)$ is the visit count of action a, and $Q(b,a)$ represents the expected cumulative reward for taking action a. Further, C is the exploration parameter. By using this action-selection formula, the MCTS algorithm balances exploration and exploitation to build a tree that represents possible outcomes and their values [202]. Finally, an optimal action is selected based on the maximum expected reward and forms the SCS, calculated as

$$\text{SCS} = \arg\max_{a \in A_r} Q(b,a). \tag{6.5}$$

The expected cumulative reward $Q(b,a)$ can be mathematically formulated using the Bellman equation as follows

$$Q(b,a) = \sum_{s \in \mathscr{S}} b(s) \sum_{s' \in \mathscr{S}} \mathscr{T}(s,a,s') \left[\mathscr{R}(s,a,s') + \gamma \sum_{o \in \mathscr{O}} \Omega(s',a,o) V(b'_{a,o}) \right], \tag{6.6}$$

where $V(b'_{a,o})$ represents the value function at the belief state b'. The vessel's guidance and control systems can adapt to the identified SCS by switching between various operational modes. The design of the switching logic, however, lies beyond the scope of this work. The MCTS algorithm and the SCS calculation process are outlined in steps 6–11 of Algorithm 6.1.

POMDP Transition Probabilities and Rewards

Next, to construct the POMDP's transition function $\mathscr{T}$, the mapping from the BBN's outputs to the POMDP transition probabilities is formalised. This is done by utilizing the recovery action activation probabilities (given by equation (6.1)) and the hazard risk indicators (given by equations (6.2),(6.3)) computed by the BBN. For each unsafe state $s_u \in S_u$, and recovery action $A_{r_i} \in A_r$, the probability of transition to a recovery state $s_{r_j} \in S_r$, is directly given by the recovery node probability, i.e.,

$$\mathscr{T}(s_u, A_{r_i}, s_{r_j}) = P_{A_{r_i}}, \quad j \in \{1,2\}. \tag{6.7}$$

Further, to determine the transition probability to an unsafe state, firstly, let's define a normalisation constant Z such that

$$Z = \rho_{\text{grd}} + \rho_{\text{col}} + \varepsilon, \tag{6.8}$$

where $\varepsilon > 0$ is a small constant representing a residual probability. Thereafter, the transition probability from a first-level unsafe state (S_{u_1}), to other unsafe states can be given by distributing

the failure probability value across each transition, such that

$$\begin{aligned}\mathscr{T}(S_{u_1},A_{r_i},S_{u_2}) &= (1-P_{A_{r_i}})\frac{\rho_{\text{col}}}{Z},\\ \mathscr{T}(S_{u_1},A_{r_i},S_{u_3}) &= (1-P_{A_{r_i}})\frac{\rho_{\text{grd}}}{Z},\\ \mathscr{T}(S_{u_1},A_{r_i},S_{u_4}) &= (1-P_{A_{r_i}})\frac{\varepsilon}{Z}.\end{aligned} \tag{6.9}$$

Finally, the transition probability to a terminal unsafe state (S_{u_4}) from a hazard-specific state (S_{u_2}, S_{u_3}) is given by

$$\begin{aligned}\mathscr{T}(S_{u_2},A_{r_i},S_{u_4}) &= 1-P_{A_{r_i}},\\ \mathscr{T}(S_{u_3},A_{r_i},S_{u_4}) &= 1-P_{A_{r_i}}.\end{aligned} \tag{6.10}$$

Regarding the rewards structure, transitions to fail-safe vessel states resulting from fail-safe control actions (A_{r_1}, A_{r_3}, A_{r_5}) are assigned lower rewards compared to those leading to a fail-operational state. Further, a state transition on taking the action A_{r_4} is allocated a smaller reward than for the rest of the fail-operational control actions. This approach is adopted to discourage excessive dependence on remote or onboard crew intervention. Finally, a transition that keeps the vessel in the same unsafe state in the subsequent time step incurs a minor penalty to promote proactive risk mitigation.

6.3 Case study: Risk Mitigation for an Inland Waterway Scenario

In this section, a case study illustrates the proposed method for an autonomous inland vessel navigating through constrained waterways. The considered scenario is detailed next.

6.3.1 Description of the Scenario

An autonomous vessel operating at CCNR automation level 3 is again considered. The vessel is navigating a moderately constrained inland waterway (e.g., a section of the Rhine with moderate channel geometry) at standard cruising speed. This case study focuses on the unsafe control action A_{u_1}, which arises from a fault in the onboard GNSS sensor and is diagnosed by the vessel's sensor monitoring module. Concurrently, rough weather conditions and moderate nearby traffic prevail. All other conditions are assumed to be in a moderate or medium state. The scenario is analysed in two phases:

- Phase 1 (Before fault occurrence): The GNSS sensor is operating normally. Based on the various GNSS integrity sources, the sensor's health is reported to be *Reliable*.
- Phase 2 (After fault detection): A severe fault develops in the GNSS sensor and is diagnosed by the vessel's sensor monitoring module. The sensor's health is flagged as *Failed*.

The environmental and traffic conditions remain unchanged between the two phases. When the new evidence corresponding to the Phase 2 is applied, the BBN performs forward inference

Table 6.7: The computed recovery action activation probabilities for Phases 1 and 2 of the considered scenario

Recovery Action Probability	$P_{A_{r_1}}$	$P_{A_{r_2}}$	$P_{A_{r_3}}$	$P_{A_{r_4}}$	$P_{A_{r_5}}$	$P_{A_{r_6}}$
Phase 1	0.0984	0.2580	0.9037	0.6472	0.6687	0.8465
Phase 2	0.0984	0.3921	0.9221	0.8988	0.7070	0.9058

Table 6.8: The transition probabilities and rewards for the POMDP model for the given scenario

Current state s	**Action** a	**Next state** s'	$\mathscr{R}$	$\mathscr{T}$
S_{u_1}	A_{r_1}	S_{r_1}	+5	0.0984
	A_{r_1}	S_{u_2}	-5	0.5507
	A_{r_1}	S_{u_3}	-5	0.3055
	A_{r_2}	S_{r_1}	+10	0.3921
	A_{r_2}	S_{u_2}	-5	0.3713
	A_{r_2}	S_{u_3}	-5	0.2060
S_{u_2}	A_{r_3}	S_{r_1}	+5	0.9221
	A_{r_3}	S_{u_4}	-50	0.0779
	A_{r_4}	S_{r_2}	+3	0.8988
	A_{r_4}	S_{u_4}	-50	0.1012
	A_{r_5}	S_{r_1}	+5	0.7070
	A_{r_5}	S_{u_4}	-50	0.2930
S_{u_3}	A_{r_4}	S_{r_2}	+3	0.8988
	A_{r_4}	S_{u_4}	-50	0.1012
	A_{r_6}	S_{r_1}	+10	0.9058
	A_{r_6}	S_{u_4}	-50	0.0942
any state	any action	same state	-1	-

through its four-layer structure. The resulting activation probabilities for the six recovery action nodes are as shown in Table 6.7. Notably, the GNSS fault increases the activation probabilities of the nodes $A_{r_2} - A_{r_6}$. Based on the BBN's outputs, the obtained POMDP transition probabilities are shown in Table 6.8. Furthermore, the reward values, which are based on the design criterion described in the previous section, are also listed.

6.3.2 Simulation Results

The results of the POMDP model-based simulation experiments are presented next to identify the SCS that mitigates the hazardous situation. The model is initialised in the unsafe state S_{u_1} (root node) resulting from taking the unsafe action A_{u_1}, and the simulation runs until a terminal state is reached. The observations are modeled as states with an additional noise component, assuming a 5% probability of receiving a false observation. Further, the initial belief (b_0) is set as the state S_{u_1} with a 90% probability. The discount factor (γ) is selected to be equal to 0.95.

The POMCP (Partially Observable Monte-Carlo Planning) solver [203] is used for implementing the MCTS algorithm, and is initialised with particles in the range of $[1000, 2000]$. The experiment runs for 20 epochs, with each epoch consisting of 1000 simulation runs performed

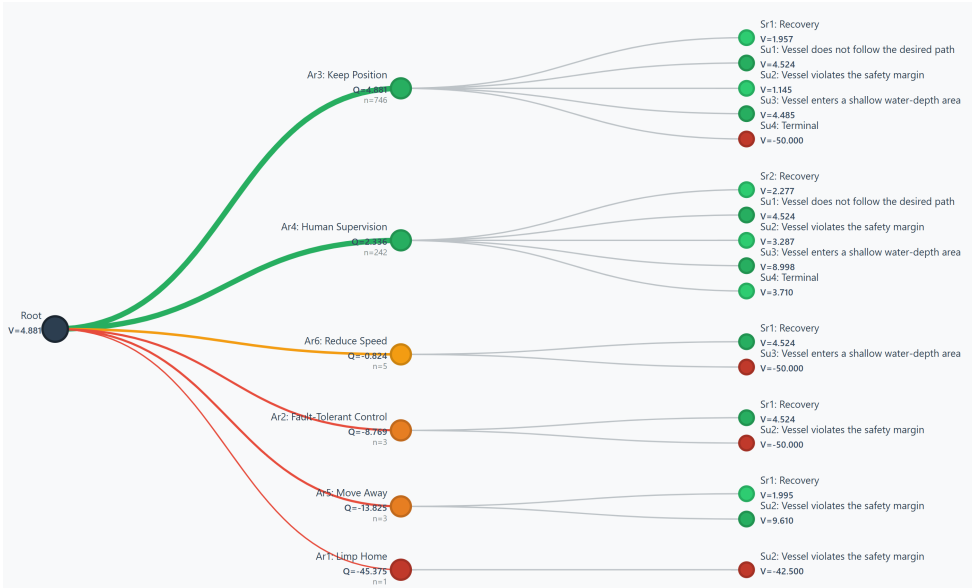

Figure 6.3: The POMDP decision tree obtained after 1000 Monte Carlo simulations

Table 6.9: Summary of the testing phase results over 20 epochs.

S. No.	Initial state	Intermediate action	Final state	Scenario count	Epochs taken
1.	S_{u_1}	A_{r_6}	S_{r_1}	14	1 step
2.	S_{u_1}	A_{r_3}	S_{r_1}	4	1 step
3.	S_{u_3}	A_{r_6}	S_{r_1}	1	1 step
4.	S_{u_1}	A_{r_6}	S_{u_4}	1	1 step

to compute the Monte Carlo decision tree starting from the given initial belief. After each epoch, the belief of states and the search tree are updated. The POMCP search tree results after the first epoch are depicted in Figure 6.3, with the most desirable actions (corresponding to the highest expected cumulative rewards $Q(b,a)$) shown in green color. In this epoch, the actions A_{r_3} and A_{r_4} yield the highest values $(Q(b_0,A_{r_3}) = 4.881, Q(b_0,A_{r_4}) = 2.336)$. The figure also highlights the expected cumulative values for each belief node $(V(b))$. For the root node, this value is equal to $V(b_0) = 4.881$, corresponding to the action A_{r_3}.

In 19 out of 20 testing epochs, the vessel recovers to the recovery state (S_{r_1}) in a single decision step, whereas in 1 epoch it ends up in an unsafe state (S_{u_4}), yielding a recovery rate of 95%. Notably, one epoch starts in (S_{u_3}) due to the initial belief allocation, and is recovered through an appropriate recovery action selection. The results from the testing phase, including the intermediate action taken, are summarised in Table 6.9.

Based on the simulation results, the SCS identified for each unsafe state and the corresponding single-step expected reward are as shown in Table 6.10. The solver identifies A_{r_6} as the primary SCS for all three unsafe states, with Ar_3 as the secondary SCS. Although S_{u_2} was not reached in any epoch, this is confirmed analytically via the expected reward. It is also worth

Table 6.10: The identified SCS for each unsafe state with the corresponding expected reward values.

Unsafe state	SCS (Primary)	Expected reward	SCS (Secondary)	Expected reward
S_{u_1}	A_{r_6}	+8.60	A_{r_3}	+4.23
S_{u_2}	A_{r_6}	+4.35	A_{r_3}	+0.71
S_{u_3}	A_{r_6}	+4.35	A_{r_3}	+0.71

noting that the reward structure successfully steers the solver towards fail-operational actions (A_{r_2}, A_{r_6}) instead of the fail-safe actions ($A_{r_1}, A_{r_3}, A_{r_5}$), consistent with the design intent. The SCS will vary based on incoming observations, assigned rewards, and transition probabilities.

6.4 Conclusions

This chapter introduces a POMDP-based online risk mitigation method for autonomous inland vessels. Thus, the following research question was addressed **RQ5:** *How can the risk of grounding and collision of autonomous vessels in inland waterways be modelled and mitigated?*

Firstly, the hazards impacting the vessel's control capabilities, which can lead to collision or grounding, were identified. Furthermore, in the proposed method, by integrating the identified unsafe control actions with recovery (fail-safe and fail-operational) actions within a sequential decision-making framework, the optimal SCS was identified. Following this strategy thereby improves the ASV's planning and control system's capability to navigate uncertain and abnormal maritime conditions. Case study results for an autonomous vessel navigating in a constrained inland waterway demonstrate that the proposed method can reliably select SCSs in a complex failure scenario while achieving a 95% recovery rate. Furthermore, the systematic BBN-POMDP pipeline and the reward structure provide traceability for the identified SCS, thereby improving safety assurance.

Chapter 7

Conclusions and Future Research

This thesis investigated the challenges underlying the safe navigation of autonomous vessels in inland waterways. In this unique environment, vessels must operate under strict physical constraints and varying environmental conditions, as well as various potential modes of onboard failures. To this end, the main research question that this thesis aimed to address was as follows: *How to design model-based control and fault diagnosis methods that ensure the safe navigation of autonomous vessels under uncertain and abnormal operational conditions?*

This chapter is structured as follows: Firstly, in Section 7.1, the main findings and conclusions are presented in the form of answers to the research sub-questions presented in Chapter 1. Thereafter, the main research question, as mentioned above, is addressed. Finally, in Section 7.2, recommendations for future research are provided.

7.1 Conclusions

The five research sub-questions and the main research question are answered in this section as follows.

RQ1: *What are the state-of-the-art and research gaps regarding the safe navigation of autonomous vessels in inland waterways?*

In Chapter 2, a systematic literature review is carried out, and the state-of-the-art as well as the main research gaps pertaining to the autonomous navigation of IWVs are identified. Firstly, the literature on **maneuvering model identification** for full-scale vessels was reviewed. Many works address the identification problem only for simplified vessel dynamics or decoupled DOFs. The resulting models include only a subset of the full set of hydrodynamic parameters that comprise the 3-DOF dynamical model. Furthermore, stochastic methods such as Kalman filtering and its variants are popular; however, they make stricter assumptions about the noise distribution and the independence of the underlying random variables. Such methods produce unbounded parameter estimates, which reduces confidence in these estimates and limits their direct application to the safety verification of autonomous systems.

The vessel **path-following control** problem has been most extensively studied in the literature, with a focus on open-sea navigation. Navigating in inland waterways introduces

additional constraints, such as the bank effect and shallow-water effect, which can significantly affect the performance of traditional controllers. Existing works do not account for the impact of these factors on vessel dynamics; therefore, the vessel control system cannot accommodate them. Furthermore, evaluation metrics for the control system's performance in confined waterways have not been considered. Ensuring navigation safety under potential hazardous conditions, such as vessel grounding and collision, requires a supervisory system to take fail-safe actions. This system must incorporate risk monitoring and higher-level decision-making systems, and their design and implementation remain open research topics.

Model-based fault diagnosis literature for marine vessels is disproportionately focused on actuator faults, such as the loss of effectiveness or bias of the thruster/propeller, a stuck rudder, etc. Limited research on sensor faults is available, and existing work considers simpler kinematic models while largely neglecting the impact of external disturbances acting on the vessel, resulting in high modeling uncertainty. In inland waterways, wind forces and shallow-water effects are among the prominent factors that affect vessel motion and maneuverability, leading to erroneous diagnostic results if not accounted for. Another key aspect that varies across vessels is the configuration of actuators and onboard sensors. While conventional vessels are often equipped with a rudder-propeller setup, azimuth thrusters with vectored thrust for steering are also common, especially on tugs, ferries, and offshore vessels. This variation determines the dynamical model used for residual generation in model-based FDI; however, it is not accounted for in existing methods.

Finally, the **risk-aware decision-making** literature for ASVs is reviewed, with some works proposing to integrate risk analysis methods directly or indirectly into the control system's decision-making. Probabilistic inference methods, such as Bayesian networks, are commonly employed for online risk modelling, providing posterior probabilities that must be paired with a control system for decision-making. However, dynamic decision-making methods that directly output control policies, such as POMDPs, have not been explored for the risk mitigation of autonomous vessels, despite their potential for online planning. Furthermore, risk-aware decision-making for collision avoidance in mixed traffic conditions is a recent topic of interest.

RQ2: *How to identify a robust and control-oriented maneuvering model of marine vessels under realistic operating conditions?*

Since this thesis employs model-based methods to design decision-making systems for fault diagnosis and control, it was deemed crucial to revisit the model identification problem for marine vessels, accounting for uncertainties impacting the identification process. To this end, in Chapter 3, an SMI approach was presented for identifying the parametric 3-DOF model of a full-scale vessel, offering a robust framework for incorporating uncertainties, including measurement noise and the effects of wind and waves. The method involves computing the DDPS polytope using input-output measurements and model assumptions, which is further used to compute an FPS. The parameter estimates are then obtained by solving a quadratic program over the FPS polytope, along with definite parametric bounds.

Compared to existing methods, the proposed method converges faster to the optimal parameters and achieves improved state prediction accuracy. Validation using maneuvering

data from a full-scale vessel demonstrated that the computational time per sample decreased by at least an order of magnitude and the prediction accuracy improved by up to 26.5%. The method also provides a framework for real-time parameter adaptation for the vessel's guidance and control systems. Various control design methods, such as robust and adaptive MPC, can utilise the set-membership approach for obtaining recursive model updates.

RQ3: *How to design and evaluate control systems that ensure safe navigation of autonomous vessels in confined waterways?*

To design model-based control systems for ASVs in confined waterways, the hydrodynamic effects of water depth, river currents, and channel banks must be effectively captured in the vessel's maneuvering model. In Chapter 4, a modified MMG model for IWVs is considered that incorporates these factors. Subsequently, an NMPC control law is designed for the path-following control of IWVs, accounting for nonlinearities in the prediction model and varying operating conditions in inland waterways.

Extensive simulations across diverse, realistic operating scenarios, including straight channels, confluences, and river bends, are performed. A significant reduction in course deviations and cross-track errors, as well as the rudder deflections, is observed across varying water depths and ship-to-bank distances, compared with the standard PID controller. Once the vessel has been steered onto the predefined route, the NMPC maintains a tracking error below 5 meters during transit, whereas the PID controller occasionally experiences an error exceeding 20 meters. To evaluate control performance, several key performance metrics are proposed based on navigation requirements specific to inland waterways. Smaller values for metrics such as MAXTE, AAXTE, and SINM are obtained for NMPC, indicating superior control performance. The smaller IWRI metric indicates greater robustness than the PID controller. Finally, the NMPC also achieves a comparatively smaller ETA, showcasing its ability to perform more efficient inland navigation.

RQ4: *How to detect and isolate multiple sensor faults affecting the navigational sensors on autonomous surface vessels?*

To detect and isolate multiple sensor faults, Chapter 5 presented an observer-based FDI scheme for the navigational sensors onboard an ASV. Multiple faults impacting the navigational sensors, including the GNSS, IMU, and gyrocompass, were considered. Modelling complexities, such as differences in vessel types, actuator configurations, and sensor setups, were accounted for by designing multiple monitoring modules tailored to different vessel dynamics and sensor measurement models.

The method was validated using the vessel model identified in Chapter 3 and an example from the literature. It was demonstrated that false alarms can be eliminated by designing adaptive thresholds that robustly bound the residuals in each monitoring module by accounting for environmental disturbances and modelling uncertainties. Furthermore, the combinatorial fault decision logic, in conjunction with monitoring modules with structurally sensitive residuals, enabled the isolation of multiple sensor faults. Finally, through sensitivity analysis, ARRs with weak fault sensitivity were identified, leading to an updated FSM with improved isolability.

RQ5: *How can the risk of grounding and collision of autonomous vessels in inland waterways be modelled and mitigated?*

Chapter 6 presents a method for the grounding and collision risk mitigation for an IWV by combining a BBN for risk modelling with a POMDP model for risk control. The method builds on the STPA hazard analysis technique to model the BBN layers, while the POMDP model provides a framework for incorporating various possible fail-safe control actions. Given a failure event affecting the vessel's GNC system, the POMDP model is trained and subsequently tested online via MCTS simulations. The results demonstrate the proposed method's capability to identify a suitable higher-level SCS with a reliable recovery rate.

Based on the above discussion, we can now proceed to answer the overall research question as follows:

How to design model-based control and fault diagnosis methods that ensure the safe navigation of autonomous vessels under uncertain and abnormal operational conditions?

In this work, safe navigation is treated as a design requirement spanning various systems in the autonomy stack, including the control, fault diagnosis and supervisory systems. By doing so, the design of the autonomous navigation system becomes a closed-loop process involving explicit modelling of physical processes (nonlinear dynamics, environmental disturbances, sensor noise, etc.), the detection of unpredictable events (faults) and the anticipation of hazardous situations (collision, grounding) through monitoring systems, and their handling through robust model-based methods (control laws, fallback strategies). This process results in improved decision-making capabilities that ensure safe autonomous navigation under realistic performance degradation.

For model-based control design, a combination of reduced model uncertainty and high controller robustness is desired. To reduce the model uncertainty, we consider the explicit modelling of environmental forces acting on the vessel sailing in confined waterways. The Abkowitz and MMG approaches are considered in this thesis for modelling the complete 3-DOF nonlinear vessel dynamics in the horizontal plane. However, realistically, it is not possible to ascertain all sources of environmental uncertainties. This is where the proposed SMI method becomes pivotal, as it allows bounding epistemic uncertainties, such as environmental disturbances and sensor noise, without requiring explicit modelling. The result is a set of identified parameters and accompanying bounds that facilitate the design of robust model-based control systems, such as NMPC for path-following control, as presented in this thesis. In addition to modelling the impact of environmental factors on the vessel, environmental characteristics such as steep river confluences and curves, obstacles requiring path replanning, and varying inflow due to currents complicate navigation in confined waterways. These factors serve as the basis for the case-study scenarios, with the key performance metrics used to evaluate the controller's performance and its ability to handle such cases. Overall, these contributions address aspects related to the vessel's autonomous navigation under uncertain operational conditions.

For model-based sensor fault diagnosis, the main challenges include the variations in sensor and actuator configurations, modelling complexities and environmental disturbances impacting the ASV. In IWVs, the lack of design standardisations significantly escalates the former challenge. These challenges are addressed by proposing an FDI scheme utilising nonlinear observers for the residual generation, and adaptive thresholds for residual bounding. The proposed

scheme addresses the aforementioned challenges by designing multiple monitoring modules that include various dynamical and sensor measurement models. As a result, given different available models, sensors, and actuator configurations, an appropriate selection of monitoring modules/residuals can be made. The adaptive thresholds act similarly to the uncertainty bounds in the SMI method, and provide robust detections by ensuring that no false alarms occur. Importantly, these thresholds can be implemented using a set of linear filters, thereby greatly simplifying the applicability of the proposed method. Finally, multiple fault isolation is achieved by designing the monitoring modules to be selectively sensitive to faults and accordingly designing the FSM. In addition to sensor fault diagnosis, a risk modelling and mitigation method is also proposed within the vessel's supervisory system to prevent hazardous situations. Overall, the proposed methods address aspects related to the vessel's autonomous navigation under abnormal operational conditions.

7.2 Future Research

The following directions are proposed for future research, and include improvements on the methods proposed in this thesis, as well as other related topics:

System Identification: Future research on vessel model identification should focus on a wide inventory of complementary models and parameter sets that can support true dock-to-dock autonomy. This would require covering the full operating envelope, including berthing/deberthing, DP, low-speed harbour maneuvers, and higher speed transits. For many vessels, this includes operating in the semi-displacement or planing speed regions where classical ship maneuvering formulations become inadequate because the hydrodynamic derivatives are strongly speed-dependent. In this case, recursive model update can be a promising approach by combining a physics-based model with data-driven corrections, thereby maintaining model validity and prediction accuracy. Set-membership methods can be employed here to maintain bounded parameter sets that are updated in real time as new measurements are received.

Control: Practical control design for IWV navigation requires discarding simplifying assumptions and design considerations such as constant propeller speeds, rudder-only control, full vessel actuation, and using only the heading angle measurements. Future research should focus on control design without these considerations and with explicit formal safety guarantees. This will not only enhance the vessel's path-following performance and maneuverability but also ensure safety under varying navigation conditions.

Fault Diagnosis: Future research should focus on improving the fault detectability of the proposed sensor FDI framework by explicitly accounting for environmental disturbances and modelling uncertainties in the observer design. Adaptive approximation methods offer a promising approach to obtain robust observer formulations by approximating lumped uncertainties either offline or online. Another research direction involves broadening the scope of anomalies considered to include degradation, partial failures, and compromised subsystems, with particular emphasis on sensing and power systems. Sensors used for environmental perception, including Radars, LIDARs, and cameras, are among the most vulnerable systems and require continuous monitoring and diagnosis.

Cybersecurity: Since autonomy will be enabled by multiple interconnected cyber-physical

systems spanning the entire IWT system, ensuring the safety and resilience of these systems is of utmost importance. Arguably, many cybersecurity risks have not yet been considered, particularly in communication, sensing, and perception systems. Therefore, designing systems that can monitor and respond to cyberattacks quickly and effectively is a crucial research direction.

Fallback Operation: Given the complexity of onboard systems and their interactions, preventing hazardous situations requires continuous risk monitoring and fail-safe decision-making. Chapter 6 briefly explores the design of risk-monitoring and mitigation methods; however, further research is required to develop these systems and thoroughly test and validate them to ensure safety in the event of a system-level failure.

Bibliography

[1] UN Trade and Development (UNCTAD). Review of maritime transport 2022: Navigating stormy waters. Available at: https://unctad.org/publication/review-maritime-transport-2022, 2022. Accessed 18-12-2025.

[2] P. de Vos. AmmoniaDrive: a solution for zero-emission shipping?! *SWZ Maritime*, 141 (3):36–37, 2020. ISSN 1876-0236.

[3] I Georgescu, RD Geertsma, A Haseltalab, K Visser, R Negenborn, M Godjevac, JJ Hopman, and G Lodewijks. Generating and controlling power. Shipdrive: Novel design and control methodologies for complex smart ship system integration, 2015. ISSN 1876-0236. Special on " Engines and Propulsion Systems ".

[4] V. Reppa, R. R. Negenborn, J. F. J. Pruyn, J. J. Hopman, J. J. Zwaginga, and N. Kougiatsos. READINESS: Robust, Effective and Adaptable Ship Designs for Uncertain Transition Paths, 2020. URL https://www.ship-readiness.nl/home.

[5] Thomas Porathe. A navigating navigator onboard or a monitoring operator ashore? Towards safe, effective, and sustainable maritime transportation: findings from five recent EU projects. *Transportation Research Procedia*, 14:233–242, 2016.

[6] Rana Saha, Yan-Yun Zhang, Martin Baerveldt, Zhongbi Luo, Hoang Anh Tran, Amirreza Haqshenas Mojaveri, Dhanika Mahipala, Chengqian Zhang, Abhishek Dhyani, Yunjia Wang, et al. Autonomous inland waterway transport for a safer and sustainable tomorrow: The AUTOBarge project. *Societal Impacts*, page 100161, 2025.

[7] International Maritime Organization (IMO). Convention on the international regulations for preventing collisions at sea, 1972 (COLREGs), 1972.

[8] International Maritime Organization. International convention for the safety of life at sea (SOLAS), 2003.

[9] ABC News. Baltimore bridge collapse timeline: Inside the cargo ship collision, 2024. URL https://abcnews.go.com/US/timeline-baltimores-key-bridge-collapse-shows-moments-cargo/story?id=108540377. Accessed: 2026-01-28.

[10] BBC News. Suez blockage is holding up $9.6bn of goods a day, 2021. URL https://www.bbc.com/news/business-56533250.

[11] Gulf Business. Ever Given grounding: Suez Canal closure highlights marine industry risks, 2021. URL https://gulfbusiness.com/ever-given-grounding-suez-canal-closure-highlights-marine-industry-risks/. Accessed: 2026-02-05.

[12] Allianz Commercial. Safety & shipping review 2025, 2025. URL https://commercial.allianz.com/news-and-insights/reports/shipping-safety.html.

[13] European Maritime Safety Agency. Annual overview of marine casualties and incidents 2025, 2025. URL https://www.emsa.europa.eu/emcip/items.html?cid=141&id=5562.

[14] Anita M Rothblum. Human error and marine safety. In *National Safety Council Congress and Expo, Orlando, FL*, volume 7, 2000.

[15] RA Shenoi, JA Bowker, Agnieszka S Dzielendziak, Artur Konrad Lidtke, G Zhu, F Cheng, D Argyos, I Fang, J Gonzalez, S Johnson, et al. Global marine technology trends 2030, 2015. URL https://www.globalmaritimehub.com/wp-content/uploads/attach_696.pdf.

[16] European Commission. MSCA-ETN-AUTOBarge, 2020. URL https://cordis.europa.eu/project/id/955768. Accessed: 2025-11-10.

[17] Jie Xue, Qianbing Li, Yuanming Song, Peijie Yang, Yuanjun Feng, and Hao Hu. A bibliometric analysis of the development of autonomous ships in inland waterway transport. *Frontiers in Marine Science*, 12:1624596, 2025.

[18] Senne Van Baelen, Gerben Peeters, Herman Bruyninckx, Paolo Pilozzi, and Peter Slaets. Dynamic semantic world models and increased situational awareness for highly automated inland waterway transport. *Frontiers in Robotics and AI*, 8:739062, 2022.

[19] Zhixiang Liu, Youmin Zhang, Xiang Yu, and Chi Yuan. Unmanned surface vehicles: An overview of developments and challenges. *Annual Reviews in Control*, 41:71–93, 2016.

[20] Zhe Du, Rudy R Negenborn, and Vasso Reppa. Multi-objective cooperative control for a ship-towing system in congested water traffic environments. *IEEE Transactions on Intelligent Transportation Systems*, 23(12):24318–24329, 2022.

[21] Pablo Segovia, Vicenç Puig, Rudy R Negenborn, and Vasso Reppa. Dynamic coordination of multiple movable bridges and vessels for time-efficient inland waterway navigation. *IEEE Transactions on Intelligent Transportation Systems*, 2025.

[22] Linying Chen, Yamin Huang, Huarong Zheng, Hans Hopman, and Rudy R Negenborn. Cooperative multi-vessel systems in urban waterway networks. *IEEE Transactions on Intelligent Transportation Systems*, 21(8):3294–3307, 2019.

[23] Rudy R Negenborn, Floris Goerlandt, Tor A Johansen, Peter Slaets, Osiris A Valdez Banda, Thierry Vanelslander, and Nikolaos P Ventikos. Autonomous ships are on the horizon: here's what we need to know. *Nature*, 615(7950):30–33, 2023.

[24] Hoang Anh Tran, Tor Arne Johansen, and Rudy R Negenborn. Collision avoidance of autonomous ships in inland waterways–a survey and open research problems. In *Journal of Physics: Conference Series*, volume 2618, page 012004. IOP Publishing, 2023.

[25] Abhishek Dhyani, Anastasios Tsolakis, Kasper van der El, Rudy R Negenborn, and Vasso Reppa. Robust vessel maneuvering modelling using set-membership identification. *Control Engineering Practice*, 173:106936, 2026.

[26] Abhishek Dhyani, Rudy R Negenborn, and Vasso Reppa. A multiple sensor fault diagnosis scheme for autonomous surface vessels. *IFAC-PapersOnLine*, 58(4):31–36, 2024.

[27] Abhishek Dhyani, Kasper van der El, Rudy R Negenborn, and Vasso Reppa. Multiple sensor fault diagnosis for safe navigation of autonomous surface vessels. *Control Engineering Practice*, 168:106673, 2026.

[28] Chengqian Zhang, Abhishek Dhyani, Jonas W Ringsberg, Fabian Thies, Vasso Reppa, and Rudy R Negenborn. Manoeuvring modelling and control design of autonomous vessels on inland waterways. In *International Conference on Offshore Mechanics and Arctic Engineering*, volume 87820, page V05AT06A046. American Society of Mechanical Engineers, 2024.

[29] Chengqian Zhang, Abhishek Dhyani, Jonas W Ringsberg, Fabian Thies, Rudy R Negenborn, and Vasso Reppa. Nonlinear model predictive control for path following of autonomous inland vessels in confined waterways. *Ocean Engineering*, 334:121592, 2025.

[30] Abhishek Dhyani, Yunjia Wang, Mathias Verbeke, Davy Pissoort, and Vasso Reppa. A POMDP model-based online risk mitigation method for autonomous inland vessels. *IFAC-PapersOnLine*, 58(20):335–340, 2024.

[31] Martin Alexandersson, Wengang Mao, and Jonas W. Ringsberg. System identification of Vessel Manoeuvring Models. *Ocean Engineering*, 266:112940, December 2022. ISSN 00298018.

[32] Lothar Birk. *ITTC 1978 Performance Prediction Method*. John Wiley & Sons, Ltd, 2019. ISBN 978-1-119-19157-5. Section: 44.

[33] Weilin Luo. Parameter identifiability of ship manoeuvring modeling using system identification. *Mathematical Problems in Engineering*, 2016(1):8909170, 2016.

[34] Elías Revestido Herrero and Francisco J. Velasco González. Two-step identification of non-linear manoeuvring models of marine vessels. *Ocean Engineering*, 53:72–82, October 2012. ISSN 00298018.

[35] Christian R Sonnenburg and Craig A Woolsey. Modeling, identification, and control of an unmanned surface vehicle. *Journal of Field Robotics*, 30(3):371–398, 2013.

[36] Bjørn-Olav Holtung Eriksen and Morten Breivik. Modeling, identification and control of high-speed ASVs: Theory and experiments. In *Sensing and control for autonomous vehicles: Applications to land, water and air vehicles*, pages 407–431. Springer, 2017.

[37] Anders Aglen Pedersen. Optimization based system identification for the milliAmpere ferry, 2019. MSc thesis, NTNU.

[38] Tobias Hahn, Robert Damerius, and Torsten Jeinsch. An Identification Scheme to determine All Off-Diagonal Elements of Added-Mass Matrix for Marine Vessels. *IFAC-PapersOnLine*, 54(16):175–180, January 2021. ISSN 2405-8963.

[39] Tobias Hahn, Björn Kolewe, and Torsten Jeinsch. Identification of a Maneuvering Vessel based on Regular Operation. *IFAC-PapersOnLine*, 56(2):11584–11589, 2023. ISSN 2405-8963.

[40] Xiufeng Zhang, Yao Meng, Zhaochun Liu, and Jinxin Zhu. Modified grey wolf optimizer-based support vector regression for ship maneuvering identification with full-scale trial. *Journal of Marine Science and Technology*, 27(1):576–588, March 2022. ISSN 1437-8213. Number: 1 Publisher: Springer Japan.

[41] Chunyu Song, Xianku Zhang, and Guoqing Zhang. Nonlinear Identification for 4-DOF Ship Maneuvering Modeling via Full-Scale Trial Data. *IEEE Transactions on Industrial Electronics*, 69(2):1829–1835, 2 2022. ISSN 0278-0046.

[42] Gongxing Wu, Jiawei Zhang, Guofu Li, Linling Wang, Qiang Yu, and Jiamin Guo. Identification method of nonlinear maneuver model for unmanned surface vehicle from sea trial data based on support vector machine. *Journal of Mechanical Science and Technology*, 36(8):4257–4267, 2022.

[43] Tongtong Wang, Guoyuan Li, Lars Ivar Hatledal, Robert Skulstad, Vilmar AEsoy, and Houxiang Zhang. Incorporating Approximate Dynamics Into Data-Driven Calibrator: A Representative Model for Ship Maneuvering Prediction. *IEEE Transactions on Industrial Informatics*, 18(3):1781–1789, 3 2022. ISSN 1551-3203.

[44] Tongtong Wang, Robert Skulstad, Motoyasu Kanazawa, Guoyuan Li, and Houxiang Zhang. Learning Nonlinear Dynamics of Ocean Surface Vessel With Multistep Constraints. *IEEE Transactions on Industrial Informatics*, 20(9):10847–10856, 9 2024. ISSN 1551-3203.

[45] Yan-Yun Zhang, Jef Billet, and Peter Slaets. Experimental identification of decoupled ship dynamic models for an autonomous catamaran urban cargo vessel. *IFAC-PapersOnLine*, 58(20):229–234, 2024. ISSN 2405-8963. 15th IFAC Conference on Control Applications in Marine Systems, Robotics and Vehicles CAMS 2024.

[46] Armen Der Kiureghian and Ove Ditlevsen. Aleatory or epistemic? does it matter? *Structural safety*, 31(2):105–112, 2009.

[47] Mario Milanese and Antonio Vicino. Optimal estimation theory for dynamic systems with set membership uncertainty: An overview. *Automatica*, 27(6):997–1009, 1991.

[48] Andreas Rauh, Marit Lahme, Simon Rohou, Luc Jaulin, Thach Ngoc Dinh, Tarek Raissi, and Mohamed Fnadi. Offline and Online Use of Interval and Set-Based Approaches for Control and State Estimation: A Review of Methodological Approaches and Their Application. *Logical Methods in Computer Science*, 2023.

[49] Marko Tanaskovic, Lorenzo Fagiano, Roy Smith, and Manfred Morari. Adaptive receding horizon control for constrained MIMO systems. *Automatica*, 50(12):3019–3029, 2014.

[50] Matthias Lorenzen, Mark Cannon, and Frank Allgöwer. Robust MPC with recursive model update. *Automatica*, 103:461–471, 2019.

[51] P Du, Abdellatif Ouahsine, P Sergent, and Haibao Hu. Resistance and wave characterizations of inland vessels in the fully-confined waterway. *Ocean Engineering*, 210:107580, 2020.

[52] K. Kijima and Y. Nakiri. Prediction method of ship manoeuvrability in deep and shallow waters, 1990. Technical report.

[53] J. Liu, R. Hekkenberg, E. Rotteveel, and H. Hopman. Literature review on evaluation and prediction methods of inland vessel manoeuvrability. *Ocean Engineering*, 106:458–471, 2015.

[54] P. Mucha, T. Dettmann, V. Ferrari, and O. el Moctar. Experimental investigation of free-running ship manoeuvers under extreme shallow water conditions. *Applied Ocean Research*, 83:155–162, 2019.

[55] Pierre-Jean Pompée. About modelling inland vessels resistance and propulsion and interaction vessel-waterway key parameters driving restricted/shallow water effects. *Proceeding of Smart Rivers 2015*, page 180, 2015.

[56] Y. Yoshimura. Mathematical model for the manoeuvring ship motion in shallow water. *Journal of the Kansai Society of Naval Architects*, 200, 1986.

[57] C.-K. Lee and S.-G. Lee. Investigation of ship maneuvering with hydrodynamic effects between ship and bank. *Journal of Mechanical Science and Technology*, 22:1230–1236, 2008.

[58] M. Vantorre, G. Delefortrie, K. Eloot, and E. Laforce. Experimental investigation of ship-bank interaction forces, 2003. Technical report.

[59] Bloomberg Businessweek. Six days in suez: The inside story of the ship that broke global trade, 2021. URL https://www.bloomberg.com/news/features/2021-06-24/how-the-billion-dollar-ever-given-cargo-ship-got-stuck-in-the-suez-canal.

[60] Martin A Abkowitz. Lectures on ship hydrodynamics–steering and manoeuvrability. Technical report, 1964.

[61] K. Nomoto, T. Taguchi, K. Honda, and S. Hirano. On the steering qualities of ships. *International Shipbuilding Progress*, 4(35):354–370, 1957.

[62] A. Ogawa and H. Kasai. On the mathematical model of manoeuvring motion of ships. *International Shipbuilding Progress*, 25(292):306–319, 1978.

[63] S. Kaidi, H. Smaoui, and P. Sergent. Numerical estimation of bank–propeller–hull interaction effect on ship manoeuvring using CFD method. *Journal of Hydrodynamics, Series B*, 29(1):154–167, 2017.

[64] D. Kim, T. Tezdogan, and A. Incecik. Hydrodynamic analysis of ship manoeuvrability in shallow water using high-fidelity URANS computations. *Applied Ocean Research*, 123: 103176, 2022. doi: 10.1016/j.apor.2022.103176.

[65] P. Mucha. *On simulation-based ship maneuvering prediction in deep and shallow water*. PhD thesis, Universit"at Duisburg-Essen, 2017.

[66] R. Okuda, H. Yasukawa, M. Sano, N. Hirata, Y. Yoshimura, Y. Furukawa, and A. Matsuda. Maneuvering simulations of twin-propeller and twin-rudder ship in shallow water using equivalent single rudder model. *Journal of Marine Science and Technology*, 27(2): 948–970, 2022.

[67] J. Liu, R. Hekkenberg, F. Quadvlieg, H. Hopman, and B. Zhao. An integrated empirical manoeuvring model for inland vessels. *Ocean Engineering*, 137:287–308, 2017.

[68] Y. Yang and O. el Moctar. A mathematical model for ships maneuvering in deep and shallow waters. *Ocean Engineering*, 295:116927, 2024.

[69] C. Zhang, Y. Ma, F. Thies, J. W. Ringsberg, and Y. Xing. Towards autonomous inland shipping: a manoeuvring model in confined waterways. *Ships and Offshore Structures*, pages 1–13, 2024.

[70] K. Koh and H. Yasukawa. Comparison study of a pusher–barge system in shallow water, medium shallow water and deep water conditions. *Ocean Engineering*, 46:9–17, 2012.

[71] L. Wang, Q. Wu, J. Liu, S. Li, and R. Negenborn. State-of-the-art research on motion control of maritime autonomous surface ships. *Journal of Marine Science and Engineering*, 7(12):440, 2019.

[72] Yung-Hsiang Chen, Ming-Zhen Ellis-Tiew, Yu-Hsiang Chan, Guan-Wun Lin, and Yung-Yue Chen. Trajectory tracking design for unmanned surface vessels: robust control approach. *Journal of Marine Science and Engineering*, 11(8):1612, 2023.

[73] N. Paulig and O. Okhrin. Robust path following on rivers using bootstrapped reinforcement learning. *Ocean Engineering*, 298:116059, 2024.

[74] T. Sun, J. Zhang, and Y. Pan. Active disturbance rejection control of surface vessels using composite error updated extended state observer. *Asian Journal of Control*, 19(5): 1802–1811, 2017.

[75] D. Xu, Y. Huang, X. Zhou, and H. Xu. Path following control for large inland ships in a restricted waterway using the nonlinear terminal sliding mode method. *Ocean Engineering*, 284:115083, 2023.

[76] B. S. Park, J.-W. Kwon, and H. Kim. Neural network-based output feedback control for reference tracking of underactuated surface vessels. *Automatica*, 77:353–359, 2017.

[77] H. Wei, Y. Zhao, and S. Changyin. Adaptive neural network control of a marine vessel with constraints using the asymmetric barrier Lyapunov function. *IEEE Transactions on Cybernetics*, 47(7):1641–1651, 2017.

[78] Huixuan Fu, Wenjing Yao, Ricardo Cajo, and Shiquan Zhao. Trajectory tracking predictive control for unmanned surface vehicles with improved nonlinear disturbance observer. *Journal of Marine Science and Engineering*, 11(10):1874, 2023.

[79] H. Zheng, R. R. Negenborn, and G. Lodewijks. Predictive path following with arrival time awareness for waterborne AGVs. *Transportation Research Part C: Emerging Technologies*, 70:214–237, 2016.

[80] F. Hart, O. Okhrin, and M. Treiber. Vessel-following model for inland waterways based on deep reinforcement learning. *Ocean Engineering*, 281:114679, 2023. doi: 10.1016/j.oceaneng.2023.114679.

[81] M. Waltz, N. Paulig, and O. Okhrin. 2-level reinforcement learning for ships on inland waterways: Path planning and following. *Expert Systems with Applications*, 274:115011, 2025.

[82] J. Zhang, S. Yu, D. Wu, and Y. Yan. Nonsingular fixed-time terminal sliding mode trajectory tracking control for marine surface vessels with anti-disturbances. *Ocean Engineering*, 217:108019, 2020.

[83] Zhe Du, Rudy R. Negenborn, and Vasso Reppa. COLREGS-Compliant collision avoidance for physically coupled multi-vessel systems with distributed MPC. *Ocean Engineering*, 260:111917, 2022. ISSN 0029-8018.

[84] Changyuan Chen, Guillaume Delefortrie, and Evert Lataire. Effects of water depth and speed on ship motion control from medium deep to very shallow water. *Ocean Engineering*, 231:109102, 2021.

[85] M. Sano, H. Yasukawa, and H. Hata. Directional stability of a ship in close proximity to channel wall. *Journal of Marine Science and Technology*, 19(4):376–393, 2014.

[86] A Alessandri, S Donnarumma, S Vignolo, M Figari, M Martelli, R Chiti, and L Sebastiani. System control design of autopilot and speed pilot for a patrol vessel by using LMIs. *Towards green marine technology and transport*, pages 577–583, 2015.

[87] Q. Zhang, Z. Y. Ding, and M. J. Zhang. Adaptive self-regulation PID control of course-keeping for ships. *Polish Maritime Research*, 27(1):39–45, 2020.

[88] S. Li, J. Liu, R. R. Negenborn, and Q. Wu. Automatic docking for underactuated ships based on multi-objective nonlinear model predictive control. *IEEE Access*, 8:70044–70057, 2020. doi: 10.1109/ACCESS.2020.2986714.

[89] H. Zheng, R. R. Negenborn, and G. Lodewijks. Trajectory tracking of autonomous vessels using model predictive control. In *Proceedings of the 19th IFAC World Congress*, 2014.

[90] A. Haseltalab and R. R. Negenborn. Model predictive maneuvering control and energy management for all-electric autonomous ships. *Applied Energy*, 251:113308, 2019. doi: 10.1016/j.apenergy.2019.113308.

[91] J. Zhang, T. Sun, and Z. Liu. Robust model predictive control for path-following of underactuated surface vessels with roll constraints. *Ocean Engineering*, 143:125–132, 2017.

[92] P. Tondel, T. A. Johansen, and A. Bemporad. An algorithm for multi-parametric quadratic programming and explicit MPC solutions. *Automatica*, 39(3):489–497, 2003.

[93] C. Kirches, L. Wirsching, H. G. Bock, and J. P. Schlöder. Efficient direct multiple shooting for nonlinear model predictive control on long horizons. *Journal of Process Control*, 22(3):540–550, 2012.

[94] S. Gros, M. Zanon, R. Quirynen, A. Bemporad, and M. Diehl. From linear to nonlinear MPC: bridging the gap via the real-time iteration. *International Journal of Control*, 93 (1):62–80, 2020. doi: 10.1080/00207179.2016.1222553.

[95] Mohamed Abdelaal, Martin Fränzle, and Axel Hahn. Nonlinear model predictive control for trajectory tracking and collision avoidance of underactuated vessels with disturbances. *Ocean Engineering*, 160:168–180, 2018.

[96] E. Kayacan, S. Park, C. Ratti, and D. Rus. Learning-based nonlinear model predictive control of reconfigurable autonomous robotic boats: Roboats. In *Proceedings of the IEEE International Conference on Robotics and Automation*, pages 8230–8237, 2019.

[97] M. Kosch, A. Elkhashap, P. Koschorrek, R. Zweigel, and D. Abel. Hardware-in-the-loop trajectory tracking and collision avoidance of automated inland vessels using model predictive control. In *Proceedings of the 2021 European Control Conference*, pages 2251–2256, 2021.

[98] Rolf Isermann. *Fault-diagnosis systems: an introduction from fault detection to fault tolerance*. Springer Science & Business Media, 2005.

[99] Rocco Tarantino, Ferenc Szigeti, and Eliezer Colina-Morles. Generalized Luenberger observer-based fault-detection filter design: an industrial application. *Control Engineering Practice*, 8(6):665–671, 2000.

[100] Weitian Chen and Mehrdad Saif. Fault detection and isolation based on novel unknown input observer design. In *2006 American Control Conference*, pages 6–pp. IEEE, 2006.

[101] Iman Shames, André MH Teixeira, Henrik Sandberg, and Karl H Johansson. Distributed fault detection for interconnected second-order systems. *Automatica*, 47(12):2757–2764, 2011.

[102] Qinghua Zhang. Adaptive Kalman filter for actuator fault diagnosis. *Automatica*, 93: 333–342, 2018.

[103] Hendrik M Odendaal and Thomas Jones. Actuator fault detection and isolation: An optimised parity space approach. *Control Engineering Practice*, 26:222–232, 2014.

[104] Janos J Gertler. *Fault detection and diagnosis in engineering systems*. CRC press, 2017.

[105] Steven X Ding. *Model-based fault diagnosis techniques: design schemes, algorithms, and tools*. Springer Science & Business Media, 2008.

[106] Teresa Escobet, Anibal Bregon, Berlamino Pulido, and Vicenç Puig. *Fault diagnosis of dynamic systems*. Springer, 2019.

[107] Jasmine Zidan, Elijah I. Adegoke, Erik Kampert, Stewart A. Birrell, Col R. Ford, and Matthew D. Higgins. GNSS Vulnerabilities and Existing Solutions: A Review of the Literature. *IEEE Access*, 9:153960–153976, 2021. doi: 10.1109/ACCESS.2020.2973759.

[108] Paul D. Groves. Shadow Matching: A New GNSS Positioning Technique for Urban Canyons. *Journal of Navigation*, 64(3):417–430, 2011. doi: 10.1017/S0373463311000087.

[109] Pau Closas, Carles Fernandez-Prades, and Juan A. Fernandez-Rubio. A bayesian approach to multipath mitigation in GNSS receivers. *IEEE Journal of Selected Topics in Signal Processing*, 3(4):695–706, 2009. doi: 10.1109/JSTSP.2009.2023831.

[110] Mogens Blanke. Diagnosis and fault-tolerant control for ship station keeping. In *Proceedings of the 2005 IEEE International Symposium on, Mediterrean Conference on Control and Automation Intelligent Control, 2005.*, pages 1379–1384. IEEE, 2005.

[111] Shaoji Fang, Mogens Blanke, and Bernt J Leira. Mooring system diagnosis and structural reliability control for position moored vessels. *Control Engineering Practice*, 36:12–26, 2015.

[112] Shaoji Fang and Mogens Blanke. Fault monitoring and fault recovery control for position-moored vessels. *International Journal of Applied Mathematics and Computer Science*, 2011.

[113] Mogens Blanke and Dong T Nguyen. Fault tolerant position-mooring control for offshore vessels. *Ocean Engineering*, 148:426–441, 2018.

[114] Mogens Blanke. Fault-tolerant sensor fusion for marine navigation. In *7th IFAC Conference on Manoeuvring and Control of Marine Craft*, pages 1385–1390. Elsevier, 2006.

[115] Chuang Zhang, Chunyan Cao, Chen Guo, Tieshan Li, and Muzhuang Guo. Navigation multisensor fault diagnosis approach for an unmanned surface vessel adopted particle-filter method. *IEEE Sensors Journal*, 21(23):27093–27105, 2021.

[116] Ruiqi Mao and Rongin Cui. Fault diagnosis for underactuated surface vessel. In *2021 40th Chinese Control Conference (CCC)*, pages 4403–4408. IEEE, 2021.

[117] Liheng Chen, Ming Liu, Yan Shi, Haijun Zhang, and Enjiao Zhao. Adaptive fault estimation for unmanned surface vessels with a neural network observer approach. *IEEE Transactions on Circuits and Systems I: Regular Papers*, 68(1):416–425, 2020.

[118] Xuerao Wang, Qingling Wang, Xiang Cao, Yuncheng Ouyang, and Changyin Sun. State recovery and fault-tolerant control of autonomous surface vehicle with actuator and sensor faults. *IEEE Transactions on Intelligent Vehicles*, pages 1–12, 2024.

[119] Ning Wang, Xinxiang Pan, and Shun-Feng Su. Finite-time fault-tolerant trajectory tracking control of an autonomous surface vehicle. *Journal of the Franklin Institute*, 357(16): 11114–11135, 2020.

[120] Qingrui Zhang, Xinyu Zhang, Bo Zhu, and Vasso Reppa. Fault tolerant control for autonomous surface vehicles via model reference reinforcement learning. In *2021 60th IEEE Conference on Decision and Control (CDC)*, pages 1536–1541. IEEE, 2021.

[121] Bong Seok Park and Sung Jin Yoo. Fault detection and accommodation of saturated actuators for underactuated surface vessels in the presence of nonlinear uncertainties. *Nonlinear Dynamics*, 85(2):1067–1077, 2016.

[122] Andrea Cristofaro and Tor Arne Johansen. Fault tolerant control allocation using unknown input observers. *Automatica*, 50(7):1891–1897, 2014.

[123] Anastasios Tsolakis, Laura Ferranti, and Vasso Reppa. Active thruster fault diagnosis for an overactuated autonomous surface vessel. *IFAC-PapersOnLine*, 58(4):43–48, 2024.

[124] Ravitej Bhagavathi, D Kwame Minde Kufoalor, and Agus Hasan. Digital twin-driven fault diagnosis for autonomous surface vehicles. *IEEE Access*, 11:41096–41104, 2023.

[125] Tahiyatul Asfihani, Fadia Lutfiani, Augie Widyotriatmo, and Agus Hasan. Sensor fault diagnosis in autonomous ships. In *2024 European Control Conference (ECC)*, pages 13–18. IEEE, 2024.

[126] Flavia Benetazzo, Gianluca Ippoliti, Sauro Longhi, and Paolo Raspa. Advanced control for fault-tolerant dynamic positioning of an offshore supply vessel. *Ocean Engineering*, 106:472–484, 2015.

[127] F Benetazzo, G Ippoliti, S Longhi, and P Raspa. Fault-tolerant variable structure control of an overactuated dynamic positioning vessel after thruster failures. *IFAC Proceedings Volumes*, 45(27):274–279, 2012.

[128] Yongyi Lin, Jialu Du, Guibing Zhu, and Huazhen Fang. Thruster fault-tolerant control for dynamic positioning of vessels. *Applied Ocean Research*, 80:118–124, 2018.

[129] Zitian Zhou, Maiying Zhong, and Youqing Wang. Fault diagnosis observer and fault-tolerant control design for unmanned surface vehicles in network environments. *IEEE Access*, 7:173694–173702, 2019.

[130] Peihua Han, Guoyuan Li, Robert Skulstad, Stian Skjong, and Houxiang Zhang. A deep learning approach to detect and isolate thruster failures for dynamically positioned vessels using motion data. *IEEE Transactions on Instrumentation and Measurement*, 70: 1–11, 2020.

[131] Robert H Rogne, Tor A Johansen, and Thor I Fossen. Observer and IMU-based detection and isolation of faults in position reference systems and gyrocompasses with dual redundancy in dynamic positioning. In *2014 IEEE Conference on Control Applications (CCA)*, pages 83–88. IEEE, 2014.

[132] Robert H Rogne, Tor A Johansen, and Thor I Fossen. On attitude observers and inertial navigation for reference system fault detection and isolation in dynamic positioning. In *2015 European Control Conference (ECC)*, pages 3665–3672. IEEE, 2015.

[133] Konstantinos Kepaptsoglou, Grigorios Fountas, and Matthew G Karlaftis. Weather impact on containership routing in closed seas: A chance-constraint optimization approach. *Transportation Research Part C: Emerging Technologies*, 55:139–155, 2015.

[134] Abhishek Dhyani, Amirreza Haqshenas Mojaveri, Chengqian Zhang, Dhanika Mahipala, Hoang Anh Tran, Yan-Yun Zhang, Zhongbi Luo, and Vasso Reppa. AUTOBargeSim: MATLAB® toolbox for the design and analysis of the guidance and control system for autonomous inland vessels. *IFAC-PapersOnLine*, 59(22):818–823, 2025. ISSN 2405-8963. 16th IFAC Conference on Control Applications in Marine Systems, Robotics and Vehicles CAMS 2025.

[135] Marc Vantorre, Katrien Eloot, Guillaume Delefortrie, Evert Lataire, Maxim Candries, and Jeroen Verwilligen. Maneuvering in shallow and confined water. *Encyclopedia of maritime and offshore engineering*, pages 1–17, 2017.

[136] Krzysztof Wróbel, Jakub Montewka, and Pentti Kujala. Towards the development of a system-theoretic model for safety assessment of autonomous merchant vessels. *Reliability Engineering & System Safety*, 178:209–224, October 2018. ISSN 09518320. doi: 10.1016/j.ress.2018.05.019.

[137] Børge Rokseth, Odd Ivar Haugen, and Ingrid Bouwer Utne. Safety Verification for Autonomous Ships. In N. Karanikas, M.M. Chatzimichailidou, and M. Rejzek, editors, *MATEC Web of Conferences*, volume 273, page 02002, 2019. doi: 10.1051/matecconf/201927302002.

[138] Christoph A Thieme, Børge Rokseth, and Ingrid B Utne. Risk-informed control systems for improved operational performance and decision-making. *Proceedings of the Institution of Mechanical Engineers, Part O: Journal of Risk and Reliability*, 237(2):332–354, April 2023. ISSN 1748-006X, 1748-0078. doi: 10.1177/1748006X211043657.

[139] GLAS DNV. DNVGL-CG-0264: Autonomous and remotely operated ships. *Retrieved July 2019*, pages 2018–09, 2018.

[140] Nicolas Lefebvre, Ingrid Schjølberg, and Ingrid B. Utne. Integration of risk in hierarchical path planning of underwater vehicles. In *IFAC-PapersOnLine*, volume 49, pages 226–231, 2016. doi: 10.1016/j.ifacol.2016.10.347.

[141] Jens E. Bremnes, Christoph A. Thieme, Asgeir J. Sørensen, Ingrid B. Utne, and Petter Norgren. A Bayesian Approach to Supervisory Risk Control of AUVs Applied to Under-Ice Operations. *Marine Technology Society Journal*, 54(4):16–39, July 2020. ISSN 0025-3324. doi: 10.4031/MTSJ.54.4.5.

[142] Ingrid Bouwer Utne, Børge Rokseth, Asgeir J. Sørensen, and Jan Erik Vinnem. Towards supervisory risk control of autonomous ships. *Reliability Engineering & System Safety*, 196:106757, April 2020. ISSN 09518320. doi: 10.1016/j.ress.2019.106757.

[143] Sverre Velten Rothmund. *Risk awareness and control of autonomous robots*. PhD thesis, NTNU, 2023.

[144] Stanley Kaplan and B John Garrick. On the quantitative definition of risk. *Risk analysis*, 1(1):11–27, 1981.

[145] GLAS DNV. Testing of RBAT on specific cases of MASS concepts. *Retrieved December 2023*, 2022.

[146] Thomas Johansen and Ingrid Bouwer Utne. Supervisory risk control of autonomous surface ships. *Ocean Engineering*, 251:111045, May 2022. ISSN 00298018. doi: 10.1016/j.oceaneng.2022.111045.

[147] Sverre Velten Rothmund, Trym Tengesdal, Edmund Førland Brekke, and Tor Arne Johansen. Intention modeling and inference for autonomous collision avoidance at sea. *Ocean Engineering*, 266:113080, December 2022. ISSN 00298018. doi: 10.1016/j.oceaneng.2022.113080.

[148] Angeliki Zacharaki, Ioannis Kostavelis, and Ioannis Dokas. Decision making with STPA through Markov Decision Process, a Theoretic Framework for Safe Human-Robot Collaboration. *Applied Sciences*, 11(11):5212, 2021.

[149] Arvind A Pereira, Jonathan Binney, Geoffrey A Hollinger, and Gaurav S Sukhatme. Risk-aware path planning for autonomous underwater vehicles using predictive ocean models. *Journal of Field Robotics*, 30(5):741–762, 2013.

[150] Miriam Gonzalez-Atienza, Dries Vanoost, Mathias Verbeke, and Davy Pissoort. Decision Algorithm Based on the Modified Bellman Equation to Deal With EMI-Induced Errors in Hamming-Based Communications. *IEEE Transactions on Electromagnetic Compatibility*, 2023.

[151] Hanna Kurniawati. Partially observable Markov decision processes and robotics. *Annual review of control, robotics, and autonomous systems*, 5(1):253–277, 2022.

[152] Thor I Fossen and Jann Peter Strand. Passive nonlinear observer design for ships using Lyapunov methods: full-scale experiments with a supply vessel. *Automatica*, 35(1): 3–16, 1999.

[153] K. K. Fedyaevsky and G. V. Sobolev. *Control and stability in ship design*. State Union Shipbuilding Industry Publishing House, 1964.

[154] Roger Skjetne, Øyvind N Smogeli, and Thor I Fossen. A nonlinear ship manoeuvering model: Identification and adaptive control with experiments for a model ship. *Modeling, Identification and Control*, 25(1):3–27, 2004.

[155] Mathias Marley, Roger Skjetne, Mateusz Gil, and Przemyslaw Krata. Four degree-of-freedom hydrodynamic maneuvering model of a small azipod-actuated ship with application to onboard decision support systems. *IEEE Access*, 11:58596–58609, 2023.

[156] Andreas B Martinsen, Anastasios M Lekkas, Sébastien Gros, Jon Arne Glomsrud, and Tom Arne Pedersen. Reinforcement learning-based tracking control of USVs in varying operational conditions. *Frontiers in Robotics and AI*, 7:32, 2020.

[157] Pradeep K Khosla and Takeo Kanade. Parameter identification of robot dynamics. In *1985 24th IEEE Conference on Decision and Control*, pages 1754–1760. IEEE, 1985.

[158] Anastasios Tsolakis, Laura Ferranti, and Vasso Reppa. Set-membership estimation for fault diagnosis of nonlinear systems. In *2025 European Control Conference (ECC)*, pages 1143–1150. IEEE, 2025.

[159] Damen. Waterbus 2907 hybrid, 2025. URL https://www.damen.com/vessels/ferries/city-ferries/waterbus-2907-hybrid.

[160] Gregory W Corder and Dale I Foreman. *Nonparametric statistics: A step-by-step approach*. John Wiley & Sons, 2014.

[161] C. Zhang, J. W. Ringsberg, and F. Thies. Development of a ship performance model for power estimation of inland waterway vessels. *Ocean Engineering*, 287:115731, 2023.

[162] Benjamin Friedhoff, Katja Hoyer, Sven List, and Matthias Tenzer. Investigation of the nominal and effective propeller inflow for a family of inland waterway vessels. *Ocean Engineering*, 187:106180, 2019.

[163] H. Yasukawa and Y. Yoshimura. Introduction of MMG standard method for ship maneuvering predictions. *Journal of Marine Science and Technology*, 20:37–52, 2015.

[164] Morten Breivik and Thor I Fossen. Guidance laws for planar motion control. In *2008 47th IEEE Conference on Decision and Control*, pages 570–577. IEEE, 2008.

[165] Thor I Fossen and Anastasios M Lekkas. Direct and indirect adaptive integral line-of-sight path-following controllers for marine craft exposed to ocean currents. *International journal of adaptive control and signal processing*, 31(4):445–463, 2017.

[166] W. Naeem, R. Sutton, S. Ahmad, and R. Burns. A review of guidance laws applicable to unmanned underwater vehicles. *Journal of Navigation*, 56(1):15–29, 2003.

[167] Vedran Bakaric, Zotan Vukic, and Radovan Antonic. Improved basic planar algorithm of vehicle guidance through waypoints by the line of sight. In *First International Symposium on Control, Communications and Signal Processing, 2004.*, pages 541–544. IEEE, 2004.

[168] Thor I Fossen, Morten Breivik, and Roger Skjetne. Line-of-sight path following of underactuated marine craft. *IFAC proceedings volumes*, 36(21):211–216, 2003.

[169] S. Saravanakumar and T. Asokan. Waypoint guidance based planar path following and obstacle avoidance of autonomous underwater vehicle. In *Proceedings of the International Conference on Informatics in Control, Automation and Robotics (ICINCO)*, pages 191–198, 2011.

[170] J. G. Ziegler and N. B. Nichols. Optimum settings for automatic controllers. *Transactions of the American Society of Mechanical Engineers*, 64(8):759–765, 1942.

[171] X. Yan, K. Wang, Y. Yuan, X. Jiang, and R. R. Negenborn. Energy-efficient shipping: An application of big data analysis for optimising engine speed of inland ships considering multiple environmental factors. *Ocean Engineering*, 169:457–468, 2018.

[172] David Q Mayne, James B Rawlings, Christopher V Rao, and Pierre OM Scokaert. Constrained model predictive control: Stability and optimality. *Automatica*, 36(6):789–814, 2000.

[173] Mircea Lazar and Martin Tetteroo. Computation of terminal costs and sets for discrete–time nonlinear MPC. *IFAC-PapersOnLine*, 51(20):141–146, 2018.

[174] Joel AE Andersson, Joris Gillis, Greg Horn, James B Rawlings, and Moritz Diehl. CasADi: a software framework for nonlinear optimization and optimal control. *Mathematical Programming Computation*, 11(1):1–36, 2019.

[175] A. Wachter and L. T. Biegler. On the implementation of an interior-point filter line-search algorithm for large-scale nonlinear programming. *Mathematical Programming*, 106(1): 25–57, 2006.

[176] Kenneth Gade. The seven ways to find heading. *The Journal of Navigation*, 69(5): 955–970, 2016.

[177] Vasso Reppa, Marios M Polycarpou, and Christos G Panayiotou. Sensor fault diagnosis. *Foundations and Trends® in Systems and Control*, 3(1-2):1–248, 2016.

[178] M. Tahk and J.L. Speyer. Target tracking problems subject to kinematic constraints. *IEEE Transactions on Automatic Control*, 35(3):324–326, 1990.

[179] Thor I Fossen. Line-of-sight path-following control utilizing an extended Kalman filter for estimation of speed and course over ground from GNSS positions. *Journal of Marine Science and Technology*, 27(1):806–813, 2022.

[180] Martin A Abkowitz. Measurement of hydrodynamic characteristics from ship maneuvering trials by system identification. *Annual Meeting of SNAME*, 1980.

[181] Thor I Fossen. *Handbook of marine craft hydrodynamics and motion control*. John Wiley & Sons, 2011.

[182] Zhe Du, Rudy R Negenborn, and Vasso Reppa. Cooperative multi-agent control for autonomous ship towing under environmental disturbances. *IEEE/CAA Journal of Automatica Sinica*, 8(8):1365–1379, 2021.

[183] A Ogawa, T Koyama, and K Kijima. MMG report-I, on the mathematical model of ship manoeuvring. *Bull Soc Naval Archit Jpn*, 575(22-28), 1977.

[184] K. Nomoto, T. Taguchi, K. Honda, and S. Hirano. On the steering qualities of ships. *International Shipbuilding Progress*, 4(35):354–370, 1957. doi: 10.3233/ISP-1957-43504.

[185] Chunchao Zhang, Zhijie Zhou, Pengyun Ning, Zhichao Ming, Chaoli Zhang, and Lingling Fang. IBRNet: Interpretable Belief Rule Network modeling method for fault diagnosis of redundant inertial navigation systems. *Control Engineering Practice*, 144: 105822, 2024.

[186] Vasso Reppa, Marios M Polycarpou, and Christos G Panayiotou. Adaptive approximation for multiple sensor fault detection and isolation of nonlinear uncertain systems. *IEEE Transactions on Neural Networks and Learning Systems*, 25(1):137–153, 2013.

[187] Chengqian Zhang, Yucong Ma, Fabian Thies, Jonas W Ringsberg, and Yihan Xing. Towards autonomous inland shipping: a manoeuvring model in confined waterways. *Ships and Offshore Structures*, pages 1–13, 2024.

[188] Carlos Conejo, Vicenç Puig, Bernardo Morcego, Francisco Navas, and Vicente Milanés. Enhancing safety in autonomous vehicles using zonotopic LPV-EKF for fault detection and isolation in state estimation. *Control Engineering Practice*, 156:106192, 2025.

[189] CCNR. International definition of levels of automation in inland navigation, Central Commission for the navigation of the Rhine. *2022 edition*, 2022.

[190] International Organization for Standardization (ISO) and International Electrotechnical Commission (IEC). Safety aspects – Guidelines for their inclusion in standards. ISO/IEC Guide 51:2014, 2014. Third edition, Geneva, Switzerland.

[191] Nancy G Leveson and John P Thomas. STPA handbook. *Cambridge, MA, USA*, 2018.

[192] ClassNK. Guidelines for automated/autonomous operation on ships. *Retrieved December 2023*, 2020.

[193] Victor Bolbot, Gerasimos Theotokatos, L Andreas Wennersberg, Jerome Faivre, Dracos Vassalos, Evangelos Boulougouris, Ørnulf Jan Rødseth, Pål Andersen, Ann-Sofie Pauwelyn, and Antoon Van Coillie. A novel risk assessment process: Application to an autonomous inland waterways ship. *Proceedings of the Institution of Mechanical Engineers, Part O: Journal of Risk and Reliability*, 237(2):436–458, 2023.

[194] Thomas Johansen, Simon Blindheim, Tobias Rye Torben, Ingrid Bouwer Utne, Tor Arne Johansen, and Asgeir J Sørensen. Development and testing of a risk-based control system for autonomous ships. *Reliability engineering & system safety*, 234:109195, 2023.

[195] Longhui Gang, Yonghui Wang, Yao Sun, Liping Zhou, and Mingheng Zhang. Estimation of vessel collision risk index based on support vector machine. *Advances in Mechanical Engineering*, 8(11):1687814016671250, 2016.

[196] Jakub Montewka, Sören Ehlers, Floris Goerlandt, Tomasz Hinz, Kristjan Tabri, and Pentti Kujala. A framework for risk assessment for maritime transportation systems—a case study for open sea collisions involving ropax vessels. *Reliability Engineering & System Safety*, 124:142–157, 2014.

[197] Arsham Mazaheri, Jakub Montewka, and Pentti Kujala. Towards an evidence-based probabilistic risk model for ship-grounding accidents. *Safety Science*, 86:195–210, 2016.

[198] SINTEF and NTNU. Offshore and onshore reliability data handbook. *6th Edition*, 2015.

[199] Christoph Alexander Thieme and Ingrid Bouwer Utne. A risk model for autonomous marine systems and operation focusing on human–autonomy collaboration. *Proceedings of the Institution of Mechanical Engineers, Part O: Journal of Risk and Reliability*, 231 (4):446–464, 2017.

[200] Norman Fenton and Martin Neil. *Risk assessment and decision analysis with Bayesian networks*. Crc Press, 2018.

[201] Børge Rokseth, Odd Ivar Haugen, and Ingrid Bouwer Utne. Safety verification for autonomous ships. In *MATEC web of conferences*, volume 273, page 02002. EDP Sciences, 2019.

[202] Peter Auer, Nicolo Cesa-Bianchi, and Paul Fischer. Finite-time analysis of the multi-armed bandit problem. *Machine learning*, 47(2):235–256, 2002.

[203] David Silver and Joel Veness. Monte-Carlo planning in large POMDPs. In J. Lafferty, C. Williams, J. Shawe-Taylor, R. Zemel, and A. Culotta, editors, *Advances in Neural Information Processing Systems*, volume 23. Curran Associates, Inc., 2010.

Glossary

Conventions

The following conventions are used in this thesis for notation and symbols:

- The time variable/index is denoted by t and k, for the continuous and discrete-time cases, respectively. They are omitted from several equations unless needed for clarity.
- Vectors are represented by lowercase letters, whereas matrices are represented by capital letters.
- A "hat" ($\hat{\cdot}$) denotes an estimated quantity.
- An overbar ($\bar{\cdot}$) denotes a known bound (e.g., noise bounds, parameter bounds or adaptive threshold bounds).
- $\mathrm{diag}(\cdot)$ forms a diagonal matrix, whereas $\mathrm{vcat}(\cdot)$ denotes vertical concatenation.
- $\tan^{-1}(\cdot)$ and $\mathrm{atan2}(\cdot,\cdot)$ denote inverse tangent functions (one-argument and two-argument forms).
- $|\cdot|$ denotes the magnitude (absolute value for scalars; element-wise magnitude when applied to vectors).

List of symbols and notations

The following is a list of the most frequently used symbols and notations in this thesis.

Variables

x_p, y_p	vessel position coordinates (NED) [m]
$\dot{x}_p$, $\dot{y}_p$	vessel velocity components (NED) [m/s]
ψ	heading (yaw) angle [rad]
u, v	surge and sway velocities (body-frame) [m/s]
v_m	sway velocity at midship (body-frame) [m/s]
r	yaw rate (body-frame) [rad/s]
r'	non-dimensional yaw rate
U	vessel speed magnitude [m/s]
χ	course angle/course over ground [rad]
β_c	crab angle [rad]
β_m	midship drift angle [rad]
β_P	inflow angle at propeller [rad]
β_{cur}	incoming current angle (earth-fixed frame) [rad]
U_C	current speed magnitude [m/s]
u_r, v_{rm}	surge and midship-sway velocities relative to current [m/s]
p	vessel position vector (NED)
η	generalized position vector (NED)
ν	generalized velocity vector (body-frame)
y_{pos}	position measurement [m]
y_ψ	heading angle measurement [rad]
y_χ	course angle measurement [rad]
y_u, y_v, y_r	surge, sway, and yaw-rate measurements [m/s, m/s, rad/s]
y_ν	velocity vector measurement

n_p, n_ψ, n_ν, n_χ	measurement noise terms for position, heading, velocity, course
f_p, f_ψ, f_ν, f_χ	sensor fault signals affecting position, heading, velocity, course
f_z	generic sensor fault affecting measurement z
T_{f_z}	occurrence time of fault f_z [s]
τ_u, τ_v, τ_r	controlled generalized forces/moments in surge, sway, yaw [N, N, N·m]
τ	controlled input forces/moments vector
τ_d	added forces/moments vector
$f(\nu, \tau)$	known nonlinear dynamics term
$\Delta(\eta, \nu)$	unknown nonlinear dynamics term
$X_{\mathrm{pr},w}$, $Y_{\mathrm{pr},w}$, $N_{\mathrm{pr},w}$	generalized force components of thruster w [N,N,N·m]
X_P	propeller-induced surge force [N]
X_R, Y_R, N_R	rudder-induced surge force, sway force, and yaw moment [N,N,N·m]
X_H, Y_H, N_H	hull surge force, sway force, and yaw moment [N,N,N·m]
X_B, Y_B, N_B	bank-effect surge, sway, and yaw forces/moments contributions [N,N,N·m]
X_W, Y_W, N_W	wind-induced surge, sway and yaw forces/moments contributions [N,N,N·m]
τ_w	wind-induced forces/moments vector
τ_H	hull forces/moments vector
$K_T(J)$	thrust coefficient function
J	propeller advance ratio
w_P	wake fraction at propeller position in maneuvering motions
n_P	propeller revolution speed [rpm]
F_N^P, F_N^S	rudder normal forces (port/starboard) [N]
δ	rudder angle [rad]
U_R	inflow speed at rudder [m/s]
u_R, v_R	longitudinal and transverse inflow velocities at rudder [m/s]

α_R	effective inflow angle at rudder [rad]
w_R	wake fraction at rudder position
δ_p, δ_s	azimuth thruster angles (port/starboard) [rad]
$\dot{\delta}_p$, $\dot{\delta}_s$	thruster angular rates (port/starboard) [rad/s]
$R(\psi)$	rotation matrix from body frame to NED
$C(\nu)$	Coriolis–centripetal matrix
$D(\nu)$	damping matrix
$D'(\nu)$	Dynamic coupling term in MMG form
$\cup(t)$	unit step function
$\tilde{\eta}^{(1)}$	estimation error for η in module 1
$\tilde{\psi}^{(2)}$	estimation error for ψ in module 2
$\tilde{\nu}^{(2)}$	estimation error for ν in module 2
$\tilde{x}_p^{(4)}$, $\tilde{y}_p^{(4)}$	estimation error for x_p, y_p in module 4
$z^{(I)}$	stacked state vector in module I
$y_z^{(I)}$	measurement of $z^{(I)}$ in module I
$\hat{z}^{(I)}$	estimate of $z^{(I)}$ in module I
$\varepsilon_{yz}^{(I)}$	residual vector in module I
$\varepsilon_{yz}^{(I,j)}$	residual component for sensor j in module I
$\bar{\varepsilon}_{yz}^{(I,j)}(t)$	adaptive threshold for $\lvert\varepsilon_{yz}^{(I,j)}(t)\rvert$
$T_D^{(I,j)}$	first time instance of the violation of j-th ARR (fault-detection time) [s]
$\mathbf{d}^{(I)}(t)$	decision vector for the I-th module
$d^{(I,j)}(t)$	binary decision for sensor j in module I
$\mathbf{d}(t)$	aggregated decision vector
$\mathcal{D}_s(t)$	diagnosis set
$\nabla\varepsilon_{yz}(f_z)$	Jacobian block matrix of residuals w.r.t. single faults

$\mathcal{J}_k$	polynomial functions of observer states
U_y	measured speed [m/s]
V	true wind speed [m/s]
β_V	true wind direction [rad]
V_r	relative wind speed [m/s]
γ_r	relative wind angle of attack [rad]
$u_r,\ v_r$	relative wind velocity components in x_p, y_p directions [m/s]
$\Phi^{(I)}(t)$	exponential bound function in adaptive thresholds
$E^{(I)}(t),\ Z^{(I)}(t)$	intermediate bound functions in adaptive thresholds
$\tilde{\gamma}_{kH}^{(I)}$	intermediate model mismatch term under healthy conditions
$XTE(t)$	cross-track error to closest point on path [m]
$SXTE(t)$	signed cross-track error [m]
$x_{cl}(t),\ y_{cl}(t)$	closest point coordinates on the desired path [m]
$\psi_{\text{ref}}(t)$	reference heading from LOS guidance law [rad]
$\psi_{\text{wp}}(t)$	waypoint-line heading component [rad]
$\psi_{\text{cross}}(t)$	LOS correction term [rad]
$d_{cl}(k)$	vessel's distance from channel centreline at step k [m]
$\psi_e(k)$	heading error at step k [rad]
$\tilde{\pi}$	cross-product between the waypoint vector and the ship's position vector [m^2]
$x_{\text{wp},k}, y_{\text{wp},k}$	k-th waypoint coordinates [m]
$q(t)$	IWV state vector
$\mathfrak{u}(t)$	IWV control input
$f(\cdot), g_2(\cdot)$	functions of vessel states in NMPC model decomposition
$g_1(\cdot)$	function of vessel states and control input in NMPC model decomposition
τ_e	vector comprising environmental forces in the IWV model

τ_c	vector comprising controlled rudder forces/moments in the IWV model
τ_o	propeller force contribution vector
$q_c(k)$, $u_c(k)$	NMPC prediction model states and input
$\omega_{c,i}$	revolutions of the $i-$th thruster [rad/s]
ϕ_i	relative fluid angle of attack for the $i-$th thruster [rad]
$\delta_{c,i}$, β_i	azimuth and flow orientation angles for the $i-$th thruster [rad]
G	nonlinear basis function in the states and controlled inputs
$X_{pr,i}$, $Y_{pr,i}$, $N_{pr,i}$	generalised force components for the $i-$th thruster, $i \in \{1,2\}$
$Y_{\text{bow}}, N_{\text{bow}}$	generalised forces due the bow thruster
$\theta^\star$	identified optimal parameter vector
θ_0	initial anchor for the parameter vector θ
$\delta\theta^\star$	smallest parameter increment for the parameter vector θ
$\Delta y(k)$	one-step difference in $y(k)$
$G_r(k)$	radius of the interval matrix $G([x(k)], u(k))$
J_{fit}	the percentage fit metric
J_{comp}	the computational time metric
J_{RMSE}	the RMSE-based performance metric
$\theta^{(s)}$	parameter vector sample
$(H, h_n/h_g)$	matrix-vector pair representing a polytope
(H_Δ, h_Δ)	matrix-vector pair representing the DDPS polytope in the variable ξ
$(H_{\Delta_\theta}, h_{\Delta_\theta})$	matrix-vector pair representing the DDPS polytope in the variable θ
(H_ξ, h_ξ)	matrix-vector pair representing the FPS polytope
(Φ, μ)	matrix-vector pairs representing the FPS polytope at the $N-$th time step
s, s'	current and next POMDP states
a	action selected at the current state s
$b(s), b_0$	POMDP belief state and initial belief

$V(b)$	value function evaluated at belief b
$Q(b,a)$	action-value function (expected cumulative return on taking action a from belief b)
P_{A_r}	activation probability of the recovery actions node A_r
T_{A_r}	transition probability associated with recovery action A_r
UCB	Upper Confidence Bound value
$N(b)$	total visit count of belief node b
$n(b,a)$	visit count of action a from belief node b
ρ_{grd}	grounding hazard risk indicator
ρ_{col}	collision hazard risk indicator

Constants / parameters

m	vessel mass [kg]
m_x, m_y	added masses in surge and sway [kg]
x_G	longitudinal position (x-coordinate) of center of gravity [m]
I_{z_p}	moment of inertia about the z_p-axis [kg·m^2]
J_{z_p}	added yaw moment of inertia [kg·m^2]
$X_{\dot{u}}$, $Y_{\dot{v}}$, $Y_{\dot{r}}$, $N_{\dot{v}}$, $N_{\dot{r}}$	added-mass hydrodynamic parameters [kg] / [kg·m] / [kg·m^2]
M	inertia matrix
M'	inertia matrix in MMG form
a_1, a_2, b_1, b_2, b_3, b_4	steering (Nomoto) model parameters
T_1, T_2, T_3	time constants in steering model
K	gain factor in steering model
K_1, K_2, K_4, K_6	diagonal observer gain matrices
K_{11}	sub-block of K_1 gain matrix

$k_{12}, k_{21}, k_{22}, k_{23},$ k_3, k_5, k_{61}, k_{62}	scalar observer gains
$\bar{n}_{z_k}^{(I,j)}$	bound on k-th element of sensor noise for sensor (I, j)
$\bar{\tau}_{d_i}$	bound on i-th element of disturbance vector τ_d
$\rho^{(I,j)}$, $\xi^{(I,j)}$ $\rho_d^{(I,j)}$, $\xi_d^{(I,j)}$	positive constants in adaptive threshold bounds
$\Lambda_I, \Lambda_\gamma$	bounds used in adaptive threshold expressions
$\bar{p}^{(I)}$, $\bar{\psi}^{(I)}$, $\bar{v}^{(I)}$	bounds on initial estimation error magnitudes
$\bar{u}$, $\bar{v}$, $\bar{r}$	bounds on velocity components
$\bar{\delta}_p$, $\bar{\delta}_s$, $\bar{\dot{\delta}}_p$, $\bar{\dot{\delta}}_s$	bounds on thruster angles and rates
$\lambda_{\gamma^{(I)}}$	Lipschitz constants
P_a	air density [kg/m^3]
ρ	freshwater density [kg/m^3]
c_x, c_y, c_n	wind coefficients
A_F, A_L	frontal and lateral projected areas above water [m^2]
L_{oa}	overall vessel length [m]
T	vessel draught [m]
S_W	wetted surface area [m^2]
C_F, C_W	frictional and wave-making resistance coefficients
x_P	propeller longitudinal position (x-coordinate) [m]
x_R	rudder longitudinal position (x-coordinate) [m]
x_H	longitudinal position at which additional lateral force acts [m]
t	thrust deduction factor
t_R	rudder surge-force correction factor during steering
w_{P0}	effective wake fraction in straight motion
γ_R	flow straightening coefficient at rudder

κ	experimental constant in rudder inflow model
α_H	rudder force increase factor (interaction coefficient)
D_P	propeller diameter [m]
A_R	rudder area [m^2]
B_R	rudder span [m]
C_R	rudder chord length [m]
Λ	rudder aspect ratio
l'_R	empirical constant for lateral inflow acting point at rudder
s	propeller slip ratio
η	propeller-to-rudder size ratio
$U_{C\mathrm{MAX}}$	maximum current speed at waterway centreline [m/s]
X'_H, Y'_H, N'_H	dimensionless hull force/moment quantities
R_{Sh}	shallow-water resistance coefficient [N]
R'_0	non-dimensional shallow-water resistance coefficient
$X'_{\beta\beta}$, $X'_{\beta r}$, X'_{rr}, $X'_{\beta\beta\beta\beta}$, Y'_{β}, Y'_{r}, $Y'_{\beta\beta\beta}$, $Y'_{\beta\beta r}$, $Y'_{\beta rr}$, Y'_{rrr}, N'_{β}, N'_{r}, $N'_{\beta\beta\beta}$, $N'_{\beta\beta r}$, $N'_{\beta rr}$, N'_{rrr}	MMG model hydrodynamic derivatives
F	fault signature matrix (FSM)
N_h	NMPC prediction horizon [s]
p_m	terminal cost weight
q_m, r_m	running cost weights
$\psi_{\min}, \psi_{\max}$	heading angle bounds [rad]
$u_{\min}, u_{\max}$	surge velocity bounds [m/s]
$v_{\min}, v_{\max}$	sway velocity bounds [m/s]
$r_{\min}, r_{\max}$	yaw-rate bounds [rad/s]

$\delta_{\min}, \delta_{\max}$	rudder angle limits [rad]
$\Delta_{\max}$	maximum rudder angle change per time step [rad]
A_{fw}, b_{fw}	fairway polyhedron constraints (H-representation)
$XTE_{\max}$	maximum allowable cross-track error [m]
$d_{cl,\min}$	minimum allowable distance from centreline [m]
σ_1, σ_2	SINM weighting scalars
XTE_{bl}, $\psi_{e,bl}$	baseline cross-track and heading errors [m], [rad]
X_D	LOS lookahead distance [m]
$C_{t,i}$	thrust force coefficient for the $i-$th thruster
$C_{d,0}$	base drag coefficient
$C_{d,1}$, $C_{l,1}$	the variation in drag and lift coefficients w.r.t. ϕ
θ	parameters vector
ξ	transformed parameters vector
$(\underline{\theta}, \overline{\theta})$	lower and upper bounds of the parameters vector
$(\underline{\xi}, \overline{\xi})$	lower and upper bounds of the transformed parameters vector
$(\underline{n}, \bar{n})$	lower and upper bounds of the noise signal
N_{total}	length of the total dataset
t_{CPU}	CPU time
ρ_s	Spearman rank correlation factor
γ	discount factor
C	UCB exploration coefficient
Z	normalisation constant
N_{sim}	total number of Monte Carlo simulation runs
ε	small constant (Chapter 3) ratio of wake fraction at rudder and propeller positions (Chapter 4) small constant representing a residual probability (Chapter 6)

Operators, Sets and Indices

$w \in \{1,2\}$	thruster index (port/starboard)
S_{pos}, S_{ψ}	position and heading sensors
S_{v}, S_{χ}	velocity and course-angle sensors
$I \in \{1,\ldots,N\}$	monitoring module / sensor-set index
$\mathcal{S}^{(I)}$	I-th sensor set
m_I	number of sensors in sensor set $\mathcal{S}^{(I)}$
$j \in \{1,\ldots,m_I\}$	sensor index within module I
$\mathcal{M}^{(I)}$	I-th monitoring module
$\mathcal{O}^{(I)}$	observer within the I-th monitoring module
$\mathcal{A}$	aggregator module
$\mathcal{E}_{yz}^{(I)}$	set of ARRs in module I
$\mathcal{E}_{yz}^{(I,j)}$	j-th ARR in module I
$*$	FSM entry indicating possible violation due to weak sensitivity
$\mathfrak{s}$	total number of monitored sensors
N_c	number of theoretical fault combinations
$\mathcal{F}_{c_q}$	q-th theoretical sensor fault combination
l	number of ARR rows in FSM
$h\|k$	prediction step h evaluated at current time k
$\Delta(k)$	DDPS at time step k
$\Delta_{\theta}(k)$	DDPS at time step k reformulated in terms of θ
$\Pi(k)$	FPS at time step k
I1-I17	input nodes of the BBN
INT1-INT6	nodes in the input RIFs layer of the BBN

D1-D7	nodes in the derived RIFs layer of the BBN
$\mathcal{P}$	POMDP tuple
$\mathcal{S}$	POMDP state space (cardinality n)
$\mathcal{A}$	POMDP action space (cardinality m)
$\mathcal{T}$	transition function
$\mathcal{R}$	reward function
$\mathcal{O}$	set of POMDP observations
Ω	observation function
S_s, S_u, S_r	sets of safe, unsafe, and recovery vessel states
A_s, A_u, A_r	sets of safe, unsafe, and recovery control actions

List of abbreviations

AACE	Average Absolute Control Effort
AAXTE	Average Absolute Cross-Track Error
AHRS	Attitude Heading Reference System
AIS	Automatic Identification System
ARR	Analytical Redundancy Relation
ASV	Autonomous Surface Vessel
BBN	Bayesian Belief Network
CCNR	Central Commission for the Navigation of the Rhine
CFD	Computational Fluid Dynamics
COG	Course Over Ground
DDPS	Data-driven Parameter Set
DOF	Degrees of Freedom
DP	Dynamic Positioning
DT-LIP	Discrete-Time Linear-In-Parameters
DVL	Doppler Velocity Log
ECDIS	Electronic Chart Display and Information System
EKF	Extended Kalman Filter
ENC	Electronic Navigational Chart
ETA	Estimated Time of Arrival
FDI	Fault Detection and Isolation
FSM	Fault Signature Matrix
FTC	Fault-Tolerant Control
FPS	Feasible Parameter Set
GNC	Guidance, Navigation and Control
GNSS	Global Navigation Satellite System
IMU	Inertial Measurement Unit
INS	Inertial Navigation System
IPOPT	Interior Point OPTimizer
IWRI	Inland Waterway Robustness Index
IWT	Inland Waterway Transport
IWV	Inland Waterway Vessel
KPI	Key Performance Index
LOS	Line-Of-Sight
LPV	Linear Parameter-Varying
MAXTE	Maximum Absolute Cross-Track Error
MCTS	Monte Carlo Tree Search
MMG	Maneuvering Modeling Group
MPC	Model Predictive Control
MRC	Minimum-Risk Condition
NED	North–East–Down
NLP	Nonlinear Programming
NMPC	Nonlinear Model Predictive Control
OCP	Optimal Control Problem
PID	Proportional-Integral-Derivative

PIV	Particle Image Velocimetry
POMCP	Partially Observable Monte-Carlo Planning
POMDP	Partially Observable Markov Decision Process
QP	Quadratic Program
RIF	Risk-Influencing Factor
RMSE	Root Mean Squared Error
RPM	Revolutions Per Minute
RTK	Real-Time Kinematic
SBAS	Satellite-Based Augmentation System
SCS	Safe Control Strategy
SINM	Safe Inland Navigation Metric
SMI	Set-Membership Identification
SOG	Speed Over Ground
STPA	Systems-Theoretic Process Analysis
SXTE	Signed Cross-Track Error
TPQR	Twin-Propeller and Quad-Rudder
UCB	Upper Confidence Bound
URANS	Unsteady Reynolds-Averaged Navier–Stokes
XTE	Cross-Track Error

Summary

Inland waterways offer a cost-effective, energy-efficient and relatively safer mode of freight transportation, and autonomous navigation presents an attractive opportunity to fully revitalise their utilisation. To enable a safe, efficient and reliable inland waterway ecosystem, autonomous inland vessels must account for uncertainties arising from environmental disturbances and modelling errors. In comparison to open-sea navigation, inland navigation involves confined waterways, frequent interaction with infrastructure and other vessels, and operational constraints that require both high situational awareness and constraint satisfaction. Furthermore, abnormal operating conditions resulting from critical sensor faults and failures must be tolerated through graceful performance degradation or, in the worst case, a fallback operation. In light of these operational requirements, this thesis investigates how autonomous vessels, especially (but not limited to) inland waterway vessels, can maintain safe, high-performance motion control while monitoring sensor faults and hazardous situations that affect their navigation.

More specifically, this thesis contributes an integrated framework that includes (a) a robust system identification methodology to obtain vessel maneuvering models for state estimation and prediction, (b) a Nonlinear Model Predictive Control (NMPC)-based control system that computes the vessel's control actions while satisfying the physical and operational constraints of inland waterways, (c) a multiple sensor Fault Detection and Isolation (FDI) scheme that monitors consistency in measurements by employing analytical redundancy relations and (d) a risk mitigation method that provides a fallback control action under complex failures.

Robust system identification for marine surface vessels

Maneuvering models play a central role in model-based control and monitoring system design by providing accurate estimates of the vessel's states and their future predictions. Identifying the parameters of a full-scale vessel from experimental data is particularly challenging due to significant modelling and measurement uncertainties. The first contribution of this thesis is a set-membership method for identifying key parameters of a nonlinear 3-Degrees of Freedom (3-DOF) vessel model that supports robust prediction and control design through a bounded error characterisation of the uncertainties. The identification process involves computing two sets: a Data-driven Parameter Set (DDPS) and a Feasible Parameter Set (FPS), using the system dynamics, uncertainty bounds and input-output measurements. Then, by solving quadratic programs over the FPS, parameter estimates and their uncertainty bounds are obtained. Validation results from full-scale trials demonstrate improved prediction accuracy and reduced computational time. In addition, through sensitivity analysis, the parameters most crucial for identification performance are identified.

Path-following control of inland waterway vessels in confined waterways

Inland waterways are characterised by tight operational and environmental constraints, leading to explicit control design specifications. The model predictive control methodology is adopted, as it naturally integrates multi-variable dynamics, actuators, state, environmental constraints and objectives to optimise performance and control effort. An NMPC path-following control scheme is proposed for Inland Waterway Vessels (IWVs), with the prediction model tailored to the hydrodynamic phenomena in confined waterways, including bank and shallow-water effects. Many challenging scenarios are considered for validating the control scheme through simulations, such as turning at a steep river confluence, sailing a curved river and avoiding a static obstacle. The impact of reduced ship-bank distances, propulsion speeds and river cross-section shapes further provides insights into control performance and design choices. In addition, key performance metrics are proposed to evaluate the controller's performance and quantify path-following accuracy, robustness and safety.

Multiple sensor fault diagnosis of autonomous surface vessels

Autonomous vessels rely on multiple heterogeneous sensors for navigation, motion control and situational awareness. Sensor faults may propagate through measurements to interconnected systems on board, thereby impacting downstream decisions. This thesis proposes a multiple-sensor FDI scheme that exploits Analytical Redundancy Relations (ARRs) derived from the vessel's dynamical model and adaptive thresholds to diagnose sensor faults.

The design methodology adopted in the proposed scheme includes (a) the generation of fault detection residuals having structural sensitivity to one or more sensor faults and (b) the computation of adaptive thresholds used for residual bounding with robustness against environmental and modelling uncertainties. As a result, false alarms can be avoided in the fault detection process. In addition, a combinatorial fault decision logic is designed, enabling the scheme to not only detect fault occurrence but also to determine the compromised sensors. Combined, the structurally sensitive residuals and the decision logic facilitate the isolation of multiple sensor faults. The proposed fault diagnosis scheme is suitable for continuous monitoring of faults during vessel operation, while easily accommodating variations in the vessel's actuator or sensor configurations. Furthermore, by identifying weak fault sensitivity by evaluating residuals with respect to fault magnitudes, improved fault isolation decisions are obtained.

Collision and grounding risk mitigation of inland waterway vessels

Finally, the risk mitigation of autonomous vessels is explored by considering the underlying sub-problems of risk modelling and control. For risk modelling, a Bayesian Belief Network (BBN) is built from hazard analysis results, providing transition probabilities for sequential decision-making. Thereafter, a Partially Observable Markov Decision Process (POMDP) model is designed to represent the vessel's states and provide a suitable higher-level control strategy that ensures the vessel's safety by preventing hazardous situations, such as grounding and collisions. The method is verified through an inland waterway navigation case study, which demonstrates SCS selection reliably during a complex failure scenario.

Samenvatting

Binnenwateren bieden een kosteneffectieve, energiezuinige en relatief veilige manier van goederenvervoer. Autonome navigatie biedt een aantrekkelijke mogelijkheid om het gebruik ervan volledig nieuw leven in te blazen. Om een veilig, efficiënt en betrouwbaar ecosysteem voor binnenwateren mogelijk te maken, moeten autonome binnenvaartschepen rekening houden met onzekerheden die voortvloeien uit verstoringen in het milieu en modelleringsfouten. In tegenstelling tot de open zee opereert de binnenvaart op beperkte waterwegen, met veelvuldig contact met infrastructuur en andere schepen, en onder operationele voorwaarden die zowel een hoog situationeel bewustzijn als strikte naleving van beperkingen vereisen. Bovendien moeten abnormale bedrijfsomstandigheden als gevolg van kritieke sensorstoringen en -uitval worden getolereerd door middel van geleidelijke prestatievermindering of, in het ergste geval, een terugvalprocedure. In het licht van deze operationele vereisten onderzoekt dit proefschrift hoe autonome schepen, met name (maar niet uitsluitend) binnenvaartschepen, veilige en hoogwaardige controle kunnen behouden terwijl ze sensorstoringen en gevaarlijke situaties die hun navigatie beïnvloeden, monitoren.

Dit proefschrift draagt meer specifiek bij aan een geïntegreerd raamwerk dat bestaat uit (a) een robuuste systeemidentificatie methodologie voor het verkrijgen van modellen voor scheepsmanoeuvres ten behoeve van toestandschatting en -voorspelling, (b) een op Niet-lineaire Model Predictive Control (NMPC) gebaseerd besturingssysteem dat de besturingsacties van het schip berekent met inachtneming van de fysieke en operationele beperkingen van binnenwateren, (c) een schema voor Fault Detection en Isolation (FDI) met meerdere sensoren dat de consistentie van metingen bewaakt door gebruik te maken van analytische redundantierelaties en (d) een risicobeperkingsmethode die een alternatieve besturingsactie biedt bij complexe storingen.

Robuuste systeemidentificatie voor oppervlakteschepen

Manoeuvreermodellen spelen een centrale rol in het ontwerp van modelgebaseerde besturings- en monitoringsystemen door nauwkeurige schattingen te leveren van de toestand van het schip en de toekomstige voorspellingen daarvan. Het identificeren van de parameters van een schip op ware grootte aan de hand van experimentele gegevens is bijzonder uitdagend vanwege de aanzienlijke onzekerheden in het modeleren en de metingen. De eerste bijdrage van dit proefschrift is een set-membership methode voor het identificeren van de belangrijkste parameters van een niet-lineair scheepsmodel met 3 Degrees of Freedom (3-DOF). Deze methode ondersteunt een robuust voorspellings- en besturingsontwerp door middel van karakterisering van de onzekerheden met een begrensde foutmarge.

Het identificatieproces omvat het berekenen van twee sets: een Data-driven Parameter Set

(DDPS) en een Feasible Parameter Set (FPS), gebruikmakend van de systeemdynamica, onzekerheidsgrenzen en input-outputmetingen. Vervolgens worden, door het oplossen van kwadratische programma's over de FPS, parameterschattingen en hun onzekerheidsgrenzen verkregen. Validatieresultaten van proeven op ware grootte tonen een verbeterde voorspellingsnauwkeurigheid en een kortere rekentijd aan. Daarnaast worden door middel van een gevoeligheidsanalyse de parameters geïdentificeerd die essential zijn voor de identificatieprestaties.

Pad volgregeling voor binnenvaartschepen in smalle waterwegen

Binnenwateren worden gekenmerkt door strenge operationele en milieueisen, welke leiden tot expliciete specificaties voor het ontwerp van de besturing. De model predictive control methode wordt toegepast, omdat deze op natuurlijke wijze multi-variabele dynamiek, actuatoren, toestand, milieueisen en doelstellingen integreert om de prestaties en de besturingsinspanning te optimaliseren. NMPC-padvolgschema is voorgesteld voor binnenvaartschepen, waarbij het voorspellingsmodel is afgestemd op de hydrodynamische verschijnselen in smalle waterwegen, inclusief oever- en ondiepwatereffecten. Veel uitdagende scenario's zijn toegepast om het besturingsschema te valideren door middel van simulaties, zoals het draaien bij een steile samenvloeiing van rivieren, varen op een bochtige rivier en het vermijden van een statisch obstakel. De impact van een kleinere afstand tussen schip en oever, voortstuwingssnelheden en rivier dwarsprofielen biedt verder inzicht in de besturingsprestaties en ontwerpkeuzes. Daarnaast worden belangrijke prestatiemaatstaven voorgesteld om de prestaties van de controller te evalueren en de nauwkeurigheid, robuustheid en veiligheid van het padvolgen te kwantificeren.

Meervoudige sensorfoutdiagnose van autonome oppervlakteschepen

Autonome schepen vertrouwen op meerdere heterogene sensoren voor navigatie, bewegingscontrole en situationeel bewustzijn. Sensorstoringen kunnen zich via metingen verspreiden naar onderling verbonden systemen aan boord, waardoor downstream beslissingen worden beïnvloed. Deze thesis presenteert een FDI-schema voor meerdere sensoren dat gebruikmaakt van Analytical Redundancy Relations (ARRs) afgeleid met behulp van het dynamische schip model en adaptieve drempelwaarden om sensorstoringen te diagnosticeren.

De ontwerpmethodologie die in het voorgestelde schema wordt toegepast, omvat (a) de generatie van foutdetectieresiduen die structurele gevoeligheid voor één of meer sensorstoringen vertonen en (b) de berekening van adaptieve drempelwaarden die worden gebruikt voor het begrenzen van residuen met robuustheid tegen omgevings- en modelleringsonzekerheden. Hierdoor kunnen valse alarmen in het foutdetectieproces worden vermeden. Daarnaast is een combinatorische foutbeslissingslogica ontworpen, waardoor het schema niet alleen storingen kan detecteren, maar ook de defecte sensoren kan identificeren. De combinatie van de structureel gevoelige residuen en de beslissingslogica maakt het mogelijk om meerdere sensorstoringen te isoleren. Het voorgestelde foutdiagnoseschema is geschikt voor het continu monitoren van storingen tijdens de operatie van een schip en kan gemakkelijk worden aangepast aan variaties in de actuatoren of sensorconfiguraties van het schip. Bovendien worden door het identificeren van zwakke foutgevoeligheden, door het evalueren van residuen ten opzichte van fout groottes, betere foutisolatiebeslissingen genomen.

Risicobeperking bij aanvaringen en strandingen van binnenvaartschepen

Ten slotte wordt de risicobeperking van autonome schepen onderzocht door de onderliggende deelproblemen van risicomodellering en -beheersing te beschouwen. Voor risicomodellering wordt een Bayesian Belief Network (BBN) opgebouwd op basis van de resultaten van een gevarenanalyse, dat overgangswaarschijnlijkheden levert voor sequentiële besluitvorming. Vervolgens wordt een Partially Observable Markov Decision Process (POMDP)-model ontworpen om de toestanden van het schip weer te geven en een geschikte besturingsstrategie te bieden die de veiligheid van het schip waarborgt door gevaarlijke situaties, zoals aan de grond lopen en aanvaringen, te voorkomen. De methode is geverifieerd door middel van een binnenvaartnavigatiecasestudy, die SCS-selectie betrouwbaar demonstreert tijdens een complex faalscenario.

About the author

Abhishek Dhyani was born in Dehradun, India. He obtained a Bachelor's in Technology (B.Tech.) degree in Electrical Engineering from G. B. Pant Institute of Engineering and Technology, Pauri Garhwal, India, in 2018. After this, he obtained an MS (Research) degree in Computing and Electrical Engineering from the Indian Institute of Technology, Mandi, India, in 2022.

In May 2022, Abhishek joined the Department of Maritime and Transport Technology at TU Delft as a PhD Candidate within the Marie Skłodowska-Curie Actions project AUTOBarge, supervised by Dr. V. Reppa and Prof. dr. R. R. Negenborn. Abhishek's PhD project was part of the Work Package 2: *Decide and Act*, which focused on developing safe, robust, and energy-efficient path-planning, motion-control, and fault-diagnosis algorithms for autonomous inland navigation and smart shipping. From April to June 2024, he worked as a visiting researcher at KU Leuven, Belgium. He also worked as a visiting researcher at Damen RD&I in the Netherlands from April to June 2025.

Publications

Journal Publications (included in this thesis)

1. **Dhyani, A.**, Tsolakis A., van der El, K., Negenborn, R.R. and Reppa, V., 2026. Robust Vessel Maneuvering Modelling using Set-membership Identification. Control Engineering Practice, 173, p.106936.
   (also accepted for presentation at the IFAC World Congress, 2026)

2. **Dhyani, A.**, van der El, K., Negenborn, R.R. and Reppa, V., 2026. Multiple sensor fault diagnosis for safe navigation of autonomous surface vessels. Control Engineering Practice, 168, p.106673.

3. Zhang, C., **Dhyani, A.**, Ringsberg, J.W., Thies, F., Negenborn, R.R. and Reppa, V., 2025. Nonlinear model predictive control for path following of autonomous inland vessels in confined waterways. Ocean Engineering, 334, p.121592.

Other Journal Publications

1. Saha, R., Zhang, Y.Y., Baerveldt, M., Luo, Z., Tran, H.A., Mojaveri, A.H., Mahipala, D., Zhang, C., **Dhyani, A.**, Wang, Y. and Al Amien, D., 2025. Autonomous inland waterway transport for a safer and sustainable tomorrow: The AUTOBarge Project. Societal Impacts, p.100161.

2. Kougiatsos, N., **Dhyani, A.**, Reppa, V., 2026. Integrating Rule Awareness and Semantic Reasoning in Collision-Free Vessel Path Planning. Submitted to a journal.

Conference Proceedings

1. **Dhyani, A.**, Mojaveri, A.H., Zhang, C., Mahipala, D., Tran, H.A., Zhang, Y.Y., Luo, Z. and Reppa, V., 2025. AUTOBargeSim: MATLAB (R) toolbox for the design and analysis of the guidance and control system for autonomous inland vessels. 16th IFAC Conference on Control Applications in Marine Systems, Robotics and Vehicles (CAMS). IFAC-PapersOnLine, 59(22), pp.818-823.

2. Zhang, C., **Dhyani, A.**, Ringsberg, J.W., Thies, F., Reppa, V. and Negenborn, R.R., 2024, June. Manoeuvring modelling and control design of autonomous vessels on inland waterways. In International Conference on Offshore Mechanics and Arctic Engineering (Vol. 87820, p. V05AT06A046). American Society of Mechanical Engineers.

3. **Dhyani, A.**, Wang, Y., Verbeke, M., Pissoort, D. and Reppa, V., 2024. A POMDP model-based online risk mitigation method for autonomous inland vessels. 15th IFAC Conference on Control Applications in Marine Systems, Robotics and Vehicles (CAMS). IFAC-PapersOnLine, 58(20), pp.335-340.

4. **Dhyani, A.**, Negenborn, R.R. and Reppa, V., 2024. A multiple sensor fault diagnosis scheme for autonomous surface vessels. 12th IFAC Symposium on Fault Detection, Supervision and Safety for Technical Processes (SAFEPROCESS). IFAC-PapersOnLine, 58(4), pp.31-36.

TRAIL Thesis Series

The following list contains the most recent dissertations in the TRAIL Thesis Series. For a complete overview of more than 400 titles, see the TRAIL website: www.rsTRAIL.nl.

The TRAIL Thesis Series is a series of the Netherlands TRAIL Research School on transport, infrastructure and logistics.

Abhishek, D., *Safe Navigation of Autonomous Vessels in Inland Waterways under Uncertain and Abnormal Operational Conditions*, T2026/11, May 2026, TRAIL Thesis Series, the Netherlands

Garrido-Valenzuela, F., *Pixels, People, Places: Computer Vision and Image Embeddings for Perception-Aware Urban Analytics*, T2026/10, April 2026, TRAIL Thesis Series, the Netherlands

Spierenburg, L., *Advances in the Analysis of Residential Segregation and Urban Riots*, T2026/, April 2026, TRAIL Thesis Series, the Netherlands

Boot, M., *Evaluating Experiences with Smart Cycling Technologies: Sensor-based evaluations of outdoor cycling experiences with Smart Cycling Technologies*, T2026/8, March 2026, TRAIL Thesis Series, the Netherlands

Wen, X., *Data-Driven Spatial-Temporal Modeling for Bicycle Traffic Prediction*, T2026/7, March 2026, TRAIL Thesis Series, the Netherlands

Wang, Z., *Optimising Performance of Automatic Train Operation on Railway Networks*, T2026/6, March 2026, TRAIL Thesis Series, the Netherlands

Hadi, A.H., *DEM Modelling of Multi-Component Segregation in the Blast Furnace Charging System*, T2026/5, February 2026, TRAIL Thesis Series, the Netherlands

Farhani, M., *Demand Management Strategies for Operations of Shared Mobility Services*, T2026/4, February 2026, TRAIL Thesis Series, the Netherlands

Yao, X., *Driving Heterogeneity in Traffic Flow Theory: An action-based framework for identification, modelling, and simulation*, T2026/3, January 2026, TRAIL Thesis Series, the Nether-

lands

Versluis, N.D., *Optimising Railway Traffic Management under Radio-Based Distance-to-Go Signalling*, T2026/2, January 2026, TRAIL Thesis Series, the Netherlands

Jiao, Y., *Proactive Collision Risk Quantification in Multi-directional Traffic Interactions*, T2026/1, January 2026, TRAIL Thesis Series, the Netherlands

Asadi, M., *Accessibility and Road Safety: Integration of road safety in accessibility evaluation*, T2025/20, November 2025, TRAIL Thesis Series, the Netherlands

Akse, R., *Understanding and untangling the uncertainty knot: How to catalyse decision-making in mobility innovations*, T2025/19, November 2025, TRAIL Thesis Series, the Netherlands

Führer, K., *Participatory Decision-making under Deep Uncertainty: Modelling mobility transitions*, T2025/18, November 2025, TRAIL Thesis Series, the Netherlands

Picco, A., *Monitoring and Feedback in Driving*, T2025/17, October 2025, TRAIL Thesis Series, the Netherlands

Cebeci, M.S., *Behaviour of Prosumers in Last-mile Logistics: The case of crowdshipping*, T2025/16, September 2025, TRAIL Thesis Series, the Netherlands

Kuijpers, A., *Enabling Inter-Organizational Collaboration Through Platforms: The role of trust*, T2025/15, September 2025, TRAIL Thesis Series, the Netherlands

Song, R., *Human-MASS Interaction in Decision-Making for Safety and Efficiency in Mixed Waterborne Transport Systems*, T2025/14, June 2025, TRAIL Thesis Series, the Netherlands

Destyanto, A.R., *A Method for Evaluating Port Resilience in an Archipelago*, T2025/13, June 2025, TRAIL Thesis Series, the Netherlands

Karademir, C., *Synchronized Two-echelon Routing Problems: Exact and approximate methods for multimodal city logistics*, T2025/12, May 2025, TRAIL Thesis Series, the Netherlands

Vial, A., *Eyes in Motion: A new traffic sensing paradigm for pedestrians and cyclists*, T2025/11, May 2025, TRAIL Thesis Series, the Netherlands

Chen, Q., *Towards Mechanical Intelligence in Soft Robotics: Model-based design of mechanically intelligent structures*, T2025/10, April 2025, TRAIL Thesis Series, the Netherlands

Eftekhar, Z., *Exploring the Spatial and Temporal Patterns in Travel Demand: A data-driven approach*, T2025/9, June 2025, TRAIL Thesis Series, the Netherlands

Reddy, N., *Human Driving Behavior when Interacting with Automated Vehicles and the Implications on Traffic Efficiency*, T2025/8, May 2025, TRAIL Thesis Series, the Netherlands

Durand, A., *Lost in Digitalisation? Navigating public transport in the digital era*, T2025/7,

May 2025, TRAIL Thesis Series, the Netherlands

Dong, Y., *Safe, Efficient, and Socially Compliant Automated Driving in Mixed Traffic: Sensing, Anomaly Detection, Planning and Control*, T2025/6, May 2025, TRAIL Thesis Series, the Netherlands

Droffelaar, I.S. van, *Simulation-optimization for Fugitive Interception*, T2025/5, May 2025, TRAIL Thesis Series, the Netherlands

TRAIL

Summary

Inland waterways offer a cost-effective and energy-efficient freight transport mode, yet their full potential remains underutilised. Autonomous navigation can revitalise this sector, but it must account for vessels operating under uncertain and abnormal conditions arising from environmental disturbances, modelling errors, and sensor faults. This thesis presents an integrated framework to ensure safe navigation of autonomous vessels by embedding robustness against uncertainties in motion control, real-time sensor monitoring, and risk-aware decision-making.

About the Author

Abhishek Dhyani received an MS Degree in Computing and Electrical Engineering from the Indian Institute of Technology, Mandi, in 2022. From 2022 onwards, he conducted his PhD research in the Maritime and Transport Technology Department of Delft University of Technology.

TRAIL Research School ISBN 978-90-5584-386-2

Erasmus University Rotterdam · Radboud University · rijksuniversiteit groningen · TU Delft Delft University of Technology · University of Twente. · TU/e Technische Universiteit Eindhoven University of Technology